Neutron Scattering and Muon-Spin Rotation Studies of Superconducting Materials

Alan J. Drew

Thesis Submitted for the Degree of Doctor of Philosophy of the University of St. Andrews on the 19^{th} of August 2004.

Neutron Scattering and Muon-Spin Rotation Studies of Superconducting Materials

Alan J. Drew
Department of Physics
University of St Andrews, 2004
Steve L. Lee, Primary Advisor

ABSTRACT

Small angle neutron scattering (SANS), muon spin rotation (μSR) and associated characterisation techniques have been used to measure novel properties of superconducting materials.

The coexistence of Type-I and Type-II behaviour in LaNiSn has been observed using μSR and the thermodynamic phase boundary has been identified between this behaviour and that of a conventional Type-I superconductor. In a zero field cooled state the existence of a pure Meissner state is observed only at this thermodynamic phase boundary.

The magnetic phase diagram of the high temperature superconductor $La_{1.83}Sr_{0.17}CuO_4$ has been investigated. SANS has provided the first microscopic observation of a vortex lattice and the first unambiguous evidence for a field induced hexagonal to square vortex lattice structural transition in the high temperature superconductors. This is supported by μSR measurements, which also yield information on vortex lattice pinning and the melting transition.

A preliminary SANS experiment on $La_{1.9}Sr_{0.1}CuO_4$ at low fields suggests a Bragg glass (BG) with nominally a hexagonal structure. μSR has provided unambiguous evidence for a field induced crossover from a BG to a more disordered vortex glass (VG) state and an upper limit on the crossover field is given. This is the first measurement of a disordered VG state on a system of well coupled vortex lines. Furthermore, a study of the evolution of short range order is presented that is of universal significance, as it provides experimental insights into space averaged many particle correlations in bulk systems.

Direct evidence for the coexistence of a spin density wave (SDW) with bulk superconductivity in a Ferromagnetic/Superconducting/Ferromagnetic trilayer has been obtained using low energy μSR. The apparent enhancement of the SDW amplitude in the superconducting state and the $\pi/2$ phase shift of one component of the SDW below T_c indicates a profound coupling of these two forms of spin order.

To Sarah.

Acknowledgements

First and foremost I would like to thank Stephen Lee, for his continued support and dedication to this work, as well as his in-depth knowledge and understanding of the subject matter. Another guiding light on the many experiments I have been on is Ted Forgan. Not only has he made the experiments extremely entertaining, his remarkable insight has led to lengthy in-depth discussions, helping me solve the many problems I have faced. One must not forget the other members of the group I have worked with at different times in St. Andrews: Feodor Ogrin, Ujjual Divakar, Shannon Brown, Colin Oates, David Heron and Matthew Wismayer. Naiahra Elejalde also deserves a special mention, as although my work did not overlap with hers, I feel the enlightening topics of conversation whilst sharing an office with her, worthy of note here.

I would like to thank Raffaele Gilardi and Joel Mesot for their contribution and foresight into the work on LSCO and for supplying the LSCO crystals (grown by M. Momono and M. Oda); Hubertus Luetkens, Andreas Suter, Tomas Prokscha and Elvezio Morenzoni for the training, advice, contribution and access to the slow muon equipment; Alessandro Potenza and Chris Marrows for the access to the sample growth equipment and their growth expertise; Charles Dewhurst, Bob Cubit, Alex Amato and Chris Baines for their help on experiments and Gautam Menon for his theoretical input into the interpretation of the μSR lineshapes. There are many others without whom this work would not be possible; these include (in no particular order), Stephen Brown, Demitris Charalambous, Chufo, Santiago Grigera, Andy Green, Alan Tennant, John Goff, John Allan, Christof Niedermayer and Graham Smith.

Finally, I would like to thank my wife, Sarah, for her understanding and patience through this testing time.

This Ph.D. was funded by an EPSRC scholarship; the research was supported by the EPSRC and the Swiss National Science Foundation.

Declaration

I, Alan J. Drew, hereby certify that this thesis, which is approximately 50,000 words in length, has been written by me, that it is the record of work carried out by me and that it has not been submitted in any previous application for a higher degree.

date 16.2.05 signature of candidate .

I was admitted as a research student in October 2000 and as a candidate for the degree of PhD in October 2001; the higher study for which this is a record was carried out in the University of St. Andrews between October 2000 and August 2004 .

date 16.2.05 signature of candidate ...

I hereby certify that the candidate has fulfilled the conditions of the Resolution and Regulations appropriate for the degree of PhD in the University of St. Andrews and that the candidate is qualified to submit this thesis in application for that degree.

date ..... signature of supervisor .....

In submitting this thesis to the University of St. Andrews I understand that I am giving permission for it to be made available for use in accordance with the regulations of the University Library for the time being in force, subject to any copyright vested in the work not being affected thereby. I also understand that the title and abstract will be published, and that a copy of the work may be made and supplied to any bona fide library or research worker.

date 16.2.05 signature of candidate .....

Contents

List of Figures

List of Tables

List of Abbreviations

B - the Backwards detector (in the context of the μSR spectrometers at PSI)
BCS - Bardeen, Cooper and Schrieffer
Bi2212 - $Bi_2Sr_2CaCu_2O_{8+x}$
BG - Bragg Glass
BSCCO - $Bi_2Sr_2CaCu_2O_{8+x}$
D - the Down detector (in the context of the μSR spectrometers at PSI)
F - the Forward detector (in the context of the μSR spectrometers at PSI)
FLL - Flux Line Lattice
FM - Ferromagnetic
FWHM - Full Width Half Maximum
GL - Ginzburg Landau theory
GPS - General Purpose Spectrometer. An instrument on the piM3 beamline at PSI
HTC - High Temperature Superconductors/Superconductivity/Superconducting
IL - Irreversibility Line
ILL - Institute Laue Langevin
L - the Left detector (in the context of the μSR spectrometers at PSI)
La214 - $La_{2-x}Sr_xCuO_4$
LEM - Low Energy Muon
LD - Line Disorder
LF - Longitudinal Field
LOFF Larkin Ovchinnikov Fulde Farrell mechanism
LSCO - $La_{2-x}Sr_xCuO_4$
LTF - Low Temperature Facility. An instrument on the piM3 beamline at PSI
M - the M counter (in the context of the μSR spectrometers at PSI)
MCP - MicroChannel Plate
ME - Maximum Entropy
MEM - Maximum Entropy Method
MORE - Muons On REquest
N - Normal metal (when used in context of thin film heterostructures)

PNR - Polarised Neutron Reflectometry/Reflectivity

PPMS - Quantum Design Physical Properties Measurements System

PSI - Paul Scherrer Institute

QP - Quasi Particles

R - the Right detector (in the context of the μSR spectrometers at PSI)

RKKY - Ruderman Kittel Kasuya Yisida

RMS - Root Mean-Square

S - Superconducting (when used in context of thin film heterostructures)

SANS - Small Angle Neutron Scattering

SDW - Spin Density Wave

SPNR - Spin Polarised Neutron Reflectometry/Reflectivity

T_c - Superconducting Critical Temperature

TD - Time Differential

TDC - Time Differential Controllers

TF - Transverse Field

TOF - Time Of Flight

U - the Up detector (in the context of the μSR spectrometers at PSI)

VG - Vortex Glass

VL - Vortex Lattice

VSM - Vibrating Sample Magnetometer

μSR - Muon Spin Rotation/Resonance/Relaxation

WiMDA - Windows Muon Data Analysis

Y123 - $YBa_2Cu_3O_x$

YBCO - $YBa_2Cu_3O_x$

ZF - Zero Field

Chapter 1

Introduction

1.1 Organisation of this Thesis

This work is devoted to the understanding of magnetic phenomenon in several superconducting materials. The main topics of interest are the superconducting properties of LaNiSn, the vortex matter of $La_{2-x}Sr_xCuO_4$ and the interaction of magnetism and superconductivity of Fe/Pb/Fe. Several complementary techniques have been employed and a summary of the techniques used and organisation of this thesis is given below. Due to the differences between the different materials used in this work, each chapter has a separate introduction and conclusion, some of which is repeated in the last chapter (Conclusions, Chapter 7). There is also some overlap between the introduction given in this chapter and with various parts of this thesis.

In Chapter 2, an introduction to some of the relevant theories of superconductivity is given. Furthermore, a summary of vortices in superconductors is given followed by an introduction to magnetism. This chapter is intended as an overview to some of the physics investigated in this thesis and not as an in-depth review.

Chapter 3 contains a review of the major experimental techniques and subsequent data analysis for the work presented in this thesis. The experimental techniques covered are Small Angle Neutron Scattering (SANS), Muon Spin Rotation (μSR) and Low Energy Muon Spin Rotation (LEM). Although other techniques have been used these are not included in this chapter, as they are either sample characterisation or are not relied upon for any major conclusions. For this reason, only a very brief description of the technique is included in the main discussion and not a more in-depth (stand alone) review, as found in Chapter 3.

Chapter 4 contains μSR measurements on LaNiSn. Measurements were performed at ISIS and the Paul Scherrer Institute (PSI). It contains a discussion of the coexistence of Type-I and Type-II behaviour in LaNiSn and subsequent interpretation.

Chapter 5 contains measurements on the HTC $La_{2-x}Sr_xCuO_4$ and it is divided into four sections. Firstly, bulk magnetisation measurements for overdoped ($La_{1.83}$ $Sr_{0.17}$ CuO_4) and underdoped ($La_{1.9}Sr_{0.1}CuO_4$) compound are considered, followed a section detailing a SANS study of the vortex lattice in the overdoped regime. Thirdly, a study of the overdoped regime using muon spin rotation is combined with the first two sections to form a magnetic phase diagram. The fourth and final section deals with muon spin rotation studies on the underdoped compound and once combined with the bulk magnetisation, a magnetic phase diagram is formed.

Chapter 6 contains the work carried out on Fe/Pb/Fe thin films. Firstly, a discussion of film preparation (Magnetron Sputtering) and characterisation is carried out. Techniques used for characterisation are Low and High Angle X-Ray Reflectivity, Polarised Neutron Reflectivity, AC-Transport and Magnetisation measurements. The final section on Low Energy Muon Spin Rotation and the associated analysis contains the main results of this chapter.

A summary of the conclusions for the whole thesis and discussion of possible further work can be found in Chapter 7.

1.2 Historical Overview

Superconductivity was first discovered in 1911, when the Dutch physicist Heike Kamerlingh Onnes measured zero electrical resistance in mercury [Onnes, 1911]. This was possible due to his successful liquification of helium on July 10 1908, thus allowing experiments to be performed at unprecedentedly low temperatures. A second characteristic of superconductors, the expulsion of an external magnetic field, was discovered later in 1933 by Meissner and Ochsenfeld [Meissner and Ochsenfeld, 1933], establishing that the superconducting state forms a new thermodynamic phase. Perfect diamagnetism was first described by the London brothers in 1935 [London and London, 1935] (as well as other numerous thermodynamic and electromagnetic aspects of the superconducting state) by assuming the superconducting state is described by a spatially invariant order parameter. However discrepancies with experiment remained, particularly in films subject to a parallel magnetic field, where the expression for the critical field $H_{c||}$ failed. The London approach was also insufficient to describe the Shubnikov phase observed in 1937 [Shubnikov *et al.*, 1937], a mixed state of normal and superconducting regions, commonly referred to as a vortex state. A spatially varying order parameter was first introduced by Ginzburg and Landau [Ginzburg and Landau, 1950] in 1950, based on Landau's phenomenological theory of phase transitions [Landau, 1937]. In setting up their famous energy functional they allowed for the presence of a magnetic field. The ability to incorporate variations in the order parameter due to boundary conditions, external magnetic fields and currents, allowed them to remedy the deficiencies of the London theory, thus providing the complete phenomenological description of a charged quantum fluid.

A convincing microscopic theory of superconductivity was developed by Bardeen,

Cooper and Schrieffer (BCS) in 1957 [Bardeen *et al.*, 1957b,a]. In the BCS-theory, an electron-phonon interaction results in the formation of pairs of electrons (Cooper pairs) below a critical temperature T_c. The different pairs are strongly coupled to each other and form a condensate consisting of a fraction of the conduction electrons. Due to a finite pair size, one cannot break up a single Cooper pair without affecting all the others. As a consequence, the amount of energy to break a Cooper pair must exceed a critical value, known as an energy gap. Another significant theoretical advancement came in 1962 when Brian D. Josephson, a graduate student at Cambridge University, predicted that electrical current would flow between two superconducting materials - even when they are separated by a non-superconductor or insulator [Josephson, 1962]. This tunnelling phenomenon is today known as the "Josephson effect" which has been applied to many electronic devices (such as a SQUID magnetometer) and is a useful construct when understanding a layered system such as the High Temperature Superconductors.

1.3 The High Temperature Superconductors

In 1986, Georg Bednorz and Alex Müller, working at IBM in Zürich, were experimenting with a particular class of metal oxide ceramics called perovskites, surveying hundreds of different oxide compounds. Working with ceramics of lanthanum, barium, copper and oxygen they found indications of superconductivity at 35 K, a startling 12 K above the old record for a superconductor [Muller and Bednorz, 1986] (see Figure 1.1). In February of 1987 [Wu *et al.*, 1987], a perovskite ceramic material was found to superconduct at 90 K. Because these materials superconduct at significantly higher temperatures than previously thought possible (currently up to 164 K for $HgBa_2Ca_2Cu_3O_9$ under pressure), they are referred to as High Temperature Superconductors (HTC).

The HTC's have a complex layered metal oxide structure and display the mechanical and physical properties of ceramics. For example, $YBa_2Cu_3O_x$ (YBCO) is a very common Type II superconductor and its crystal structure is depicted in Figure 1.2. A key element to the behaviour of these materials is the presence of planes containing copper and oxygen, yielding anisotropic electrical and magnetic properties (both in the normal and superconducting state). The HTC's are considerably different from their conventional counterparts. Not only do they have much larger

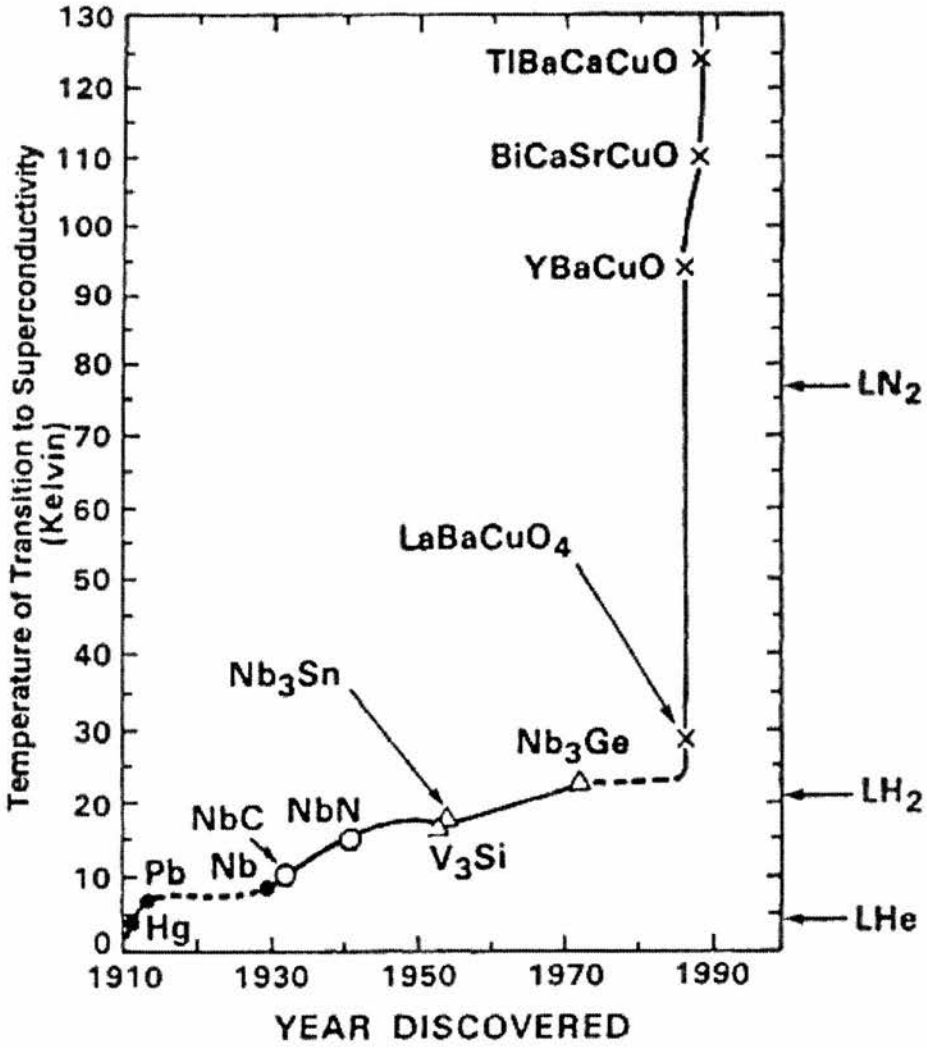

Figure 1.1: The history of superconducting transition temperatures.

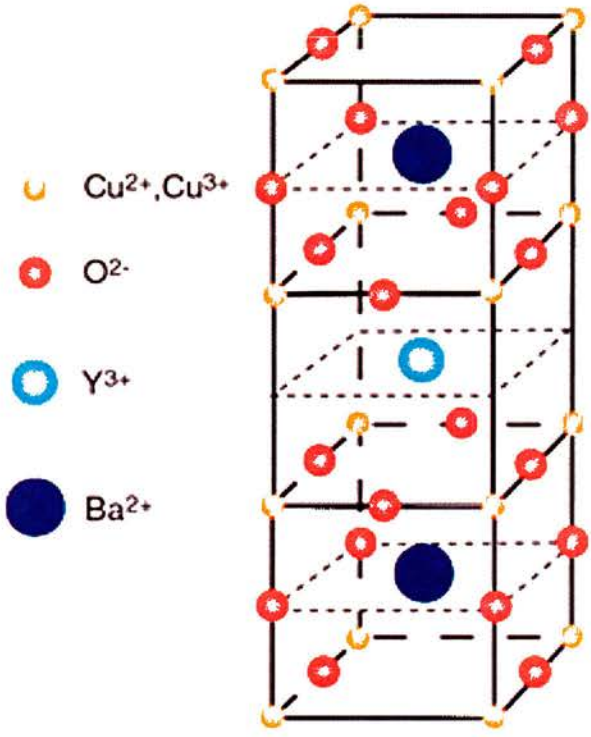

Figure 1.2: The crystal structure of YBCO

critical temperatures, the current density and upper critical field are also considerably higher, as can be seen from Figure 1.3. Furthermore, the HTC's anisotropy coupled with the higher temperatures and fields allows an interesting and varied vortex matter behaviour to be measured.

All cuprates have similar properties and structural peculiarities. These materials are all built of a stacking of CuO_2 planes separated by different layers (the charge reservoirs) and it is generally believed that the copper oxide planes are essential to the mechanism of the HTC's. While conventional superconductors are good metals in their normal state and are well described by the Fermi liquid theory, HTC's are highly correlated electron systems and bad metals, with normal state properties that do not resemble at all those of a Fermi liquid [Varma *et al.*, 1989; Varma, 1997; Nakamae *et al.*, 2003].

The parent (non-superconducting) compound of each family of the HTC's is an antiferromagnetic Mott insulator, which is transformed into a metal by introducing a concentration of doped charge carriers into the CuO_2 planes. The doping is usually done by chemical substitution: for example, one can induce holes by substituting La^{3+} ions with Sr^{2+} ions in $La_{2-x}Sr_xCuO_4$(LSCO) or increase the oxygen content in YBCO and $Bi_2Sr_2CaCu_2O_{8+x}$(BSCCO). The generic phase diagram of an HTC

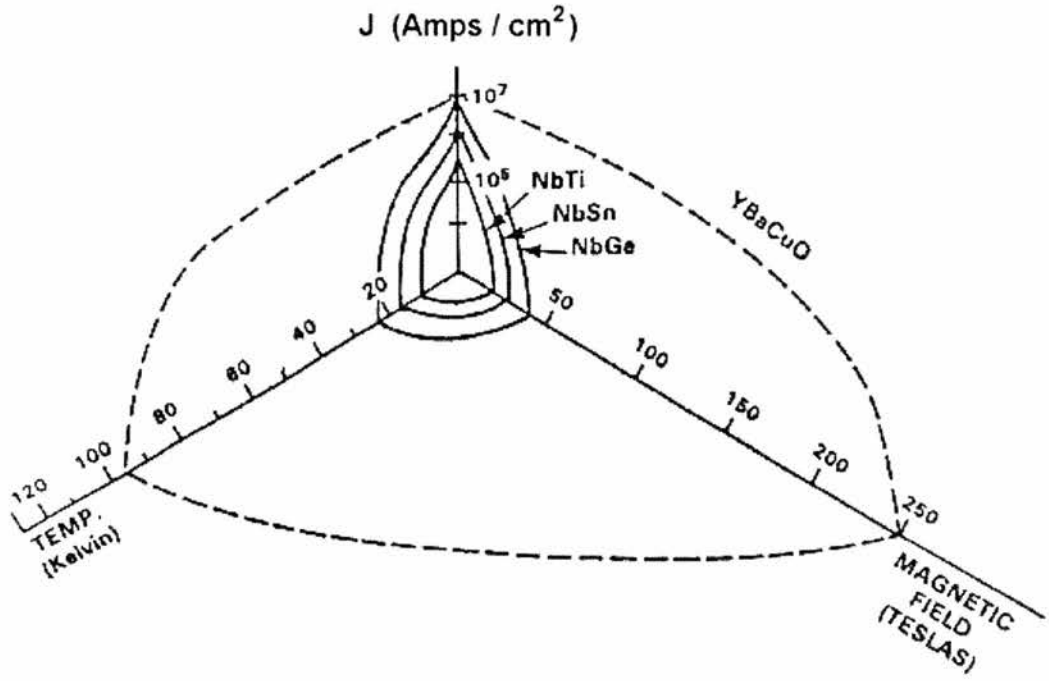

Figure 1.3: The relationship between critical current, critical field and critical temperature for several superconductors.

is shown in Figure 1.4. As a function of increasing doping, the Neel temperature is suppressed to zero and long-ranged antiferromagnetism is replaced by a "strange" metal. At low temperatures the system eventually becomes superconducting with a transition temperature T_c which first increases (underdoped region), then reaches a maximum value at an optimal doping level, decreases (overdoped region) and finally vanishes. The so called "pseudogap" corresponds to a region in which a number of quantities, including the spin susceptibility and electronic density of states, are suppressed [Timusk and Statt, 1999].

μSR reveal the presence of a "spin-glass" like state in the underdoped regime of LSCO [Niedermayer *et al.*, 1998] and inelastic neutron scattering experiments reveal the existence of spin excitations in the overdoped regime [Yamada *et al.*, 1998]. In optimally doped YBCO, the spin excitation spectrum obtained from inelastic neutron scattering experiments is dominated by a so-called "magnetic resonance" located at the commensurate AF zone centre (π, π) [Rossat-Mignod *et al.*, 1991], which has been shown to be of magnetic origin [Mook *et al.*, 1993]. Similar observations have been noted in other HTC systems [Fong *et al.*, 1999; He *et al.*, 2001; Mesot *et al.*, 2000; He *et al.*, 2002]. More recently, incommensurate peaks have been observed in YBCO [Bourges *et al.*, 2000; Dai *et al.*, 2001; Hayden *et al.*, 2004]. An

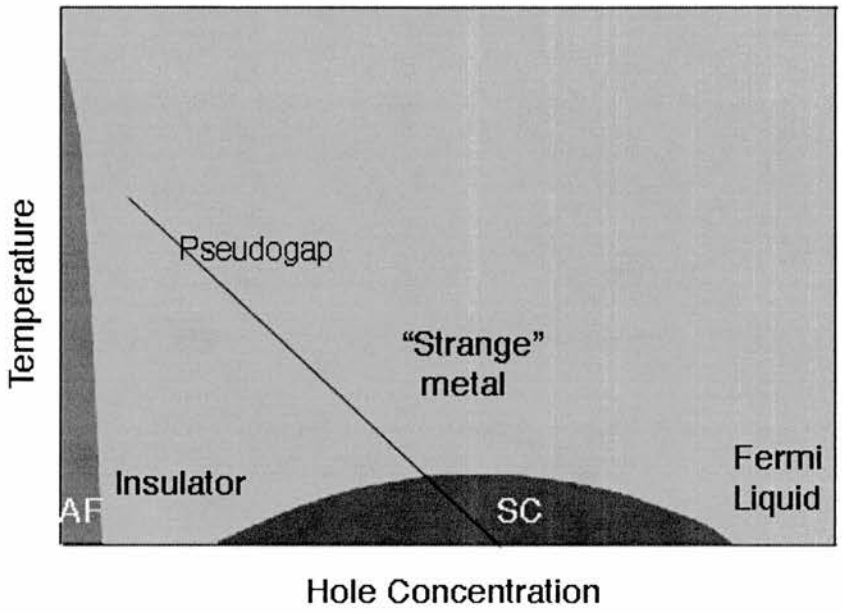

Figure 1.4: Generic phase diagram of an HTC.

introduction to some of the issues specific to LSCO can be found in Chapter 5.

The numerous types of competing magnetic order that coexist with the HTC's and the failure of Fermi liquid theory to describe the normal state requires an entirely different approach to understand much of the physics and the mechanism of the HTC's. Almost 20 years after their discovery and after ~100,000 scientific papers, the mystery of the HTC's is still unresolved.

1.4 The Magnetic Phase Diagram

The superconducting mixed state provides an intriguing system for investigation, from both a fundamental research and applications point of view. Superconducting vortex physics provides a unique system to study the crystal structure, as one can change the vortex density simply by varying the magnetic field. By performing investigations as a function of applied field, temperature and anisotropy (by varying doping in the HTC's, for example), it is possible to measure a wealth of information as the vortices go through various thermodynamic phase transitions. Furthermore, the "magnetic crystal" has a considerably larger lattice parameter than any perturbing influence (such as pinning to the crystal lattice), providing the

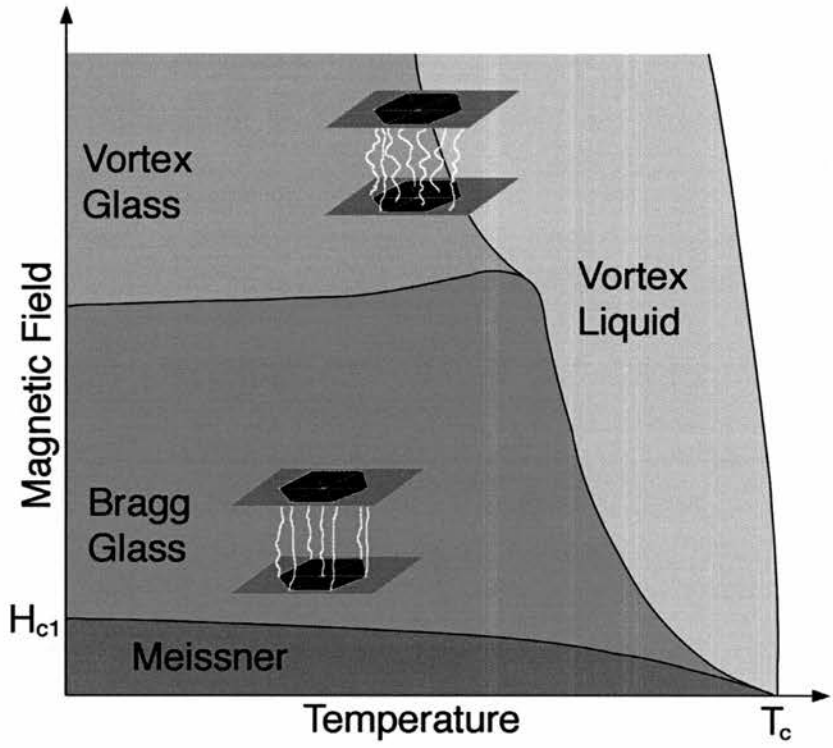

Figure 1.5: Schematic diagram of the generic magnetic phase diagram for an HTC, consisting of the Meissner state, a Bragg Glass, Vortex Glass and Vortex Liquid.

unique opportunity to investigate the combined effects of disorder and thermal fluctuations on a crystal. For the HTC's, some of these features are depicted in Figure 1.5. This will be dealt with in more detail in Chapters 2 and 3 [for a full review, please consult Blatter *et al.*, 1994].

From a practical point of view, several of the applications of superconductivity require operation at high temperatures (i.e above liquid N_2) and high magnetic fields, as well as the capability to deal with large currents without dissipation. From Figure 1.3, it is clear HTC's are well suited to these requirements. However, if an external current is applied perpendicular to the vortex lattice, the field generated due to this current will create vortices. These vortices feel a Lorentz force which causes them to move, resulting in an electric field. Therefore the system would have finite resistance. In order to have resistance-free bulk transport one must reduce flux-flow to a minimum, which can be achieved by introducing additional pin sites by materials processing.

1.5 Previous Work on Vortices in the High Temperature Superconductors

Macroscopic measurements (e.g. DC magnetisation, AC susceptibility, resistivity...) have been extensively used to characterise the properties of the HTC's. Not only are these techniques extremely useful to check sample quality (e.g width of superconducting transition) one can extract some key parameters, such as the coherence length, penetration depth and the anisotropy [See, for example, Sasagawa *et al.*, 1998, 2000; Li *et al.*, 1993; Suzuki and Hikita, 1991; Hofer *et al.*, 2000]. Furthermore, large scale changes in the vortex behaviour can be mapped out with magnetisation data. A considerable body of literature is devoted to such studies [See, for example, Dewhurst *et al.*, 1996; Kes *et al.*, 1996; Klein *et al.*, 1994]. A full review of vortex matter in the HTC's can be found elsewhere [Blatter *et al.*, 1994].

Despite belonging to the family of the first HTSC to be discovered, the magnetic phase diagram of LSCO has not been extensively investigated using microscopic techniques when compared with some of the other cuprates, such as YBCO or BSCCO. This is in part due to large, high quality single crystals being unavailable until recently and some limitations due to fundamental parameters.[1] As a consequence, studies of the vortex matter phase diagram for single crystal LSCO have mainly been restricted to magnetisation measurements [See, for example, Radzyner *et al.*, 2002b,a; Kimura *et al.*, 1992; Kodama *et al.*, 1997]. A second peak in the M-H loops ("fishtail") is observed and usually interpreted as indicating a vortex order-disorder transition. In depth studies of the subtle differences in the details of the fishtail anomaly (width, temperature dependence, time dependence and history effects) have yielded many conclusions regarding the vortex matter of LSCO, but few or no microscopic measurements were taken in support. Although features in magnetisation data can be useful to track large scale vortex transitions in considerable detail, any attempt to interpret these features without a good microscopic investigation should be treated with caution. Similar bodies of evidence exist for YBCO and BSCCO [See, for example, Dewhurst *et al.*, 1996; Kes *et al.*, 1996; Klein *et al.*, 1994], but with the advantage of microscopic studies being available to aid the interpretation.

There is a large body of literature associated with the microscopic study of vortex matter of YBCO and the discussion here has been limited to the study

[1] e.g the penetration depth is much longer for LSCO than in either BSCCO or YBCO, yielding difficult SANS experiments.

of microscopic single crystal data.[2] Most of the work has been measured using twinned crystals (until around 1999, when large de-twinned crystals necessary for SANS and μSR experiments became available), leading to confusion over the origin of observed vortex matter phenomenon. For example, although an intrinsic square flux line lattice (FLL) in YBCO has very recently[3] been observed in an untwinned crystal [Brown *et al.*, 2004], the origin of an observed square diffraction pattern in a SANS experiment remained a source of debate for some time [Keimer *et al.*, 1994; Johnson *et al.*, 1999; Yethiraj *et al.*, 1993; Forgan and Lee, 1995]. It was found that twin plane pinning has a significant effect on the vortex orientation [Johnson *et al.*, 1999], explaining the misinterpretation of the original diffraction data [Keimer *et al.*, 1994]. Despite this confusion, it is now generally believed that the intrinsic vortex lattice symmetry of untwinned YBCO is hexagonal at low magnetic fields, gradually changing to square on approaching 11T [Brown *et al.*, 2004].

In YBCO, SANS experiments gave the first indications for an abrupt change of the flux lattice structure along a line in the B-T phase diagram [Forgan *et al.*, 1990; Yethiraj *et al.*, 1993], commonly referred to as a "melting line". However, the twin planes in YBCO can also mask the underlying nature of the melting transition. The melting transition has been argued to be a continuous transition [Gammel *et al.*, 1988], which was later shown to be a 1st order transition [Schilling *et al.*, 1997] in untwinned samples using differential thermal analysis. It was found the order of the transition is influenced by the number of defects within the crystal, where an "excess" of pinning of any kind drives the transition to be second order. However, it is possible to achieve a first order transition in a heavily twinned sample above a field of 6T, but second order transition is observed at lower fields [Junod *et al.*, 1997], indicating the nature of the transition has a field dependence. Microscopic measurements remained elusive until relatively recently due to the effects of twin planes [Aegerter *et al.*, 1998], where a second order melting transition was observed in a twinned crystal. However, SANS experiments indicate a "smoothed" first order transition in untwinned crystals [Aegerter *et al.*, 1999].

The question regarding what a melting transition actually "is", is considered in the literature [for a review, see Blatter *et al.*, 1994]. The point at which the vortices become irreversible, corresponding to when the vortices have sufficient energy to overcome the pinning potentials, does not always coincide with the melting line. There is debate regarding whether one can describe the FLL to be melted when it is

[2]There is also a large(r) body of work performed on polycrystalline samples. This work has not been discussed.

[3]The results on LSCO presented in this thesis precedes the YBCO work by around 2 years

still irreversible; the vortices can not be interacting as a "liquid" when their motion is still governed by pinning potential. The related effect that is commonly referred to as the "depinning" line [See, for example Brandt, 1991b; Bondarenko *et al.*, 2004] is readily observed in the HT phase diagram of the HTC's. As discussed above, features observed in the magnetisation data are usually attributed to a change in the pinning regime. There is no firm consensus between experimental results from different samples of nominally the same compound or the exact origin of the observed features, as individual samples will have different crystallographic defects or sample geometry. The features, however, are generally present in all HTC's, even if they are not completely reproducible.

The highly anisotropic nature of BSCCO complicates the vortex structure in this compound considerably, as highly flexible vortex lines make them extremely susceptible to thermally and pinning induced disorder [Cubitt *et al.*, 1993; Lee *et al.*, 1993, 1995]. A more appropriate description is obtained by considering the vortices as a string of 2D "pancake" vortices, each confined to a CuO layer weakly coupled between layers [Lee *et al.*, 1997]. Weak electromagnetic coupling dominates large areas of the magnetic phase diagram. Consequently, a first order melting transition is easily observed well below T_c [Cubitt *et al.*, 1993; Lee *et al.*, 1993, 1995, 1997], where the vortices melt into a 2D pancake gas. The 2D nature of the vortices in BSCCO allowed the melting line to be measured with relative ease [Cubitt *et al.*, 1993; Lee *et al.*, 1993, 1995], where it is also possible to measure a crossover from a 3D to 2D state as the magnetic field is increased.

As briefly mentioned above, the measurement of microscopic transitions of the FLL in LSCO has remained elusive. SANS measurements remain difficult, as the penetration depth is λ_{ab}=2400Å for x=0.17, which is considerably longer than in BSCCO or YBCO. This reduces the neutron scattering intensity considerably in a SANS experiment, as $I \propto 1/\lambda_{ab}^4$ (Equation 3.31). There is also a problem with twin planes as the low temperature CuO structure is orthorhombic, yielding multi-domain vortex lattices with different orientations governed by the twin orientation, increasing the complexity of SANS diffraction patterns considerably. Another obstacle is that it is relatively difficult to grow the high quality, large single crystals needed for both μSR and SANS experiments. Experiments on polycrystalline samples yield results that are averaged over many different magnetic (vortex) domains pinned to different crystal orientations and grain boundaries.

Despite these problems, LSCO has some very attractive properties for studying

the FLL. LSCO has an anisotropy in the region of $\gamma \sim 20$, which puts it directly between the extreme 2D nature of BSCCO and the 3D nature of YBCO. Additionally, γ can be controlled systematically by varying the Sr doping. The significance of these parameters can be understood by considering the Josephson length $\lambda_J = \gamma s$, where s is the spacing between CuO planes. The ratio of λ_J to λ_{ab} determines the effectiveness of the Josephson currents tunnelling between planes which maintain the stiffness of the vortex. In BSCCO $\lambda_J/\lambda_{ab} > 1$ leading to extremely flexible 2D vortices and in YBCO $\lambda_J/\lambda_{ab} \ll 1$, so rigid vortex lines are formed. LSCO has a $\lambda_J \approx 250$Å, meaning the vortices are relatively straight but susceptible to transverse fluctuations.

Quenched random pinning of vortices destabilises the long ranged translational order of the vortex lattice, leading to a disordered "glassy" phase [Blatter *et al.*, 1994]. At least two glassy phases exist as a consequence of such disorder [Fisher *et al.*, 1991; Nattermann, 1990; Giamarchi and Doussal, 1995, 1997]. The most ordered of these phases is the Bragg glass phase,[4] where translational correlations decay as power laws [Nattermann, 1990; Giamarchi and Doussal, 1995, 1997], leading to quasi-long range order of vortices in the superconductor. At increased levels of pinning, the Bragg glass is unstable and a vortex glass (VG) phase is formed, where the translational correlations decay exponentially [Giamarchi and Doussal, 1997; Gingras and Huse, 1996]. The VG phase has been reported to be a distinct thermodynamic phase [Fisher *et al.*, 1991], separated from the disordered liquid phase by a continuous phase transition [Giller *et al.*, 1997; Misat *et al.*, 1999], also known as a crossover. The properties of LSCO make it an ideal candidate for microscopically measuring the predicted VG phase [Brandt and Mikitik, 2001; Giamarchi and Doussal, 1997], as the vortices are still "lines" but susceptible to transverse fluctuations.

1.6 Previous Work on Magnetic/Superconducting Multilayers

Advances in thin film fabrication techniques [Jin and Ketterson, 1989, and references therein] have renewed research interest in Superconducting (S) / Ferromagnetic (FM) multilayers and a number of new and sometimes controversial phenomena

[4] When referring to a "vortex lattice", one usually means a "Bragg glass". These two terms are used indistinguishably in this thesis.

have been observed. For S/FM multilayers, it is expected that the superconducting transition temperature decreases monotonically with increasing magnetic layer thickness. Not long after non-monotonic behaviour was observed [see, for example Wong *et al.*, 1986], the possibility of an oscillating T_c as the magnetic layer thickness increased was shown theoretically [Radovic *et al.*, 1991], where it was found the phase of the superconducting wavefunction exhibits oscillations in the FM layer.

For the case of a magnetic layer bounded on both sides by superconducting material, the phase of the order parameter across the two superconducting layers can be different, which was convincingly reported recently [Kontos *et al.*, 2001, 2002; Guichard *et al.*, 2003]. The value of the phase difference depends on the layer thickness compared to the wavelength of the spatial oscillation. For example, with an odd number of half wavelengths across the layer the phase difference would be π radians. However, the theoretical construct outlined above [Radovic *et al.*, 1991] is only valid in the case of high transparency of the S/F boundary and for the specific structure of a FM between two superconducting films. Although a number of publications observed the non-monotonic behaviour of T_c in relevant systems see for example, [Strunk *et al.*, 1994; Jiang *et al.*, 1995; Ogrin *et al.*, 2000]), which is predicted by this theory, a number of groups observed similar behaviour in FM/S/FM tri-layers [Muhge *et al.*, 1996, 1997]. This theoretical description is therefore insufficiently general to explain these results.

An alternative theory explains both the trilayer and multilayer phenomena [Khusainov and Proshin, 1997, 2000] with no limitations on boundary transparency. The mechanism is built on a Larkin Ovchinnikov Fulde Farrell (LOFF) type mechanism, where the superconducting pairs tunnel into the FM region (the proximity effect) and acquire finite momentum. The superconducting ground state is therefore different from that of a BCS paired state. In this theory, the exchange field is periodically compensated by oscillations in the superconducting pair amplitude, leading to an oscillatory SDW. This oscillatory behaviour leads to a non-monotonic oscillatory dependence of the critical temperature as a function of FM thickness.

The theoretical advances described above have led to considerable experimental interest in S/FM thin films. Unfortunately, in most experimental systems studied, complications due to interface roughness/alloying mean there is not always a sharp S/FM interface, but a continuous change between the superconducting and ferromagnetic properties; the theoretical predictions are only valid for clean S/FM interfaces. Firstly, oscillatory behaviour of T_c was observed in V/Fe multilayers [Wong *et al.*, 1986], but later not observed in the same system [Koorevaar *et al.*, 1994]. The

non-monotonic behaviour was reported for Nb/Gd multilayers and Nb/Gs/Nb trilayers [Jiang *et al.*, 1996, 1995], for Fe/Nb/Fe trilayers [Muhge *et al.*, 1996, 1997] and for Nb/Co and V/Co multilayers [Obi *et al.*, 1999]. However, negative results were reported for Nb/Gd/Nb trilayers [Strunk *et al.*, 1994], for Ge/Nb bilayers [Muhge *et al.*, 1998] and for Nb/Fe multilayers [Verbanck *et al.*, 1998]. Therefore it is highly desirable to have a system in which very little alloying occurs. For this reason the Pb/Fe system is an ideal system, as there is very little solubility between the metals (even in the liquid state!) [Kubaschewski, 1982; Lazar *et al.*, 2000]. Indeed, non-monotonic oscillations in T_c as a function of FM thickness are observed in sputtered Fe/Pb/Fe trilayers [Lazar *et al.*, 2000], although a non-ideal growth mechanism can lead to large interface roughness [Garif'yanov *et al.*, 1998].

For a normal metal/ferromagnet multilayer, the exchange field can cause a periodic oscillation of the electron-spin density inside the normal layer. The period of the oscillation is determined by extremal spanning vectors of the Fermi surface, via an enhancement of the wavevector-dependent susceptibility at these values [Martin, 1967], similar to the RKKY interaction. Using a spherical Fermi surface, RKKY predicts a single short oscillation [Yafet, 1987], corresponding to the Fermi wavevector. When a more realistic Fermi surface is used (i.e non-spherical), however, multiple-period oscillations are expected [Roth *et al.*, 1966], corresponding to spanning vectors connecting different parts of the Fermi surface. Another model which may be used in this situation is a quantum confinement of conduction electrons in the normal metal spacer layer [Bruno and Chappert, 1991; Bruno, 1991; Bruno and Chappert, 1992], leading to sharp features in the density of states at specific q-vectors.

There have been a number of observations of multi-periodic oscillations in the coupling of two FM layers across a non-magnetic wedge shaped spacer (using scanning electron microscopy with polarisation analysis), most notably in the Fe/Cr/Fe(001) system [Unguris *et al.*, 1991], with the superposition of short ($\sim$2 monolayers) and long ($\sim$10 monolayers) periods. Other systems to have been measured are Fe/Mn/Fe(001) [Purcell *et al.*, 1992], Co/Cu/Co(001) [Johnson *et al.*, 1992] and Fe/Au/Fe(001)[Fuss *et al.*, 1992]. Further observations of interlayer exchange coupling in ferromagnetic/normal metal thin films are numerous. For example, systems such as Fe/Cu, Pd, Ag, Au/Fe trilayers [Celinski and Heinrich, 1991], Co/Cu and Fe/Cu trilayers [Coehoorn, 1991], Fe/Ag trilayers [Celinski *et al.*, 1993; Unguris *et al.*, 1993, 1994, 1997] and Gd/Y trilayers [Majkrzak *et al.*, 1986] have been studied. These experimental observations agree well with current theoretical understanding.

Low Energy μSR has recently been successfully applied to investigating the properties of an Fe/Ag/Fe film [Luetkens *et al.*, 2003], where a Spin Density Wave (SDW) emanating from the Fe into the Ag has been *directly* observed. As mentioned above, the existence of a LOFF type state inside the ferromagnetic layers has been convincingly reported [Khusainov and Proshin, 1997, 2000; Kontos *et al.*, 2001, 2002; Guichard *et al.*, 2003], but relatively little attention has been paid to the related effects in the superconducting layer. The Low Energy μSR technique is ideally suited to investigating these superconducting properties.

Chapter 2

Introduction to Theory

2.1 Introduction to Superconductivity

2.1.1 The London Model

In 1935 the London brothers [London and London, 1935] showed that perfect diamagnetism observed in 1933 [Meissner and Ochsenfeld, 1933] could be described easily by the assumption that the supercurrent density $\boldsymbol{J_s}$ is proportional[1] to the vector potential $\boldsymbol{A}$. They suggested that for a superconductor

$$\Lambda \boldsymbol{J_s} = -\mu_o \boldsymbol{A} \tag{2.1}$$

where $\Lambda = m_e/2n_c e^2$ and m_e is the effective mass of the current carriers, n_c the corresponding Cooper pair number density and e electronic charge. Substituting Maxwell's equations into Equation 2.1 yields the following result

$$\nabla^2 \boldsymbol{B} = \frac{\boldsymbol{B}}{{\lambda_L}^2} \tag{2.2}$$

where λ_L is the characteristic length known as the London penetration depth $(\Lambda/\mu_o)^{\frac{1}{2}}$ $= (m_e/2n_c e^2)^{\frac{1}{2}}$. A simple solution to this is of the form $\boldsymbol{B}(r) = \boldsymbol{B}_o \exp(-r/\lambda_L)$, where $\boldsymbol{B}(r)$ is the magnetic field penetrating the sample at a distance r from the surface and $\boldsymbol{B}_o$ is the field at $r = 0$. It follows that any applied magnetic field will penetrate the sample with an exponential decay, characterised by λ_L, which has the effect of expelling flux from the bulk of the sample, thus explaining perfect diamagnetism.

The crucial assumption made by the London brothers was that the superconducting state can be described by a spatially invariant macroscopic order parameter[2], Ψ, and related to the current density as

$$\boldsymbol{J_s} = \frac{ie\hbar}{2m_e}(\Psi^*\nabla\Psi - \Psi\nabla\Psi^*) - \frac{2e^2}{m_e}\Psi\Psi^*\boldsymbol{A} \tag{2.3}$$

which can be simplified by writing Ψ as an amplitude and phase $\sqrt{n_s}e^{i\theta}$, to

$$\Lambda \boldsymbol{J_s} = -\left(\frac{\hbar}{2e}\nabla\theta + \boldsymbol{A}\right) \tag{2.4}$$

[1]Since the London formalism directly relates the supercurrent density with the vector potential (and not the spatial or time derivative of the vector potential), it will only be valid for a particular choice of gauge - in this case the London gauge $\boldsymbol{\nabla} \cdot \boldsymbol{A} = 0$.

[2]The macroscopic order parameter is defined here to be $n_s = 2n_c$, the supercurrent number density, which does not vary in the London formalism. An explanation of this definition is dealt with in the section on Ginzburg Landau theory.

from which Equation 2.1 can be calculated. This does not allow for areas of the superconductor which are non-uniform such as magnetic domain boundaries, surface superconductivity and the proximity effect. In particular it does not explain the existence of the Schubnikov phase, more commonly known as the vortex state, which was first observed in 1937 [Schubnikov, 1937]. In 1950, a modification to London theory allowed for possible spatial variation of Ψ [Ginzburg and Landau, 1950].

2.1.2 The Two Fluid Model

The two fluid model is a phenomenological description of the temperature dependence of the superconducting pair density. Electronic heat capacity measurements of tin in the superconducting state vary roughly as T^3 [Tinkham, 1996; Waldram, 1996], increasing to above the linear heat capacity of the normal state, only to reduce to the normal state level sharply at T_c. This anomaly was similar to one associated with a higher order[3] phase transition to an ordered state. This and other evidence [Tinkham, 1996], suggested the existence of a group of electrons which have condensed into a new type of ordered quantum state, so a two fluid model was introduced. The electrons are divided into a normal fluid and a superconducting fluid, carrying no entropy and subject to no scattering. It was proposed the free energy of the normal fluid was proportional to $\sqrt{f_n}$, where f_n is the fraction of normal electrons. This was to take account of the T^3 dependency of the heat capacity. The density of the superfluid is

$$n_s(T) = n_s(0)[1 - (T/T_c)^4], \tag{2.5}$$

meaning the temperature dependence of the penetration depth is

$$\lambda(T) = \lambda(0)\frac{1}{\sqrt{1 - (T/T_c)^4}}. \tag{2.6}$$

It should be noted that this model has some basis in microscopic theory, but should be used with some caution as it is only very approximate in certain limits.

2.1.3 The Ginzburg Landau Free Energy

Ginzburg Landau (GL) theory was developed from the Landau theory of phase transitions [Landau, 1937] and allowed for the spatial variation of the superconducting order parameter. For a more complete review, it is best to consult one of the many

[3]Greater than 1st order

books concerning this subject [including Waldram, 1996; de Gennes, 1966; Tinkham, 1996]).

Landau's fundamental postulate is that a phase transition can be regarded as a transition from an ordered to a disordered state. It can be shown by thermodynamic arguments that when a phase transition occurs, one of the free-energy functions is the same for both phases; for example, in the liquid-vapour transition it is the Gibbs free energy.

In a first order transition the first order derivatives of the free energy are different in the two phases. This means there is a latent heat associated with the phase transition. In a second (or higher) order transition, the first order derivatives of the free energy are continuous, but quantities which are proportional to higher order derivatives (such as heat capacity) are discontinuous.

For a first order transition, suppose the free energy, $F(\Psi)$, has two separate minima whose heights change with temperature. The transition will occur when one minima moves below the other minima. The higher minimum, although less thermodynamically stable, may be more locally stable (thus providing a model for supercooled/superheated states, often seen in liquid-vapour transitions). The phases corresponding to the two minima will be distinct from one another.

For a second order transition, suppose at the transition temperature T_c, the minima at $\Psi = 0$ becomes a local maximum and two *new* minima appear at $\Psi = \pm\psi_o$. As the temperature falls, these minima move further away from $\Psi = 0$, as shown in Figure 2.1. Thus, there are no supercooled or superheated states and there is no distinction between ordered and disordered states. This is the model used for the superconducting transition in zero magnetic field.

The order/disorder transition can be described by an order parameter Ψ, such as the magnetisation in ferromagnetism or the effective pair density in superconductivity $n_c = n_s/2$. If this order parameter can be externally constrained, the Helmholtz[4] free energy will be a definite function $F(\Psi)$, with the order of the transition dependent on the *form* of $F(\Psi)$.

Landau proposed that $F(\Psi, T)$ was an analytic function which can be expanded in powers[5] of Ψ and $(T - T_c)$

$$F(\Psi, T) = F_n(T) + \Gamma(T)\Psi + \alpha(T)\Psi^2 + \gamma(T)\Psi^3 + \frac{1}{2}\beta(T)\Psi^4 + \cdots . \tag{2.7}$$

[4]In the case of superconductivity, the relevant free energy is the Helmholtz.

[5]There are systems where this simple expansion is not possible, but this assumption holds for superconductivity.

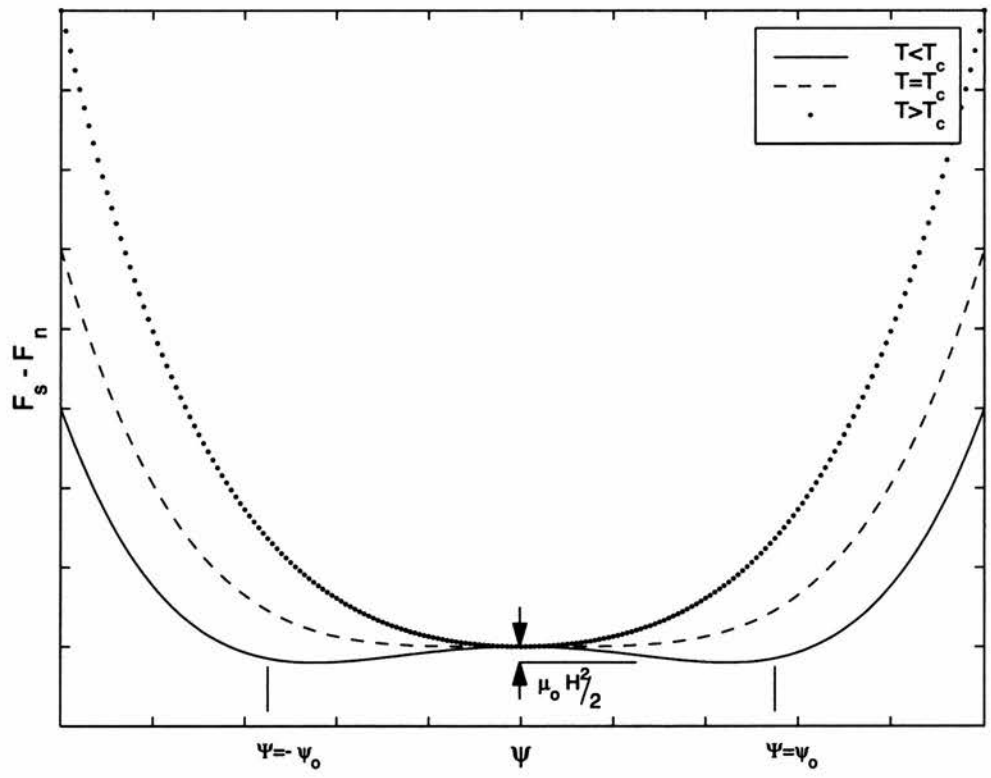

Figure 2.1: The GL free energy for $T < T_c$ ($\alpha < 0$) , $T = T_c$ ($\alpha = 0$) and $T > T_c$ ($\alpha > 0$).

The equilibrium phase corresponds to a minimum in $F(\Psi, T)$

$$\frac{\partial F}{\partial \Psi} = 0. \tag{2.8}$$

When $\Psi = 0$ (in the normal state) there must be a minimum, which suggests $\Gamma = 0$ for $T > T_c$. The assumption that Γ can be expanded as a power series in $(T - T_c)$ leads to $\Gamma = 0$ at all temperatures. Furthermore, it is not possible to have a measurable quantity [6] proportional to a wavefunction, so the Ψ^3 term should also be removed, leaving

$$F(\Psi, T) = F_n(T) + \alpha(T)\Psi^2 + \frac{1}{2}\beta(T)\Psi^4. \tag{2.9}$$

For $\Psi = \psi_o$, Equation 2.8 gives

$$\alpha\psi_o + \beta\psi_o^3 = 0 \tag{2.10}$$

which has solutions $\psi_o = 0$ and $\psi_o^2 = -\alpha/\beta$.

It is required that the only solution above T_c is $\psi_o = 0$ and for below T_c $\psi_o \neq 0$. This can be achieved if $-\alpha/\beta < 0$ above T_c and $-\alpha/\beta > 0$ below T_c. If $\beta < 0$, the free energy would decrease indefinitely for large values of Ψ. Therefore β must be positive for all temperatures and the simplest solutions are

$$\begin{aligned} \alpha(T) &= A(T - T_c) \\ \beta(T) &= \beta(T_c) = \beta \end{aligned} \tag{2.11}$$

where A and β are positive constants. This leads to Equation 2.10 having the following solutions

$$\begin{aligned} T > T_c \quad & \psi_o = 0 \\ T < T_c \quad & \psi_o = \frac{\pm A^{1/2}(T_c - T)^{1/2}}{\beta^{1/2}} \end{aligned} \tag{2.12}$$

which represent the minima shown in Figure 2.1. In addition to these solutions, there exists a solution at $\psi_o = 0$ for $T < T_c$, which corresponds to the maxima.

It was stated earlier that GL theory allows the order parameter to be a function

[6] Odd powers of Ψ leads to the free energy being proportional to Ψ, and Ψ^2 is defined here as the supercurrent density n_s which is a measureable quantity.

of position. This can be achieved by redefining Equation 2.9 to be an expression for the free energy density at position r, which is integrated over volume to get the total free energy density. If Ψ is a function of position, a kinetic (gradient) term of the form $|\nabla\Psi|^2$ is also expected in the free energy

$$F(r) = F_n + \alpha|\Psi(r)|^2 + \frac{1}{2}\beta|\Psi(r)|^4 + \frac{\hbar^2}{2m}|\nabla\Psi(r)|^2. \tag{2.13}$$

A magnetic term must also be included in the GL free energy by adding a vector potential A, which gives rise to a field $\boldsymbol{H} = \nabla \times \boldsymbol{A}$. This is achieved by the replacement $\nabla \rightarrow \nabla \pm 2ieA/\hbar$ in Equation 2.13. A magnetic field energy of the sample and of the coils must also be added thus

$$F(r) = F_n+\alpha|\Psi(r)|^2+\frac{1}{2}\beta|\Psi(r)|^4+\frac{1}{2m}|(-i\hbar\nabla+2e\boldsymbol{A})\Psi(r)|^2+\frac{\boldsymbol{B}^2}{2\mu_o}+\frac{\mu_o\boldsymbol{H}^2}{2}. \tag{2.14}$$

The volume integral of F(r) is the Gibbs free energy density $G = U - TS + H \cdot M$. The coefficient in the kinetic term is $\hbar/2m$, where m is the electronic mass and has no physical meaning [de Gennes, 1966]. It only determines the normalisation of Ψ.

The introduction of the kinetic term effectively limits Ψ from changing too rapidly, as a large gradient in Ψ would lead to a large contribution to F(r). This is characterised by a length scale over which Ψ can vary, the GL coherence length [Waldram, 1996]

$$\xi(T) = (\hbar^2/2m|\alpha|)^{\frac{1}{2}} \tag{2.15}$$

with a corresponding second critical field

$$H_{c2} = \Psi_0/2\pi\mu_0\xi^2(T). \tag{2.16}$$

By minimising Equation 2.14 with respect to Ψ using the Euler-Lagrange equations of the calculus of variation[7] and choosing the correct gauge ($\nabla \cdot \boldsymbol{A} = 0$) the 1st GL equation can be formed

$$\frac{1}{2m}(-i\hbar\nabla - 2e\boldsymbol{A})^2\Psi + \alpha\Psi + \beta|\Psi|^2\Psi = 0. \tag{2.17}$$

By minimising Equation 2.14 with respect to $\boldsymbol{A}$ and applying Maxwell's equations, the second GL equation is formed

[7]This is beyond the scope of this thesis.

$$\boldsymbol{J}_e = \frac{ie\hbar}{m}(\Psi^*\nabla\Psi - \Psi\nabla\Psi^*) - \frac{4e^2}{m}\Psi^*\Psi\boldsymbol{A}. \tag{2.18}$$

If a non-spatially varying wavefunction is imposed, $\nabla\Psi = 0$ the current density simply becomes

$$\boldsymbol{J}_e = -\frac{4e^2|\alpha|}{m\beta}\boldsymbol{A} \tag{2.19}$$

so the penetration depth can be defined

$$\lambda = \left(\frac{m\beta}{4e^2\mu_0|\alpha|}\right)^{1/2}, \tag{2.20}$$

which is in agreement with the London formalism. The two lengths λ and ξ have the same dependency on α and hence T. They both diverge as $(T_c - T)^{-\frac{1}{2}}$ when approaching T_c.

2.1.4 The NS Boundary Energy

Circumstances can arise where there is a boundary between a normal (N) and superconducting (S) region. In general, the boundary is able to move and if there is a magnetic field of magnitude B_c in the N region, the movement of the boundary will not change the total free energy. If the boundary contributes a positive free energy to the system then the boundary will be stable and will lead to large normal regions, but a negative free energy contributed to the system implies an unstable system. A system trying to maximise the area of boundaries will lead to the normal region breaking up into a finely divided structure of N and S regions.

Pippard was the first to point out that the free energy depends on the relative magnitudes of λ and ξ, as shown in Figure 2.2 [de Gennes, 1966]. If $\lambda \gg \xi$ the magnetic field will penetrate some distance into the superconductor but the free energy will not be depressed significantly. The reduction in the field self energy per unit area due to the penetration will be of the order $\lambda F \gg f$, so a negative boundary energy is expected. If $\xi \gg \lambda$, the opposite is true.

The ratio $\kappa = \lambda/\xi$ can be used to determine whether the boundary energy is positive or negative. It can be shown [Waldram, 1996] by considering the extreme values of κ that the condition $\kappa = 1/\sqrt{2}$ separates two types of behaviour. Type I superconductors have $\kappa < 1\sqrt{2}$ and positive NS boundary energy, whilst Type II superconductors have $\kappa > 1\sqrt{2}$ and negative NS boundary energy.

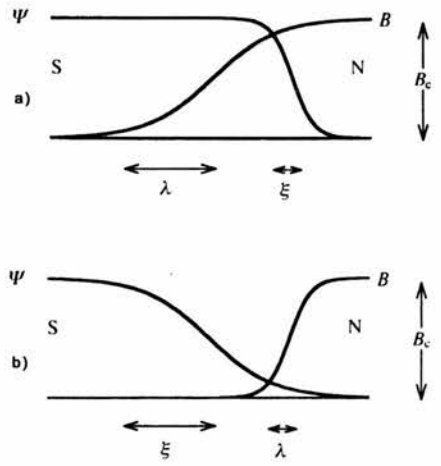

Figure 2.2: The coherence length, ξ, and penetration depth, λ, for two different κ values: a) $\kappa > 1/\sqrt{2}$ negative boundary energy b) $\kappa < 1/\sqrt{2}$ positive boundary energy.

2.1.5 Type II Superconductivity

When the NS boundary energy is negative, it is energetically favourable to try and maximise the size of the NS boundaries. Consequently, tiny lines of magnetic flux thread through the superconductor, with the flux density within minimised. A flux-line consists of a normal (non-superconducting) core with a radius of the order of ξ (the distance at which the order parameter can change), with circulating supercurrents falling off as $\exp(-r/\lambda)$ at large distances. The nature of the circulating supercurrents is similar to a vortex in a non-viscous liquid, so the flux lines are often referred to as vortices. The vortices are also quantised. By taking a line integral of Equation 2.4 around a loop which remains entirely inside a superconductor, it is clear that it must be a multiple of 2π and leads to

$$\oint (\boldsymbol{A} + \Lambda \boldsymbol{J}_s) \cdot d\boldsymbol{l} = \frac{\hbar}{2e} 2\pi n \tag{2.21}$$

where n is an integer. Well away from an isolated vortex core, $\boldsymbol{J}_s = 0$, so the left hand side becomes $\oint \boldsymbol{A} \cdot d\boldsymbol{l}$, which is just the flux Φ passing through the loop. Thus

$$\Phi = n\Phi_0 \tag{2.22}$$

where Φ_0 is the flux quantum

$$\Phi_0 = \frac{h}{2e}. \tag{2.23}$$

For a system with negative NS boundary energy, the minimum energy state will be one where the NS boundary area is maximised. It follows that n=1. Note that this argument only holds on a loop where $\boldsymbol{J}_s = 0$, which is not possible in rings thin compared to the penetration depth and in Josephson junctions, to mention just two.

The interactions between vortices are strong, but become vanishingly small when the average distance between the vortices is much larger than the penetration depth. For isotropic superconductors, the net interaction between vortices is repulsive and a perfect lattice of flux lines is formed[8]. Abrikosov [Abrikosov, 1957] first predicted the lowest free energy for a flux line lattice (FLL) was square, but it was subsequently shown that the lowest free energy is in fact gained from a hexagonal symmetry [Matricon, 1964].

[8]Assuming there is no disorder introduced by pinning or thermal fluctuations, for example.

2.2 High Temperature Superconductors

2.2.1 Anisotropy

In the Lawrence-Dorniach model [Lawrence and Doniach, 1970], layered superconductors are modelled as a stack of two dimensional superconductors coupled via Josephson currents between layers. The GL free energy for such a system is then [Tinkham, 1996]

$$F(r) = \sum_i F_n + \alpha|\Psi(r)|^2 + \frac{1}{2}\beta|\Psi(r)|^4 + \frac{\hbar^2}{2m_{ab}}\left(\left|\frac{\partial\Psi_i(r)}{\partial x}\right|^2 + \left|\frac{\partial\Psi_i(r)}{\partial y}\right|^2\right) + \frac{\hbar^2}{2m_c s^2}|\Psi_i(r) - \Psi_{i-1}(r)|^2 \quad (2.24)$$

where the vector potential and magnetic field energy have been removed from the free energy and an expansion of the derivative for the z term is added, both for simplicity. The summation is performed over i layers, z is the coordinate along the c-axis, x and y are the coordinates along the ab-plane, s is the inter-planar distance and the masses m_{ab} and m_c are the anisotropic effective masses of the electrons. The mass anisotropy alters the definition of the coherence length, so that it is anisotropic, to

$$\xi(T) = (\hbar^2/2m_j|\alpha|)^{\frac{1}{2}} \quad (2.25)$$

where m_j are components of the anisotropic mass tensor for the three principle axes a, b and c. The quantity γ can be defined as the anisotropy factor [Tinkham, 1996]

$$\gamma \equiv \left(\frac{m_c}{m_{ab}}\right)^{1/2} = \frac{\lambda_c}{\lambda_{ab}} = \frac{\xi_{ab}}{\xi_c} = \frac{H_{c2\|ab}}{H_{c2\|c}} = \frac{H_{c1\|ab}}{II_{c1\|c}}. \quad (2.26)$$

It is clear that when applying a magnetic field parallel to the c-axis, the structure of the induced vortices will be affected by anisotropy of the system. In a layered system like the HT_c's, one can think of the superconductor as an array of thin films separated by insulating layers. Two situations arise that are of interest and can be thought of in the following manners.

Firstly, the case where the tunnel currents between layers are assumed to be zero [Efetov, 1979; Artemenko and Kruglov, 1990; Buzdin and Feinberg, 1990]. In this case, the vortices form 2D pancakes which are coupled together logarithmically and

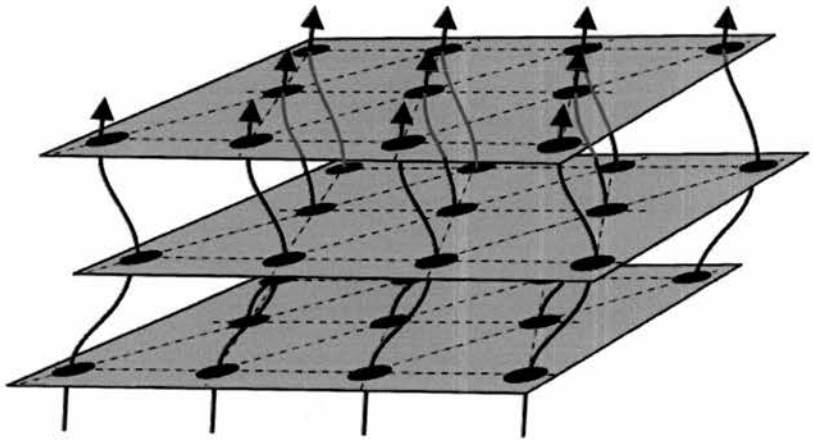

Figure 2.3: Schematic diagram of a layered vortex structure.

are schematically shown in Figure 2.3. The attractive interaction potential $V(\boldsymbol{R})$ between two isolated pancake vortices at a distance $\boldsymbol{R}$ from one another on different superconducting layers is purely of electromagnetic origin [Blatter *et al.*, 1994] and is given by

$$V_{em}(\boldsymbol{R}) \approx \frac{1}{2} d\epsilon_0 \frac{d}{\lambda} e^{-|z|/\lambda} \ln\left(\frac{\lambda}{\boldsymbol{R}}\right) \tag{2.27}$$

for $\lambda \ll \boldsymbol{R}$ and

$$V_{em}(\boldsymbol{R}) \approx 2d\epsilon_0 \ln\left(\frac{\lambda}{\boldsymbol{R}}\right) \tag{2.28}$$

for $|z| \ll \boldsymbol{R} \ll \lambda$, where d is the superconducting layer thickness, z the pancake separation perpendicular to the film surface, which is approximately the layer separation $z \approx s$.

The second situation is when the currents between layers are not negligible, where in addition to the electromagnetic coupling, Josephson coupling occurs [Artemenko and Kruglov, 1990; Chakravarty *et al.*, 1990; Feigelman and Vinokur, 1990]. At this point it becomes convenient to introduce a screening length [Blatter *et al.*, 1994]

$$\Gamma = d/\gamma. \tag{2.29}$$

For $\boldsymbol{R} < \Gamma$, the Josephson currents are small and the system essentially acts as a system of 2D layers, where electromagnetic coupling is dominant, as above. For $\boldsymbol{R} > \Gamma$, currents between layers are present and continuous anisotropic 3D behaviour occurs. The interaction potential is given by [Blatter *et al.*, 1994]

$$V_J(\boldsymbol{R}) = d\epsilon_0(\boldsymbol{R}/\Gamma)^2 \ln\left(\frac{\Gamma}{\boldsymbol{R}}\right) \tag{2.30}$$

for $\boldsymbol{R} \ll \Gamma$,

$$V_J(\boldsymbol{R}) \approx 2d\epsilon_0\left(\frac{\boldsymbol{R}}{\Gamma} - \frac{\Gamma}{4\boldsymbol{R}}\right) \tag{2.31}$$

for $\Gamma \ll \boldsymbol{R} \ll \lambda/\gamma$, and

$$V_J(\boldsymbol{R}) \approx 2d\epsilon_0\frac{\boldsymbol{R}}{\Gamma} \tag{2.32}$$

for $\lambda/\gamma \ll \boldsymbol{R}$.

When considering the role of electromagnetic coupling and Josephson coupling, it becomes clear electromagnetic coupling is larger at very small distances, rapidly falling off at larger distances but extends weakly over very large (infinite) distance. Consequently, predominantly 2D behaviour is predicted, with pancake vortices formed within the layers that interact weakly between the layers. The vortices exhibit long range ordering (of sorts) along the c-axis, but with large short wavelength transverse fluctuations. Josephson coupling is dominant if the currents are able to flow between layers ($\boldsymbol{R} > \Gamma$). Consequently, in the Josephson coupling regime, one would expect some flexibility within a vortex *line*, compared to the weakly interacting 2D pancakes observed when electromagnetic coupling is dominant.

2.2.2 Pinning

Inhomogeneities in the crystal structure can perturb the superconducting wavefunction and act as pinning sites for vortices, thus disturbing both the short and long range order of the FLL. The pinning sites can originate from point-like defects of similar size to ξ (such as oxygen defects in the high temperature superconductors (HT_c's)) or from extended defects (such as twinning or grain boundaries). It has been shown [Giamarchi and Ledoussal, 1994; Blatter *et al.*, 1994] that in equilibrium, the crystalline long range order of the vortex lattice is unstable when random pinning is introduced, for dimensions less than 4. Thus, real vortex systems can never have a long range ordered lattice in the presence of arbitrarily small quenched disorder [Blatter *et al.*, 1994]. Hence the phrase Bragg Glass (BG) has been coined as a better description than flux line lattice. In this thesis, BG and FLL are used indiscriminately. For an extensive review of the effect of pinning on vortices (among

other things), please refer to Blatter [Blatter *et al.*, 1994].

Single point-like defects will have a small effect on stiff vortices, as the reduction in the free energy due to the single pinning defect will be much smaller than the effect of the Lorentz force acting on the vortex. Vortices pinned to correlated collective inhomogeneities, on the other hand, may reduce the free energy of the superconductor significantly, as the reduction in free energy due to the pinning defects along the line of the vortex are added together. When the disorder is produced by an extended defect, the pinning potential is correlated over the size of the defect. For point-like defects perturbing the superconductor, the correlation lengthscale is smaller than the coherence length and therefore is effectively zero. In this case, the smallest possible transverse fluctuations are given by the coherence length [Blatter *et al.*, 1994]. Correlated pinning, such as twin boundary pinning, therefore has a much larger effect on the vortex lattice compared to uncorrelated pinning. The vortices are attracted to the twin planes, leading to a higher concentration of vortices in the twin boundaries than in the bulk. Motion along the twin boundaries is also affected, as demonstrated by the field and current density along the twin planes, which are more hindered than in the bulk [Blatter *et al.*, 1994].

2.2.3 FLL Melting

Another property of the vortex lattice is the appearance of a vortex liquid; a state in which the vortices are free to move and all long range spatial order is absent, occurring within a particular temperature and field range of the magnetic phase diagram. Fluctuations give rise to overdamped phonon-like excitations of the vortex position and when these fluctuations get sufficiently large, the lattice melts into a liquid. In conventional superconductors fluctuation effects are generally quite small, since the fluctuation length is determined by the flux quantum and temperature [Fisher *et al.*, 1991]

$$\Gamma_T = \frac{\Phi_0^2}{16\pi^2 T} \tag{2.33}$$

which is much larger than any other length (penetration depth, coherence length etc.), unless close to T_c. The comparatively large superconducting transition temperature of the HT_c's, large anisotropy, shorter coherence length and longer penetration depth increase the effects of thermal fluctuations. A consistent theory for bulk 3D melting is lacking, so the position and shape of the vortex lattice melting

is usually (somewhat unsatisfactorily) determined by the Lindemann criterion [Lindemann, 1910; Blatter *et al.*, 1994]. In the intermediate range $H_{c1} \ll H \ll H_{c2}$, the melting line takes the form

$$B_M(T) \approx \left(\frac{5.6c_L^4}{G_i}\right) H_{c2}(0) \left(1 - \frac{T}{T_c}\right)^2 \tag{2.34}$$

where the Lindemann number $c_L \simeq 0.1 - 0.2$ and G_i is the GL number. Not only does the melting line depend on the temperature, but also the applied field. With decreasing field, the vortices increase their separation and eventually the vortex-vortex interaction becomes exponentially small, so consequently the shear modulus decays rapidly and the melting line develops a re-entrant behaviour [Blatter *et al.*, 1994].

A related effect is the irreversibility line (IL), where the vortices cross over from a dissipative to non-dissipative regime. If one increases the temperature at a fixed field (such that it will cross the melting line), one would expect the vortices to overcome any pinning potential and be free to move. However, vortices that have melted may still be dissipative due to the pinning landscape still having an effect on the vortices. By increasing the temperature further, there comes a point where the vortices are no longer dissipative due to their increased thermal energy. The superconductor is said to be irreversible and features related to this can be observed in magnetisation measurements.

2.3 Introduction to Magnetism

2.3.1 Overview

From a simplistic point of view, a magnetic moment is a vector quantity and is due to moving charges. In atomic systems there is a contribution from both spin and orbital angular momentum (AM). Atomic systems have many electrons contributing to the magnetic moment and in this case the total momentum is the vector sum of all contributions from all electrons. Classically, when electrons are paired, the contribution from the two electrons "cancel" each other out, analogous with the two electrons orbiting "clockwise" and "anti-clockwise". Systems with non-interacting unpaired electrons, where orbital and/or spin AM are not cancelled, are known as paramagnetic. Materials without a paramagnetic moment show a weak negative susceptibility and are known as diamagnetic. Ferromagnetic materials exhibit a long-range ordering phenomenon which causes unpaired electron spins to line up parallel with each other via an exchange interaction. An anti-parallel alignment of spins can occur, known as antiferromagnetism, which depends on the details of the interaction between spins.

For a single electron, the orbital AM contributes

$$|\boldsymbol{\mu}| = \mu_B \sqrt{l(l+1)} \tag{2.35}$$

to the magnetic moment, where μ_B is the Bohr magneton, l is the quantum number associated with orbital AM and takes a value $l = 0, 1, 2....$ The spin AM can be treated in a similar manner to orbital AM and contributes

$$|\boldsymbol{\mu}| = g_s \mu_B \sqrt{s(s+1)} \tag{2.36}$$

where s is the spin quantum number, g_s is the Lande g-factor and for an electron, $s = \pm\frac{1}{2}$. For a multi-electron atom,[9] where the electrons are combined via Hund's rules, the magnetic moment of the atom can be thought of as a vector sum of all contributions from all electrons in the atom. The total angular momentum, $\boldsymbol{J}$, for an atom is then given by the addition of the orbital $\boldsymbol{L} = \sum l$ and spin $\boldsymbol{S} = \sum s$ angular momentum contribution

$$\boldsymbol{J} = \boldsymbol{S} + \boldsymbol{L} \tag{2.37}$$

[9]Valid for a "light" atom, where j-j coupling is negligible.

and the magnetic moment is

$$\mu = \mu_B g_J \boldsymbol{J}, \tag{2.38}$$

where g_J is the Lande g-value [Blundell, 2001].

In an applied magnetic field, $\boldsymbol{B}$, the energy of the system is

$$U = -\boldsymbol{\mu} \cdot \boldsymbol{B} = -\mu B \cos\theta. \tag{2.39}$$

The minimum energy of the system is when $\cos\theta = 1$, so there is a torque on the moment to align it with the applied field. If an object has an AM, whose magnitude is constant, the moment associated with that AM is at an angle to the applied field. A torque is present that can not align the moment with the applied field, leading to a precession around the field. The total AM must change direction with respect to time but with constant magnitude and projection along field (m_z).

2.3.2 The Different Types of Magnetism

In the non-relativistic limit, the Hamiltonian for a charged particle i at position $\boldsymbol{r}$ in a magnetic vector potential, assuming non interacting electrons, is [Blundell, 2001]

$$\hat{\mathcal{H}} = \hat{\mathcal{H}}_0 + \mu_B(\boldsymbol{L} + g_s\boldsymbol{S}) \cdot \boldsymbol{B} + \frac{e^2}{8m_e}\sum_i (\boldsymbol{B} \times \boldsymbol{r}_i)^2. \tag{2.40}$$

The dominant perturbation to the original Hamiltonian, $\hat{\mathcal{H}}_0$ is usually $\mu_B(\boldsymbol{L}+g_s\boldsymbol{S})\cdot \boldsymbol{B}$, the paramagnetic term and requires "unpaired spins". In the absence of interactions between the unpaired spins, the paramagnetic term will only present in an applied field. The third term, $(e^2/8m_e)\sum_i(\boldsymbol{B} \times \boldsymbol{r}_i)^2$, is the diamagnetic moment and is summed over all electrons and only present in an applied field.

All materials exhibit diamagnetism. The effect is often explained using a classical view. However, the origin of diamagnetism is purely quantum mechanical. Assuming the paramagnetic part of Equation 2.40 is zero (i.e no unpaired electrons) and using 1st order perturbation theory, it can be shown that the diamagnetic susceptibility is [Blundell, 2001]

$$\chi = -\frac{N}{V}\frac{e^2\mu_0}{6m_e}\sum_{i=1}^{Z}\langle r_i^2\rangle \tag{2.41}$$

for N ions, each with Z electrons.

Paramagnetism corresponds to a positive susceptibility with respect to an applied

magnetic field and one has to take into account the total AM, as demonstrated in Equation 2.40. For free paramagnetic ions in the absence of an applied field, the paramagnetic moments point in random directions. Using semi-classical arguments, it can be shown that the paramagnetic susceptibility is [Blundell, 2001]

$$\chi = \frac{n\mu_0\mu^2}{2k_BT} \tag{2.42}$$

for n magnetic moments, μ, per unit volume. This is inversely proportional to temperature and known as the Curie law.

In order to understand ferromagnetism, antiferromagnetism or any other type of long-range magnetic order, one must consider the exchange interaction. This is nothing more than the Coulomb interaction reducing or raising the energy when two or more electron wavefunctions overlap. The spin dependent term in the effective Hamiltonian between the ith and jth interacting spins, $\boldsymbol{S}_i$ and $\boldsymbol{S}_j$, can be written

$$\hat{\mathcal{H}}_{spin} = -\sum_{i,j} J_{i,j}\boldsymbol{S}_i \cdot \boldsymbol{S}_j \tag{2.43}$$

where J is the exchange constant between the two electrons and the sign of the exchange constant determines whether there is ferromagnetism or antiferromagnetism. If two electrons on neighbouring atoms interact via an exchange interaction, then this is known as "direct exchange". Direct exchange between magnetic ions is relatively uncommon. Usually long range magnetic order occurs via one or more complex mechanisms; for example, super-exchange, band ferromagnetism and coupling via spin density waves.

2.3.3 Spin Susceptibility of the Electron Gas

When a magnetic field is applied to a metal, the energy of each electron is raised or lowered according to the electron's spin. This is schematically shown in Figure 2.4. For non-interacting particles, neglecting Fermi surface smearing at finite temperatures and the orbital AM contribution, the magnetisation of a state with unequal spin up and down electrons is

$$\boldsymbol{M} = \mu_B(n_\uparrow - n_\downarrow) = \frac{\mathcal{N}}{2}\mu_B^2\boldsymbol{B} \tag{2.44}$$

assuming the Lande factor, g_s=2. The magnetic susceptibility is then [Blundell, 2001]

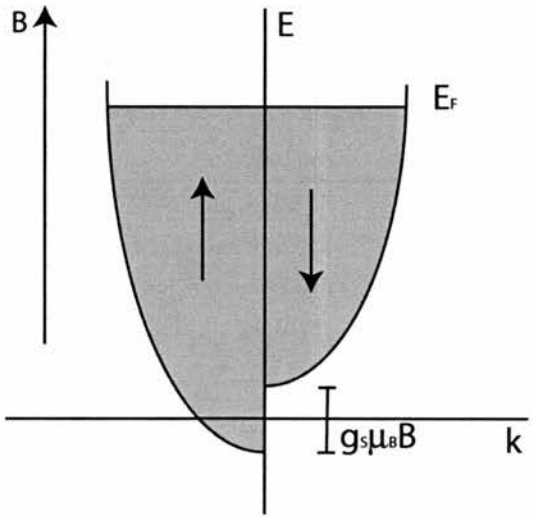

Figure 2.4: Occupied electronic states in an applied field. Those electrons with spins parallel to the applied field are of lower energy. The energy gap is greatly exaggerated.

$$\chi(0) = \frac{\boldsymbol{M}}{\boldsymbol{H}} = \frac{3n\mu_0\mu_B^2}{2E_F}. \tag{2.45}$$

This simple approach is more commonly referred to as Pauli Paramagnetism. Even though the expression in Equation 2.45 is temperature independent, if the temperature dependence was included via the Fermi-Dirac function, it would only show moderate temperature dependence. This is in direct contrast with the susceptibility of paramagnetic insulators (see above), where there is a large temperature dependence as described by the Curie law. This is due to the number of electrons involved, as generally in an insulator at least one electron per magnetic atom contributes to the susceptibility. By contrast, it is only those electrons close to the Fermi surface that contribute in a metal. This is in good qualitative agreement with experimental evidence, as the susceptibility of many metals[10] varies only by a few percent over a 500K range [Martin, 1967].

Implicit in the argument presented above is a non-spatially varying magnetic field, which is insufficient to describe a number of systems. For example, in metallic systems with dilute paramagnetic impurities, the electron gas will respond to this perturbation according to the wavevector dependent spin susceptibility [Blundell, 2001; Martin, 1967]. Assuming the electrons see a spatially varying magnetic field

[10]Transition metals can be somewhat more complicated and will not be dealt with here.

$$\boldsymbol{H}(\boldsymbol{r}) = \boldsymbol{H}_{\boldsymbol{q}} \cos(\boldsymbol{q} \cdot \boldsymbol{r}) \tag{2.46}$$

the perturbing Hamiltonian is

$$\mathcal{H}_m = \pm \frac{2\mu_0 \mu_B}{2} |\boldsymbol{H}_{\boldsymbol{q}}| \cos(\boldsymbol{q} \cdot \boldsymbol{r}) \tag{2.47}$$

for both spin orientations. A plane wave $\psi_{\boldsymbol{k}\pm}(\boldsymbol{r}) = (1/\sqrt{V}) e^{i\boldsymbol{k}\cdot\boldsymbol{r}} |\pm\rangle$ is weakly perturbed into $\psi_{(\boldsymbol{k}+\boldsymbol{q})\pm}(\boldsymbol{r})$ and $\psi_{(\boldsymbol{k}-\boldsymbol{q})\pm}(\boldsymbol{r})$ such that the wavefunction becomes

$$\psi_{\boldsymbol{k}\pm}(\boldsymbol{r}) = \frac{1}{\sqrt{V}} \left(e^{i\boldsymbol{k}\cdot\boldsymbol{r}} \pm \frac{\mu_0 \mu_B \boldsymbol{H}_{\boldsymbol{q}}}{2} \left[\frac{e^{i(\boldsymbol{q}+\boldsymbol{k})\cdot\boldsymbol{r}}}{E_{\boldsymbol{k}+\boldsymbol{q}} - E_{\boldsymbol{k}}} + \frac{e^{i(\boldsymbol{q}-\boldsymbol{k})\cdot\boldsymbol{r}}}{E_{\boldsymbol{k}-\boldsymbol{q}} - E_{\boldsymbol{k}}} \right] \right) |\pm\rangle \tag{2.48}$$

where $E_{\boldsymbol{k}} = \hbar^2 k^2 / 2m_e$. It can be shown that [Blundell, 2001]

$$|\psi_{\boldsymbol{k}\pm}(\boldsymbol{r})|^2 = \frac{1}{V} \left(1 \pm \frac{g\mu_o \mu_B H_{\boldsymbol{q}} m_e}{\hbar^2} \left[\frac{1}{(\boldsymbol{k}+\boldsymbol{q})^2 - k^2} + \frac{1}{(\boldsymbol{k}-\boldsymbol{q})^2 - k^2} \right] \cos \boldsymbol{q} \cdot \boldsymbol{r} \right), \tag{2.49}$$

and by summing over all electrons in the Fermi sphere and using

$$M(\boldsymbol{r}) = \frac{g\mu_o \mu_B}{2} (|\psi_{k+}(\boldsymbol{r})|^2 - |\psi_{k-}(\boldsymbol{r})|^2) \tag{2.50}$$

it can be shown that [Blundell, 2001]

$$\chi(\boldsymbol{q}) = M_{\boldsymbol{q}} / H_{\boldsymbol{q}} = \chi(0) \left(\frac{1}{2} + \frac{4k_F^2 - q^2}{8k_F q} \ln \left| \frac{2k_F + q}{2k_F - q} \right| \right). \tag{2.51}$$

This neglects the Coulomb and direct exchange interaction of the itinerant electron gas and assumes the electrons are in quasi-free plane wave states.

The q-dependent paramagnetic susceptibility of the electron gas has significant consequences for the real space magnetic behaviour of a system with a delta function perturbation. A delta function can be decomposed into a sum of all frequencies

$$\boldsymbol{H}(\boldsymbol{r}) = \delta(\boldsymbol{r}) \boldsymbol{H} = \frac{1}{(2\pi)^3} \int \boldsymbol{H}_{\boldsymbol{q}} \exp^{i\boldsymbol{q}\cdot\boldsymbol{r}} d^3 q. \tag{2.52}$$

The response of the electron gas to a delta function can be calculated by a simple Fourier transform [Martin, 1967]

$$\chi(\boldsymbol{r}) = \frac{1}{(2\pi)^3} \int \frac{\chi(0)}{2} \left(1 + \frac{4k_F^2 - q^2}{4k_F q} \ln \left| \frac{2k_F + q}{2k_F - q} \right| \right) \exp^{i\boldsymbol{q}\cdot\boldsymbol{r}} d^3 \boldsymbol{q} \tag{2.53}$$

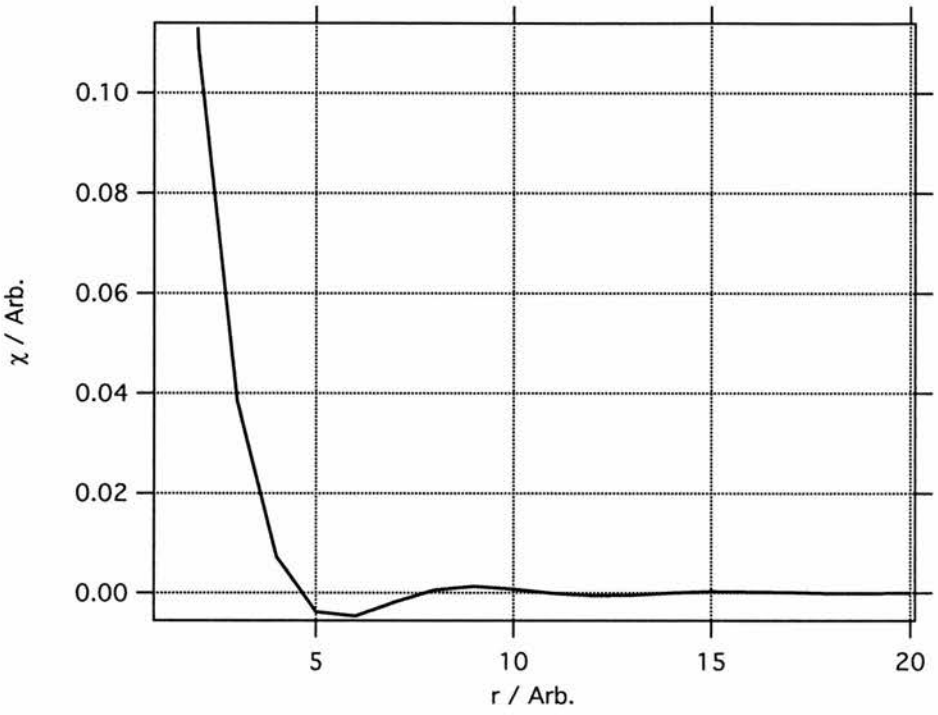

Figure 2.5: A plot of the RKKY interaction.

which reduces to

$$\chi(\boldsymbol{r}) = \frac{2k_F^3\chi(0)}{\pi}\left(\frac{\sin(2k_F\boldsymbol{r}) - 2k_F\boldsymbol{r}\cos(2k_F\boldsymbol{r})}{(2k_F\boldsymbol{r})^4}\right) \tag{2.54}$$

and is plotted in Figure 2.5. This is more commonly referred to as the Ruderman Kittel Kasuya Yisida (RKKY) interaction. The susceptibility (and hence magnetisation) is proportional to $\cos(2k_F\boldsymbol{r})/\boldsymbol{r}^3$ at large distances and diverges at small $\boldsymbol{r}$. This divergence is a consequence of the assumed delta function and is a reasonable approximation for the effect the RKKY interaction was initially proposed for. It was used to explain a localised nuclear moment polarising the electron gas and the subsequent interaction of the electron gas with a second nuclear moment. This indirect exchange can be ferromagnetic or antiferromagnetic, depending on the distance (and oscillation period) between nuclear moments (which determines the sign of the exchange constant). The influence of a non-spherical fermi surface [Roth *et al.*, 1966] or of quantum confinement of electrons in metallic thin films [Bruno and Chappert, 1991; Bruno, 1991; Bruno and Chappert, 1992] in the context of the RKKY interaction will be dealt with in Chapter 6.

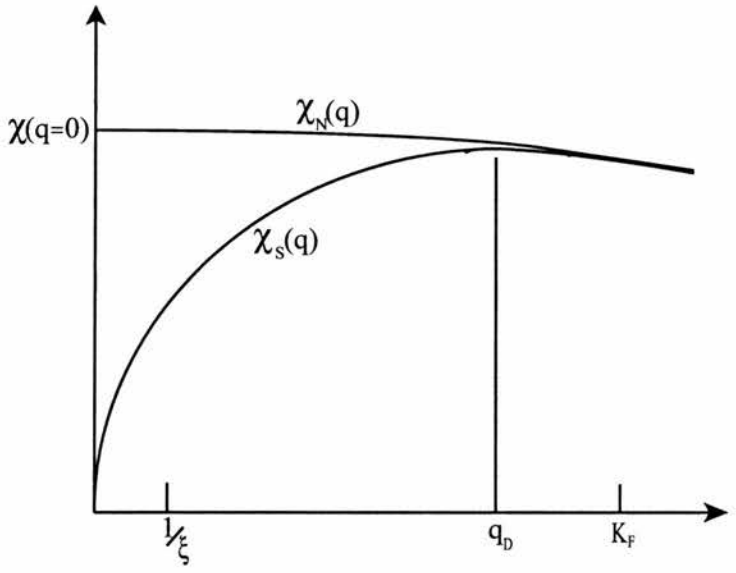

Figure 2.6: $\chi(q)$ in the normal and superconducting state.

2.3.4 Magnetism and Superconductivity

Until the Bardeen, Cooper and Schrieffer (BCS) theory of superconductivity [Waldram, 1996] the only magnetic effects taken into account were in prevailing phenomenological theories associated with the motion of the superfluid. These were described by the London equation or Pippard's generalisation [Waldram, 1996]. BCS theory predicts that the superconducting state could be described by the tendency of the electrons near the Fermi surface to form a coherent state in which pairs of electrons, known as Cooper pairs, are bound with anti-parallel spins and equal and opposite momentum. Because the Cooper pairs are of finite size and not point-like particles, they spatially overlap with one another and strongly interact. Consequently the binding energy becomes *cooperative* and the energy released when a new pair joins the condensate depends on how many pairs are already bound [Waldram, 1996]. Thus, BCS predicts a single transition temperature, below which bound pairs exist in equilibrium with common pair momentum, above which no pairs exist. In a spatially varying exchange field, such as one described in the section above, the conduction electrons must have an average polarisation which is not possible according to the "simple" BCS picture.

However, the coexistence of superconductivity with magnetism is indeed observed. There are a number of possibilities that exist in the BCS formalism that can take account of this. A spin dependent scattering process can restore some electron spin polarisability in the superconducting state in a particular direction in k-space. Another possible mechanism is a non uniform arrangement of spin impurities (paramagnetic impurities) which favour one particular Fourier component of the electron gas [Anderson and Suhl, 1959]. The spin susceptibility of the superconductor χ_s with zero wavenumber is zero. At wavenumbers approaching the coherence length, χ_s approaches the normal state susceptibility χ_n, although it is always less than χ_n. Figure 2.6 shows a schematic diagram of the different q-dependent susceptibilities for a normal metal and a superconductor. By considering free energy arguments, it has been shown that the maximum in $\chi_s(q)$ is [Anderson and Suhl, 1959]

$$q_D \sim (3\pi k_f^2/\xi_0)^{1/3} \tag{2.55}$$

and for a typical metal, $1/q_D \sim 50\mathring{A}$.

Ferromagnetic alignment of paramagnetic impurities when dissolved in non-magnetic metals is a well known phenomenon. However, when the host metal is a superconductor, Larkin, Ovchinnikov, Fulde, and Ferrell (LOFF) proposed [Fulde and Ferrell, 1964] a theoretical construct to take account of the experimental evidence of the ferromagnetic alignment persisting into superconducting state [Matthias *et al.*, 1958; Phillips and Matthias, 1961; Matthias, 1962]. This superconducting ground state is indeed quite different from that of a conventional BCS ground state. To tackle the problem, it is assumed there is no superelectron scattering and the superconducting electrons are assumed to be in a constant exchange field which only acts upon their spin. By assuming the exchange field can split *some* of the Cooper pairs into "normal" electrons, whilst some coherent pairing takes place, it was shown the pairing state has finite momentum. This is because the Fermi surface is assumed to have a cap-shaped portion which is only occupied by unpaired electrons of one spin orientation (along the exchange field), with the corresponding opposite portion absent of electrons of opposite spin. These regions, whilst lowering the magnetic energy, are lost to the BCS pairing state, which therefore gives less energy lowering than the BCS state. The pairing state must also be modified for another reason. The asymmetric distribution of spins in the Fermi surface implies a net current, so the remaining super-electrons must carry a counter current. Therefore the super-electrons are paired with wavenumbers of -k and k+Q, such that the momenta do not lie in the "blocked" region of unpaired electrons. The choice of Q depends on

the size of the "blocking" region and the magnitude of the superconducting gap.

Chapter 3

Experimental Techniques

3.1 Small Angle Neutron Scattering

3.1.1 Overview

Small angle neutron scattering is a well established technique in condensed matter physics. The neutron can penetrate most materials deeply into the bulk and since the wavelength of thermal neutrons is comparable to atomic spacing, diffraction (and coherent interference) from periodic structures yields unique information on the microscopic scale. The neutron's magnetic moment also allows scattering from magnetic structures, so SANS is a useful technique in investigating magnetism and superconductivity; it allows scattering from vortices and magnetic moments. The technique will be summarised in this section, but a more rigourous and in-depth review can be found elsewhere [for example, Byrne, 1994; Bacon, 1975]).

3.1.2 Fundamentals of Neutron Scattering

The neutron is a spin-half particle, with zero overall charge, a mass of 1.007 a.m.u. and a magnetic dipole moment of -1.913μ_N. In the neutron scattering experiments presented here, the neutrons are produced by either a spallation source (at the Paul Scherrer Institute (PSI)) or result from a nuclear fission process (at the Institute Laue Langevin (ILL)).

SINQ is situated at the end of a cascade of three accelerators that deliver a proton beam of 590 MeV in energy at a current up to 1.8 mA. The neutron beams are extracted from a heavy water moderator surrounding the target, which is an array of lead rods enclosed in stainless steel tubes and cooled in cross flow by heavy water coolant. The Small Angle Neutron Scattering (SANS) instrument covers the Q-range from 6 x 10^{-3} nm^{-1} to 5.4 nm^{-1} for the detector displaced laterally by 50 cm up to 10.5 cm. Incident neutron flux is 9.02×10^7 $Ncm^{-2}s^{-1}$. The two-dimensional detector has 128 x 128 elements of 7.5 x 7.5 mm^2 and can be positioned at any distance between 1.4 and 20 m from the sample. The magnet used is an 11T cryomagnet, which can be tilted in both directions by up to 10° and rotated through a full circle and has a sample temperature range of 1.5K to 300K. The investigation of structures ranging from about 1 to 400nm can be measured by this instrument, making it ideally suited for investigations of fluxlines in superconductors.

At the ILL, the "high-flux" reactor operates at a thermal power of 58 MW using a single fuel element and an operating cycle of 50 days. There are hot, thermal and cold neutrons available at different beam tubes. The single fuel element sits in the

centre of a tank of 2.5m diameter containing the heavy water moderator. Cooling and moderation is by heavy water circulation passing through the fuel element, which is then cooled by the heat exchangers. Biological shielding is provided by a light water assembly surrounding the reflector tank, encased in dense concrete. D22 has a very high flux ($1.2\times10^{8}\mathrm{Ncm}^{-2}\mathrm{s}^{-1}$) at the sample in a wavelength range of 0.45 to 4 nm. The detector is similar to that of the PSI SANS detector with 128 x 128, 7.5 mm^2 pixels and can be positioned from 1.25 to 18m. The horizontal offset can be set from -5cm to 50cm and the rotation about both axis is $\pm2°$. The magnet used is a 3T cryomagnet which has a sample temperature range of 1.8K to 300K.

Neutrons undergo both nuclear and magnetic scattering and can be understood by a simple optical model. The refractive index n of the neutron, in accordance to Snell's law, is

$$\frac{\sin\alpha_1}{\sin\alpha_2} = \frac{V_1}{V_2} = n \tag{3.1}$$

where 1 and 2 correspond to two different media, α is the angle of incoming/outgoing neutrons and V is the neutron velocity. For de Broglie waves, where the relevant velocity is the group velocity (and not the phase velocity as is the case with electromagnetic waves), the correct definition of the refractive index is

$$n = \frac{k_2}{k_1} = \frac{\lambda_1}{\lambda_2} \tag{3.2}$$

where k is the wavevector and λ is the wavelength of the neutron. The neutron refraction phenomena can be understood in terms of the neutron's total energy. If a neutron with a kinetic energy of $E_k = \frac{1}{2}mv_1^2$ enters a medium where the neutron interacts, the total energy of the neutron must remain constant. For a constant interaction energy U, the total energy of the neutron is

$$\frac{1}{2}mv_1^2 = \frac{\hbar^2k_1^2}{2m} - \frac{\hbar^2k_2^2}{2m} + U. \tag{3.3}$$

Thus, the refractive index is related to the kinetic energy relative to the interaction energy

$$n = \sqrt{1 - \frac{U}{E_{k,1}}}. \tag{3.4}$$

The interaction potential of a neutron in a simple form is

$$V(\boldsymbol{r}) = \frac{2\pi\hbar^2}{m} b\delta(\boldsymbol{r} - \boldsymbol{r}_N) \tag{3.5}$$

where $\delta(\boldsymbol{r} - \boldsymbol{r}_N)$ is a Dirac delta function and the vectors $\boldsymbol{r}$ and $\boldsymbol{r}_N$ the position of the nucleus and neutron respectively. The total interaction energy is the sum of all potentials over all positions $\boldsymbol{r}_N$, which leads to a refractive index of

$$n = \sqrt{1 - \frac{4\pi N\bar{b}}{k_1^2}} \tag{3.6}$$

where the average coherent scattering length is given by

$$\bar{b} = \frac{1}{N}\sum_{l=1}^{N} b_l. \tag{3.7}$$

This scattering length is general for both magnetic and nuclear scattering, as the neutron has a magnetic moment. In fact, if a ferromagnet is used as the scattering surface inside a beam guide, the spin dependence of the refractive index is an effective way of producing spin polarised neutrons. This is possible because it can be arranged that only one spin state will undergo specular reflection inside a beam guide. Neutron scattering lengths for both nuclear and magnetic scattering will be discussed in more detail later.

A typical value for the refractive index (from nuclear scattering only) is 10^{-6}, which is extremely small compared to unity. This leads to a small critical angle $\theta_c = \cos^{-1} n \approx 10^{-3}$ degrees. This principle is the one used to transport low background, long wavelength neutrons from the source to the instruments. The extremely low critical angle reduces flux considerably, as many neutrons escape the beam pipe near the source. But this in fact acts as a filter, as fast (short wavelength) neutrons will not fulfill the critical reflection condition, resulting in a beam consisting of only long wavelengths and experimental areas relatively free from gamma radiation, as typical neutron guides are 10-100m away from the production target/reactor.

Both SANS instruments used here use similar physical and experimental principles and a diagram of a SANS instrument is shown in Figure 3.1. The velocity selector consists of a spinning drum of neutron absorbing material, with propagation channels to let the neutrons through. By placing the velocity selector at an angle to the incident beam and rotating the drum at a given speed, both neutron velocity (hence wavelength) and bandwidth can be selected. The collimation section is used to define beam divergence and comprises of two pinholes of varying sizes and separation. Typical diameter used is 16-25mm, with a spacing of up to 20m (depending on detector distance). The detector consists of a 20m long stainless steel tube (18m on D22), with a ^{3}He enriched gas inside. As the neutron passes through the gas, it undergoes nuclear capture (n+^{3}He$\rightarrow$ p+^{3}H) and the proton consequently ionises

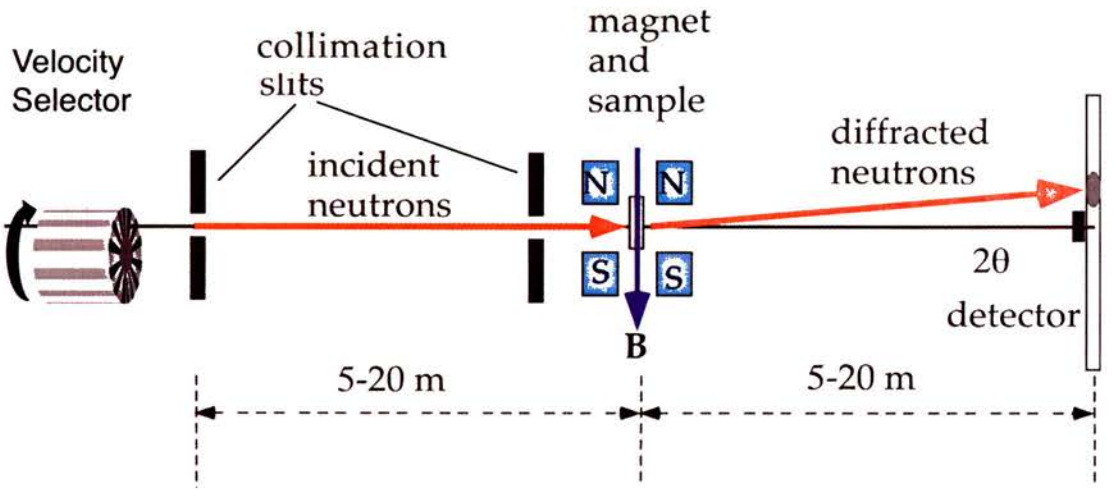

Figure 3.1: A schematic diagram of a SANS instrument.

^{3}He, which is detected by a grid of wires (anode) at a high potential. The grid is moveable within the detector tube, to allow a large range of scattering angles to be measured.

3.1.3 Neutron Diffraction, the Reciprocal Lattice and the Ewald Sphere

Standard methods of optics can be used to describe neutron diffraction from slits and periodic arrays. The similarities between neutron diffraction and X-ray diffraction are apparent and it is immediately obvious that if a beam of neutrons leaves a system of slits in a neutron absorber (shown in Figure 3.2), the condition of constructive interference is

$$n\lambda = d\sin\theta. \tag{3.8}$$

For a periodic lattice of scatterers in 3 dimensions, diffraction is easier to understand in terms of translational vectors of a unit cell. The unit cell of a Bravis lattice can be described by three basis vectors, $\boldsymbol{a}$, $\boldsymbol{b}$ and $\boldsymbol{c}$, such that the unit cell position is given by

$$\boldsymbol{r} = n_1\boldsymbol{a} + n_2\boldsymbol{b} + n_3\boldsymbol{c} \tag{3.9}$$

where $0 \leq n_i \leq N_i - 1$ and $N = N_1N_2N_3$ is the total number of unit cells. The basis vectors of the reciprocal lattice $\boldsymbol{a}^*$, $\boldsymbol{b}^*$ and $\boldsymbol{c}^*$ are defined as

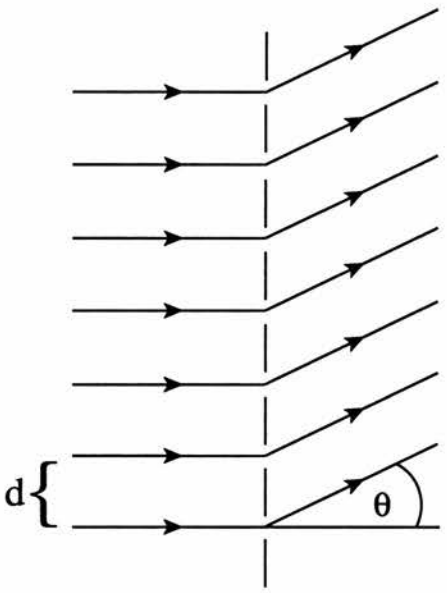

Figure 3.2: Periodic slit diffraction.

$$\begin{aligned} \boldsymbol{a}^* &= \frac{2\pi}{V_o}\boldsymbol{b} \times \boldsymbol{c} \\ \boldsymbol{b}^* &= \frac{2\pi}{V_o}\boldsymbol{c} \times \boldsymbol{a} \\ \boldsymbol{c}^* &= \frac{2\pi}{V_o}\boldsymbol{a} \times \boldsymbol{b} \end{aligned} \tag{3.10}$$

where V_o is the unit cell volume. The amplitude of the incident neutrons at $\boldsymbol{r}$ is

$$A = A_o e^{i\boldsymbol{K}\cdot\boldsymbol{r}}, \tag{3.11}$$

which are diffracted by the lattice. Assuming only elastic scattering, the observed amplitude at a point $\boldsymbol{R}$ is

$$A = A_o e^{i\boldsymbol{K}'\cdot\boldsymbol{R}} f e^{i(\boldsymbol{K}'-\boldsymbol{K})\cdot\boldsymbol{r}} \tag{3.12}$$

where the initial and propagation vectors of the incident and scattered neutrons are denoted by $\boldsymbol{K}$ and $\boldsymbol{K}'$, respectively, and f is the fraction scattered. The scattering vector $\boldsymbol{q}$ can be defined as

$$\boldsymbol{K}' = \boldsymbol{K} - \boldsymbol{q}. \tag{3.13}$$

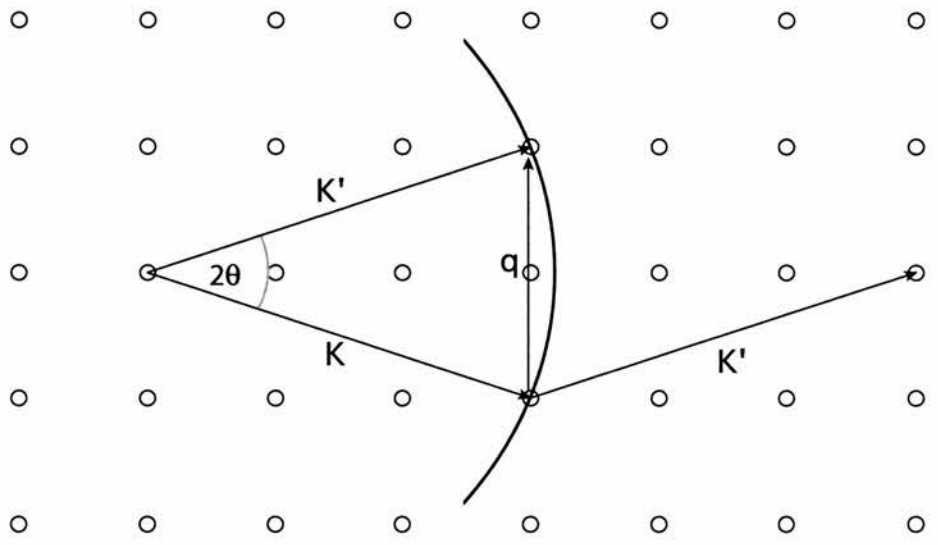

Figure 3.3: The Ewald Sphere construct in Reciprocal space. In order to satisfy the Bragg condition the scattering vector must coincide with a reciprocal lattice vector, which is also demonstrated by the reciprocal lattice points lying on the Ewald Sphere.

The sum of scattered neutrons over all lattice sites is

$$A = A_o e^{i\boldsymbol{K'}\cdot\boldsymbol{R}} f \sum_{n_1,n_2,n_3} e^{i(\boldsymbol{K'}-\boldsymbol{K})\cdot(n_1\boldsymbol{a}+n_2\boldsymbol{b}+n_3\boldsymbol{c})}. \tag{3.14}$$

In order to see non-zero diffraction, all unit cells must add up in phase, which implies

$$\begin{aligned} \boldsymbol{q}\cdot\boldsymbol{a} &= 2\pi h \\ \boldsymbol{q}\cdot\boldsymbol{b} &= 2\pi k \\ \boldsymbol{q}\cdot\boldsymbol{c} &= 2\pi l \end{aligned} \tag{3.15}$$

where h,k and l are integers. From equations 3.10 and 3.15 it can be seen that the diffraction condition is

$$\boldsymbol{q} = h\boldsymbol{a}^* + k\boldsymbol{b}^* + l\boldsymbol{c}^* \tag{3.16}$$

for planes with Miller indices (h,k,l), i.e $\boldsymbol{q}$ is confined to a reciprocal lattice vector. It is useful to conceptualise this with the Ewald sphere construct, as shown in Figure 3.3. It is clear from the Ewald condition that Equation 3.13 corresponds to the Bragg condition

$$q = 2K \sin\theta. \tag{3.17}$$

Unless a quantitative set of scattering intensities is required, Bragg's law is all that is needed to conduct a Small Angle Neutron Scattering (SANS) experiment. However, detailed analysis of the scattered intensities allows the absolute form factor to be determined and thus physical quantities may be extracted, as discussed for the flux line lattice in Section 3.1.7.

3.1.4 The Differential Scattering Cross Section

The scattering intensity is found from the differential scattering cross section, which describes the fraction of neutrons per second that are scattered into a solid angle $d\Omega$, and is given by

$$\frac{d\sigma}{d\Omega} = \left| \sum_n b_n e^{i\boldsymbol{q}\cdot\boldsymbol{r}_n} \right|^2 \tag{3.18}$$

where n is the sum over all scatters and b_n is the scattering length of the n'th scatterer. Magnetic and nuclear scattering is contained within the different expressions for the scattering length.

3.1.5 Nuclear Scattering

Nuclear scattering is a short range interaction that acts over distances of the order 10^{-14}m and a schematic diagram of potentials is shown in Figure 3.4. The nuclear cross section is calculated from the sum of scattering over all atoms, which can be split into two sums: the first sum is over atomic positions within one unit cell and the second over all unit cells in the crystal. Given the position of atoms to be $(n_1\boldsymbol{h} + n_2\boldsymbol{k} + n_3\boldsymbol{l})+\boldsymbol{r}_m$, where $\boldsymbol{r}_m$ is the atomic position within the unit cell, the nuclear differential cross section is

$$\frac{d\sigma}{d\Omega} = \left| \sum_{n_{1,2,3}} e^{2\pi i(n_1 h+n_2 k+n_3 l)} \sum_m b_m e^{i\boldsymbol{q}\cdot\boldsymbol{r}_m} \right|^2 \tag{3.19}$$

where b_m is the nuclear scattering length for elements/isotopes. The first sum in

Equation 3.19 can be expressed as a sum of delta functions, positioned at all reciprocal lattice vectors $\boldsymbol{Q} = h\boldsymbol{a}^* + k\boldsymbol{b}^* + l\boldsymbol{c}^*$ [Eskildsen, 1998; Bacon, 1975]

$$\left| \sum_{n_{1,2,3}} e^{2\pi i(n_1 h + n_2 k + n_3 l)} \right|^2 = \frac{(2\pi)^3}{V_0} N \sum_{\boldsymbol{Q}} \delta(\boldsymbol{q} - \boldsymbol{Q}). \tag{3.20}$$

The nuclear structure factor can be defined as

$$F(\boldsymbol{q}) = \sum_m b_m e^{i\boldsymbol{q}\cdot\boldsymbol{r}_m} \tag{3.21}$$

which leads to the following expression for the nuclear differential scattering cross section

$$\frac{d\sigma}{d\Omega} = \frac{(2\pi)^3}{V_0} \sum_{\boldsymbol{Q}} \delta(\boldsymbol{q} - \boldsymbol{Q}) |F(\boldsymbol{q})|^2. \tag{3.22}$$

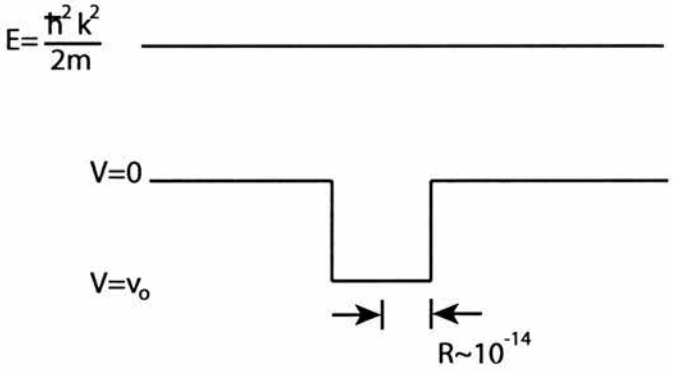

Figure 3.4: Potential well representing the neutron-nucleus interaction.

3.1.6 Magnetic Scattering

Any ordered magnetic structure in a sample will produce scattering due to the neutron's magnetic moment. This leads to the scattering cross section having two parts; nuclear (b_N) and magnetic (b_M) scattering. The magnetic moments and fields have a direction associated with them, which means the scattering length becomes a vector quantity, with scattering dependent on the neutron spin, $\frac{1}{2}\hat{\boldsymbol{\sigma}}$, relative to the magnetic moments/fields. Thus

$$b = b_N + b_M \tag{3.23}$$

where

$$b_M = \hat{\boldsymbol{\sigma}} \cdot \boldsymbol{b}_M. \tag{3.24}$$

In the Born approximation, the scattering length for a magnetic field distribution is

$$b_M = \frac{V(\boldsymbol{q})}{4\pi\hbar^2/2m_n} \tag{3.25}$$

where m_n is the neutron mass, $V(\boldsymbol{q})$ is the Fourier transform of the interaction potential, $V(\boldsymbol{r})$, is

$$V(\boldsymbol{r}) = \gamma\mu_N \hat{\boldsymbol{\sigma}} \cdot \boldsymbol{B}(\boldsymbol{r}), \tag{3.26}$$

where $\gamma = 1.91$ is the neutron gyromagnetic ratio and $\mu_N = -9.65 \times 10^{-27} JT^{-1}$. The potential can arise from any magnetic structure, such as the FLL, or magnetism from the electronic structure of atoms. If the magnetic structure is commensurate, a magnetic structure factor can be found in a similar way to the nuclear scattering by summing just the magnetic unit cell. If it is incommensurate, the whole crystal must be evaluated.

3.1.7 Scattering from the FLL

Scattering from the FLL can be thought of as scattering from periodic magnetic moments. The scattering length for an Abrikosov lattice is

$$b_{FLL} = \frac{\gamma\mu_N}{4\pi\hbar^2/2m_n}\boldsymbol{\sigma} \cdot \int \boldsymbol{B}(\boldsymbol{r}) e^{i\boldsymbol{q}\cdot\boldsymbol{r}} d\boldsymbol{r} \tag{3.27}$$

where $\boldsymbol{B}(\boldsymbol{r})$ is given by the Fourier series

$$\boldsymbol{B}(\boldsymbol{r}) = \sum_{\boldsymbol{q}} \boldsymbol{h}(\boldsymbol{q}) e^{i\boldsymbol{q}\cdot\boldsymbol{r}}. \tag{3.28}$$

Thus from Equation 3.22, by measuring the scattered intensity from the FLL, the magnetic form factor, $|\boldsymbol{h}(\boldsymbol{q})|^2$, can be obtained. Due to imperfections in the FLL and the finite instrument resolution, the Bragg peaks are not delta functions. In order to relate the measured spot intensity to the form factor, the integrated intensity must be measured by "rocking" through the reflections. The integrated reflectivity for a FLL can be calculated from magnetic cross sections [Squires, 1978] and is given by [Christen *et al.*, 1977]

$$I(\boldsymbol{q}_{hk}) = 2\pi\phi \left(\frac{\mu_N}{4}\right)^2 \frac{V\lambda_n}{\Phi_o^2 \boldsymbol{q}_{hk}} |h(\boldsymbol{q}_{hk})|^2, \tag{3.29}$$

where ϕ is the incident neutron flux and V the sample volume. In practice the integrated intensity is measured by fitting a Gaussian or Lorentzian to the intensities (normalised to the full beam intensity) collected at discrete angles.

Calculating the magnetic form factor of a FLL requires an in-depth knowledge of the exact field distribution. The simplest approximation is using the London equations, which can be modified to contain a FLL

$$\lambda_L \boldsymbol{\nabla} \times \boldsymbol{\nabla} \times \boldsymbol{B} + \boldsymbol{B} = \hat{z}\Phi_0 \sum_i \delta_{2D}(r - r_i). \tag{3.30}$$

By taking the Fourier expansion in Equation 3.28,

$$\boldsymbol{h}(\boldsymbol{q}) = \frac{\boldsymbol{B}}{1 + \lambda_L^2 \boldsymbol{q}_{hk}^2} \tag{3.31}$$

which is completely unphysical as it assumes zero core size. It is, however, a good approximation for extreme type II superconductors [Aegerter *et al.*, 1998]. HTC's are a good example of extreme type II superconductors due to their long penetration depth and very short coherence length. Unfortunately, due to the long penetration depths, the total scattering intensity of HTC's is considerably lower than for conventional superconductors.

For superconductors where the coherence becomes an issue, the effect of a finite core of radius ξ can be represented by a Gaussian cut off $e^{c\xi^2 q^2}$, where c is a constant [Yaouanc *et al.*, 1997]. Therefore, measurements of the FLL form factor can be used to calculate values for the penetration depth and coherence length. A more realistic model for the form factor is the Clem model [Clem, 1975], which is more accurate in the vicinity of the vortex core. This will not, however, be covered here.

3.2 The μSR Technique

3.2.1 Overview

Muons are spin 1/2 leptons with a halflife $\tau_\mu = 2.19709(5)\mu s$, $\pm$ one electronic charge and a mass 105.65839(29) MeVc^{-2} [Anon., 1984]. The use of spin polarised muons to probe solids, liquids and gases is referred to as μSR: Muon Spin Rotation/Relaxation/Resonance, where the "R" is determined by the nature of application of the muon. Both positively and negatively charged muons are used as probes. When a negative muon is implanted into a solid, it is captured by an atom and cascades into the lowest muonic orbital. This is comparable with the radii of a heavy nuclei, so it would normally undergo nuclear capture ($\mu^- p \rightarrow n\nu_\mu$). This results in complex behaviour beyond the scope of this thesis, as this thesis is concerned only with the use of positive muons. Positive muons implanted into a solid undergo a rapid Coulombic thermalisation [Blundell, 1999], after which muons "stop" at interstitial sites due to electrostatic repulsion. Typical surface muon implantation depths are 1.5mm in polythene and 0.65mm in aluminium. Time differential (TD) spectra are produced by timing muons on entering the spectrometer and stopping the timer when a positron is detected from the muon decay.

Positive muons implanted into a sample precess with a Larmor frequency $\omega_\mu = \gamma_\mu B$ in the presence of a magnetic field B, the vector sum of the applied field and local field due to the sample. The muon gyromagnetic ratio is $\gamma_\mu/2\pi$=0.0135534(5) MHzG^{-1} [Schenck, 1985]. The simplest TD μSR technique is transverse field (TF) muon spin rotation, where the magnetic field is applied transverse to the muon polarisation. This technique is most widely used in the study of vortex lattices (VL) in superconductors. Depolarisation due to irreversible processes, such as muon diffusion and muon spin flipping due to hyperfine interactions with electrons and nuclei, is referred to as muon spin relaxation and is usually performed in a longitudinal field (LF) or zero field (ZF).

μSR experiments are performed at the Paul Scherrer Institute (PSI), Villigen, Switzerland which is a continuous source beam and ISIS, Rutherford Appleton, Abingdon, Oxon, UK which is a pulsed source.

3.2.2 Muon Production

At PSI, protons accelerated by a 590MeV ring cyclotron are guided to a pyrolytic graphite target, either 5cm thick (target M) or 4cm thick (target E). The muon

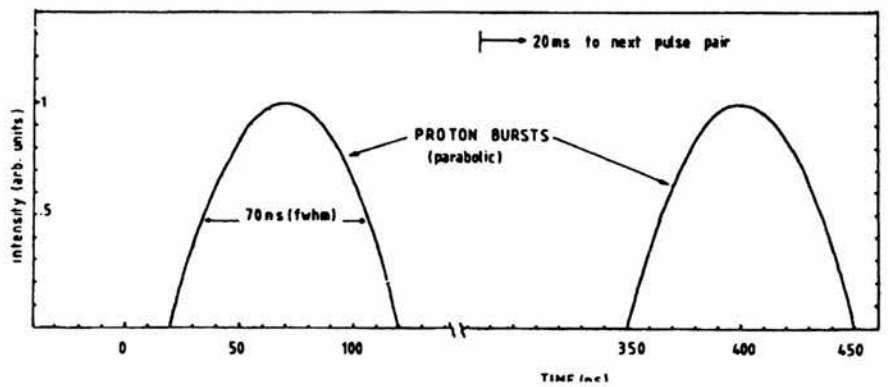

Figure 3.5: The time structure of the proton beam at ISIS. The muon beam preserves this time structure, at 50Hz with a double pulse separated by 330ns and each sub-pulse with a full width half maxima (FWHM) of 70ns [Lee *et al.*, 1998a]

facilities at PSI are effectively a continuous beam. At ISIS, protons are accelerated by a 800MeV synchrotron at a working frequency of 100Hz, but protons are produced at a frequency of 50Hz with a double pulse structure, as shown in Figure3.5. The muon target at ISIS is 5-10mm thick pyrolytic graphite, with 2-3% of the incident protons interacting with the target.

Pions (π) are produced by reactions of the incident protons (p) with protons and neutrons (n) of the graphite production target

$$\begin{aligned} p + p &\rightarrow \pi^+ + p + n \\ p + n &\rightarrow \pi^+ + n + n \\ p + n &\rightarrow \pi^- + p + p. \end{aligned} \tag{3.32}$$

The pions then decay via the weak interaction into muons (μ) and muon neutrinos (ν_μ) with a half life of 26.030(23) ns [Anon., 1984]

$$\begin{aligned} \pi^+ &\rightarrow \mu^+ + \nu_\mu \\ \pi^- &\rightarrow \mu^- + \overline{\nu}_\mu. \end{aligned} \tag{3.33}$$

This is a two body decay, so the muon and neutrino are emitted in opposite directions in the pion's rest frame in order to conserve momentum. The pion has

spin zero and since neutrinos have their spins antiparallel to their momentum, the muon from the pion decay must also have spin. Thus, the decay of positive pions produces 100% longitudinally polarised positive muons [Riseman, 1993].

The positive muon decays in a vacuum with a mean half life $\tau_\mu = 2.19709(5)\mu$s into a positron (e^+) and neutrino-antineutrino pair

$$\mu^+ \rightarrow e^+ + \nu_e + \overline{\nu}_\mu \tag{3.34}$$

and the positrons are subsequently detected using an array of photomultiplier tubes.

The positron is emitted primarily along the spin muon's direction. After integrating over all possible neutrino momenta, the probability W per unit time that a positron will be emitted at an angle θ with respect to the muon spin at time of decay is

$$dW(\epsilon,\theta) = \frac{e^{t/\tau_\mu}}{\tau_\mu}[1 + a(\epsilon)\cos\theta]n(\epsilon)d\epsilon d\cos\theta dt, \tag{3.35}$$

where $a(\epsilon) = (2\epsilon - 1)/(3 - 2\epsilon)$, $n(\epsilon) = 2\epsilon^2(3 - 2\epsilon)$ and the reduced positron energy ϵ is defined as $\epsilon = E/E_{max}$, where E_{max} is the maximum positron energy $E_{max} = 52.83$ MeV. This relation is shown in Figure3.6.

3.2.3 PSI: Bulk μSR

The bulk μSR facility used at PSI in the work presented in this thesis is situated on the piM3 beamline. Two cryostats are permanently installed on piM3. The Low Temperature Facility (LTF) instrument is an Oxford Instruments top-loading ^{3}He dilution refrigerator, with an operational temperature range of 20.3mK to 10K. A 3T superconducting magnet is contained within the cryostat which is parallel to the muon momentum. An auxiliary 100Oe electromagnet perpendicular to the muon momentum is also available. The General Purpose Spectrometer (GPS) instrument is a Quantum Technology top loading continuous flow ^{4}He evaporation cryostat with an operational temperature range of 2K to 300K. The instrument has two sets of Helmholtz coils to produce magnetic fields at the sample position. A 6.4kOe set of coils along the muon direction used for LF and TF depending on the polarisation of the muon spin and a 60Oe horizontal field perpendicular to the muon direction. The latter field is usually used for calibration purposes or "T20" measurements in LF, but can also be used in addition to the main coils to investigate the angular field dependence of a sample at low fields. Both instruments have a typical muon polarisation >95%, with the muon spin 6-60 degrees with respect to the muon

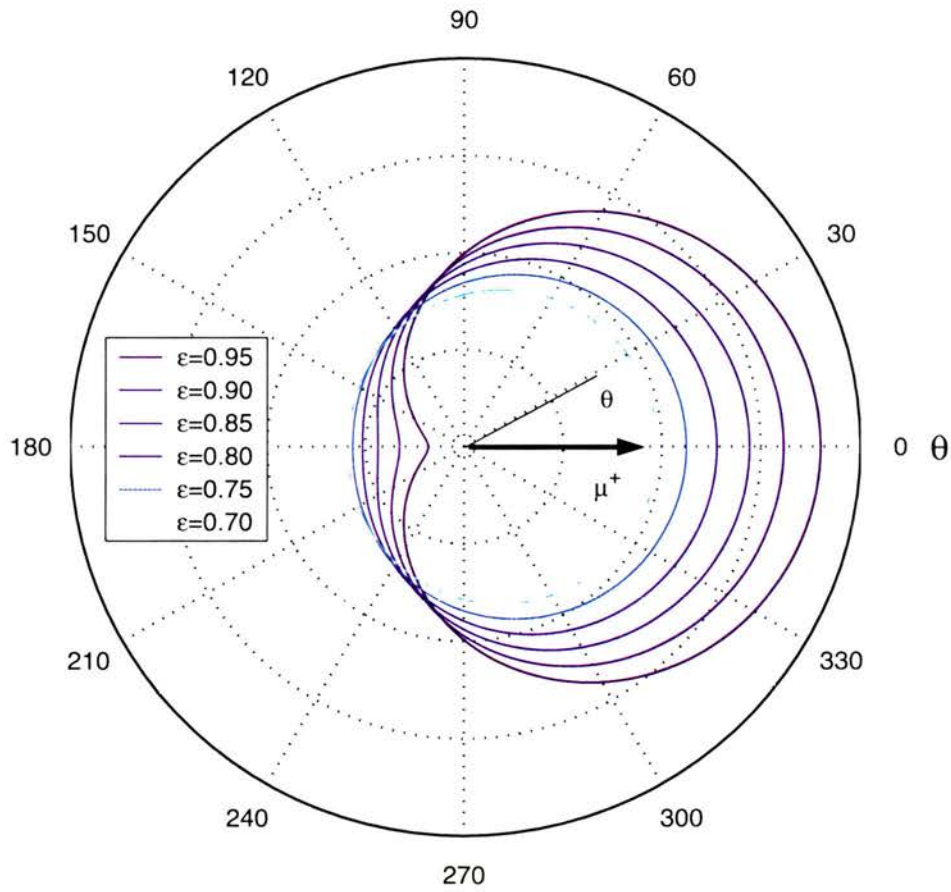

Figure 3.6: Polar plot of positron emission probability as a function of reduced positron energy, ϵ.

momentum.

Figure 3.7 shows the detector arrangement for both the GPS and the LTF instruments. The GPS instrument has a detector arrangement which consists of a muon detector (M) that is connected to two photomultipliers. This is the detector which triggers the start of the timer. The five positron detectors are Forward (F), Backward (B), Up(U), Down (D) and Right (R), which detect the decay positrons from the muons and are used to trigger the timer to stop. It is not possible to have a sixth (Left) detector due to the sample mount and helium inlet. The F and B detectors are connected to two photomultipliers to allow for the beam and veto detectors. The B veto detector allows for any muons which do not enter the sample area by rejecting the muons (and associated positrons) - a form of "active collimation". The F veto detector rejects any muons that do not stop in the sample and is used with small samples. The LTF instrument has a similar arrangement, but due to the nature of the dilution refrigerator it is only possible to have 4 detectors - Forward, Back, Left (L) and Right. The active collimation/veto is currently under development, but should work in a similar way to the GPS instrument. In addition to the active vetos, the electronics for both instruments checks for and discard double events (i.e more than one muon entering the sample area), as it would not be possible to connect a detected positron unambiguously to a given muon.

The muons are directed from the target with electrostatic fields, quadropole magnets and dipole magnets through an evacuated beamline. Figure3.9 shows a schematic diagram of the piM3 beamline magnets. Quadropole magnets are used for beam focusing, dipole magnets direct the beam and electrostatic fields are used to deflect muons either in combination with magnets or on their own. The intensity of the incoming beam is controlled by variable slits positioned in front of the septum magnets. It is possible to change the event rate of the two instruments individually. As the number of incident muons increase the probability for a double event increases, so opening the slits completely actually decreases the "good" events. It can be observed experimentally that the optimum number of events per second is approximately 30,000. Beam collimators are placed in front of the septum magnet to allow the beam FWHM to be varied, so reducing the background from muons hitting the sample surroundings. A typical muon beam profile is shown in Figure3.8.

In an ideal experiment, a TD spectra contains start/stop events belonging to the same muon. The muon that starts the timer is the same muon that decays and is detected to stop the timer. Experiments using continuous beams, however, have a random background due to a number of muons escaping detection [Abela

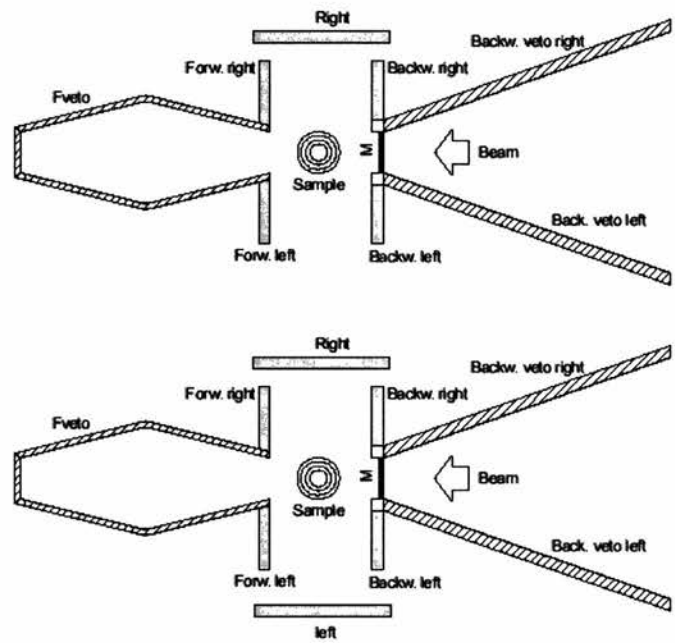

Figure 3.7: The piM3 detector arrangement. Top: GPS facility - note the top and bottom detectors have been removed for clarity. Bottom: The LTF facility - note the active veto is currently under development for the LTF facility.

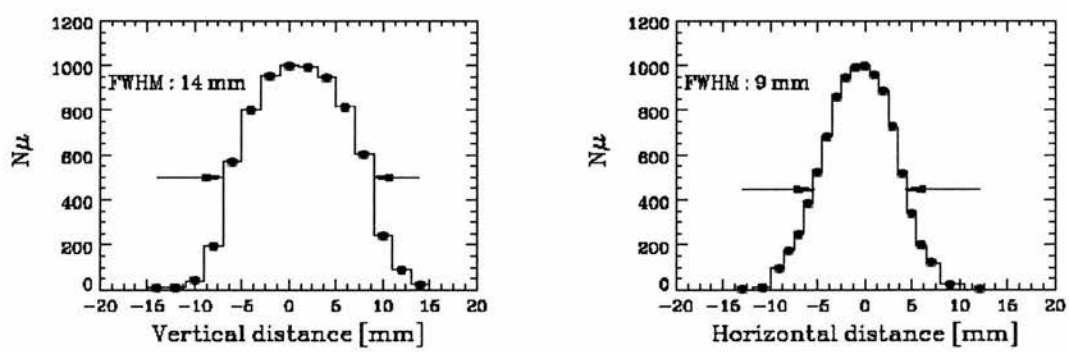

Figure 3.8: The beam profiles at the piM3 GPS focus. This also represents the beam profile at the LTF instrument. [Amato, 2003]

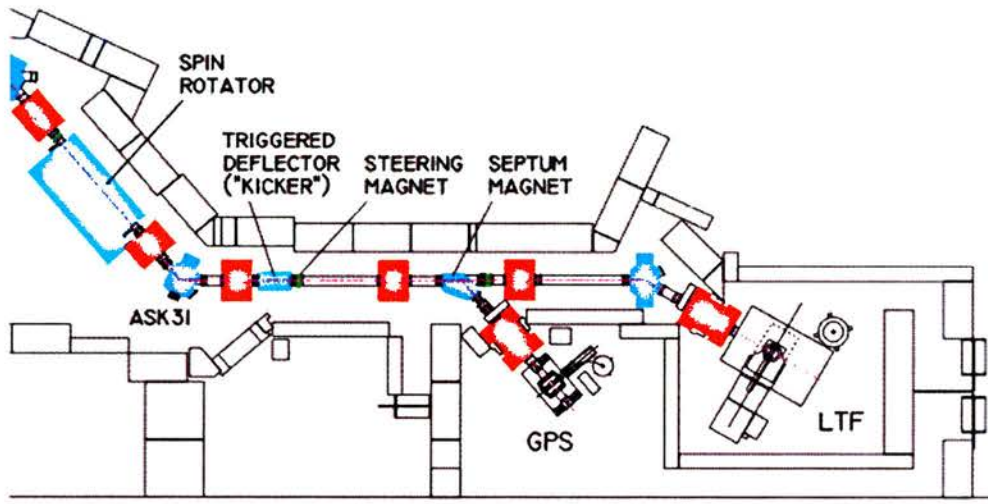

Figure 3.9: The piM3 beamline at PSI. Items coloured red are quadropole focussing magnets; items coloured blue are dipole steering magnets and items coloured light blue are electrostatic fields. [Amato, 2003]

et al., 1999] or double events. This has the effect of limiting the histogram time interval to no more than 10μs and excludes investigations of low spin precession frequency or slow relaxation rates. Pulsed muon beams do not suffer this problem, as the muons are timed from the start of the moun pulse. In this technique time resolution is limited by the width of the muon pulse, but backgrounds are typically three orders of magnitude lower. The method to solve the large random background problem is solved by extracting one muon at a time from a continuous beam - Muons On REquest (MORE). This is achieved by means of a fast switching electrostatic "kicker", as shown in Fig 3.9. It consists of two 1m long, 20cm wide electrodes situated 20cm apart. They are powered by dc voltages up to $\pm$5kV via switches which contain fifteen fast (40kHz) high voltage MOSFET transistors. This allows a potential difference of 20 kV, separating the muon trajectories by 5cm at 5m from the kicker exit. A 0.1mm thick plastic scintillation counter is placed at the bending magnet ASK31 to trigger the kicker. Alternatively, the muon detector in the spectrometer (M-counter, Fig 3.7) can be used to trigger the kicker. The kicker is switched to the spectrometer running in MORE mode a maximum of 40kHz at 5μs. After the signal of the first muon to enter the spectrometer is detected (via ASK31 or M-counter), a minimum delay of 200ns is added before the kicker is switched back to the spectrometer running in "parasitic" mode.

The application of MORE does not significantly reduce the count rate of the

spectrometer. This is due to MORE producing twice as many results of higher quality than a conventional experiment, as double events and escaped muons are less likely. The background in MORE mode is at least two orders of magnitude lower than conventional mode, but a small distortion in the spectra at times t < 450ns is observed due to the delay in passage of the muon and the arrival of the trigger signal at the kicker. This distortion is less pronounced if ASK31 is used rather than M-counter, but the count rate is 6 times less when ASK31 is used. This is because the beam is kicked back to the parasitic spectrometer even if the muon does not reach the M-counter (e.g. hits the slits in the septum magnet). The MORE technique is therefore not useful for fast relaxing signals, as cutting off the first channels has a significant effect.

3.2.4 ISIS: Bulk μSR

The μSR spectrometer at ISIS is a multi-purpose spectrometer which can be rotated with respect to the incoming muon beam momentum, according to the required experimental geometry. The detector array consists of 32 detectors arranged around two circles, as shown in Figure 3.10. The number of detectors is considerably more than at the PSI spectrometers, since ISIS is a pulsed source. Typically hundreds of muons stop in the sample in each pulse, which is too high considering the typical dead time of the detectors. Thus 32 detectors are used and the final data files contain 32 separate histograms, which can be reduced to a more convenient number at the data analysis stage. When used in LF mode, the detectors are grouped together into two groups - the forward and backward detectors each consisting of 16 segments. In TF mode, the detector assembly is rotated by 90° and there are 16 detectors each with 2 segments. The magnetic field is generated by water cooled copper coils with an iron yolk present to maximise the field at the sample area.

The maximum field attainable in TF at ISIS is limited by the finite pulse width, where the maximum field attainable at PSI is limited by the histogram time resolution. Thus, it is possible to use much higher fields at PSI than at ISIS. The pulse FWHM at ISIS is 70ns and the pulse is "smeared" further by the 26ns lifetime of the parent pions. It follows that the time dependant count rate is convolved with the pulse shape of the incoming muon beam, which will have a significant effect when there are variations in the count rate on a time scale comparable with this pulse width. Thus, it is only important when the Larmor precession frequency is high or there is a rapid muon depolarisation. Given that the muon pulse shape

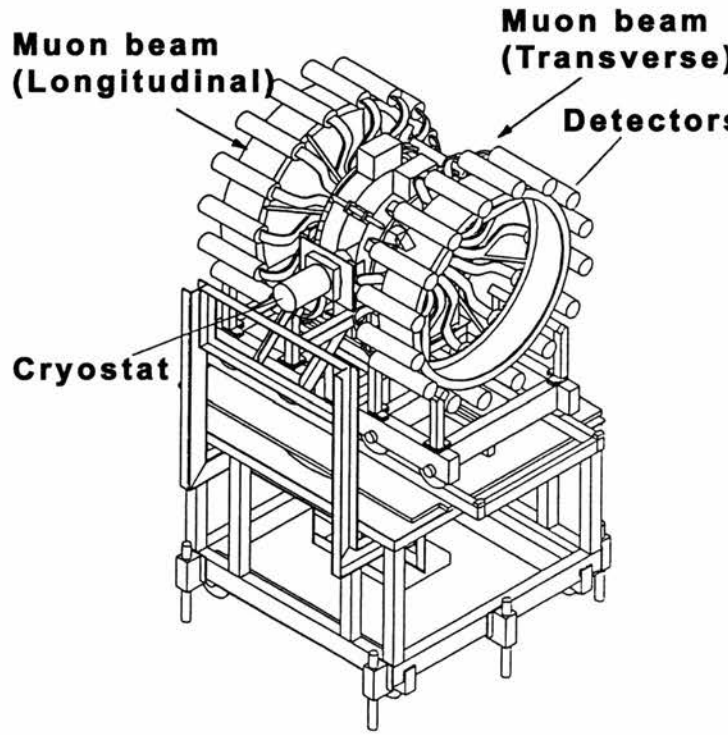

Figure 3.10: The μSR spectrometer at ISIS [Scott, 1996].

is a Gaussian[1] $W(t) = \exp(-t^2/\tau_w^2)$, if studying a weakly damped sample such as silver, the resulting signal would be a convolution of the ideal signal $(1 + A\cos(\omega_\mu t))$ with $W(t)$, where A is the ideal asymmetry and τ_w is the pulse width. The effect of the convolution is to reduce the asymmetry to a value $A\exp(-\omega_\mu^2\tau_w^2/4)$. Thus the asymmetry falls by 1/e of its ideal value at an applied field B given by $(\omega_\mu/2\pi) = (\gamma_\mu/2\pi)B_{1/e} = 1/(\pi\tau_w)$. So for a pulse FWHM of 70ns, τ_w =42ns leading to a corresponding $B_{1/e}$=560G.

Detector deadtime is a well known problem in particle physics, but in the case of μSR, it is a larger problem with a pulsed technique than continuous source due to the increased incident muon rate. The detectors have limitations on the speed at which they are are able to respond, leading to a failure to record two positrons as separate events. This is dealt with, to a certain degree, by increasing the number of detectors around the sample. However, there is still a detector deadtime which will lead to an observed event rate, which is less than the true rate obtained for a system with negligible deadtime. In the simplest case, for a true rate, r, there is no response for a time τ_d after each pulse but a perfect recovery after that. The observed rate, r_{ob}, is then

$$r_{ob} = r/(1 + r\tau_d). \tag{3.36}$$

It is found experimentally that the distortion is typically 5% at the beginning of the histogram [Scott, 1996], i.e. $r_{ob}\tau_d \approx 0.05$ and Equation 3.36 is adequate to adjust the data.

3.2.5 PSI: Low Energy Muons

Conventional μSR beams deliver spin polarised muons in the MeV energy range, resulting in a deep penetration depth into the sample. This renders conventional μSR only suitable for investigations into bulk properties of materials. A tertiary beam of spin polarised muons has been developed at PSI where the muon energy is tuneable between 10eV and 20KeV, leading to a muon penetration depth of fractions of a nm to a few hundred nm. Thus μSR becomes accessible for the investigation of thin films and surface physics.

The Low Energy Muon apparatus is situated on the piE3 beamline[2], tuned to

[1]This is a gross over simplification. A better muon pulse shape is an inverted parabola convoluted with a decaying exponential. However, a Gaussian dramatically simplifies the arguments put forward here and does not detract from any conclusions made.

[2]The LEM apparatus is currently being moved to the purpose built beamline piE4.

deliver a secondary surface muon momentum of 27.3MeV/c and an energy 4MeV. Positron background in the beam is suppressed by an $\boldsymbol{E}$x$\boldsymbol{B}$ separator adjusted to transmit μ^+, similar to the one situated on the piM3 beamline. Lead and copper collimators define the beam spot before the muons enter the ultra high vacuum (UHV) chamber through a 50μm thick stainless steel vacuum window, shown in Figure3.11.

Once inside the HV chamber, the muons are incident on a cooled 125μm Ag foil with a downside solid rare gas (Ar, Ne), or solid nitrogen deposit 200 - 300nm thick. This acts as a moderator, slowing the incident high energy muons to spin polarised epithermal muons with an efficiency of 10^{-5} to 10^{-4} [Morenzoni *et al.*, 1994]. The beam momentum quoted above is chosen to maximise the stopping density on the solid gas layer of the substrate, thus maximising the yield of epithermal muons emerging from the moderator.

The main part of the moderation process consists of degrading a fraction of the beam in the substrate to energies of a few tens of keV by ordinary ionisation processes. These keV muons are further decelerated when passing through the solid gas layer. In the solid gas layer, at energies of less than a few keV charge-exchange processes are the dominant inelastic processes [Morenzoni *et al.*, 1996]. The solid gas layer is a wide band gap insulator, resulting in it being ionised by the incident muons (and muonium), followed by the formation of muonium and subsequent break up by further collisions with electrons. The band gap energy of the Noble gases are of the order 20eV [Klein and Venables, 1976], so at energies approaching this the inelastic energy loss mechanisms is strongly suppressed. Elastic energy loss resulting from collisions with nuclei is inefficient as the muon is much lighter than the nuclei, so once the muons are at epithermal energies they are emitted with no efficient energy loss process. The number of elastic collisions at epithermal energies is sufficient to ensure an isotropic angular distribution of muons. The moderation process in the solid gas layer leads to an enhancement in the number of emitted muons with an energy of 15eV with a FWHM of 20eV [Morenzoni *et al.*, 1994]. Other materials act as a degrader, resulting in a relatively flat energy spectrum down to zero eV. Only a small fraction of the beam is moderated in the solid gas layer, with the majority of muons leaving the moderator target with a mean energy of 500keV. There is also 80% probability that the muons will create muonium and thermalise or leave the layer as muonium, which further reduces the efficiency to 10^{-4} - 10^{-5}.

The epithermal muons are accelerated from the production area by electrostatic fields to energies up to 20keV. Physical limiting apertures are not used once the

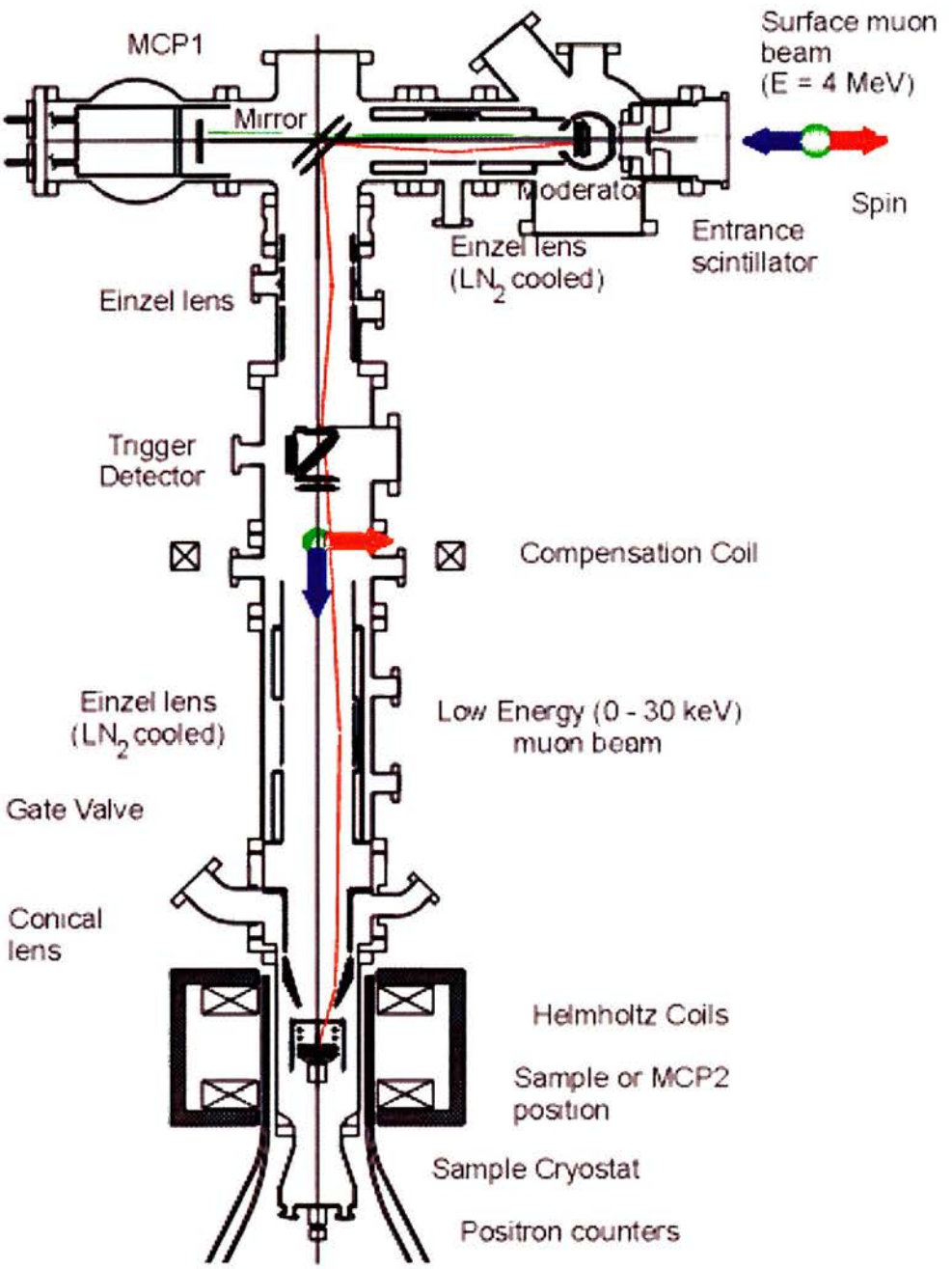

Figure 3.11: Schematic diagram of the LEM apparatus.

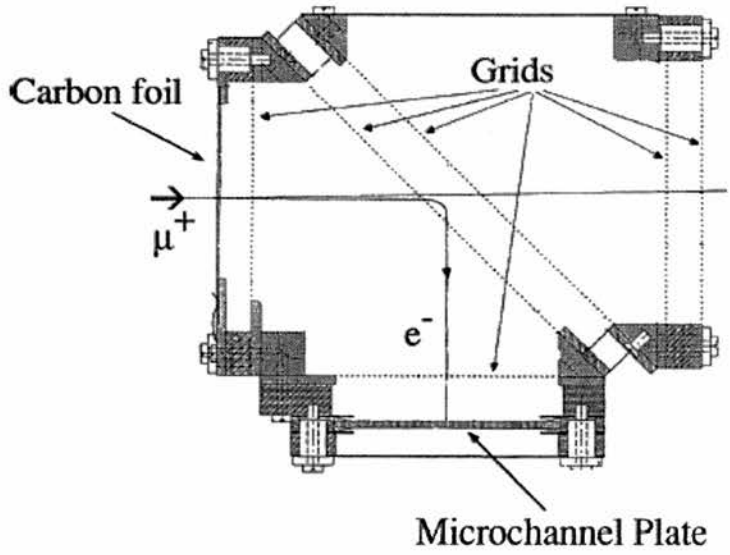

Figure 3.12: The trigger detector in the LEM apparatus [Morenzoni *et al.*, 1996].

muons have been through the moderation process, as a significant reduction in the count rate would result. The muons are focused by several liquid nitrogen cooled "einzel" electrostatic lenses, one before the electrostatic mirror and two after. The electrostatic mirror acts as an energy selector as high energy muons deflect little and are subsequently detected on the MCP1 detector. This is used as a beam monitor and to optimise the muon beam. The mirror has the effect of rotating the spin from parallel to the muon momentum to perpendicular to the muon momentum. Between the electrostatic mirror and sample, the trigger detector is used to start the timing circuits used for TD μSR. Since the yield of slow muons to incoming high energy muons is $<<1$, a trigger detector in the main beam will not result in an accurate start signal. Unfortunately a standard scintillation counter would significantly (if not entirely) reduce the slow muon count rate at the sample if used for a trigger detector. A specially developed detector has been implemented to deal with this problem, as shown in Figure3.11. It consists of a carbon foil of about 50 - 70 atomic layers combined with a microchannel plate[3] (MCP) perpendicular to the foil. The muons eject a few electrons from the foil, which are directed using electrostatically charged grids to the MCP, as shown in Fig 3.12. This has the consequence of

[3]An MCP is related to the photomultiplier tube. It consists of an annular array of tiny glass tubes (12-23mm diameter and 0.5 to 1mm long) fused together to form an array of thousands of independent electron multipliers.

scattering the muons, accompanied by a spread in energy and the possible muonium formation.

At the sample position, Helmholtz coils generate a 3000Oe field parallel to the muon momentum and perpendicular to the sample surface. For experiments presented in this thesis, a field parallel to the sample surface is used. This limits the size of field available to $\sim$200Oe, as the sample cryostat region is crowded in the area the magnets would need to be placed.

3.3 μSR Data and Analysis

3.3.1 Overview

μSR data from each detector consists of the time decay from an ensemble of muon spins, typically 20 million events per detector for conventional μSR and 2 million events per detector for slow μSR. Consequently, considerable attention needs to be paid to data manipulation and analysis, as described in this section.

3.3.2 Data

The raw histogram data for a given detector m is given by

$$N_m(t_h) = N_m(0)n_b\delta t e^{-t_h/\tau_\mu}[1 + A_m\alpha(t_h, \phi_m)] + b_m n_b \delta t \tag{3.37}$$

where δt is the original time binning, n_b is the additional software time binning (dealt with below), $N_m(0)$ is the event rate at time $t = 0$, b_m the background. The scaling factor A_m takes into account that the measured total asymmetry may differ between histograms, due to differing detector efficiencies. For a given time $t_h = h\Delta t = hn_b\delta t$, $\alpha(t_h, \phi_m)$ is the asymmetry with the initial phase of the muons with respect to the detector given by ϕ_m. A histogram may be a sum of counts from different detectors, as in the μSR facility at ISIS. The exponential decay asymmetry

$$D_m(t_h) = N_m(0)\Delta t e^{-t_h/\tau_\mu} A_m \alpha(t_h, \phi_m) \tag{3.38}$$

is the signal which is used in the subsequent analysis. Since the exponential decay is not of interest, it is useful to combine two histograms 180° apart to remove the effect of the muon lifetime

$$A_{LR}(t_h) = \frac{[N_L(t_h) - b_L] - [N_R(t_h) - b_R]}{[N_L(t_h) - b_L] + [N_R(t_h) - b_R]}. \tag{3.39}$$

3.3.3 Analysis in the Frequency Domain: Maxent

It is possible to attach a single number to a probability distribution which measures the amount of uncertainty in that probability distribution; this number is known as entropy. The Maximum Entropy Method (MEM) maximises this number in order to reduce uncertainty. In the simplest case, consider N propositions labelled by n=1, 2,

..., N and exactly one is true. Now assign to each of these propositions a probability P_n of being true. The amount of uncertainty in this situation is [Shannon, 1948]

$$S = -k \sum_{n=1}^{N} P_n \ln P_n \tag{3.40}$$

where k is an arbitrary positive constant[4]. Equation 3.40 can represent the number of questions (assuming yes/no answers) needed to isolate the true proposition, given a suitable choice of k. For many applications, Equation 3.40 needs to be modified to allow continuous probability distributions to be handled. The entropy for a continuous distribution P(x) is

$$S = -\int P(x) \ln \frac{P(x)}{M(x)} dx, \tag{3.41}$$

where $M(x)$ is a function determined by the exact nature of the problem. Maximising this quantity when $M(x)$ is constant, with mean and variance specified, leads to a Gaussian distribution.

Maximum Entropy as applied to μSR uses a trial probability distribution $P(B_i)$ where in effect the magnitude of each probability at B_i is a fit parameter, implying that no theoretical model is assumed when calculating the ME spectra. Effectively, each parameter $P(B_i)$ adds a non-relaxing cosine to the time domain asymmetry, with hundreds of fields B_i leading to an underdetermined problem unless constraints are added. Ideally, χ^2 should be constrained to the number of observable data points $\chi^2 = MN$, where M is the number of histograms and N is the number of bins per histogram. This leads to an infinite number of solutions [Buck and Macaulay, 1994].

When dealing with underdetermined problems, MEM has been shown to be the only consistent method for selecting a single spectra from a large number of spectra that fit the data [Skilling and Bryan, 1984]. The final MEM spectra must be the one which contains the minimum of information required to describe the data [Gull, 1989]. Thus, any departure from uniformity has to be present in the data and a MEM spectra should not contain artefacts. However, because of the pressure of χ^2 towards unity, the peaks and troughs of a MEM spectra tend to be too low and high respectively. Another limitation of the use of MEM is that the resulting spectra must always be positive and non-complex, which is due to the logarithm used when defining entropy in Equation 3.40. In μSR this assumption is justified [Buck and Macaulay, 1994].

[4]Equation 3.40 is identical in form to Planck's expression for thermodynamic entropy, when k is chosen to be the Maxwell-Boltzman constant.

In the algorithm used here, the trial distribution $P(B_i)$ is inverse Fourier transformed to provide a theoretical fit function $D_m(t_h)$, from which χ^2 can be calculated

$$\chi^2 = \sum_{m=1}^{M} \sum_{h=t_1/\Delta t}^{t_2/\Delta t} \frac{[D_m(t_h) - d_m(t_h)]^2}{\sigma_m^2(t_h)}. \tag{3.42}$$

where $d_m(t_h)$ is the experimental data. An entropy of

$$S = -\sum_i \frac{P(B_i)}{eP_d} \ln \frac{P(B_i)}{eP_d} \tag{3.43}$$

is used to select the most likely solution, where P_d is related to the noise level in $P(B)$. The gradients of χ^2 and S are calculated with respect to $P(B_i)$ to select the next set of values for the trial $P(B_i)$. The χ^2 term is added by use of a Lagrange multiplier λ to form the constrained entropy S_c, which is then maximised

$$S_c = \lambda S - \frac{\chi^2}{2l^2} \tag{3.44}$$

where l is the "looseness". Looseness allows the user to change the emphasis between χ^2 and the entropy term in the fit to allow for errors not already accounted for in the experimental errors[5]. A positive value of the looseness (typically not exceeding 1.02 for PSI and 1.04 for ISIS) allows the reduced χ^2 value to vary from 1, thus shifting the emphasis in the fit towards the entropy. This changes the constraint to $\chi^2 \equiv l^2 MN$.

3.3.4 The MEM Kernel

The MEM *Opus* kernel, $\boldsymbol{O}_{m,h,i}$, can be broken down into the following parts:

$$D_m(t_h) = \sum_i \boldsymbol{O}_{m,h,i} P_g(B_i) = K^{\mu}_{h,m} \sum_h K^t_{h,m} \left[K^{aft}_h \sum_i IFT_{h,i} K^{fore}_i \right] \sum_i K^B_{i,h} P(B_i) \tag{3.45}$$

where $K^B_{i,h}$ allows for a finite field range of $P(B_i)$ and performs zero padding in the frequency domain, K^{fore}_i is used to model the effect of convolutions in the time domain which are then Fourier transformed to the frequency domain. IFT is the discrete inverse Fourier transform, K^{aft}_h performs the convolution operation due to dipolar fields, $K^t_{h,m}$ is a matrix which contains the zero padded data and $K^{\mu}_{i,m}$ maps the trial data in $K^t_{h,m}$ onto histogram m.

[5]A typical example of errors introduced which are not accounted for in the standard statistical error is "jitter" in the timing circuitry.

The kernel $K^{\mu}_{h,m}$ maps the orthogonal complex trial distribution $Y_{m,h}$ onto the purely real histogram m with a phase ϕ_m

$$D_m(t_h) = K^{\mu}_{h,m} Y_{m,h} = N_0 \delta t A_m e^{-t_h/\tau_\mu} \Re[e^{-i\phi_m} Y_{m,h}]. \tag{3.46}$$

The experimental data is available only during the time window t_1 and t_2, where $0 < t_1 < t_2$. Zero padding to a value of $N = 2^z$ is required by the IFT kernel to lessen the number of calculations from N^2 to $N \log_2 N$ [Press *et al.*, 1986]. The IFT kernel requires a square matrix with 2^z rows/columns. The IFT is discussed in more detail below. The two kernels $K^{t}_{h,m}$ and $K^{B}_{i,h}$ deal with the need for zero padding. $K^{t}_{h,m}$ is a rectangular matrix with $1 + (t_2 - t_1)/\Delta t$ columns and $2^z > t_2/\Delta t$ rows. It is comprised of zeros apart from the diagonal starting at row t_1 and finishing at row t_2. The amount of zero padding gives the field resolution $\Delta B = 2\pi/(\gamma_\mu 2^z \Delta t)$. The field range $B_1 \rightarrow B_2$ does not have to range from zero to $2^z \Delta B$ and is given by $K^{B}_{i,h}$. This is a rectangular matrix with 2^z columns and $1 + (B_2 - B_1)/\Delta B$ rows and the maximum possible field is given by $B_2 = 2\pi/(\gamma_\mu 2^z \Delta t)$. Again, it is comprised of zeros, apart from the diagonal starting at column $B_1/\Delta B$ and finishing $B_2/\Delta B$. This imposes the assumption that $P(B)$ is zero outside the field range.

The K^{aft}_{h} calculates the resolution function of the MEM lineshape by inverse Fourier transforming a dipolar lineshape $P_{dip}(B_i)$. The final MEM lineshape is deconvolved from the resolution function.

The K^{aft}_{h} kernel is used to model convolutions in the time domain, such as a distribution of arrival times found in pulsed sources. It also performs the convolution needed to have arbitrary time binning (greater than the intrinsic histogram binning). The fore kernel is a complex quantity comprised of

$$K^{fore}_{i} = K^{bin}_{i} K^{P}_{i} K^{\pi}_{i}, \tag{3.47}$$

where K^{bin}_{i}, K^{P}_{i} and K^{π}_{i} are defined below.

Binning in the time domain is achieved by convolving the data with a square function

$$N^{bin}_{m}(t_h) = \sum_{n=hn_{bin}-(n_{bin}/2)}^{hn_{bin}+(n_{bin}/2)} N_m(n_{bin}\delta t), \tag{3.48}$$

where n_{bin} is the bin factor and the new time binning resolution $\Delta t = n_{bin}\delta t$. This binning further limits the maximum B_2 for $P(B)$ as discussed earlier. The actual convolution function has an asymmetric shape to account for the muon lifetime and the Fourier transform of this forms part of the fore kernel

$$\Re K_i^{bin} = \eta \left[\cos\left(\frac{B_i\gamma_\mu\Delta t}{2}\right) \sinh\left(\frac{\Delta t}{2\tau_\mu}\right) + B_i\gamma_\mu\tau_\mu \sin\left(\frac{B_n\gamma_\mu\Delta t}{2}\right) \cosh\left(\frac{\Delta t}{2\tau_\mu}\right)\right]$$
$$\Im K_i^{bin} = \eta \left[B_i\gamma_\mu\tau_\mu \cos\left(\frac{B_i\gamma_\mu\Delta t}{2}\right) \sinh\left(\frac{\Delta t}{2\tau_\mu}\right) - \sin\left(\frac{B_i\gamma_\mu\Delta t}{2}\right) \cosh\left(\frac{\Delta t}{2\tau_\mu}\right)\right] \quad (3.49)$$

where $\eta = 2\tau_\mu/(\Delta t(1 + B_i\gamma_\mu\tau_\mu))$. The imaginary portion causes the asymmetry function to change phase, but is negligible when $\Delta t/2\tau_\mu \ll 1$.

The distribution of muon lifetimes observed in the pulse at ISIS is due to the pion lifetime and proton pulse shape. The proton pulse is Fourier transformed to give the purely real

$$K_i^P = 3\left(\frac{\sin(w\omega_i)}{(w\omega_i)^3} - \frac{\cos(w\omega_i)}{(w\omega_i)^2}\right), \quad (3.50)$$

where $\omega_i = \gamma_\mu B_i$. The muon time spectra is also convoluted by $\exp(-t/\tau_\pi)$ due to the pion lifetime τ_π and when Fourier transformed results in

$$\Re K_i^\pi = \frac{1}{1 + (\omega_i\tau_\pi)^2)}$$
$$\Im K_i^\pi = \frac{-\omega_i\tau_\pi}{1 + (\omega_i\tau_\pi)^2)}. \quad (3.51)$$

An additional sub-kernel has been added to the fore kernel in order to deal with LEM. With LEM experiments the muons have a distribution of arrival times due to the straggle in energy, which has to be removed in order to use ME successfully.

3.3.5 MEM: Lagrange Multiplier

The ME search algorithm searches for the location in the "parameter space" $P(B_i)$, on a circle with $\chi^2 \equiv l^2MN$, where normalised gradients of χ^2 and S are anti-parallel. The ME calculation is seen to be complete when

$$C_{test} = 1 - \frac{\nabla S \cdot \nabla\chi^2}{|\nabla S||\nabla\chi^2|} \leq C_{ME} \quad (3.52)$$

where C_{ME} is a set convergence criteria, typically C_{ME}=0.001. The Lagrange multiplier, λ, seen in Equation 3.44 is not needed in the search, but is calculated from the final solution. From the final solution, the first derivatives S_c are zero and can be used to determine the "local" Lagrange multiplier λ_i at each point

$$0 \equiv \frac{\partial S_c}{\partial P(B_i)} = \lambda_i \nabla_i S - \frac{1}{2}\frac{1}{l^2}\nabla_i \chi^2. \tag{3.53}$$

The gradient of the entropy is easily calculated by

$$\nabla_i S = -\frac{1}{P_d} \ln \frac{P(B_i)}{P_d}. \tag{3.54}$$

The gradient of χ^2, however, is more complicated since χ^2 is calculated in the time domain but $P_m(B_i)$ is in the frequency domain. Thus

$$\nabla \chi^2 = \boldsymbol{O}^\dagger \left(\frac{2(D_m(t_h) - d_m(t_h))}{\sigma^2(t_h)} \right). \tag{3.55}$$

3.3.6 MEM Errors: The Hessian and Covariance Matrix

The second derivative of S_c is used to calculate how much each parameter $P(B_i)$ needs to be changed to increase S_c by 1, which estimates the standard deviation of errors. The second derivatives of S_c define the Hessian[6] matrix thus:

$$\boldsymbol{H} = [-\nabla_i \nabla_j S_c] = \left[\lambda_i \nabla_i \nabla_j S + \frac{1}{2}\frac{1}{l^2}\nabla_i \nabla_i \chi^2 \right] \tag{3.56}$$

where the second derivative of the entropy is

$$\nabla_i \nabla_j S = -\frac{1}{e P_d P(B_i)} \delta_{ij} \tag{3.57}$$

and χ^2

$$\nabla_i \nabla_j \chi^2 \approx 2\boldsymbol{O}^\dagger \left(\frac{1}{\sigma^2(t_h)} \boldsymbol{O}\boldsymbol{I} \right) \tag{3.58}$$

where the cross terms have been removed [Press *et al.*, 1986] and $\boldsymbol{I}$ is the identity matrix. The Covariance matrix is then calculated by inverting the Hessian $\boldsymbol{C} = \boldsymbol{H}^{-1}$.

In order to ease the understanding of how $\nabla\nabla S$ and $\nabla\nabla\chi^2$ effect the covariance matrix, it is beneficial to consider them separately. $\nabla\nabla S$ is simply inversely proportional to $P(B_i)$. However, $\nabla\nabla\chi^2$ is of Lorentzian nature

$$\nabla_1 \nabla_j \chi^2 \alpha \frac{1}{1 + ((B_j - B_1)\gamma_\mu \tau_\mu)^2} \tag{3.59}$$

which implies that the width and shape is independent of the time resolution of

[6]Note the indices i and j here simply an index to the 2D Hessian matrix.

the data, the statistics, the time range zero padding and the nature of the relaxing signal. This is representative, as $\boldsymbol{O}^{\dagger}$ acts as a Fourier transform of $1/\sigma(t_h)^2 \propto \exp(-t_h/\tau_\mu)$, producing a Lorentzian. This indicates any correlations seen in $P(B_i)$ are predominantly due to the muon lifetime.

The covariance matrix $\boldsymbol{C}$ is sharply peaked around the diagonal, with a damped oscillatory behaviour around both sides of the diagonal. The probability densities $P(B_i)$ and $P(B_j)$ are *nearly* uncorrelated when B_i and B_j are far apart. However, the large (but negative) value of the covariance matrix for $P(B_{i+1})$ adjacent to the diagonal $P(B_i)$ shows that the two are anti-correlated. That is, if $P(B_i)$ is increased and $P(B_{i+1})$ is decreased by the same amount, then there is little change in $D_m(t_j)$. For this reason, $\sqrt{(\boldsymbol{C}_{ii})}$ cannot be used as independent errors for $P(B_i)$, as the nearby off-diagonal negative elements lead to over estimates. However, it is still possible to fit the data weighted by the inverse of the covariance matrix [Eadie and Drijard, 1971].

In order to calculate independent errors it is necessary to use the method developed by Sivia [Sivia, 1996]. Consider a point $P(B_i)$ for which an estimate of the independent error, e_i, is required. If the ME lineshape is convoluted with a weighting function $w_i(B_j)$, which is a vector with its maximum at the field B_i and a summation is performed

$$P_c(B_i) = \frac{\sum_j w_i(B_j)P(B_j)}{\sum_j w_i(B_j)} \tag{3.60}$$

the error can be calculated

$$e^2(B_i) = \frac{\sum_{jk} w_i(B_j)\boldsymbol{C}_{jk}w_i(B_k)}{\sum_{jk} w_i(B_j)w_i(B_k)}. \tag{3.61}$$

The natural choice for the weighting function $w_i(B_j)$ is the Hessian [Eadie and Drijard, 1971], meaning for a given value $P(B_i)$, near the peak value of $P(B)$, the Hessian matrix, $u_i(B_i)$, is dominated by the χ^2 term. For a given value $P(B_i)$ far away from the peak value of $P(B)$, $u_i(B_i)$ is dominated by the entropy term.

The error, $e(B_i)$, from the convoluted lineshape is a good estimate of the "independent" error[7] on $P(B_i)$ [Riseman and Forgan, 2002]. This can then be used to estimate the noise level[8], P_n, such that the fractional error $e(B_i)/P(B_i) < 1$ for all $P(B_i) \geq P_n$.

[7]This is not a true measure of the "independent" errors, as they may appear too large by a factor related to the amount of time range padding [Riseman and Forgan, 2002].

[8]The default level P_d need not equal P_n.

It is now possible to calculate first, second and third moments of $P(B_i)$ representing the mean, width and skewness of $P(B_i)$ respectively and the associated errors on the quantities. Given a function $y = F(P(B_1), P(B_2), ...)$ the error σ_y associated with y is given by[Bevington, 1969]

$$\sigma_y^2 = \sum_{ij} v(i) \boldsymbol{C}_{ij} v(j) \frac{\partial y}{\partial P(B_i)} \frac{\partial y}{\partial P(B_j)} \tag{3.62}$$

where v is defined as 1 where $P(B_i) \geq P_n$ and 0 where $P(B_i) < P_n$. Including v in the calculation of moments and associated errors ensures the values are not distorted by points deemed to be below the noise level. The rth moment, M_r with respect to $\bar{B}$ is

$$M_r = \frac{\sum_i v(i) P(B_i)(B_i - \bar{B})^r}{\sum_k v(k) P(B_k)} \tag{3.63}$$

and the ratio $\alpha = M_3^{1/3}/M_2^{1/2}$ can be used to measure the skewness of $P(B_i)$ independent of the distribution's width.

3.3.7 Analysis in the Time Domain: WiMDA

With a number of experiments it is not possible or sensible to work in the frequency domain. Typical examples of this is LF μSR or TF μSR where there is a large background, obscuring the signal of interest and confusing the search algorithm. However, data presented in this thesis is predominantly analysed in the frequency domain, as in order to fit in the time domain a model must be imposed on the data. For example, it is common to assume the time domain relaxation is of Gaussian or Lorentzian form. This has no solid theoretical grounding, as the distribution of local fields in a VL is not Gaussian. For this reason, time domain fitting is has not been used greatly in the work presented in this thesis, but should be mentioned as a possible alternative analysis technique.

Windows Muon Data Analysis (WiMDA) is able to fit individual or multiple raw data histograms and the asymmetry of two paired detectors (as in Equation 3.39). It is possible to remove the muon decay from the raw data histograms. In the TF configuration, WiMDA estimates the relative detector efficiencies by adding the front/back detector groups together. The added asymmetries should be zero when the detector efficiencies are correct. WiMDA has automatic deadtime correction which is calculated from a calibration run at the beginning of each cycle, using silver. The relevant data is read from the headers of the data files and applied to the

analysis automatically. Alternatively, deadtime can be estimated from measuring silver at the beginning of an experiment. It is possible to bin the data in the time domain in a similar manner to that used in MEM.

3.4 μSR and the Vortex Lattice

3.4.1 μSR Lineshapes

Studies of vortex lattices are almost exclusively performed in TF, which means Fourier analysis is best suited since there is no analytical function in the time domain to fit to. The form of the magnetic field, B(r), will determine the relaxation of the signal, as illustrated in Figure 3.13. Fourier analysis gives the probability, P(B), of a particular magnetic field inside the sample, as the atomic spacing is much smaller than the lengthscales of the vortex lattice, so the muons sample the internal flux density randomly. The probability distribution is also shown in Figure 3.13 and some distinctive features are present in the lineshape. The minimum field, B_{min} is from fields such as those labelled by a in the inset, the maximum field B_{core} is the core of the vortex and B_{pk} the most probable field which lies on the line between point a and b.

P(B) can be easily calculated from a numerical calculation. In the high-κ regime, where $\lambda \gg \xi$, the London equations govern the response of the superconductor to magnetic fields. The method is to calculate the FLL in real-space, approximating the field h at a distance r from the vortex site is given by

$$h(r) = \frac{\Phi_0}{2\pi\lambda^2} K_0 \frac{r}{\lambda} \tag{3.64}$$

where K_0 is a zeroth-order Bessel function of the second kind. The London equations are only valid in the vanishing vortex core limit, which is nonetheless valid for high-κ regimes such as the HT_c's.

For an ideal FLL in intermediate fields ($B_{c1} \ll B \ll B_{c2}$), the magnetic field will be periodic and can therefore be represented by a Fourier series

$$B(r) = \langle B \rangle \sum_{\boldsymbol{G}} b_G \exp^{(i\boldsymbol{G}\cdot\boldsymbol{r})} \tag{3.65}$$

where **G** is a vector of the reciprocal lattice and the mean field is $\langle B \rangle$. In the London limit, the Fourier components b_G are given by

$$b_G = \frac{1}{1 + \lambda^2 |\boldsymbol{G}|^2} \tag{3.66}$$

where the reciprocal lattice vectors are defined in Figure 3.14. In the simplest case, the temperature dependence of λ follows the two fluid model, $\lambda(T)\alpha\lambda(0)/(1-t^n)^{1/2}$

where $t = T/T_c$ and $n = 4$.

The results from a μSR experiment is the probability distribution of flux density which can be calculated from B(r). It is convenient to write the calculation as [Aegerter and Lee, 1997]

$$P(B') = \frac{1}{L}\int \left(\left|\frac{\partial B(x,y)}{\partial y}\right|\right)^{-1} dx \tag{3.67}$$

where the integration is carried out over lines, L, of constant field $B(x,y) = B'$. P(B) is thus a direct measure of the superconducting penetration depth.

3.4.2 μSR Lineshapes and Properties of the FLL

The second and third moments of field distribution can be calculated from Equation 3.63. Care has to be taken with performing this analysis, as it is highly dependent on the counting statistics. The noise in the frequency domain reduces the more statistics you have, so the long tail becomes increasingly relevant. The moments can yield intimate information regarding the FLL structure and provide a direct measurement of the penetration depth (the same calculation as in Equation 3.65). The second moment is related to the penetration depth thus

$$\langle \Delta B^2 \rangle = \sum_{\boldsymbol{G},|\boldsymbol{G}|\neq 0} \frac{B^2}{(1+\lambda^2|\boldsymbol{G}|^2)^2} \tag{3.68}$$

and in the limit $\lambda|\boldsymbol{G}| \gg 1$, an evaluation of the sum for a hexagonal lattice yields [Brandt, 1988]

$$\langle \Delta B^2 \rangle = 0.00371\frac{\Phi_0^2}{\lambda^4}. \tag{3.69}$$

The structure of the vortex lattice can be determined from the following [Sidorenko *et al.*, 1990b]

$$\Gamma = \frac{B_{core} - B_{pk}}{B_{pk} - B_{min}} \tag{3.70}$$

which for a hexagonal lattice Γ=8 and for a square lattice Γ=2.5. Care must be taken again, as counting statistics will effect the estimation of B_{core}. The penetration depth can also be extracted from [Sidorenko *et al.*, 1990b,a]

$$\langle B \rangle - B_{pk} = \ln\frac{4}{3}\frac{\Phi_0}{4\pi\lambda_{ab}^2} \tag{3.71}$$

where the mode of the distribution B_{pk} is statistics independent and $\langle B \rangle$ can be

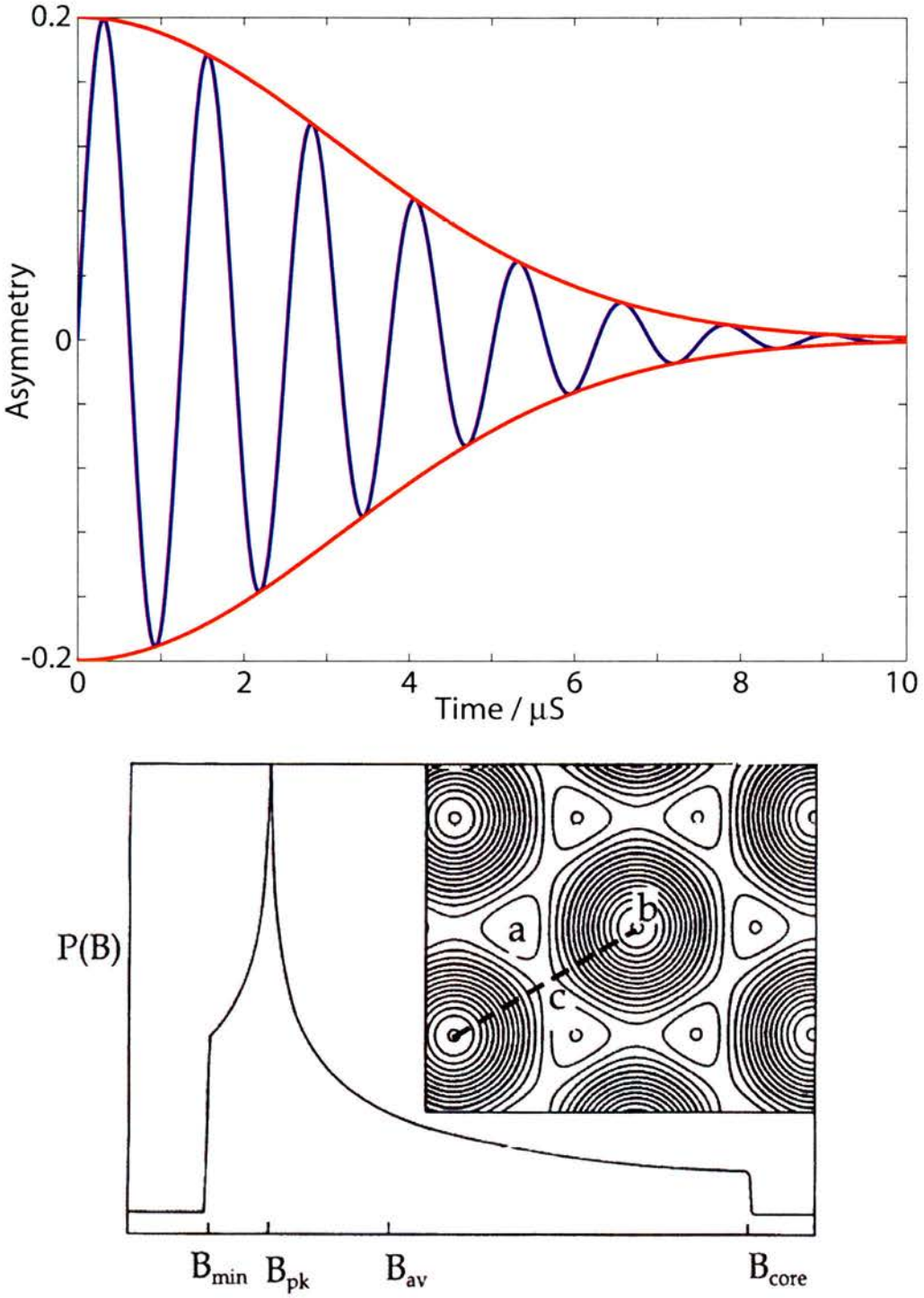

Figure 3.13: Top: Schematic diagram of the damped asymmetry arising from the vortex lattice, after removing the muon lifetime. The form of this is intimately related to the form of the flux density inside the sample. Bottom: Probability distribution of the internal flux density for a superconductor in the mixed state, calculated by performing a Fourier transform of the asymmetry above. The flux density is shown in the inset [Lee *et al.*, 1998a].

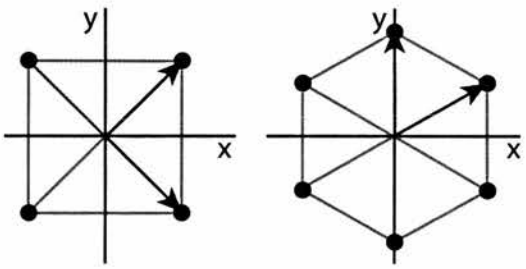

Figure 3.14: Schematic diagram of the reciprocal lattice for two vortex geometries: hexagonal and square.

measure from magnetisation measurements.

Thermal fluctuations of vortices will have a significant effect on the shape of a lineshape. The thermal melting of a FLL is observed by a sharp reduction in skewness of the distribution, due to the truncation of the high field tail because of the smearing of the core fields [Lee *et al.*, 1993, 1997], as the fluctuations the muons see are time-averaged due to their short timescale. The change in the lineshape asymmetry can be observed in a change in sign of the parameter [Aegerter and Lee, 1997]

$$\alpha = \frac{\langle \Delta B^3 \rangle^{1/3}}{\langle \Delta B^2 \rangle^{1/2}}. \tag{3.72}$$

A reduction in lineshape width would also be expected from thermal fluctuations. The fluctuations of vortex positions can be taken into account by introducing a Debye-Waller factor [Harshman *et al.*, 1991] into Equation 3.68, yielding

$$\langle \Delta B^2 \rangle = \sum_{\boldsymbol{G},|\boldsymbol{G}|\neq 0} \frac{B^2 \exp^{-\boldsymbol{G}^2\langle u^2\rangle}}{(1+\lambda^2|\boldsymbol{G}|^2)^2}. \tag{3.73}$$

where $\langle u^2 \rangle$ is the mean square displacement of the vortices from their equilibrium positions [Song *et al.*, 1993; Song, 1995; Brandt, 1991a]. This is valid for dynamic and 2D static disorder if the timescale for the fluctuations is much greater than the timescale of the measurement. Brandt showed that for extreme anisotropic pancake vortex systems, transverse static disorder with short wavelength would lead to a narrowing of the field distribution [Brandt, 1991a]. This has been observed in the quasi-2-dimensional system BSCCO-2212 [Lee *et al.*, 1993].

For dynamic disorder, the form of $\langle u^2 \rangle$ depends on the relations between the applied field and the field at which the vortices become 2 dimensional, $B_{2D} \sim \Phi_0/s^2\gamma^2$, where s is the interlayer spacing [Glazman and Koshelev, 1991]. For $B \ll B_{2D}$

$$\langle u_{3D}^2(B,T)\rangle \approx \frac{3\pi^{1/2}\mu_0 k_B \gamma \lambda_{ab}^2(T)T}{\ln^{1/2}(k_{max}\alpha)\Phi_0^{3/2}B^{1/2}} \tag{3.74}$$

where α is the vortex lattice parameter and k_{max} is defined in Glazman [Glazman and Koshelev, 1991]. At fields above B_{2D} the interactions between pancakes within the layers become greater than the interactions between layers. This quasi-2D fluctuation can be described as [Lee *et al.*, 1995]

$$\langle u_{2D}^2(B,T)\rangle = \frac{4\mu_0 k_B \lambda_{ab}^2(T)T}{s\Phi_0 B}\ln\left[\gamma s\left(\frac{\sqrt{3}B}{2\Phi_0}\right)^{1/2}\right]. \tag{3.75}$$

As the magnetic field is increased, the effect of the vortices becoming closer is that any thermal fluctuations present will have a greater effect on the lineshape, as the probability of a muon stopping near a core is increased as the density of the cores increases. Also, at lower applied fields the ratio $\langle u^2\rangle / d^2$ in Equation 3.73 is much more significant. Thus, both the width and the skewness of the lineshape are expected to have a field dependence.

The effect of the coherence length on the lineshape can be dealt with in a similar way to the effects of disorder. The effects of the core can be approximated by inserting $\exp(-\sqrt{2}\xi G)$ [Yaouanc *et al.*, 1997] into the sum in Equation 3.68, or alternatively $\exp(-2\xi^2 G^2)$ [Brandt, 1992].

The effects of 3D static pinning will increase the width of the P(B)'s and are best modelled in real space and not Fourier space, as the vortices cease to be periodic over long lengthscales. It is possible, however, to model disorder analytically in Fourier space given a suitable approximation for the disorder.

Chapter 4

μSR Measurements of the Vortex Lattice of LaNiSn

4.1 Overview

LaNiSn has generated interest in recent times due to its structural analogue, CeNiSn. Both CeNiSn and LaNiSn have an orthorhombic crystal structure [Daams and Buschow, 1984], but LaNiSn is the non-magnetic analogue of the $4f$ Kondo insulator CeNiSn. CeNiSn forms a small pseudo-gap at the Fermi Energy measured by both NMR [Kyogaku *et al.*, 1990] and magneto resistance [Takabatake *et al.*, 1987, 1998], which is due to the anisotropic hybridisation between the $4f$ electrons and conduction electrons [Ikeda and Miyake, 1996] in the orthorhombic structure. Thus, a study of LaNiSn can lead to a greater understanding of CeNiSn. LaNiSn is known to be a good metal [Takabatake *et al.*, 1987; Nishigori *et al.*, 1996] with a electronic specific heat coefficient γ=11.4 mJ mol^{-1} K^{-2}. With the onset of high quality single crystals, LaNiSn was found to show evidence of superconductivity at 0.6K [Echizen *et al.*, 1999].

This chapter describes TF μSR measurements of the superconducting state in LaNiSn performed on the LTF instrument at PSI and on the μSR instrument at ISIS. The results presented are from μSR experiments on a large single crystal, as a function of temperature and applied field. The field dependence of the FC μSR linewidths allow an estimate of the penetration depth and coherence length of this system. The existence of an intermediate state below H_{c1} in FC experiments has also been directly observed. On cooling in zero field, complete flux expulsion occurs only very close to the H_{c1} phase boundary.

4.2 Experimental Setup

Until recently [Echizen *et al.*, 1999] previous experiments on LaNiSn were performed using polycrystalline samples [Takabatake *et al.*, 1987, 1998; Nishigori *et al.*, 1996]. The sample used here was a high quality single crystal grown by Takabatake's group at the Department of Quantum Matter, ADSM, Hiroshima University and all subsequent sample processing was performed by this group. High purity constituent materials La, Ni and Sn were melted into a polycrystalline ingot in a cold copper crucible under a purified argon atmosphere. The single crystal was then grown using the Chzochralsky pulling method [Echizen *et al.*, 1999] using a radio frequency induction furnace with a hot tungsten crucible. The crystal was cylindrical with a diameter of ~5mm and a length of ~25mm. In order to decrease defects, strains

and impurity ions, the as grown crystal rod was treated using solid-state electro-transport. The rod was heated to 1000°C by a direct current of 250Acm^{-2} for two weeks under a vacuum of greater than 3x10^{-8}Pa. Crystallographic orientation was determined by the back-scattering Laue method.

At PSI the temperature was varied over a range of 50mK - 1.1K, as T_c is ~0.6K, with a typical magnetic field ranging 0 - 600Oe applied perpendicular to the sample's cylindrical axis and transverse to the muon spin direction. Figure 4.1 shows a schematic diagram of the experimental setup and a schematic diagram of the LaNiSn crystal structure [Daams and Buschow, 1984]. The sample was glued using an epoxy to a copper sample holder and surrounded by ~5mm of annealed haematite (Fe_2O_3) paste to ensure a rapid random depolarisation of any muons not hitting the sample, thus reducing the background. The copper sample holder ensured the sample was in good thermal contact with the heaters/cold finger and an accurate sample temperature could be measured. The entire sample holder was covered in a ~1mm thick silver protective case with a thin mylar thin ~0.1mm window to allow muons to enter the sample. The beam was focused to ensure as little beam as possible strayed from the sample.

The detectors were set up in order to attain maximum time range due to the slow relaxation rate found in this sample. The Time Differential Controller (TDC) resolution was set to 2.5ns, with 8000 bins per histogram, which meant the maximum time attainable was 20.480μs. In order to measure successfully at large times (typically >12μs) MORE is required. This has the effect of distorting the data at early times but greatly improves the data taken at large times. This is seen as acceptable considering the small relaxation in this sample.

The superconducting magnet was quenched prior to the experiment and the earth's magnetic field was compensated by three electromagnets around the sample space. Any remnant field remaining in the sample area was checked using a 3D Gaussmeter and found to be negligible (5mG approx.). It is not possible to check remnant field at the exact position of the sample using the Gauss meter, but only around the outside of the instrument. Thus, a further check of remnant field in the sample space was performed using muons and again any remnant magnetic field was found to be negligible. All ZF measurements were performed before any field was applied to the sample from the superconducting magnet, unless otherwise stated. The sample had been stable at 50 $\pm$ 1mK for an hour prior to commencing the experiment to ensure the sample was in equilibrium.

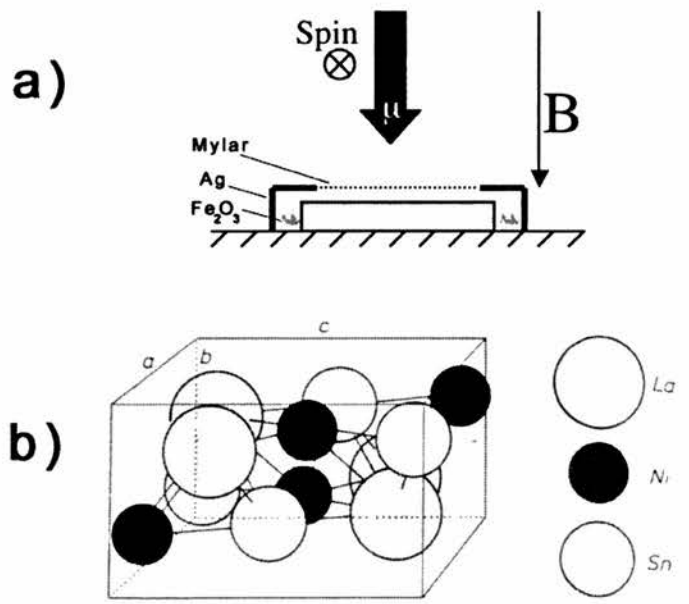

Figure 4.1: a) Schematic diagram of experimental setup at PSI. b) Schematic diagram of LaNiSn orthorhombic crystal structure [Daams and Buschow, 1984]. Crystalographic orientations are labelled a,b and c.

At ISIS the sample was mounted with one of the principal crystallographic parallel to the incoming beam direction. Unfortunately this meant applying the magnetic field at 28° to the cylindrical axis, leading to an unknown demagnetisation factor. The sample was mounted on and surrounded by a number of 3mm thick Heamatite sintered plates, with any gaps filled in by Heamatite paste. The entire sample holder was covered with a 12.5μm thick silver foil.

As the data taken at ISIS was the first experiment to be performed on this sample, applying the field parallel to a crystallographic axis was deemed more important than any effects the geometry has on the demagnetisation factor. This was not found to be the case, as LaNiSn has relatively isotropic superconducting properties [Echizen *et al.*, 1999] and the effects of the demagnetising factor was found to be important, as can be seen from the "messy" lineshapes. This does not effect mapping out the magnetic phase diagram using the ISIS data, but these lineshapes were difficult to interpret until "cleaner" linshapes were taken at PSI.

4.3 Demagnetisation Factor for the Geometry Used at PSI

If a magnetic field is applied to a superconductor which has a non-zero demagnetisation factor, the magnetic field over part of the surface may exceed the critical field even though the applied field is less than the critical field. The value of the demagnetisation factor is dependent on the shape of the sample with respect to the magnetic field, This can be calculated analytically in certain geometries by considering Laplace's equation for a vector potential, $\boldsymbol{A}$, [Kenyon, 1997]

$$\frac{1}{r}\frac{\partial}{\partial r}\left(r\frac{\partial \boldsymbol{A}}{\partial r}\right)+\frac{1}{r^2}\frac{\partial^2 \boldsymbol{A}}{\partial \theta^2}+\frac{\partial^2 \boldsymbol{A}}{\partial z^2}=-\mu_0 \boldsymbol{J} \tag{4.1}$$

where r, θ and z are standard cylindrical coordinates, $\boldsymbol{J}$ is the current density and μ_0 the permeability of free space. Assuming no z dependence (i.e. an infinitely long cylinder) and zero current density in the bulk of the superconductor, the two dimensional Laplace equation becomes

$$\frac{1}{r}\frac{\partial}{\partial r}\left(r\frac{\partial \boldsymbol{A}}{\partial r}\right)+\frac{1}{r^2}\frac{\partial^2 \boldsymbol{A}}{\partial \theta^2}=0 \tag{4.2}$$

and for an applied field B_e, perpendicular to the length of the cylinder, the solution is expected to be a cylindrical harmonic [Bleaney and Bleaney, 1963]. As a trial

solution, the first order cylindrical harmonics[1] are

$$\begin{aligned} A_1 &= b_1 r\cos(\theta) + b_2 r^{-1}\cos(\theta) \\ A_2 &= -B_e r\cos(\theta) + r^{-1}\cos(\theta) \end{aligned} \tag{4.3}$$

where b and a are the coefficients to be solved using Equation 4.2, for inside and outside the superconductor denoted by 1 and 2 respectively. After imposing the boundary condition that the vector potential is continuous across the superconductor/air interface and solving at $r = R$, the cylinder diameter, the following solution is found

$$B_1 = -\frac{2(1-\mu_1)}{1+\mu_1} R B_e \sin(\theta) \tag{4.4}$$

where μ_1 is the effective permeability of the superconductor. Defining the demagnetisation factor, n, as [Waldram, 1996]

$$\mu_0 M = \frac{(\mu_1 - 1)B_e}{1 + n(\mu_1 - 1)} \tag{4.5}$$

leads to a demagnetisation factor n=1/2 for this sample. Figure 4.2 shows the magnetisation of a cylinder in an applied magnetic field parallel and perpendicular to the cylinder axis, where the demagnetisation factor changes from n=0 to n=1/2. It can be seen that the magnetic field at which the superconductor changes from being in a Meissner to an intermediate state is nB_c for a Type I and nB_{c1} for a Type II superconductor [Waldram, 1996].

4.4 Description of Data Analysis

The PSI data has been analysed using MEM with the following adjustable parameters. Since MORE was used on the LTF experiment, the first 0.5μs of data is distorted and therefore discarded. Thus, the time range used is 0.5μs to 19.7μs, the maximum attainable with a histogram time resolution of 2.5ns. T_0's and T_1's were estimated in the time domain from the positron peak and subsequent fall off for each

[1] Higher order coefficients are found to be zero. This is because terms such as $\cos(n\theta)$ and $\sin(m\theta)$ do not satisfy the boundary conditions for *all* θ because the potential varies only as $\cos(\theta)$ [Bleaney and Bleaney, 1963].

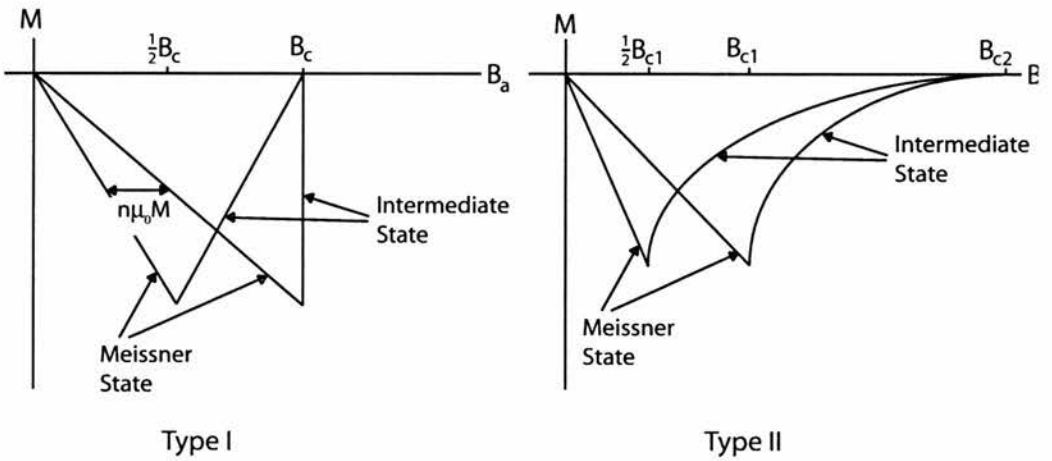

Figure 4.2: Ideal reversible magnetisation curves as a function of applied field B_a, for a long rod with field applied parallel (n=0) and perpendicular to the cylinder axis for a Type I and Type II superconductor. The area of the curves is unaffected by changes in n or κ.

individual histogram. No additional time binning was required, as in all measurements the statistics were high enough at large times to satisfy standard errors. The time range was zero padded typically by a factor of 10^2 in order to visually improve the lineshapes. It was not necessary to use apodisation of errors in this analysis as the errors had already become large enough at large times to mask any time window cut off on the data. A looseness of 1.02 was used throughout the analysis to tackle any discrepancies in the data not accounted for by standard errors, such as "jitter" in the timing electronics.

The ISIS data was analysed under similar conditions, but apodisation of errors is required to reduce the influence of data cut off at the end of the time window as the maximum time range available is only 10μs. Exponential apodisation of errors with a time constant of 7μs was found to sufficiently reduce the "ringing" without overly broadening the lineshape. The data was analysed from T_1 as there is no distortion at the beginning of the time window as with the PSI data. Detector deadtime was estimated for different fields using a standard silver target, which was found to be approximately τ_d=26ns and was removed using Equation 3.36.

4.5 Field Cooled Measurements

Figure 4.4 shows the P(B)'s for a range of temperatures taken at PSI. The sample was FC in 20Oe from above T_c to 50mK and measurements were taken on heating in steps to above T_c. To ensure the sample was in thermal equilibrium, measurements were not started until it was stable for more than 10 minutes at the desired temperature.

An initial qualitative description of the data shown in Figure 4.4 shows an *increase* in internal field as T_c is passed followed by a splitting of the peaks at lower temperatures, one slightly lower than the applied field and the other at more than twice the applied field. It is clear that if the whole sample was superconducting there would not be an increase in mean field inside the sample. This has been interpreted as two magnetic phases in the sample, as considering that the sample is of high quality [Takabatake, 2001], it is unlikely the two phases are explained by structural or chemical inhomogeneities. Since this sample has a non-zero demagnetising factor, the two magnetic phases observed at the low temperatures are an intermediate state, with vortices in the superconducting regions explaining the lower peak.

Figure 4.5 shows the two peak positions of a double Gaussian fitted[2] to the P(B) lineshapes shown in Figure 4.4. The lineshape was fitted with a Levenberg-Marquardt non-linear regression, with errors estimated from the diagonalised covariance matrix of the fitting parameters [Dewhurst, 2001]. It is clear that there is a suppression of magnetic field inside the superconducting region at lower temperatures, although there seems to be a discrepancy with the two lowest temperatures.

The *rise* in peak position between 550 and 500mK seen in Figure 4.5 is taken to be T_c and agrees well with T_c measured using resistivity and susceptibility [Echizen *et al.*, 1999] on different samples. The increase in peak position at T_c is initially a surprising result, as the mean magnetic field inside a superconductor is expected to reduce when going through the transition. However, the associated reduction in asymmetry as seen in Figure 4.6 can offer insight into this problem. A superconductor which is in an intermediate state contains large volumes which are normal and large volumes which are in the pure Meissner state. As the temperature is reduced the Meissner volume fraction increases, with a corresponding reduction in the normal volume fraction. Since the Meissner state is one of total flux expulsion it is expected that the asymmetry reduces as the Meissner volume fraction increases, which is indeed observed. Figure 4.3 shows a schematic diagram of the proposed transition.

[2]See Appendix B for the details of the fitting routine[Dewhurst, 2001].

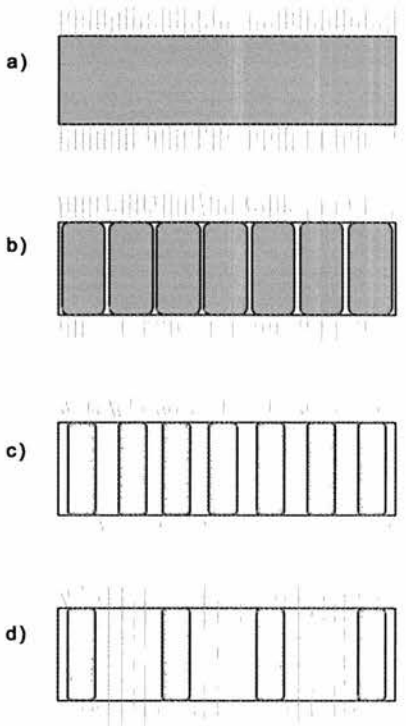

Figure 4.3: A schematic magnetic field distribution. Blue: magnetic flux. White: zero field. a) Normal state. b) Just below T_c. A very small volume of the sample is in the Meissner state, whilst the normal regions experience a slightly larger flux density due to this expulsion. c) At a lower temperature the Meissner regions become larger, reducing the asymmetry of the muon signal, pushing more flux into the normal state regions increasing the flux density further. d) The sample is now dominated by the Meissner state, lowering the total asymmetry significantly further and pushing much more flux into the ever smaller normal state regions. A small volume fraction also contains a vortex lattice.

Applied Field / Oe	15	25	30	37	45	50	55
T_c / mK	480	390	380	325	280	185	170

Table 4.1: Table of T_c's at different applied fields, estimated from Figure 4.11.

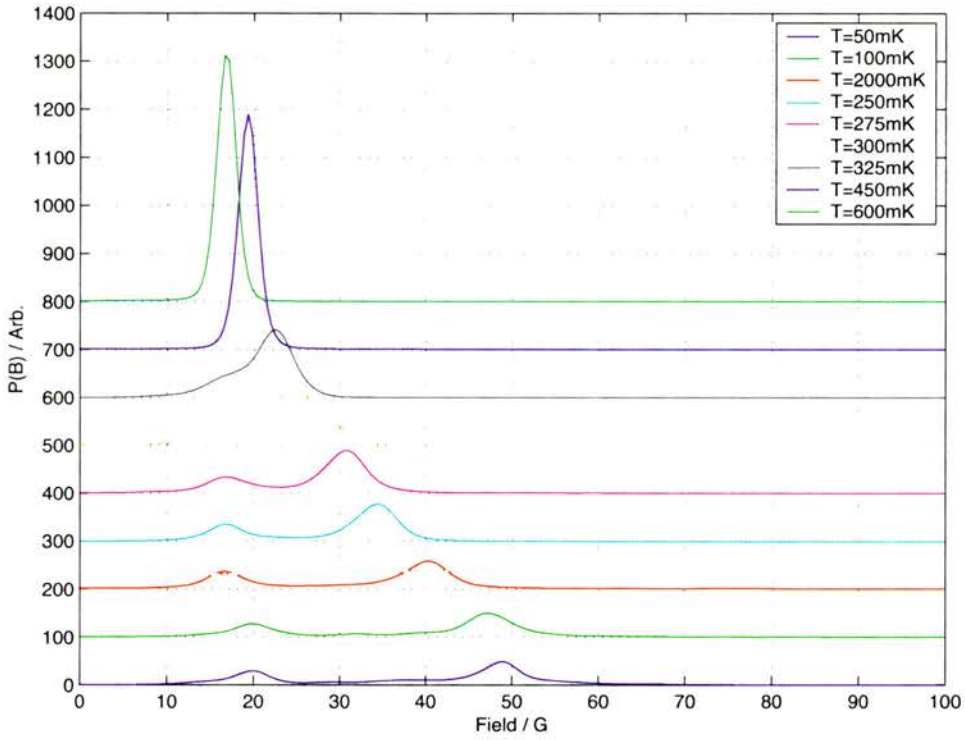

Figure 4.4: P(B) for 20Oe FC for a range of temperatures taken at PSI. Error bars have been removed for clarity; typical errors on the amplitude do not exceed ± 0.5, so the line width is a good representation of the error. Plots are on the same linear scale with arbitrary units and have been offset from the previous temperature by 100. The P(B)'s for T=500mK and T=550mK have not been included, but are consistent with the general trends shown here.

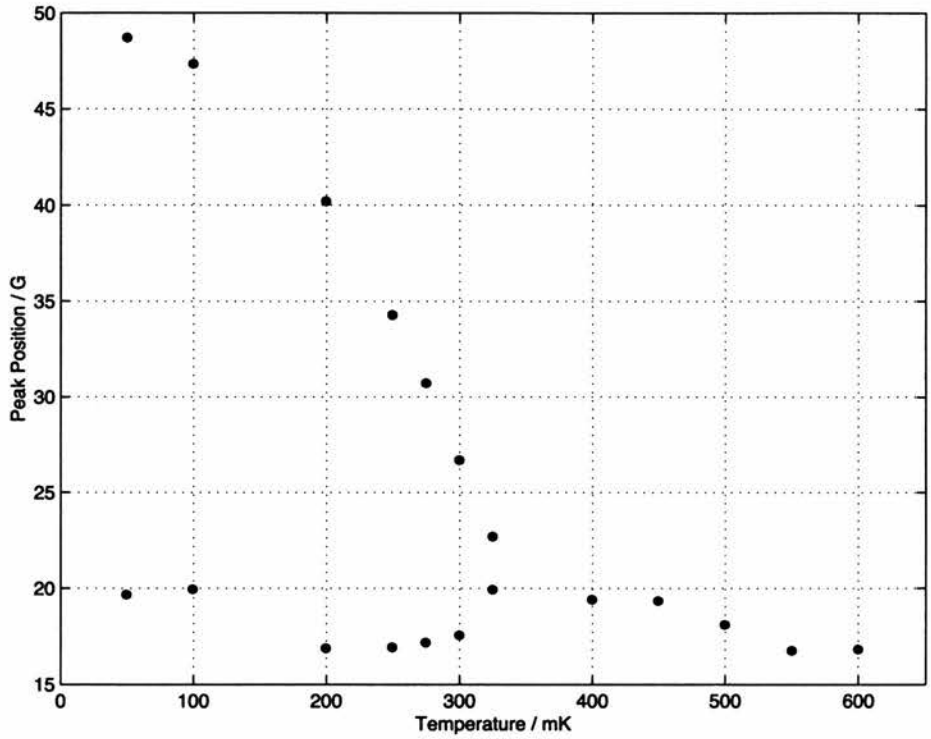

Figure 4.5: Peak position of Gaussian fits to the P(B)'s shown in Figure 4.4. The size of the points are representative of the errors.

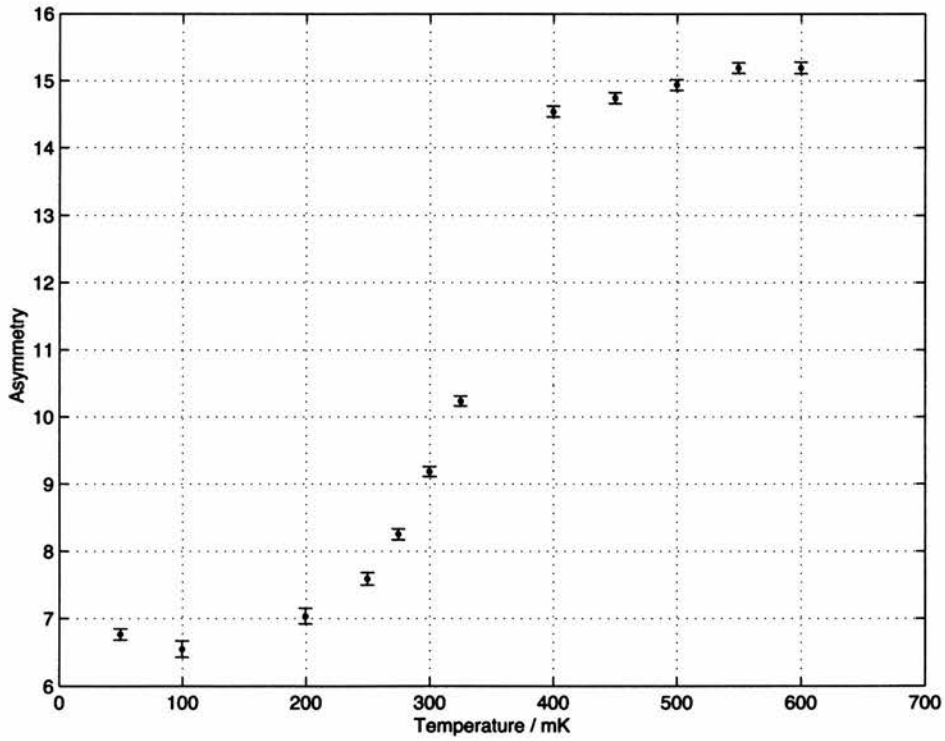

Figure 4.6: Total percentage asymmetry of the P(B)'s shown in Figure 4.4.

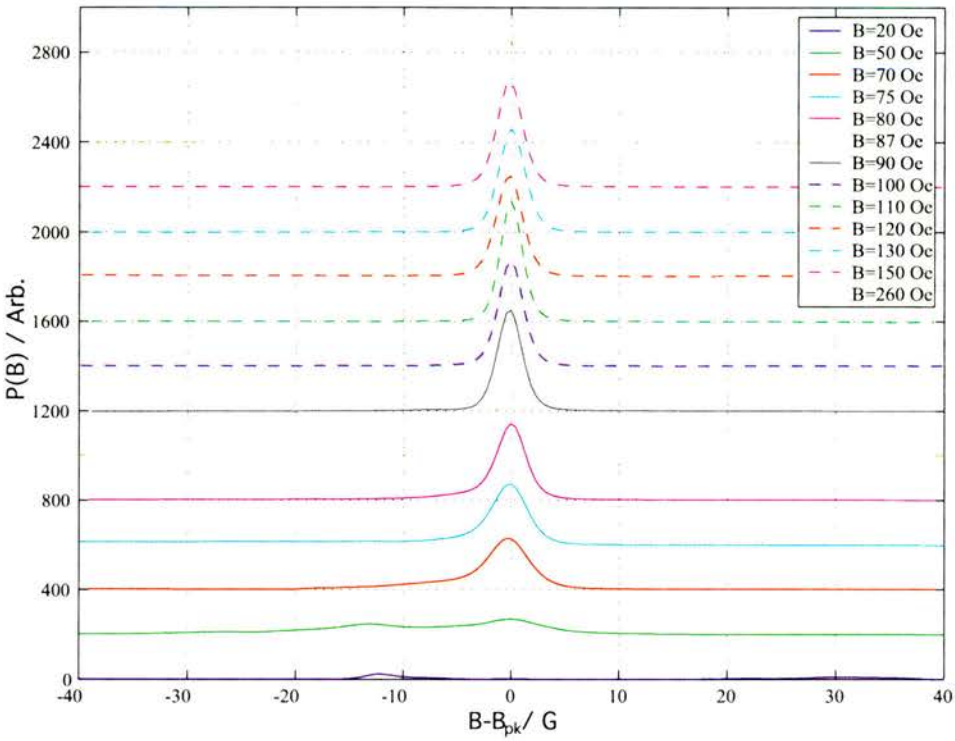

Figure 4.7: Field dependence of FC P(B)'s at 50mK, taken at PSI.

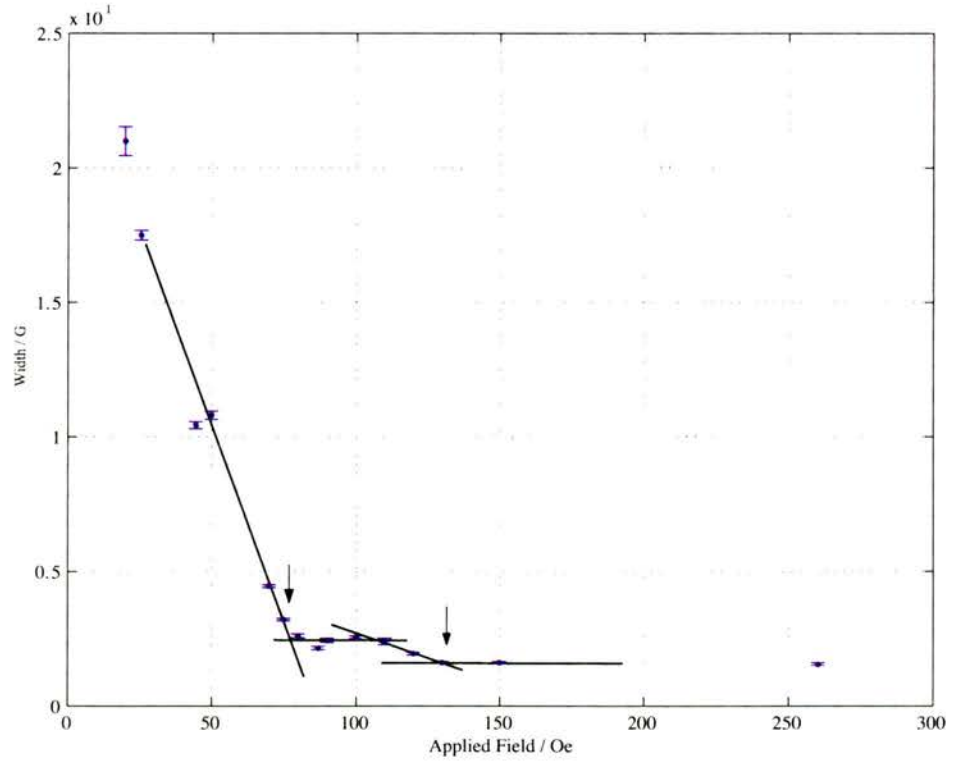

Figure 4.8: Field dependence of the second moment of the P(B)'s shown in Figure 4.7.

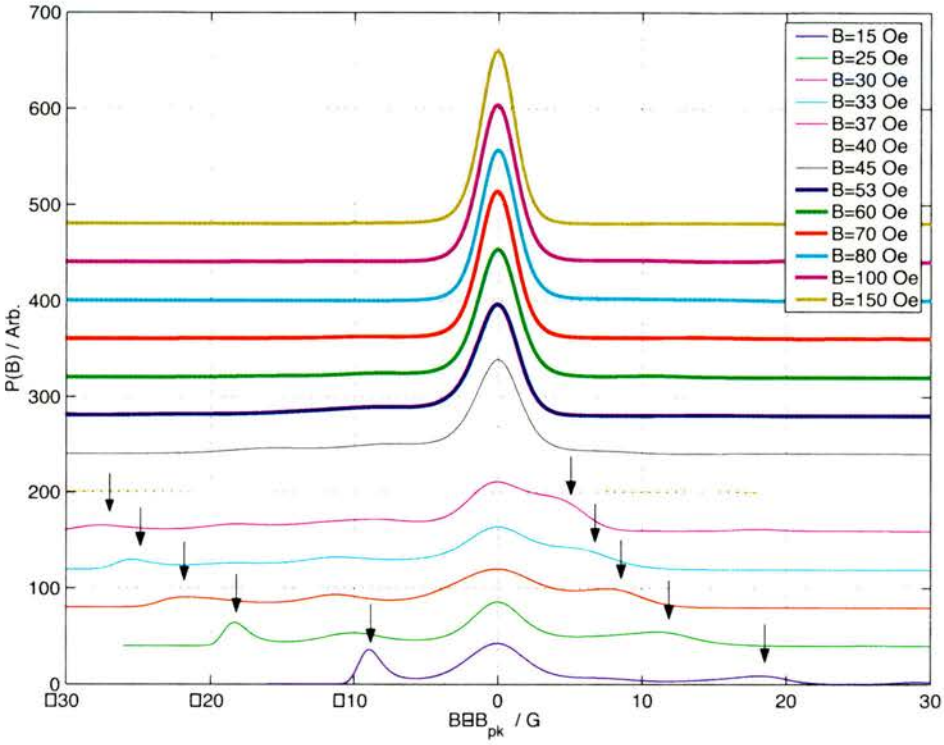

Figure 4.9: Field dependence of lineshapes at 47mK, taken at ISIS.

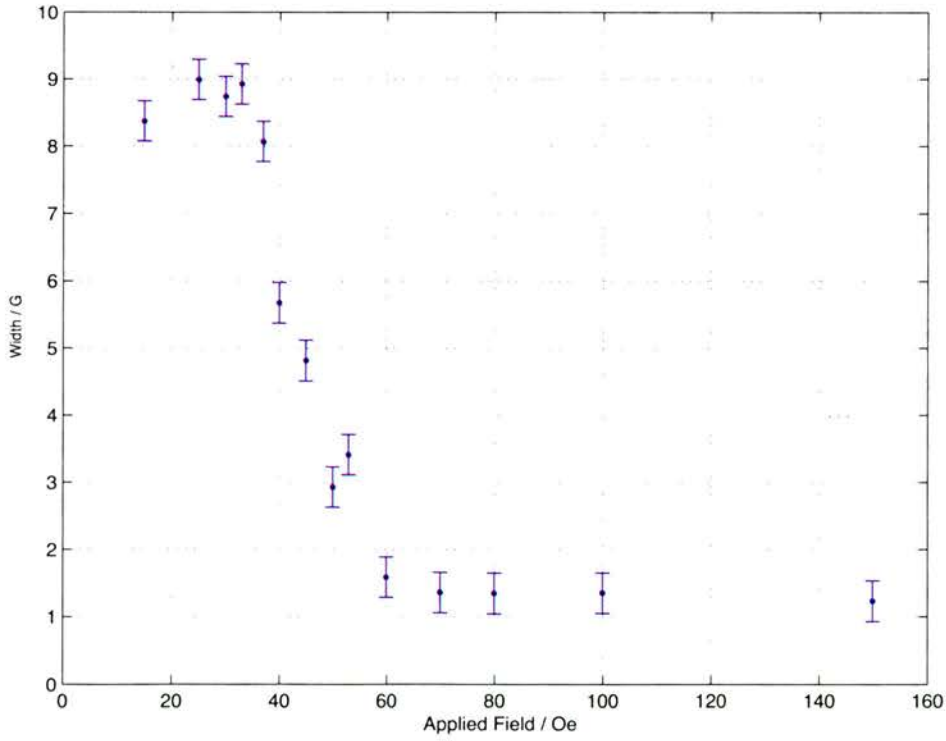

Figure 4.10: Field dependence of the second moment for the lineshapes shown in Figure 4.9. Errors are approximate.

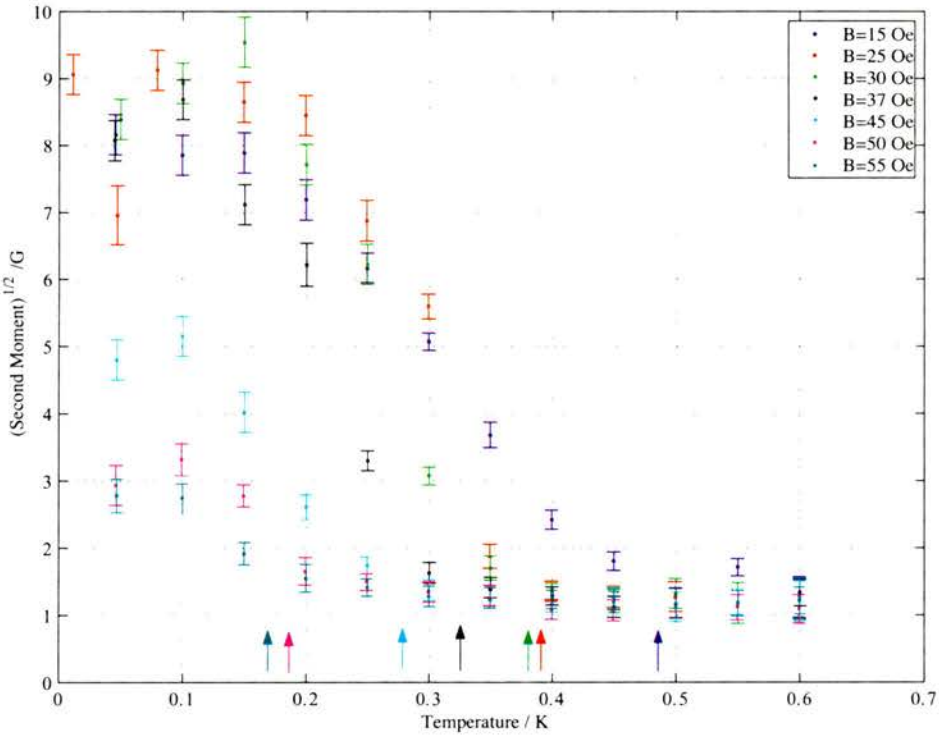

Figure 4.11: Temperature dependence of the second moment at a number of fields, taken at ISIS.

The point where the two peaks appear at ~320mK is taken to be the point at which the sample goes through the phase transition shown in Figure 4.2. The appearance of the second peak at a field below that of the applied field indicates part of the superconducting region is no longer in the Meissner or normal state. The significant increase in the peak corresponding to the normal fraction and the sudden drop in asymmetry indicates a decrease in the volume fraction of the normal state and increase in the volume fraction of the Meissner state. Thus the low temperature lineshapes are consistent with a sample mainly comprised of the Meissner state with some normal regions and a small fraction of the superconducting region in the vortex state. This mixture of Type I and Type II superconductivity can be explained when considering a superconductor on the Type I / Type II boundary, where small local variations in the coherence length and/or penetration depth govern the nature of the superconductor. There are few experimental studies in the literature which probe the superconductivity of LaNiSn, so one can only suggest this as a possible reason. κ is unknown for this compound, as the penetration depth has not been measured. However, the coherence length has been measured to be 1200Å [Echizen *et al.*, 1999]. Another possible explanation is the sample is of finite length and may not be perfectly cylindrical. Thus, different parts of the sample may have a different demagnetisation factor, which could also govern the nature of the superconductor (Type I or II behaviour).

Figure 4.7 shows the lineshapes of 50mK FC measurements taken at PSI. In order to make a direct comparison between different fields, it was necessary to plot $P(B)$ as a function of $(B_i - B_{peak})$, where B_{peak} is the field corresponding to the largest peak and B_i is the magnetic field at a bin i. It is clear that changes in the lineshape as the applied field is varied are more subtle than changes seen in Figure 4.4. Plotting the lineshapes full width as a function of applied field is a more sensitive measure of changes in the lineshape than simply inspecting it or fitting multiple Gaussian, as can be seen in Figure 4.8. There is an initial increase in the width indicated with an arrow, which is taken to be the onset of superconductivity. By fitting a number of straight lines to a limited range of data, the critical field can be estimated to be H_c ~135Oe. After a plateau there is a dramatic increase in width indicated by the second arrow, which is estimated to be ~70Oe and corresponds to the field at which the intermediate state occurs. From these estimates it is possible to determine a demagnetisation factor for this geometry to be ~0.5, which is consistent with the calculations outlined above.

Figure 4.10 shows the lineshapes of field cooled measurements for different fields

at a temperature 47mK taken at ISIS. The data has been plotted in a similar manner to Figure 4.7. It is clear that the lineshapes shown here are not as "clean" as those measured at PSI, but show the same generic trends seen in the PSI data as shown by the two sets of arrows. Fitting two Gaussians to the data would not accurately describe the situation as it did in the PSI data, as each lineshape would need to be fitted to a different number of Gaussians. A better representation of this data is simply to plot the second moment as a function of magnetic field, as shown in Figure 4.9, where it can be seen there is a significant increase in second moment at ~60Oe. This point can be taken to be the second phase transition seen in the PSI data at ~70Oe. Unfortunately due to the "messy" lineshapes and the lack of relevant data it is not possible to estimate H_c as in the PSI data. However, the temperature dependent changes in lineshapes are significantly larger and it is possible to estimate T_c for different applied fields from the ISIS data. Figure 4.11 shows the temperature dependence of the second moment for a number of fields. The critical temperature, T_c, is estimated by the initial increase in width, which is indicated by the arrows for different fields. A summary can be found in Table 4.1.

4.6 Zero Field Cooled Measurements

The sample was zero field cooled to 50mK and kept constant throughout the measurement. A magnetic field of 25Oe was applied and field increased by 5Oe increments and a spectra measured at each field. Figure 4.12 shows the muon decay time spectra for three applied fields. At 25Oe, a weak oscillation in the decay spectra is evident, which can be accounted for by areas of normal material due to an intermediate state in the sample. As the field approached $\sim \frac{1}{2}B_c$, an almost complete Meissner state is observed, which is evident from the 60Oe decay spectra. As the applied field is increased, it is expected the normal regions of the intermediate state become larger, making an oscillation of larger amplitude. This result is repeatable at both ISIS and PSI, although only the PSI data is shown here. If this result is compared to the plots in Figures 4.8 and 4.10, it is clear this "entrant" Meissner state at 60Oe corresponds to the thermodynamic phase boundary. Curiously, only at this transition is a pure Meissner state truly observed. There is currently no explanation for this phenomenon.

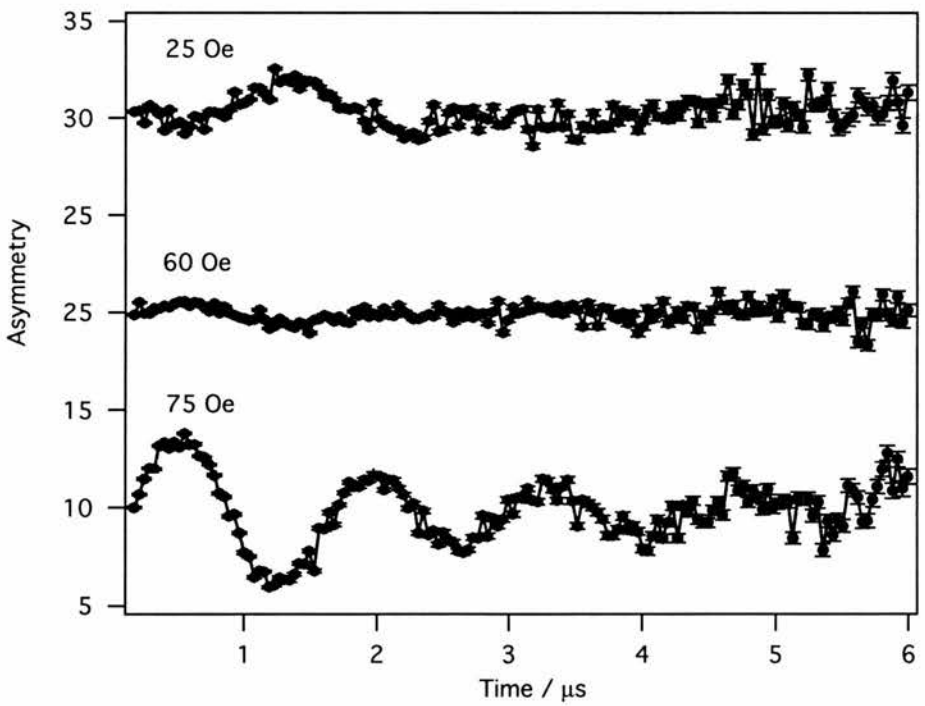

Figure 4.12: The asymmetry of LaNiSn initially cooled in zero field, then the three different fields were applied. An offset on the y-axis has been included to improve presentation.

4.7 Concluding Remarks

The measurements presented in this thesis are the only microscopic study of the superconducting properties LaNiSn. In a FC state, a combination of Type-I and Type-II properties has been observed; both a vortex lattice and intermediate state is found to coexist. From the loss in asymmetry and the complex P(B)'s, the only plausible explanation for this compound in a field cooled state is an intermediate state with vortices in the Meissner state (between the normal regions). This has been explained by a combination of the sample geometry with respect to the applied magnetic field and the possible vicinity of LaNiSn to the Type-I/Type-II boundary. In the ZFC state, a Meissner state is only observed on the thermodynamic phase boundary where vortices begin to appear. These conclusions are only tentative, as a full study of the bulk magnetisation has not been carried out. Consequently, a full understanding and explanation of these results is not possible.

Chapter 5

Measurements on the Flux Line Lattice in $La_{2-x}Sr_xCuO_4$

5.1 Overview

One of the principle findings of the measurements on overdoped LSCO presented in this thesis is the magnetic field induced square to hexagonal transition [Gilardi *et al.*, 2002], which is discussed in this chapter. An intrinsic square lattice indicates the vortex lattice is coupled to some source of anisotropy, such as the effect of the d-wave order parameter [Berlinsky *et al.*, 1995; Xu *et al.*, 1996; Shiraishi *et al.*, 1999; Ichioka *et al.*, 1999] or the presence of stripes [Tranquada *et al.*, 1995]. A fourfold pattern could also result in pinning to twin planes [Johnson *et al.*, 1999], but this has been found not to be the case. An intrinsic square vortex lattice has not been observed in an HTC before the work presented here, although it was claimed [Keimer *et al.*, 1994] to have been observed in twinned $YBa_2Cu_3O_{7-\delta}$ (YBCO). After some debate [Yethiraj *et al.*, 1993; Forgan and Lee, 1995] it was confirmed that the square SANS diffraction pattern observed was due to the effects of twin plane pinning [Johnson *et al.*, 1999], where a number of intrinsic hexagonal FLLs were pinned to particular alignments which lead to overlapping of diffraction spots and therefore confusion over the intrinsic symmetry. More recently than the work presented in this thesis, however, a field induced intrinsic hexagonal to square transition has been observed in YBCO [Brown *et al.*, 2004].

Another measurement performed and presented here is the measurement of the FLL melting at a temperature below T_C, which is highly dependent on the anisotropy of the material in question. The degree of anisotropy in LSCO lies between that of the two archetypical HTC's, YBCO and $Ba_2Sr_2CaCu_2O_{8+x}$ (BSCCO). The extreme anisotropy of BSCCO leads to unusual vortex properties, as highly flexible vortex lines make them extremely susceptible to thermally and pinning induced disorder[Cubitt *et al.*, 1993; Lee *et al.*, 1993, 1995]. A more appropriate description is obtained by considering the vortices as a string of 2D "pancake" vortices, each confined to a CuO layer weakly coupled between layers [Lee *et al.*, 1997]. BSCCO has λ_{ab}=1800Å [Lee *et al.*, 1993], $\gamma \sim$150 [Martinez *et al.*, 1992] and the layer spacing s=15Å [Lee *et al.*, 1997], which means electromagnetic coupling dominates large areas of the magnetic phase diagram. This is considerably weaker than Josephson coupling. Consequently a first order melting transition is observed well below T_c [Lee *et al.*, 1993, 1995, 1997], where the vortices melt into a 2D pancake gas.

In YBCO, however, microscopic measurements remained elusive [Aegerter *et al.*, 1998] until relatively recently, where a second order melting transition was observed. Until this measurement, microscopic measurements of melting transitions in YBCO

were obscured by the effects of twin plane boundaries, which act as strong pinning sites. Until large, high quality untwinned YBCO crystals were available, it was necessary to rotate the applied field at large angles to the c-axis (51°) and twin planes (45°)[Aegerter *et al.*, 1998]. This minimised the effects of twin planes on the vortex behaviour, but influenced the structure of the FLL considerably. YBCO is considerably less anisotropic than BSCCO, with $\gamma \sim 5$ [Palstra *et al.*, 1990; Shibauchi *et al.*, 1994; Willemin *et al.*, 1999]. The penetration depth of YBCO is λ_{ab}=1400Å and a layer spacing of s=8Å leads to the coupling between layers being dominated by Josephson coupling. Consequently the vortices after melting are considerably more coupled than in BSCCO, so remain as vortices and do not melt into a 2D gas.

The measurement of microscopic transitions of the FLL in LSCO is even more elusive, as the penetration depth is λ_{ab}=2400Å for x=0.17 (see Table 5.1), which is considerably longer than BSCCO or YBCO. This reduces the neutron scattering intensity considerably, as in a SANS experiment (Equation 3.31) $I \propto 1/\lambda_{ab}^4$. There is also a problem with twin planes, as the low temperature CuO structure is orthorhombic, which distorts the FLL due to pinning. Another obstacle is that it is relatively difficult to grow high quality, large single crystals, which are required for both muon and neutron experiments.

Despite these problems, for studying the FLL, LSCO has some very attractive properties. LSCO has an anisotropy in the region of $\gamma \sim 20$, which puts it directly between the extreme 2D nature of BSCCO and the 3D nature of YBCO. Additionally, γ can be controlled systematically by varying the Sr doping. The significance of these parameters can be understood by considering the Josephson length $\lambda_J = \gamma s$, where s is the spacing between CuO planes. The ratio of λ_J to λ_{ab} determines the effectiveness of the Josephson currents tunnelling between planes which maintain the stiffness of the vortex. In BSCCO $\lambda_J/\lambda_{ab} > 1$ leading to extremely flexible 2D vortices and in YBCO $\lambda_J/\lambda_{ab} \ll 1$, so rigid vortex lines are formed. LSCO has a $\lambda_J \approx 250$Å, meaning the vortices are relatively straight but susceptible to transverse fluctuations.

As the Sr doping of LSCO is decreased, SANS experiments become increasingly difficult as λ_{ab} increases to approximately 3000Å at x=0.10. For this reason most of the work at x=0.10 is μSR as the signal is not as limited by λ_{ab}[1]. A further complication is that at this doping the vortex lattice is extremely susceptible to disorder; the SANS intensity would fall off rapidly as the disorder is increased. Muon probe measures the local field, which is determined by contributions from

[1]In reality, a SANS experiment becomes difficult due to the reduced intensity at $\lambda \sim$3000Å, where as a μSR experiment becomes difficult due to field resolution at $\lambda \sim$6000Å.

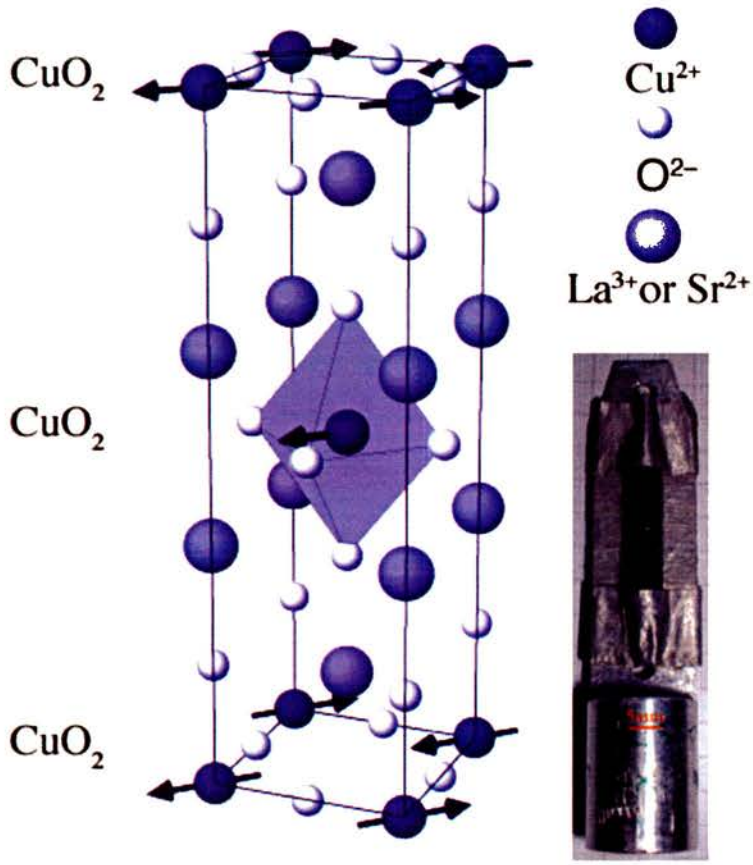

Figure 5.1: Crystal structure of $La_{1.83}Sr_{0.17}CuO_4$. Inset: a sample mounted for a SANS experiment.

vortices only within λ_{ab} of the muon; hence, the general form of P(B) is remarkably robust to changes in long range order [Brandt, 1988]. In contrast, the technique can be highly sensitive to changes in the local environment due to thermally induced or pinning-induced distortions [Aegerter and Lee, 1997], which allows the observation of the transition from the ordered state to the VG phase. Consequently μSR is the main probe for the underdoped regime.

The structure of LSCO is a stack of CuO_2 planes separated by La(Sr)O blocks, as can be seen in Figure 5.1. The room temperature lattice constants for La_2CuO_4 are a≈5.36Å, b≈5.40Åand c≈13.16Å [Radaelli *et al.*, 1994]. At low temperatures, the crystal structure of LSCO is orthorhombic whilst at higher temperatures the structure is tetragonal and the doping dependence of the transition temperature is shown in Figure 5.1. In the low temperature orthorhombic (LTO) phase, planar defects which mark the separation between domains of interchanging a and b are present. As evidence of this, scattering from twin planes are clearly present in unsubtracted SANS diffraction patterns (see Figure 5.8). The second order phase

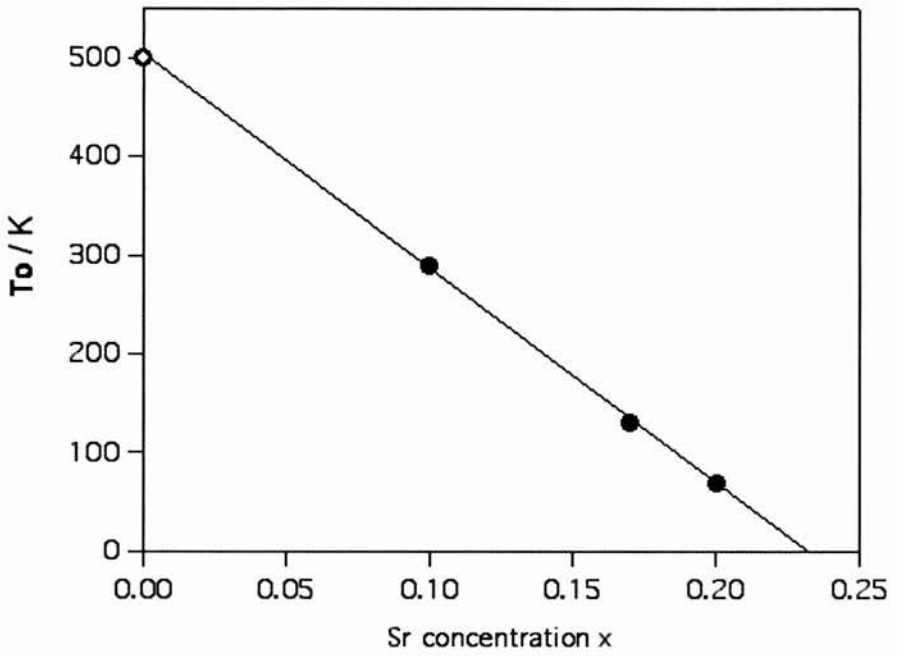

Figure 5.2: Transition temperatures of the tetragonal - orthorhombic transition in LSCO as a function of Sr doping, x. Closed circle: transition temperature was measured by our principle collaborators [Gilardi, 2003] using the same samples as presented here. Open circles: Measurements performed elsewhere [Böni *et al.*, 1988] on different crystals than those used here.

transition to the LTO structure is cause by a tilting of the CuO_6 octahedra and is related to the softening of phonon modes [Birgeneau *et al.*, 1987]. The structural phase transition is easily measured using elastic neutron scattering [Radaelli *et al.*, 1994; Birgeneau *et al.*, 1987], as the crystallographic reflections for the two phases will be different. Twin planes can have a significant impact on the vortex behaviour of LSCO, as the twin planes are a ready source of pinning.

The phase diagram for LSCO is shown in Figure 5.3. It is characterised at low Sr doping by an antiferromagnetic insulating phase, followed by a superconducting phase at higher doping. The electron configuration of copper and oxygen is $3d^9$ and $2p^6$ respectively. Therefore, the copper has a spin 1/2 in the d-shell. By substituting Sr^{2+} for La^{3+}, charge carriers are introduced and to maintain the charge balance electrons are removed from the CuO_2 planes. At a large enough concentration of holes the superconducting phase appears ($0.05 \leq x \leq 0.27$). Above T_c, a "pseudogap" has been observed in the underdoped regime [See, for example, Julien, 2003]. However, most of the results have been obtained by indirect methods such as resistivity, susceptibility, specific heat and neutron crystal field spectroscopy

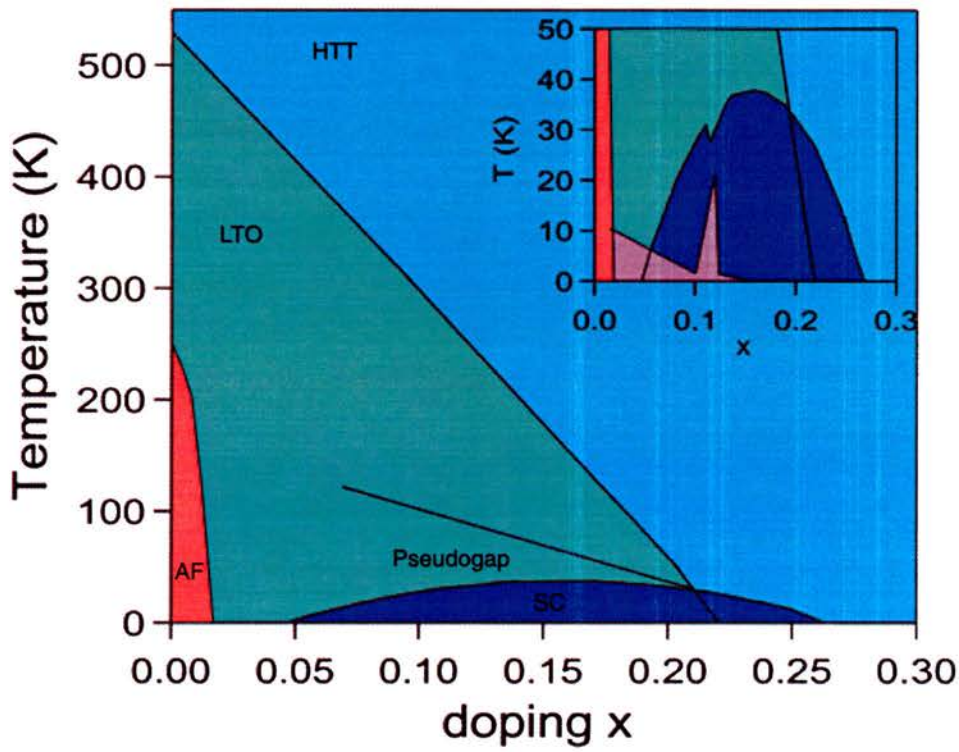

Figure 5.3: Generic phase diagram for LSCO. Inset shows the area in which dynamic magnetic excitations exist, including the 1/8th phenomenon [Julien, 2003; Ido *et al.*, 1999; Braden *et al.*, 1992; Yoshizaki *et al.*, 1988; Takagi *et al.*, 1992].

measurements [Rubio-Temprano *et al.*, 2002]. Reliable and detailed tunneling and photoemission investigations of the pseudogap are not possible because of the difficulty to obtain high quality cleaved planes, although there is a body of evidence from NMR measurements [See, for example, Walstedt *et al.*, 1994].

From a magnetic point of view, the single layered LSCO compounds are rather interesting. In the insulating AF region, LSCO has a magnetic peak at (π, π) seen in neutron diffraction studies [Vaknin *et al.*, 1987], which is common in all HTC's. Only a small number of holes are required to destroy AF order [Niedermayer *et al.*, 1998], at which point a "spin glass" is seen. Between the insulating and the superconducting phase, this spin glass phase has been observed in μSR [Niedermayer *et al.*, 1998] and NMR experiments [Julien, 2003] as well as in magnetic susceptibility measurements [Chou *et al.*, 1995; Wakimoto *et al.*, 2000] and it survives in the underdoped (superconducting) region. Interestingly, the spin glass freezing temperature is enhanced around x=1/8, which coincides with a suppression of T_c. This phenomena is referred in the literature as the "1/8 anomaly" and could be explained by the formation of spin/charge order [Kivelson *et al.*, 2003; Chen *et al.*, 2002]. Both the 1D stripe model [Kivelson *et al.*, 2003] and the 2D checkerboard model [Chen *et al.*, 2002] adequately explain the dominant magic doping fraction at $x = 1/8$ observed in LSCO.

In optimally doped YBCO, the spin excitation spectrum obtained from inelastic neutron scattering experiments is dominated by a "magnetic resonance" located at the commensurate AF zone centre (π, π) [Rossat-Mignod *et al.*, 1991] which was subsequently shown to be of magnetic origin [Mook *et al.*, 1993]. The phenomenon was observed below T_c [Bourges *et al.*, 1996] up to the psuedogap [Dai *et al.*, 1999]. Similar observations have been reported in BSCO [Fong *et al.*, 1999; He *et al.*, 2001; Mesot *et al.*, 2000] and in the single layer system $Tl_2Ba_2CuO_6$ [He *et al.*, 2002]. This is not present in LSCO. For LSCO in the doping region $0.02 < x < 0.05$, the system is characterised by diagonal incommensurate peaks at $(\frac{1}{2} \pm \frac{\delta}{\sqrt{2}}, \frac{1}{2} \pm \frac{\delta}{\sqrt{2}})$ [Wakimoto *et al.*, 1999, 2000; Fujita *et al.*, 2002]. On increasing the hole concentration further, parallel incommensurate peaks are observed at $(\frac{1}{2}, \frac{1}{2} \pm \frac{\delta}{\sqrt{2}})$ for the doping region $0.05 < x < 0.25$ [Cheong *et al.*, 1991; Yamada *et al.*, 1998; Wakimoto *et al.*, 2003]. Recently, however, incommensurate peaks have been observed in YBCO similar to those found in LSCO [Bourges *et al.*, 2000; Dai *et al.*, 2001; Hayden *et al.*, 2004], indicating some universality between the HTC's.

Some of the current theories which attempt to explain these phenomena are SO(5) theory [Demler *et al.*, 2004], a Fermi surface/stripes approach [Si *et al.*, 1993;

Kivelson *et al.*, 2003], but a detailed review is beyond the scope of this thesis. However, recent experimental evidence for field induced magnetism inside the superconducting dome of $La_{2-x}Sr_xCuO_4$(x=0.1) [Lake *et al.*, 2002] have some important implications on these theories. The results obtained are not compatible with the Fermi surface/stripes picture, because of the prediction that the Neel temperature rises significantly as the zero temperature ordered moment increases. This is not observed; as the magnetic field is increased at base temperature, the magnitude of magnetic moment per Cu^{2+} increases significantly, with no associated increase in the Neel temperature at these fields. Secondly, the "hidden" SO(5) symmetry theories have predicted antiferromagnetic vortices in an applied magnetic field, but are confined to the vortex cores [Arovas *et al.*, 1997]. However, the magnetic correlation length was measured to be greater than 400Å [Lake *et al.*, 2002], indicating the magnetism is not confined to the vortex cores, but magnetism and superconductivity exists simultaneously. By relaxing some of the constraints on the SO(5) symmetry, it is possible to have antiferromagnetic correlations beyond the vortex cores [Demler *et al.*, 2001]. However, the approximations have been called into question in such a model [Lake *et al.*, 2002].

In order to ensure the effects of magnetism do not alter the results and conclusions presented in this thesis, LF-μSR experiments were performed on the underdoped samples. A magnetic signal suggesting the existence of a spin glass was observed at low temperatures, disappearing at temperatures above 5K. For this reason, all data presented in this thesis and the subsequent conclusions have been restricted to temperatures no lower than 5K. Although magnetic fluctuations may still exist at higher temperatures, the muon is not sensitive to them as they fluctuate too fast.

This chapter is divided into several sections. First, DC magnetisation and AC susceptibility measurements have been carried out to characterise the vortex phase of $La_{2-x}Sr_xCuO_4$ for the two dopings examined in this thesis; x=0.17 and x=0.1. The magnetic field range in these measurements varies from 0 to 8T, perpendicular to the CuO_2 planes. From these measurements, it is easy to see that the magnetic phase diagram has a strong doping dependance, which supports the microscopic measurements of the vortex state performed on these crystals. The second chapter is concerned with a SANS experiment on the x=0.17 compound. Here, a field induced hexagonal to intrinsic square transition is observed to occur at around 0.4T, which persists up to the vortex lattice melting temperature. Further analysis of the magnetic phase diagram of the x=0.17 compound is found in the third section, by

μSR measurements, where FLL melting and static disorder are investigated. Finally, μSR measurements on the x=0.10 compound are discussed in the fourth section, where a Bragg glass to vortex glass transition is observed.

5.2 Magnetisation Measurements on $La_{2-x}Sr_xCuO_4$

5.2.1 Experimental Method

Macroscopic measurements have been extensively used to characterise the properties of HT_c's and is evident from the vast amount of literature available (see, for example, [Sasagawa *et al.*, 1998; Kobayashi *et al.*, 1998; Cooper *et al.*, 1997]). For example, one can extract some key parameters, such as the coherence length, the penetration depth and the anisotropy [Li *et al.*, 1993; Sasagawa *et al.*, 2000]. Magnetisation measurements also offer useful information regarding vortex dynamics and transitions, which can be directly compared to the results obtained from microscopic techniques.

DC magnetisation and AC susceptibility measurements were performed on $La_{1.83}Sr_{0.17}CuO_4$ using a commercial Quantum Design Properties Measurements System (PPMS), situated at PSI. Measurements were performed by one of our principle collaborators, Raffaele Gilardi and have been included here as the magnetisation data is directly related to the interpretation of the microscopic measurements presented in this thesis. DC Magnetisation measurements on $La_{1.9}Sr_{0.10}CuO_4$ were performed in St. Andrews on a Quantum Design MPMS SQUID. The magnetic field, in both sets of data, was applied approximately along the c-axis, which was determined by x-ray Laue.

The x=0.17 crystal is a part of the crystal used for SANS and μSR experiments. The crystal used for most magnetisation measurements was a 293 mg cylindrical crystal, but when performing zero-field cooled measurements the crystal was cut to a 84 mg plate with the c-axis parallel to the largest face, because the diamagnetic signal was too large to be measured. The x=0.10 crystal is a 37 mg plate with the c-axis parallel to the largest face, which was cut from the larger crystal used in μSR experiments.

DC magnetisation measurements determine the equilibrium magnetisation of the sample, measured by induction, for a given magnetic field. In AC susceptibility measurements, the DC magnetic field is applied in addition to a small AC field, causing a time dependent magnetisation in the sample. At low frequencies, the magnetisation inside the sample is similar to the DC magnetisation; $M_{AC} = \chi H_{AC} \cos(\omega_{AC} t)$. At higher frequencies, the induced AC moment lags behind the driving field. In this case, χ can be thought of as being complex; the real (in phase) and imaginary (out of phase) components are

$$\chi' = \frac{1}{\pi H_{AC}} \int_0^{2\pi} M(\omega_{AC}t) \cos(\omega_{AC}t) d(\omega t) \tag{5.1}$$

and

$$\chi'' = \frac{1}{\pi H_{AC}} \int_0^{2\pi} M(\omega_{AC}t) \sin(\omega_{AC}t) d(\omega t) \tag{5.2}$$

where $\chi = \chi' + \imath\chi''$. χ' is proportional to the time averaged magnetic energy stored in the sample and χ'' is proportional to the energy converted into heat during the cycle of AC field.

5.2.2 Temperature Dependence

Figure 5.5 and 5.4 show a set of FC temperature scans of χ'(T) for the two LSCO samples at different magnetic fields. The magnitude of χ'(0) is different between the two samples, most probably because of the difference in shape of the crystals leading to different demagnetisation factors. Although the ZF data is not included in these plots, the sharpness of the superconducting transition (defined by the 10%-90% criterion for χ'(T) or by the width of the peak in χ"(T)) is small, indicating the samples are of high quality as the transition width is very small. The critical temperature for the two samples are shown in Table 5.1, measured by ZF magnetisation measurements, resistivity and specific heat [Momono, 2003].

DC magnetisation measurements provide additional information regarding the vortex behaviour. In Figure 5.6, ZFC and FC temperature scans are shown for the two samples for different magnetic fields. Whilst AC susceptibility measurements show little or no differences between a FC and ZFC state, the temperature at which the DC magnetisation differs between the ZFC and FC measurements is the point at which the superconductor becomes irreversible. It is due to the crossover from a regime of pinned vortices which has finite critical current, to a regime of unpinned vortices with zero critical current. This can be defined as the irreversibility temperature, T_{ir}, when the vortex lines are thermally activated and can exit the pinning centres. Note the peak in the DC magnetisation just before the irreversibility temperature, indicating that the irreversibility in magnetisation and the peak in χ"(T) are intimately related.

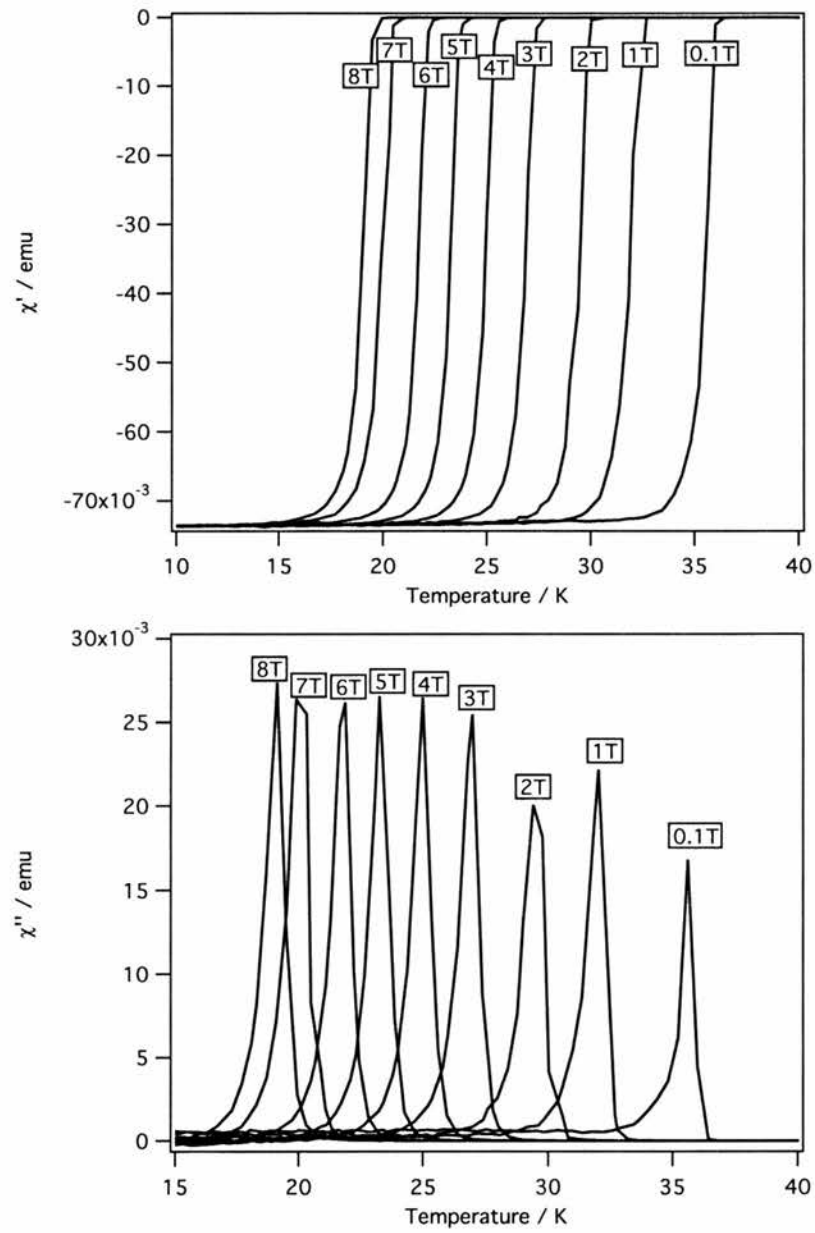

Figure 5.4: Temperature dependence of the AC susceptibility for x=0.17 (R. Gilardi).

$Doping, x$	T_C/K	$\Delta T_C/K$	λ_{ab}/nm	γ
0.10	29.2	1.3	300	40-50
0.17	36.2	1.5	240	15-20

Table 5.1: List of samples and associated parameters, obtained from magnetisation measurements. For completeness, the penetration depth and anisotropy parameter measured elsewhere have been included.

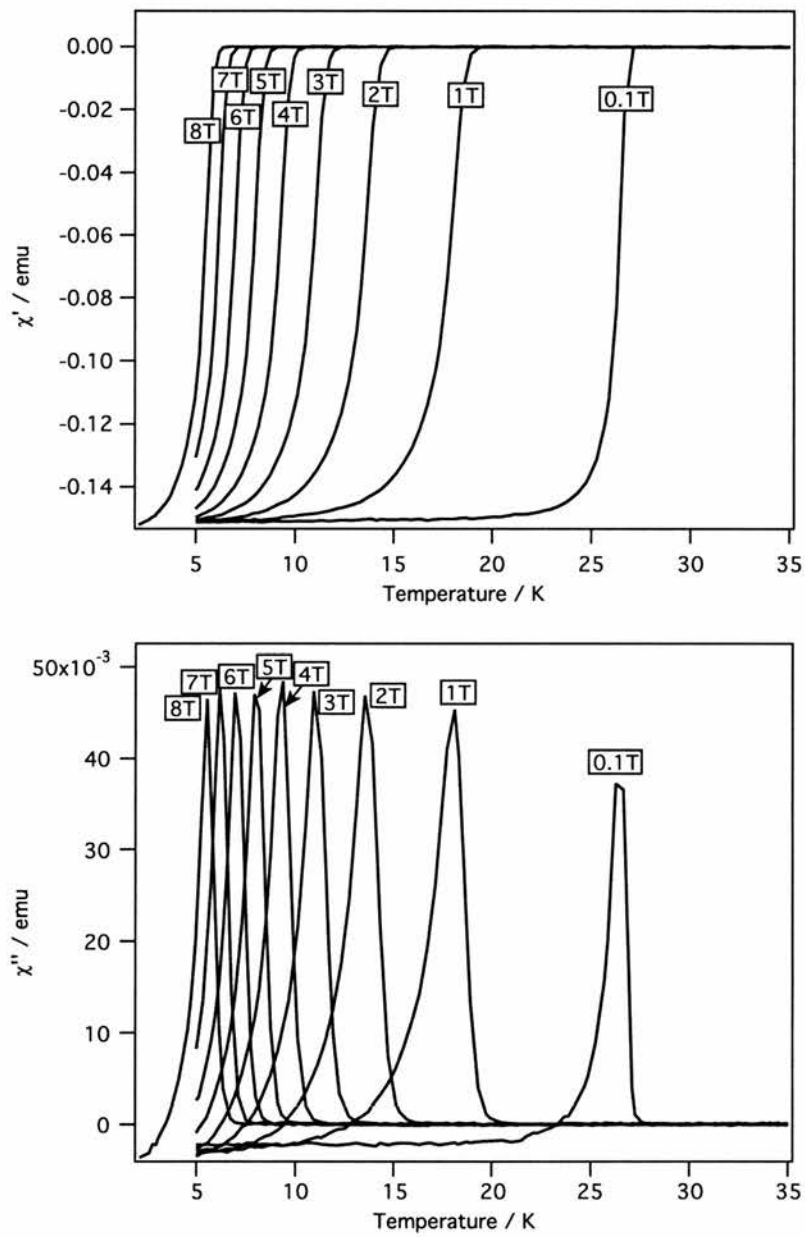

Figure 5.5: Temperature dependence of the AC susceptibility for x=0.10 (R. Gilardi).

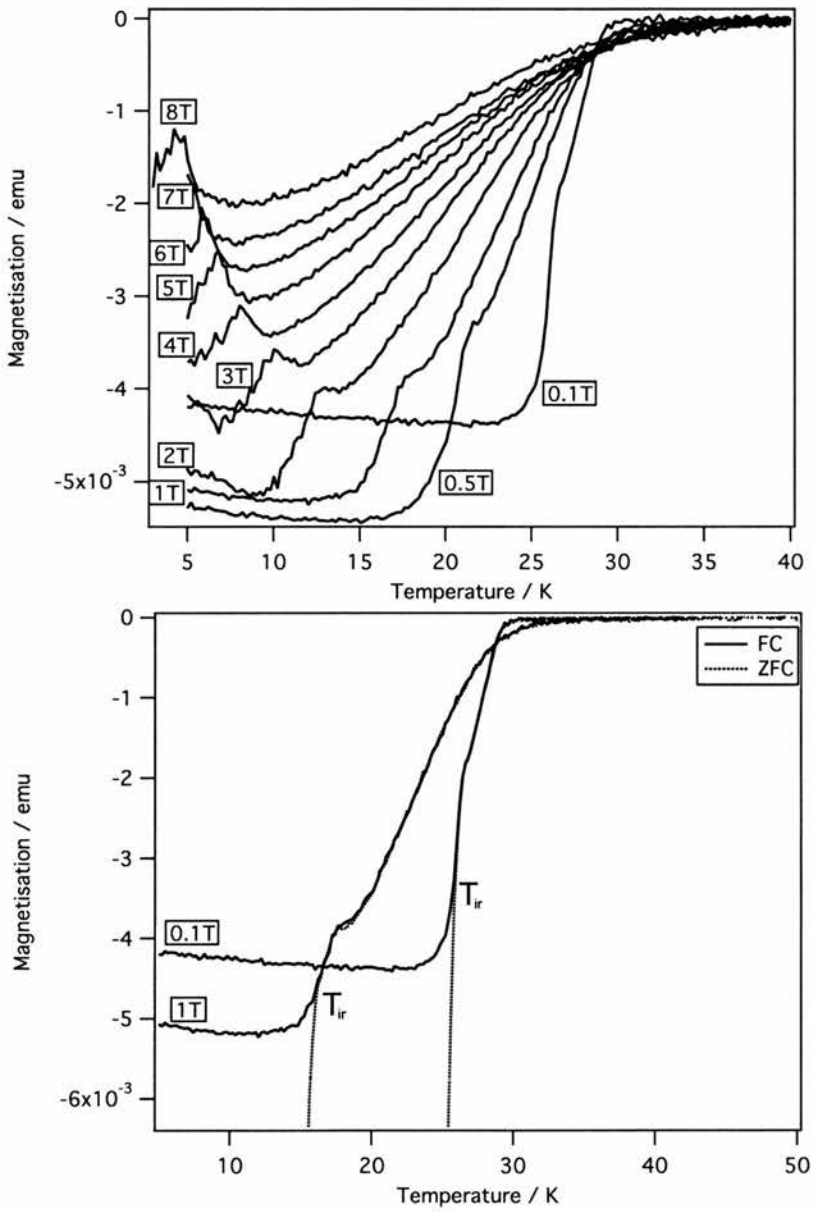

Figure 5.6: Temperature dependence of the field cooled DC magnetisation for x=0.10 (R. Gilardi) and x=0.10 (R. Gilardi).

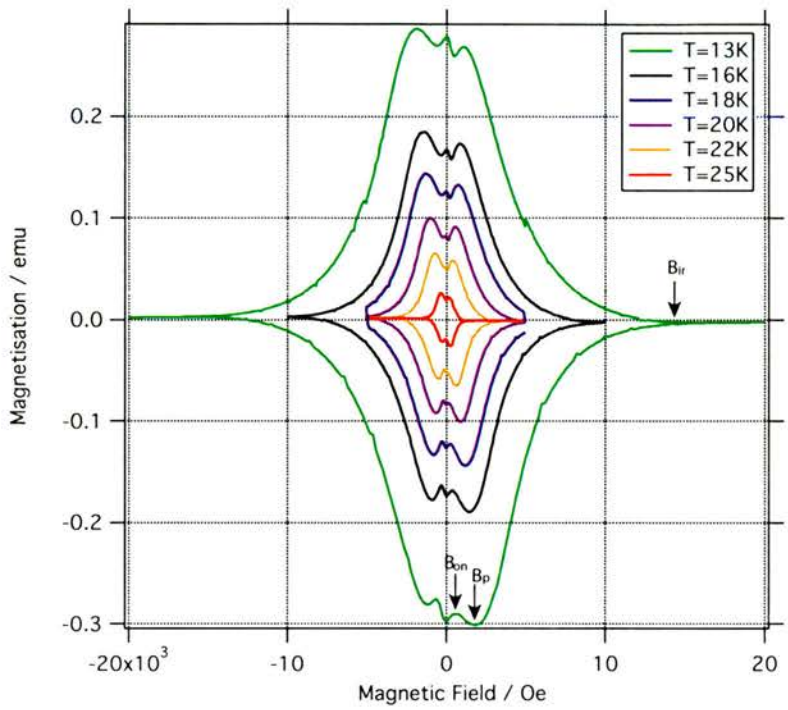

Figure 5.7: ZFC M-H loop for x=0.10 at various temperatures. Measurements taken on the St. Andrews SQUID.

5.2.3 Field Dependence of the Magnetisation

ZFC magnetisation measurements at different temperatures for x=0.10 are shown in Figure 5.7. Starting from zero field, a maximum is observed which is labelled B_{on}, followed by a minimum at B_p. B_{on} is related to flux-pinning [Koshelev and Vinokur, 1998], whose origin is still a matter of debate amongst the literature. It is clear, however, it must be related to a change in the pinning regime. A third field can be identified at the point that the vortices become reversible, labelled with B_{ir}. These parameters can be plotted on a magnetic phase diagram as a function of applied field and temperature. However, it is more informative to combine this with microscopic measurements of the vortex lattice, so it will not be done at this time (see Figures 5.31 and 5.42 for phase diagrams compiled from magnetisation and microscopic measurements).

5.3 Small Angle Neutron Scattering on $La_{1.83}Sr_{0.17}$ CuO_4

5.3.1 Experimental Detail

All measurements reported in this section were performed on $La_{1.93}Sr_{0.17}CuO_4$ with a magnetic field ranging from 1000Oe to 10T, applied parallel to the crystallographic c-axis after a field cool, unless otherwise stated. Measurements were carried out on the SANS-I spectrometer at the PSI and on D22 at the ILL. The neutron wavelength was varied from 5Å to 16Å, with the collimator distance varied between 5m and 18m. The detector was a 128x128 multidetector, with a pixel size of 7.5mm, whose distance from the sample could also be varied depending on the applied field and q-range required. The undiffracted main beam was intercepted by a cadmium beamstop. The cryostat at PSI consisted of an 11T magnet and a variable temperature insert containing He exchange gas, allowing sample temperatures to be controlled from 1.5K to 300K. At the ILL, the cryostat was an AS-Orange with a 3T magnet and a variable temperature insert containing He exchange gas, allowing sample temperatures to be controlled from 1.5K to 300K. In order to satisfy the Bragg condition for all spots, the cryostat could be rotated or tilted relative to the incident neutrons in order to bring the FLL Bragg spots onto the Ewald sphere. Very long counting times were required (1-3 hours per field/temperature plus a similar background measurement) due to strong background scattering from crystal defects and a small magnetic (superconducting) cross section.

5.3.2 Data Analysis

Data was analysed using Grasp [Dewhurst, 2004]. In order to see the signal due to the FLL above the small angle crystal defect scattering, it is necessary to subtract a background from the data, which was obtained at low temperatures in zero field or well above the superconducting transition temperature. The beam centre is found from fitting a 2 dimensional Gaussian to an attenuated run without the beamstop, for all wavelengths/detector distances. In order to stop bad background subtraction in the central area distorting the scale, it was necessary to mask it out. Care was taken to ensure the outer limit of the mask was well away from the expected position of the FLL. Figure 5.8 shows a comparison between non-subtracted data below T_c and the same data which has had a background subtracted. Smoothing is used when

displaying 2D detector images for clarity, with a smoothing kernel consisting of a 3x3 pixel box, but all analysis is performed on the raw unsmoothed data.

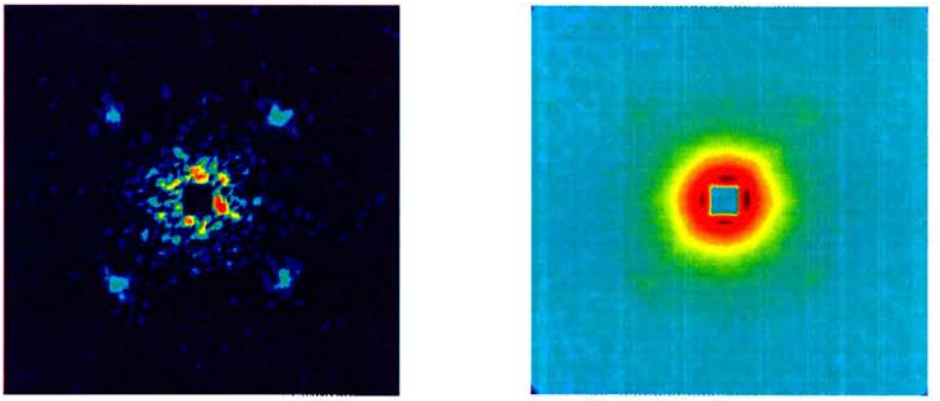

Figure 5.8: Comparison of data with and without background subtraction. Left: with subtraction, where the four diffraction spots are clearly evident. Notice the bad background subtraction around the central beamstop, where crystallographic scattering is large. Right: without subtraction. When plotted on a log scale, the diffraction spots are barely visible.

5.3.3 Field Induced Hexagonal - Square FLL Transition

Figure 5.9 shows two plots of data when cooled to 1.5K in a 2kOe field, taken at PSI. The left-hand side plot shows the data taken with the field parallel to the c-axis and it is clear that it is difficult to determine the symmetry of the vortex lattice, as there are a large number of spots distributed about a ring, representing a FLL which is effectively polycrystalline. This diffraction pattern is very reminiscent of the one found in untwinned YBCO [Johnson *et al.*, 1999]. The wavevector of this ring is consistent with the value expected of a hexagonal lattice, which can be calculated using a Gaussian fit to a tangential average and will be discussed later. At this stage, the low field symmetry needs to be clarified. In order to do this, it is necessary to remove the large degree of degeneracy between the different FLL orientations. One way to do this is to rotate the crystal such that the c-axis is at a large angle with respect to the applied field, thus reducing the effects of twin planes [Johnson *et al.*, 1999].

Figure 5.9 also shows the diffraction pattern for the same field, with the c-axis of the crystal at an angle θ=10° to the field. It is clear from this that the low field structure is of hexagonal symmetry. Even at relatively large angles of ~5° a fraction of vortices can remain pinned to the c-axis, since the vortices bend in order for part

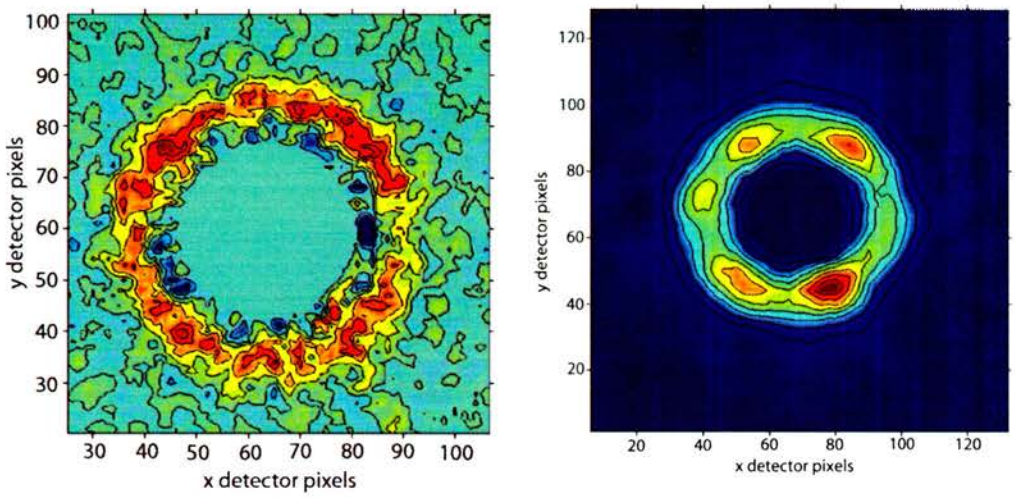

Figure 5.9: Left: SANS diffraction pattern taken at 1.5K after cooling in a field of 1kOe. A zero field background at 1.5K is subtracted. The c-axis is along the direction of the field. Data taken at PSI. Right: SANS diffraction pattern taken at 1.5K after cooling in a field of 1kOe. A zero field background at 1.5K is subtracted. The c-axis is rotated off θ =10° in order to lift the degeneracy between different FLL orientations. Data taken at the ILL.

of their length to lie on the planar defects [Blatter *et al.*, 1994; Yethiraj *et al.*, 1993]. For larger angles, the vortices tend to lie along the direction of the applied field [Yethiraj *et al.*, 1993]. Precise values for the critical angle, Θ_c, at which the vortices overcome this pinning are not easily obtained [Blatter *et al.*, 1994], but are expected to decrease with field and they are not expected to be very different from YBCO considering the values of γ and λ [Gilardi *et al.*, 2002]. However, it is clear that in this sample at low fields, Θ_c <10°.

Below Θ_c an intrinsic hexagonal lattice may not manifest itself as a diffraction pattern with hexagonal symmetry, but in fact could appear fourfold. This fourfold pattern was first observed by Keimer [Keimer *et al.*, 1994] in twinned YBCO, but unfortunately was attributed to an intrinsic fourfold symmetry and not the true hexagonal symmetry [Johnson *et al.*, 1999; Brown *et al.*, 2004]. Distortion from the a/b plane anisotropy present in the orthorhombic domain [Forgan and Lee, 1995; Walker and Timusk, 1995] distorts the ring in which the Bragg spots lie. Coupled with an overlapping of diffraction spots, it leads to four very strong spots with what appears to be second order spots, which can be easily mistaken for an intrinsic square pattern. This interpretation was confirmed on an untwinned YBCO sample [Johnson *et al.*, 1999] where diffraction spots were found distributed around an ellipse. This indicates how large an effect twin planes have on the FLL orientation, as the sample

Domain	*X/pix*	*Y/pix*	*Angle/deg*
[$\bar{1}$00]	40.0 (0.9)	73.8 (0.6)	0.0 (4.0)
[$\bar{1}$00]	61.6 (0.4)	82.9 (0.4)	59.1 (1.1)
[$\bar{1}$00]	79.7 (0.7)	71.5 (1.0)	123.6 (0.8)
[$\bar{1}$00]	79.1 (0.9)	52.7 (0.7)	178.4 (0.7)
[$\bar{1}$00]	60.8 (1.3)	44.7 (0.4)	239.7 (4.0)
[$\bar{1}$00]	44.7 (2.1)	52.5 (0.1)	295.7 (14.0)
[$\bar{1}$00]	47.2 (0.4)	78.0 (0.6)	0.0 (1.0)
[$\bar{1}$00]	66.5 (0.5)	81.1 (0.4)	59.5 (1.0)
[$\bar{1}$00]	41.1 (0.5)	58.8 (0.6)	301.45 (4.0)
[$\bar{1}$00]	48.8 (0.2)	80.9 (0.2)	0.0 (1.5)
[$\bar{1}$00]	73.7 (0.5)	46.7 (0.4)	177.9 (0.4)
[$\bar{1}$00]	53.4 (0.4)	44.4 (0.6)	238.0 (2.1)
[$\bar{1}$00]	55.5 (0.9)	83.0 (0.9)	0.0 (3.9)
[$\bar{1}$00]	78.4 (0.9)	77.0 (1.2)	60.3 (1.5)
[$\bar{1}$00]	81.1 (1.0)	59.1 (0.9)	117.9 (3.0)
[$\bar{1}$00]	66.6 (0.4)	41.6 (0.1)	182. (0.9)
[$\bar{1}$00]	46.9 (0.5)	49.1 (0.5)	242.2 (4.0)

Table 5.2: Spots shown in Figure 5.10 fitted to a 2D Gaussian. Errors have been estimated from the fits using the Jacobian matrix and calculated using Adding in Quadrature. The angle is defined as the angle between the first spot and current spot. The arbitrary zero is defined by the first spot.

used in the experiment was a high quality untwinned single crystal with very few residual twin planes. Multiple domains were superpositioned around the ellipse as the FLL orientations were degenerate due to the residual twin planes. In the LSCO sample measured in this work, many boundaries between twins are formed as the sample goes through a tetragonal - orthorhombic transition between 80K - 300K (depending on doping), as can be seen in Figure 5.2.

Now the underlying low field FLL symmetry is known, one must turn to a detailed analysis of the polycrystalline FLL structure seen in Figure 5.9 to ascertain if the role of the twin planes are similar to that found in underdoped YBCO. Ideally, one must choose the lowest applied field possible. At 1kOe the diffraction spots fall at such a low q that there is considerable crystallographic scattering to deal with.[2] This leads to bad background subtraction and some difficulty in fitting the spots, even though the initial inspection of the smoothed data shown in Figure 5.9 is good.

[2]Scattering from randomly orientated scattering sites (such as the crystal defects in these samples) for *any* distribution of sizes, is proportional to $1/q^4$ [Porod, 1951, 1952a,b], which is the same as the magnetic scattering from a FLL. So in effect, it makes *no difference* whether measuring FLL diffraction close to the central beam spot or not (since the q-dependence is the same), as long as the spots are well separated from the beamstop. However, the lower error bars associated at higher q allow easier representation of the data. Large error bars also confuse fitting routines!

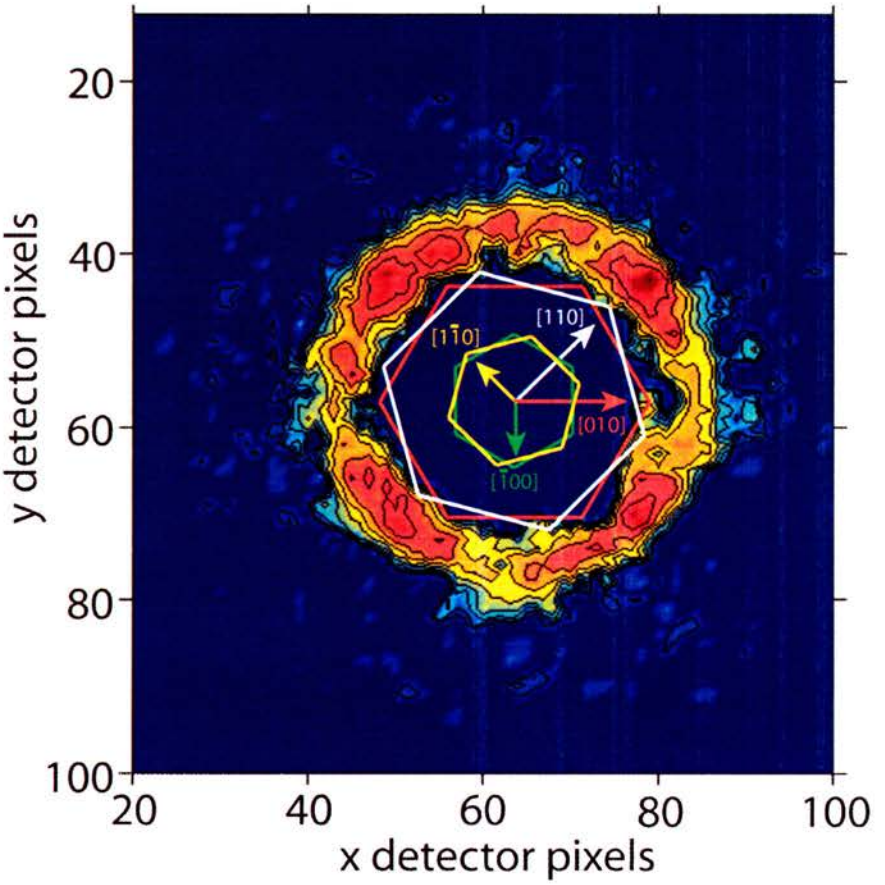

Figure 5.10: SANS diffraction pattern taken at 1.5K after cooling in a field of 2kOe. A zero field background at 1.5K is subtracted. The c-axis is along the direction of the field. Data taken at PSI.

Increasing the magnetic field will move the diffraction spots to higher q and lead to better background subtraction. A further reason to not choose the 1kOe data is that not enough statistics were taken to accurately judge whether a diffraction peak is above the noise or not, due to a limited experimental time. Simply increasing counting statistics considerably increases the ability to fit diffraction spots.

For these reasons, the 2kOe diffraction pattern shown in Figure 5.10 has been fitted to a 2D Gaussian function and is shown in Table 5.2, where more statistics are available and the diffraction spots are at a higher q. Although it has not been possible to fit every spot of every domain, it is clear from the fits that there are four hexagonal domain orientations; that is, 6 spots per domain separated by 60°. One pair of orthogonal domain orientations have Bragg spots corresponding to the a/b directions of the crystal, while the other pair correspond to an orientation along each of the ⟨110⟩ directions of the crystal lattice. These domains are schematically shown in Figure 5.2 and agree with the interpretation of untwinned YBCO [Brown *et al.*, 2004]. There is considerable error in spot positions and therefore angle, which is understandable considering the expected intensity of the diffraction spots due to the sample parameters ($\lambda \approx 2400$Å) and the considerable crystallographic scattering. The structure could equally well be 6 domains of 4 spots, although this is considered unlikely, as there is no reason for there to be 6 domains, the data rotated off is hexagonal and the spots fall on the desired q for a hexagonal lattice at this applied field.

Now it is time to turn to the high field symmetry. As the magnetic field is increased, the pattern changes such that there are four clear spots along the ⟨110⟩ directions which form a perfect square, corresponding to the CuO bond direction. This orientation does not change all the way up to the highest field attainable 10T. Figure 5.11a shows the diffraction pattern taken at 1T and Table 5.3 shows the position and angles of the spots obtained from 2D Gaussian fits. In order to ascertain whether the square pattern observed is from an intrinsic square FLL or from the effect of twin planes, the sample was rotated such that the c-axis is 30° to the applied field and neutron momentum. Figure 5.11b shows the diffraction pattern observed. Θ_c falls as the field is increased, so using a value of $\Theta_c \approx 30°$ one can be sure the critical angle is exceeded considering $\Theta_c < 10°$ for low fields. Therefore, the square symmetry observed is extremely unlikely to be an effect of twin plane pinning. This data represents the first measurement of an intrinsic square FLL in a cuprate HTC.

When rotated off the diffraction spots do not form a perfect square, as shown

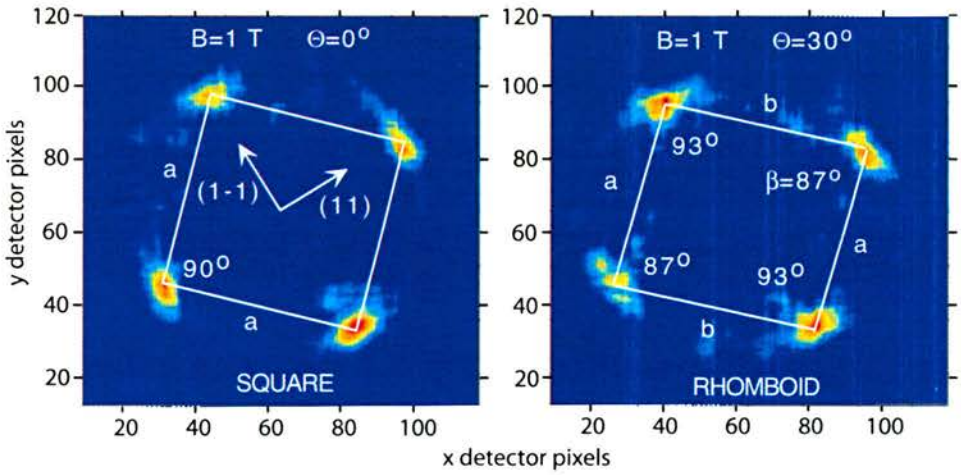

Figure 5.11: SANS diffraction pattern taken at 1.5K, after cooling from above T_c in a 1T field for B parallel to the c-axis and B rotated off the c-axis by 10°. A zero field 1.5K background is subtracted.

Spot	***X/pix***	***Y/pix***	***Angle/deg***
1	41.0 (0.3)	95.8 (0.5)	90.7 (0.4)
2	92.9 (0.2)	84.1 (0.3)	90.1 (0.5)
3	81.1 (0.6)	31.2 (0.7)	89.8 (0.4)
4	28.4 (0.4)	43.2 (0.5)	89.4 (0.5)

Table 5.3: Spots shown in Figure 5.11a fitted to a 2D Gaussian. The angle is defined as the angle between the labelled spot and the next spot.

in Table 5.4. The spots actually form a rhomboid, which can be explained by the distortion of the FLL due to an increase in penetration depth in one direction, as LSCO is uniaxially anisotropic. λ^2 can be thought of as proportional to the effective mass tensor $m_{i,k} = M_{i,k}/M_{av}$, where $M_{i,k}$ is the mass tensor defined in Thiemann's work [Thiemann *et al.*, 1988]. The free energy per unit length in the direction of the vortices is then [Campbell *et al.*, 1988][3]

$$F = \frac{1}{8\pi}\int(\boldsymbol{H}^2 + \lambda^2 m_{i,k}\nabla_i \boldsymbol{H}\nabla_k \boldsymbol{H})dxdy \tag{5.3}$$

where $dxdy$ is an element of area in the plane orthogonal to the vortex axis. The vortices that are considered here are ones orientated at an arbitrary angle, θ with respect to the crystal frame (X,Y,Z), as shown in Figure 5.12a. In order to do this, $m_{i,k}$ is transformed from the crystal frame (where $m_{XX} = m_{YY} = m_1$ and $m_{ZZ} = m_3$) to the vortex frame (x,y,z), also shown in Figure 5.12a, to

$$\begin{aligned} m_{xx} &= m_1\cos^2\theta + m_3\sin^2\theta \\ m_{xy} &= m_{yz} = 0 \\ m_{yy} &= m_1 \\ m_{zz} &= m_1\sin^2\theta + m_3\cos^2\theta \\ m_{xz} &= (m_1 - m_3)\sin\theta\cos\theta. \end{aligned} \tag{5.4}$$

For a vortex lattice, $\boldsymbol{H}$ is a periodic function which can be represented by a Fourier series with non zero components $H(\boldsymbol{G})$, where $\boldsymbol{G}$ form the reciprocal lattice. The free energy density is then [Kogan, 1981; Campbell *et al.*, 1988]

$$F = \frac{1}{8\pi}B^2\sum_{\boldsymbol{G}}\frac{1+\lambda^2 m_{zz}G^2}{(1+\lambda^2 m_{zz}G_x^2 + \lambda^2 m_3 G_y^2)(1+\lambda^2 m_1 G^2)}. \tag{5.5}$$

The basis vectors, shown in Figure 5.12b, for the case where z$\|$Z are given by

$$\begin{aligned} \boldsymbol{r}_1 &= L(\hat{\boldsymbol{x}}\sin\alpha + \hat{\boldsymbol{y}}\cos\alpha) \\ \boldsymbol{r}_2 &= L(\hat{\boldsymbol{x}}\cos\alpha - \hat{\boldsymbol{y}}\sin\alpha). \end{aligned} \tag{5.6}$$

With uniform deformations due to rotating off (i.e $\boldsymbol{H}$ is still periodic), the deformation in the x direction γ_x differs from the deformation in the y direction γ_y and the

[3]Note: this is in CGS units and free energies have been previously represented in SI. This has been kept in the original form of the paper and not converted to SI.

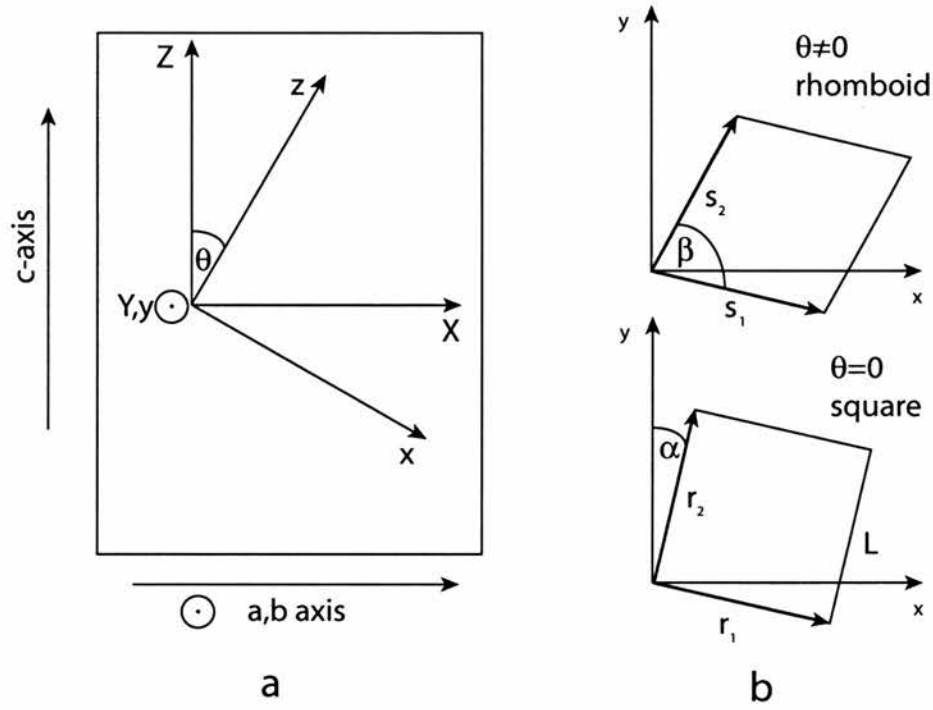

Figure 5.12: a: Diagram of the crystal frame and vortex frame. (X,Y,Z) is the crystal frame, with the XY coinciding with the a,b planes. The (x,y,z) frame is the vortex frame, where z is the applied field direction and is obtained by rotating θ about the Y axis. b: Diagram of pattern observed on the detector for the two cases.

Spot	***X/pix***	***Y/pix***	***Angle/deg***
1	40.8 (0.2)	94.1 (0.1)	92.4 (0.3)
2	96.4 (0.1)	81.3 (0.1)	87.0 (0.1)
3	82.4 (0.1)	32.0 (0.1)	93.3 (0.3)
4	27.1 (0.1)	44.3 (0.4)	87.2 (0.1)

Table 5.4: Spots shown in Figure 5.11b fitted to a 2D Gaussian. The angle is defined as the angle between the labelled spot and the next spot.

basis vectors then become

$$\begin{aligned} \boldsymbol{s}_1 &= L(\gamma_x \hat{\boldsymbol{x}} \sin\alpha + \gamma_y \hat{\boldsymbol{y}} \cos\alpha) \\ \boldsymbol{s}_2 &= L(\gamma_x \hat{\boldsymbol{x}} \cos\alpha - \gamma_y \hat{\boldsymbol{y}} \sin\alpha). \end{aligned} \tag{5.7}$$

Flux quantisation leads to the constraint that $\gamma_x\gamma_y = 1$, as the unit cell area must be conserved. Thus, γ is defined

$$\gamma = \gamma_x = \frac{1}{\gamma_y}. \tag{5.8}$$

By expanding Equation 5.5 in terms of L^2/λ^2 it has been shown that [Campbell *et al.*, 1988]

$$\gamma = (m_{zz}/m_3)^{1/4}. \tag{5.9}$$

By substituting m_{zz} from Equation 5.4

$$\gamma^2 = \left[\frac{m_1}{m_3}\sin^2\theta + \cos^2\theta\right]^{1/2} \approx \cos\theta. \tag{5.10}$$

It is now possible to compare the rhomboid distortion found to that expected from a uniaxial anisotropic superconductor. The best way to do this is to define two quantities,

$$\eta = \frac{|\boldsymbol{s_1}|}{|\boldsymbol{s_2}|} = \sqrt{\frac{\gamma^4\cos^2\alpha + \sin^2\alpha}{\gamma^4\sin^2\alpha + \cos^2\alpha}} \tag{5.11}$$

$$\cos\beta = \frac{\boldsymbol{s_1}.\boldsymbol{s_2}}{|\boldsymbol{s_1}||\boldsymbol{s_2}|} = \frac{(\gamma^{-2} - \gamma^2)\sin\alpha\cos\alpha}{\sqrt{\gamma^4\sin^2\alpha\cos^2\alpha + sin^4\alpha + \cos^4\alpha + \gamma^{-4}\sin^2\alpha\cos^2\alpha}}. \tag{5.12}$$

Substituting $\alpha = 14$ and $\theta = 30$ into Equation's 5.11 and 5.12 yields $\eta = 0.88$ and $\beta = 86.4$, which are both in good agreement with the experimental values of $\eta = 0.9$ and $\beta = 87$.

Further evidence for the hexagonal to square transition is in the position of the diffraction spots in q-space. The relationship between position and magnetic field depends on a structure dependent quantity $\sigma = (2\pi/q)^2 B/\Phi_0$, where σ is $\sqrt{3}/2$ and 1 for hexagonal and square symmetries respectively, representing the cosine of the angle between spots. Figure 5.13 shows the field dependence of this parameter and is is clear that there is good agreement. An alternative way of measuring the

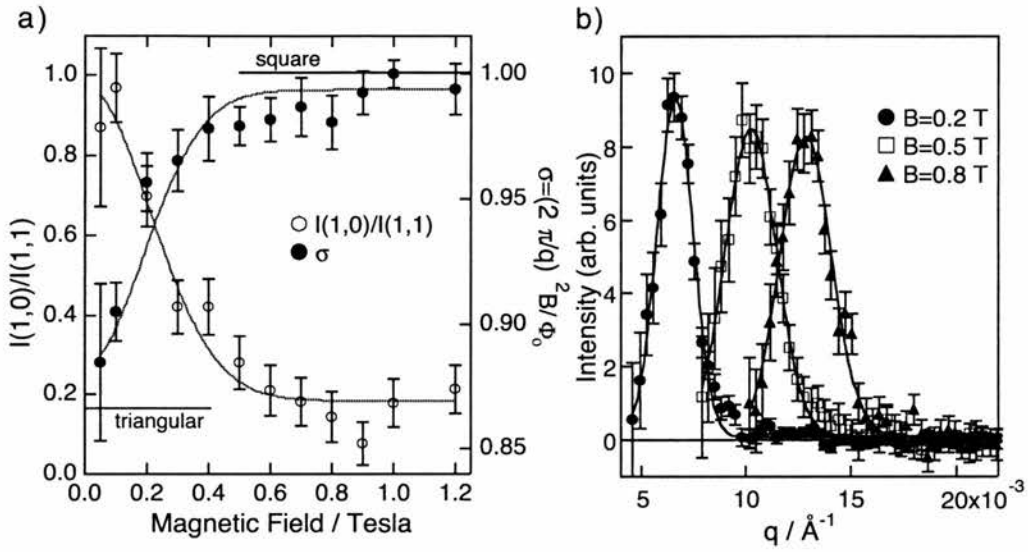

Figure 5.13: a) Field dependence of $\sigma = (2\pi/q)^2 B/\Phi_0$ at T=1.5K (black circles) obtained from fits to the tangential averages, some of which are shown in b. The expected values of σ are 1 for square and $\sqrt{3}/2$ for hexagonal FLL symmetry and are shown on the plot. Also shown (open circles) is the intensity ratio of sectors corresponding to the $\langle 1,0 \rangle$ and $\langle 1,1 \rangle$ directions. For a square FLL symmetry, this ratio should approach 0 and for a hexagonal symmetry it should approach 1. b) Tangential average of the 2D diffraction pattern for B=0.1T (circles), B=0.5T (squares) and B=1T (triangles), fitted to a Gaussian. The y-axis has been rescaled to allow a common vertical axis.

transition is to monitor the ratio of intensities along the $\langle 1,0 \rangle$ and $\langle 1,1 \rangle$ directions, where for a square FLL symmetry significant intensity along the $\langle 1,1 \rangle$ direction is expected. This is in good agreement with the spot positions. Spot positions were calculated by performing a tangential average and fitting a Gaussian to the resulting spot q-dependent intensity and three typical examples at different fields are shown in Figure 5.13b. All data and fits are of similar quality, but have not been shown to improve clarity.

One further investigation which is of interest is the temperature dependence of the square-hexagonal transition. A field cool (for different applied fields) to the base temperature was performed, taking a diffraction pattern at different temperatures on warming. Figure 5.14 shows σ, the same parameter that has been plotted in Figure 5.13, as a function of temperature for 3 applied fields around the transition. It is clear that within the errors of the measurement σ is relatively flat, indicating that the transition field does not change significantly as the temperature is increased.

As a general rule of thumb, the position relative to the crystal lattice of the FLL

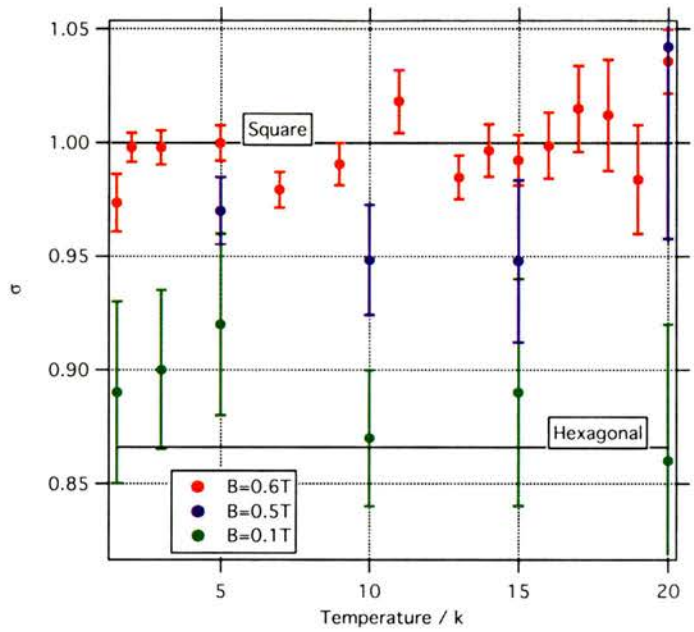

Figure 5.14: Temperature dependence of the spot position in q-space for three magnetic fields, obtained from fits to tangential averages. See Figure 5.13 and the text for details.

is determined by the different forms of anisotropy present in the superconductor. For example, the positioning of the FLL within the twin planes, already discussed above. Other forms of anisotropy can originate from electronic anisotropy, such as the anisotropic energy gap present in HT_c's, which can alter the FLL symmetry from the lowest energy, the hexagonal form. Since the difference in energy between a square and hexagonal orientation is relatively low (~2%), relatively weak differences in electronic properties can change the symmetry significantly.

Square FLL have been observed in many systems and can occur for many reasons. In low-κ superconductors the cores are large, resulting in much larger non-linear electrodynamic effects due to the large vortex cores [Waldram, 1996]. This may result in a square FLL coordination, but at low magnetic fields, where the vortices are well separated, or close to T_c where non-local effects are smaller, the FLL may revert to a hexagonal symmetry. This, combined with the anisotropy in the Fermi surface, is an explanation of the boron carbides [Levett *et al.*, 2002; Kogan *et al.*, 1997].

The presence of an anisotropic superconducting gap can also give to rise a square FLL symmetry. Many theoretical papers [Franz *et al.*, 1997; Won and Maki, 1996; Han and Zhang, 1997; Morita *et al.*, 1997; Ichioka *et al.*, 1995; Chang *et al.*, 1998]

have been stimulated, albeit incorrectly, by the claimed observation of a square FLL in YBCO [Keimer *et al.*, 1994]. One such attempt is the theoretical study of an isolated vortex, which finds the magnetic and supercurrent distributions around the core have a fourfold symmetry [Ichioka *et al.*, 1996; Mandal and Ramakrishnan, 2002]. At low magnetic fields, the vortex cores have a square like pattern but are too far apart for inter-vortex interactions. As the magnetic field increases, the cores become closer together and the square symmetry gradually increases its effect on the whole FLL. The field at which the FLL goes square is calculated to be $0.15H_{c2}$, which corresponds to an applied field of ~4.5T in LSCO, much higher than the field at which LSCO becomes square. The square FLL nearest neighbour is found to be energetically more favourable along the gap node directions. The square lattice observed here has the lattice aligned along the Cu-O bond direction, corresponding to the minima in the Fermi velocity and not along the nodes of the energy gap. The FLL remains along the Cu-O bond direction until the highest field, 10T, which means the measurements are inconsistent with current theoretical constructs.

5.3.4 Temperature Effects on the FLL

Thermal fluctuations can make flux lines deviate from their ideal, rigid lattice. A large number of techniques are available to study the melting transition in cuprates, but most are macroscopic techniques, such as magnetisation and transport measurements. The best techniques that can be used to understand the details of vortex lattice transitions are those which probe on the microscopic scale, such as SANS and μSR. This has been shown convincingly in the literature on YBCO and BSCCO [See, for example, Aegerter *et al.*, 1998; Sonier *et al.*, 2000; Aegerter *et al.*, 2003; Kes *et al.*, 1996; Lee *et al.*, 1998b; Yethiraj *et al.*, 1993].

Figure 5.15 shows the temperature dependence of the neutron scattering intensity of four boxes at an applied field of 5T and 0.5T. Both have been normalised to the neutron monitor counts and then the box area. At this point, it is not possible to directly compare the intensities of the two sets of data, as the dependence of the scattering intensity on the neutron wavelength has not been taken into account and this is a straight through, non-rocked intensity. This will be dealt with later, when the integrated intensity, which can be obtained from the rocking curve, is considered.

The temperature dependence is expected to arise from two causes: a) the variation of superconducting penetration depth for a perfect FLL would give a temperature dependence of the intensity according to Equations 3.31 ($I \propto 1/\lambda_{ab}^4$, assuming

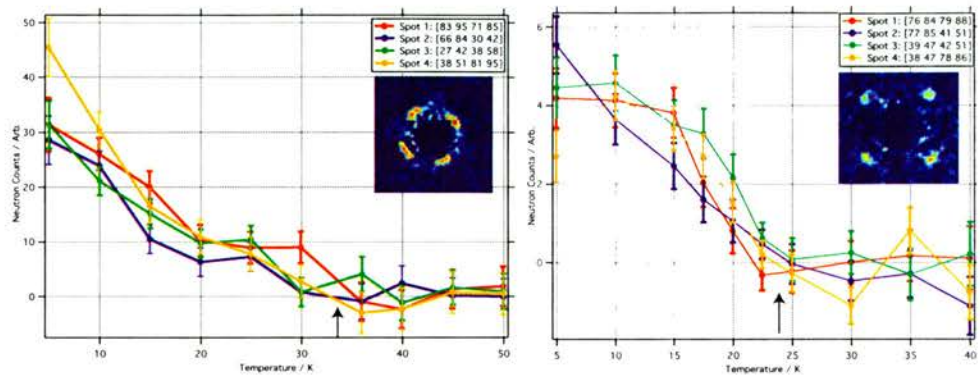

Figure 5.15: The temperature dependence of neutron intensity for 4 boxes, where in the legend the coordinates are [x_{min} x_{max} y_{min} y_{max}] pixels. The 2D detector diffraction pattern is shown in the inset, with the boxes used shown in red. The sample was cooled to 5K in an applied field of 0.5T(left) and 5T(right). The intensity is normalised to the neutron monitor counts and then to the box area. The temperature at which the FLL melts is defined to be where the scattering intensity falls to zero. Consequently T_m is shown by the arrows.

GL behaviour); b) thermal disruption of FLL order increases as the temperature increases. Clearly, the latter cause is responsible for the intensity dropping to zero as the FLL melts, which from now on will be the definition of the melting temperature, T_m. This term also contributes to the temperature dependence *below* T_m, as vibrations in the FLL are still present. The first term also contributes to the temperature dependence below T_m and therefore the shape of the temperature dependence of the intensity, so should be taken into account.

In a conventional superconductor, the temperature dependence of the superfluid density is weak at low temperatures as the superconducting gap is isotropic and therefore reduces the ability to form quasiparticle (QP) excitations exponentially with temperature [Uemura *et al.*, 1991]. In a d-wave superconductor, the present of nodes in the superconducting gap allows extremely low energy QP's to form [Hardy *et al.*, 1993]. Consequently a linear temperature dependence of λ^{-2} is expected [Amin *et al.*, 1998]. Such behaviour has been observed in YBCO and LSCO using μSR, but the data here is not seen to agree with such work [Amin *et al.*, 2000; Luke *et al.*, 1997; Sonier *et al.*, 1999]. As can be seen from Figure 5.16, the temperature dependence at all the fields measured flattens off to a finite value. There are a number of explanations for this discrepancy; such behaviour could be explained by a decrease in the superfluid density at lower temperatures [Sonier *et al.*, 1999], a fully gapped state [Beck *et al.*, 2004] or alternatively it could be due to non-linear or non-local effects [Amin *et al.*, 2000]. It should be noted that there is no appreciable

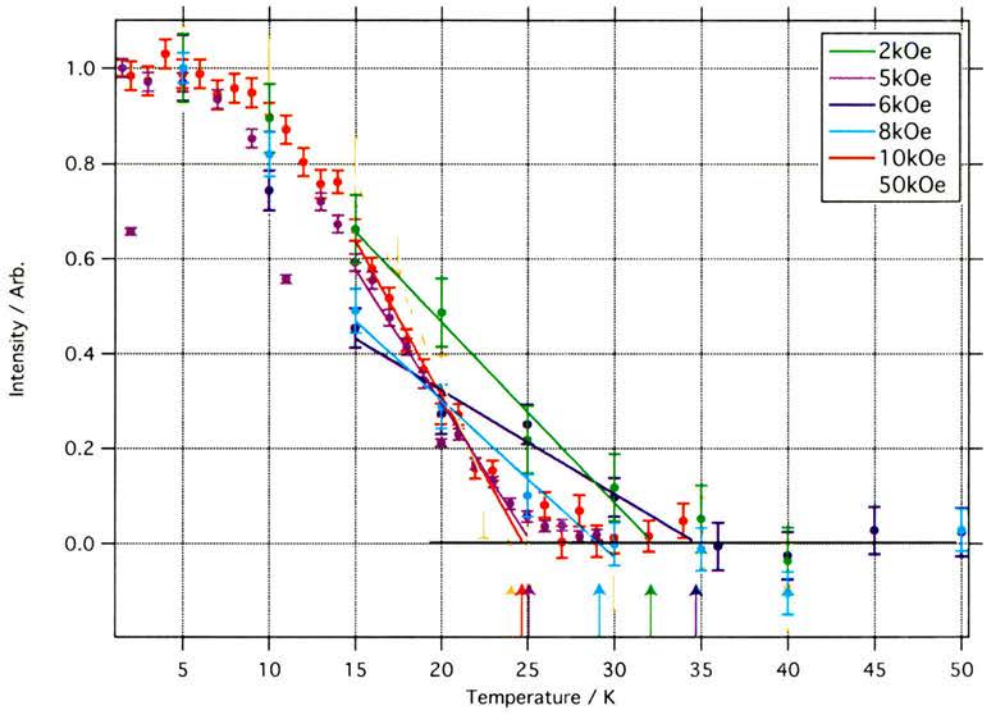

Figure 5.16: Box intensity of spots at all the magnetic fields measured. Intensity is arbitrary, normalised such that I=1 for the lowest temperature. The points are data and lines are linear fits to a selection of data near T_m. The black line at I=0 was compared to the fits and used to estimate T_m by eye, shown by the coloured arrows.

$Field/T$	T_m/K	$ErrT_m/K$
0.2	32	3
0.5	25	4
0.6	34.5	3
0.8	29	2
1.0	24.5	1
5.0	24	2

Table 5.5: Table of fitted T_m at the different fields, as shown in Figure 5.31. T_m was estimated by fitting a straight line to the intermediate temperatures, just below the point at which the neutron intensity falls to zero and compared with the I=0 line. Errors have been estimated using χ^2 (not shown) as a guide to the goodness of fit, but additional errors are introduced by the density of points and deviations from linear behaviour, which can not be estimated with a numerical technique.

field dependence observed in Figure 5.16 and all of these possible explanations would have a field dependence which would tend to enhance the deviation from linearity as the field is increased.

It is possible to estimate T_m more accurately than "just by eye", by fitting a straight line to the data at intermediate temperatures, close to the transition and taking its intercept with I=0 to be the melting temperature. This is achieved by assuming the intensity for $T<T_m$ is a straight line and for $T>T_m$ I=0. This analysis relies on no solid foundation, but by inspection of the data seems a reasonable method to extract T_m. Figure 5.16 shows the sum of all spot intensities at different applied magnetic fields and Table 5.5 shows T_m for different fields obtained from the fits. Again, absolute intensities are arbitrary, so have been omitted from the table. Combining this melting transition with the square-hexagonal transition it is possible to form a magnetic phase diagram. The low field phase diagram, however, is better investigated by μSR, as it is not limited by the intensity fall off with penetration depth and one does not have to deal with bad data subtraction due to large crystallographic scattering. Further analysis and interpretation of the FLL melting will be dealt with when considering the data obtained by μSR experiments, where a phase diagram is compiled from a combination of SANS, magnetisation and μSR measurements.

5.3.5 The Rocking Curve

The Φ rocking curve for an applied field of 0.8T at a temperature of 2K is shown in Figure 5.17 for the four diffraction spots on the detector image. It is clear no peak is seen and consequently no additional information can be obtained from performing rocking curve analysis. This result is most likely due to the entanglement of the vortices (disorder along their length) and has also been observed in YBCO using an electrical transport technique [Safran *et al.*, 1992]. Numerical simulations have shown this is the expected behaviour [Nordborg and Blatter, 1997] in SANS measurements for entangled vortices. Any change in intensity as a function of angle can not be seen outside of experimental error, so it is not possible to measure the integrated intensity and therefore penetration depth in these samples using this method.

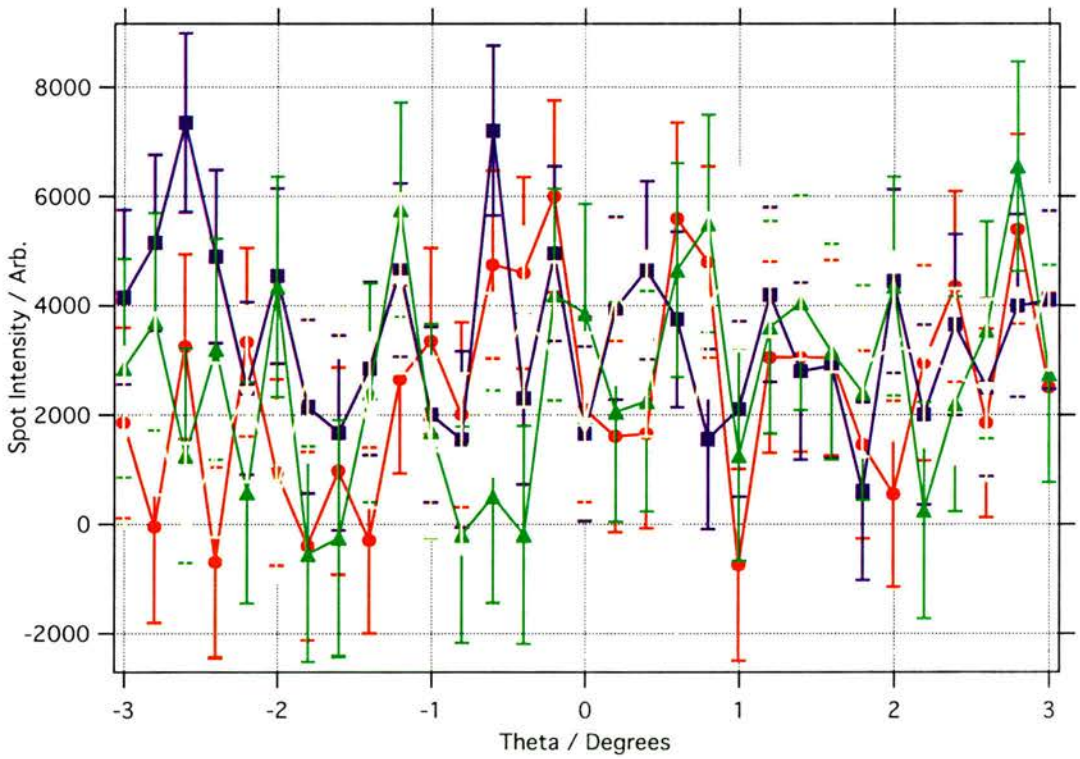

Figure 5.17: The rocking curve taken at PSI in a field of 0.8T and at a temperature of 2K. Rocking curves were calculated from the intensities in framed spots and normalised to the standard monitor and box area. It is clear no information can be obtained from performing rocking curve analysis.

5.4 μSR Measurements on $La_{1.83}Sr_{0.17}CuO_4$

5.4.1 Experimental Detail

All measurements reported in this section were performed on $La_{1.93}Sr_{0.17}CuO_4$ using the GPS spectrometer at PSI. The sample environment was the Quantum continuous flow cryostat, with a base temperature of 1.7K. The sample was mounted with the c-axis perpendicular to the applied magnetic field and was aligned by eye to within 2 degrees of the crystal orientations measured by Laue x-ray diffraction. The sample holder was a standard copper holder to ensure good thermal conductivity between the sample environment and thermometers. The holder was encased in polycrystalline haematite (Fe_2O_3) and the sample was mounted on top. This ensured any stray muons not hitting the sample would not add a background frequency, as the haematite used is an antiferromagnet with an internal magnetic field of 1.6T in a random orientation. Typical statistics are 20 million muon detection events over three detectors. Three detectors were used: Left, Right and Top. The time binning was 625ps with a maximum count time of around 10μs.

5.4.2 Data Analysis

The data was analysed using the Maximum Entropy Technique. Sigma Looseness was 1.02 to account systematic errors in the data which are not reflected in the statistics. This shifts the emphasis in the algorithm from the entropy term to the χ^2 term. This has the effect of slightly broadening and smoothing out any sharp changes in the frequency spectrum. The apodisation of errors was set to 7μs, which artificially increases the weight the algorithm puts on the data at lower times by increasing the errors slightly at large times. This is to take account of the Central Limit Theorem's break down with low statistics. It also helps to reduce "sincing"; a convolution (in the frequency domain) of a sinc function with the intrinsic lineshape of the data, due to the abrupt cut off at the end of the time window.[4] This has the effect of broadening the lineshape slightly, but reduces abrupt changes in frequency amplitude. The data was not binned other than that from the intrinsic binning of the instrument and the full time measured range was used. The number of points in the Fourier spectrum was 2^{15}, effectively "overbinning" by padding with zeros.

[4]The data in the time domain is described by the intrinsic data of the measurement multiplied by a "top hat" function representing the finite window that is measured. The Fourier transform of a top hat function is a sinc function, which is then convoluted with the data in the frequency domain.

This has no effect on the analysis other than to artificially increase the number of points in the frequency domain; effectively an interpolation.

5.4.3 Hexagonal to Square Transition

Figure 5.18 shows the field cooled field dependence of the μSR lineshape at 1.7K. Although some differences can be seen between the lineshapes, it is not at all obvious. For the manner in which the data is represented here, the lower applied fields extend to a larger high field cut off than the high applied field, but it is hard to tell without resorting to a logarithmic scale, as shown in Figure 5.19. On the logarithmic plot, the instabilities in the lineshapes are a lot more obvious. Instabilities can occur for a variety of reasons, for example the sincing effect discussed earlier or systematic errors in the data which can not be accounted for using Gaussian errors. Outliers can also confuse the maxent algorithm, but the algorithm will tend to reduce the weighting put on them and so this is of less significance than the other factors.

These instabilities obscure the estimation of different parameters, such as the high field cut off and the minimum point. However, FLL structural changes can still be detected using these parameters and is a useful exercise to help map out the phase transition. Table 5.6 shows estimated values for the minimum field B_{min}, the high field cut off B_{core} and the most probable field B_{pk} from which Γ (Equation 3.70) can be calculated. These have been estimated by referring to the "default level" - a parameter calculated by maxent which represents the noise in the lineshape.

It is clear that Γ gradually falls from around 6 at low fields to around 3 at higher fields. Although this is only an approximate guide to the FLL symmetry, Γ is expected to be 2.5 with a square symmetry and 8 with a hexagonal symmetry [Lee *et al.*, 1998a]. This analysis relies on the Abrikosov limit to the GL equations, where $H \sim H_{c2}$, which is not the case. Furthermore, the measurement of the core field is intimately related to the counting statistics, as there is a small probability of the muons sampling the core and is not observable above the experimental noise. Therefore an underestimation of the core field can result in an underestimate of Γ's value, as is the case. This analysis can, however, be a good indicator to the FLL symmetry and is consistent when combined with the SANS results (shown in Figure 5.13). Figure 5.20 shows this comparison, with a transition field estimated to be approximately 0.4T with 0.5T obtained from the SANS data. This transition field is estimated by taking the point at which any no large change is observed in the parameters and is only to indicate the consistency between the two sets of data.

Ideally model lineshapes should be calculated and directly compared to the data,

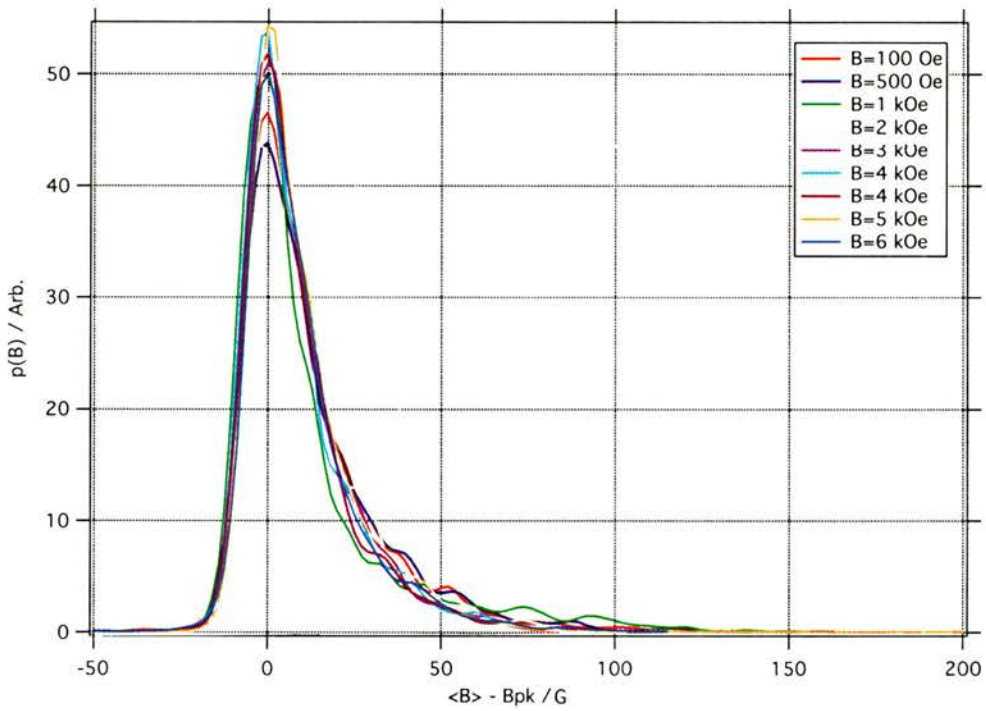

Figure 5.18: Field dependent lineshapes at all fields measured for T=1.7K.

B/G	B_{min}/G	B_{pk}/G	B_{core}/G	d	Γ
100	-50 (10)	0 (2)	227 (15)	0.015	5.7 (0.3)
500	-50 (20)	0 (2)	219 (15)	0.019	5.5 (0.5)
1000	-50 (10)	0 (2)	185 (30)	0.039	4.6 (0.3)
2000	-50 (10)	0 (2)	168 (10)	0.011	4.2 (0.3)
3000	-50 (10)	0 (2)	153 (10)	0.011	3.8 (0.3)
4000	-50 (10)	0 (2)	133 (20)	0.014	3.3 (0.3)
4500	-50 (30)	0 (2)	131 (15)	0.028	3.3 (0.7)
5000	-50 (20)	0 (2)	116 (15)	0.011	2.9 (0.5)
6000	-50 (10)	0 (2)	124 (30)	0.038	3.1 (0.4)

Table 5.6: Parameters estimated from the lineshapes shown in Figure 5.18. Errors, estimated by eye are shown in brackets and are generally consistent with the default level. Errors on Γ are calculated by Adding in Quadrature.

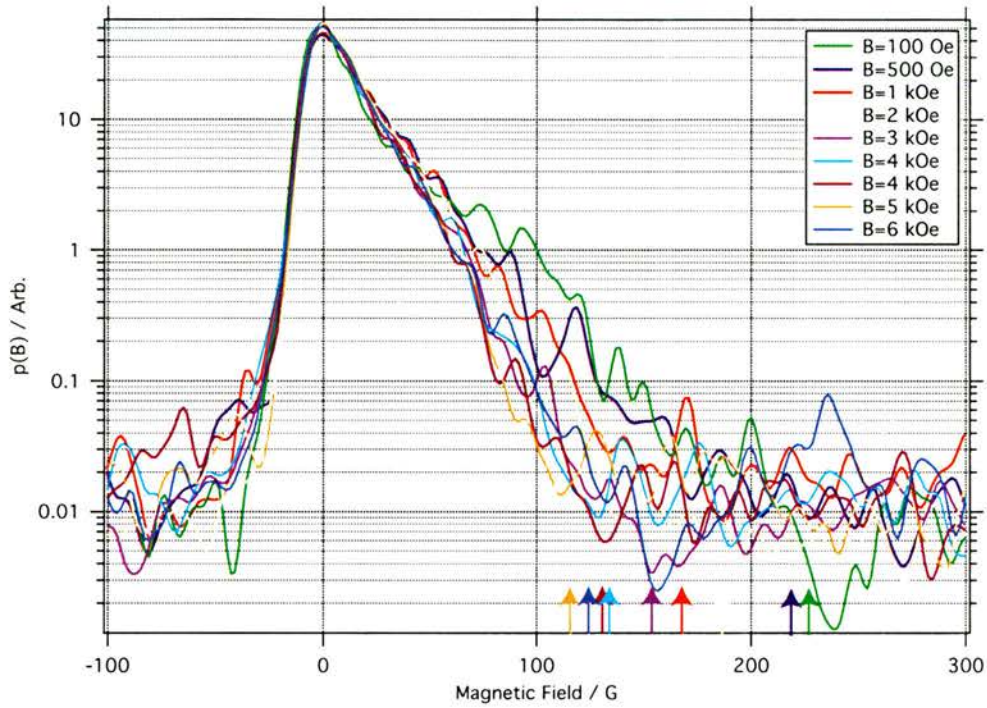

Figure 5.19: Field dependent lineshapes (in Figure 5.18) at all fields measured for T=1.7K, with a logarithmic scale. The estimation for B_{pk} is indicated by the arrows.

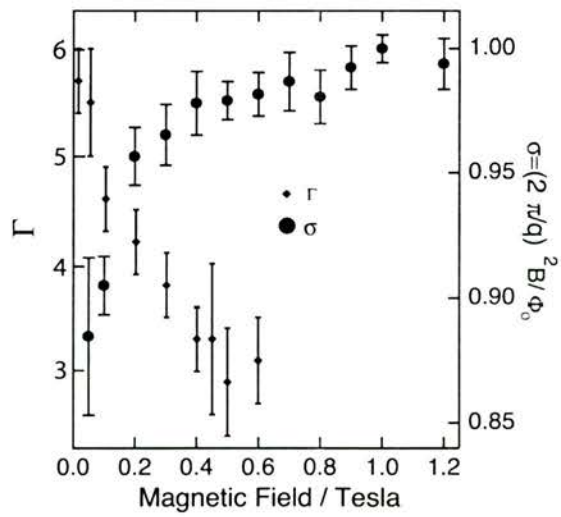

Figure 5.20: A comparison of the SANS parameter σ (defined in Figure 5.13) and the μSR parameter Γ (in Table 5.6). It is clear the hexagonal - square transition is consistent for both techniques.

but it is difficult to model the FLL when it is neither a pure square or hexagonal structure, especially so when the FLL is disordered. For intermediate fields, the FLL is periodic (assuming little disorder) and can be represented with a Fourier series (see page 75). Clem reported a solution to the GL equations for isotropic superconductors at low applied fields ($B \ll B_{c2}$) [Clem, 1975]. For a Lorentzian order parameter of an isolated vortex and large κ

$$B(\boldsymbol{G}) = \frac{\Phi_0}{S} \frac{g K_1(\boldsymbol{g})}{1 + \lambda^2 \boldsymbol{G}^2} \tag{5.13}$$

where

$$\boldsymbol{g} = \sqrt{2}\xi(\boldsymbol{G}^2 + \lambda^{-2})^{1/2} \tag{5.14}$$

S is the surface of the FLL unit cell and $K_1(x) = -K_0'(x)$, from which the London solution can be recovered at vanishing core size [Clem, 1975]. The calculation is performed by a sum over reciprocal lattice, $\boldsymbol{G}$ and is defined in Figure 3.14 for a square and hexagonal lattice. This can be extended to the case of anisotropic superconductors by use of an effective mass tensor [Hao *et al.*, 1991]. The cut off due to the core, $gK_1(\boldsymbol{g})$, can be approximated by $\exp(-\sqrt{2}\xi\boldsymbol{G})$ [Yaouanc *et al.*, 1997] for all values of g, or alternatively $\exp(-2\xi^2\boldsymbol{G}^2)$ [Brandt, 1992]. Figure 5.21 shows a 2D contour plot of the hexagonal and square FLL using typical parameters for LSCO. Although a core correction was made [Brandt, 1992], it has a very small effect due to a coherence length of ~20Å and can not be observed in the plots. However, if dynamic fluctuations of the vortices were taken into account, the effective size of the core from the muon's perspective would increase.

Using the FLL calculated in Figure 5.21, it is possible to calculate P(B) and compare directly with the data. Figure 5.22 shows the P(B) calculated for $\lambda = 2400$Å and $\xi = 20$Å compared to the low field data shown in Figure 5.18. The penetration depth here is consistent with surface impedance measurements performed for a similar Sr content to the crystal used here [Shibauchi *et al.*, 1994]. Only the P(B) calculated for the hexagonal geometry is shown and the instrument resolution has been taken into account by convoluting the model with a Gaussian fit to the normal state lineshape, shown in Figure 5.23. The normal state lineshapes were found to have a width of 3.6 ±0.05G for both the lowest and highest applied fields of 100Oe and 6kOe. As can be seen from Figure 5.22, there is considerable differences between the data and the calculated lineshapes; the lineshape has to be convoluted with a Gaussian of nearly double the width in order to be a fair representation of

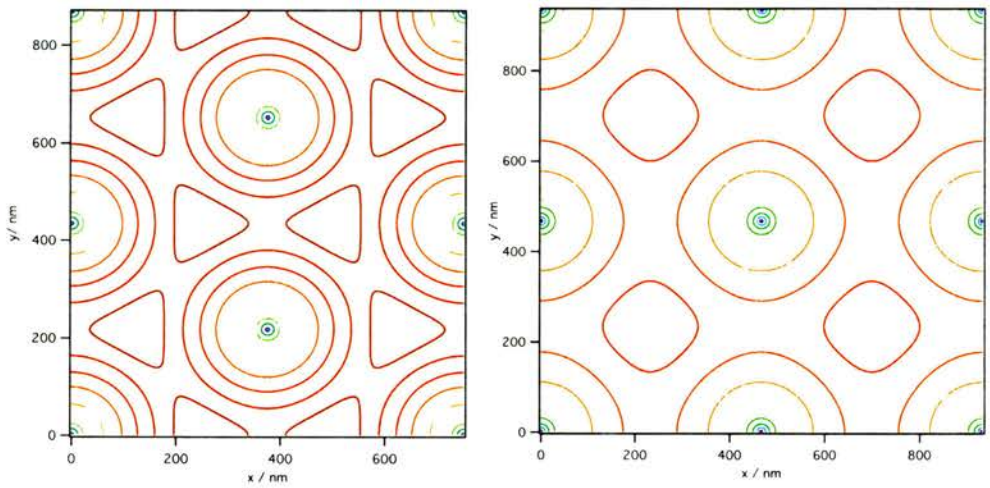

Figure 5.21: A hexagonal and square FLL has been calculated for an applied field of 100Oe, with the penetration depth 2400Å. P(B) can be directly calculated from this and compared to experimental data.

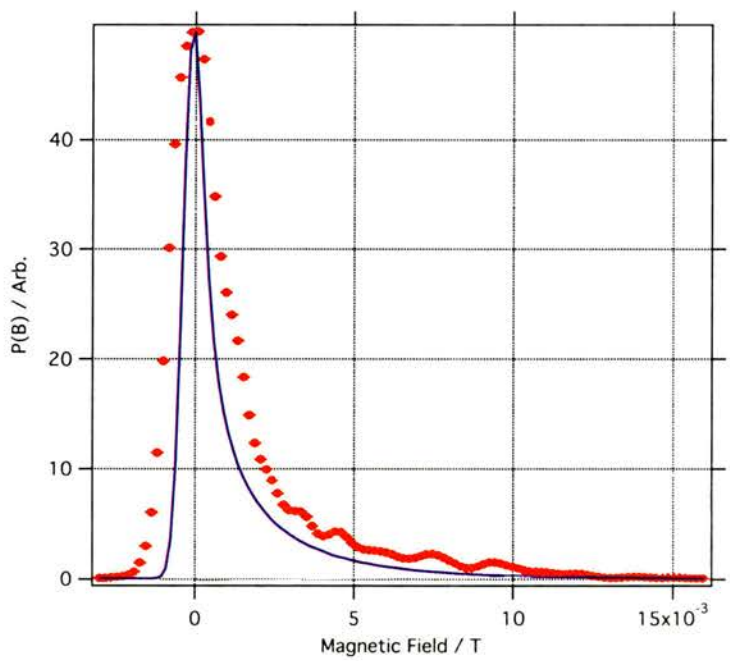

Figure 5.22: Comparison of the lineshape calculated for a square and hexagonal FLL for an applied field of 100Oe. The penetration depth is 2400Å and the coherence length is 20Å. An unrealistic convolution width of 6.5G would be needed to represent the data well.

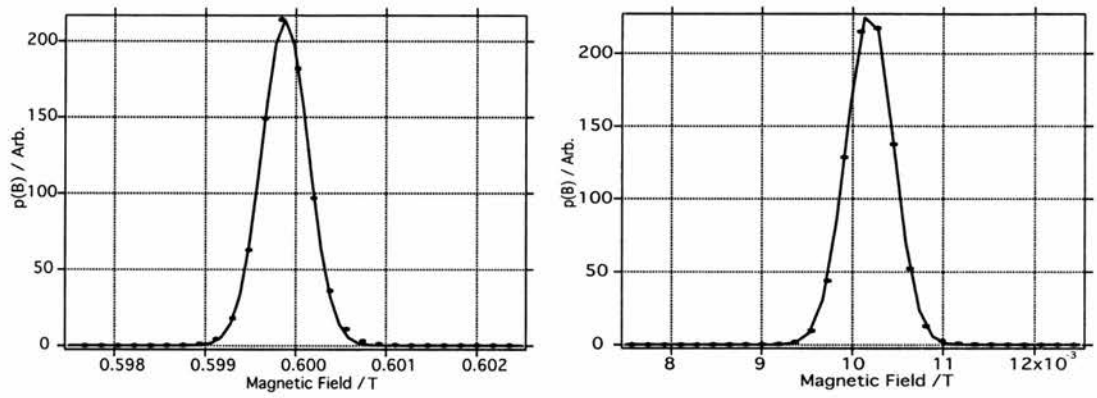

Figure 5.23: Gaussian fits to the normal state lineshape for 6kOe and 100Oe. Both have width's of 3.6 $\pm$0.05G. The fitting routine is explained in Appendix B.

the data. Another, more physically realistic solution is to include pinning into the simulation. Unfortunately the effect of pinning on the lineshape is not possible to calculate using a Fourier series, as the FLL is no longer periodic.

A simple model consisting of a random array of point-like defects [Chudnovsky, 1990] can describe this data, but must be calculated in real space, leading to a slow bulky calculation which must be repeated multiple times. The calculation of a FLL in real space is outlined on page 75, with the addition of the following simple model for pinning. The pinning array is calculated by creating a X$\times$Y array mostly consisting of zeros, with a probability *pp* for a particular array position to have a 1, which are taken as pin sites. If the position of the ordered vortices are within a given distance of the pin site, the vortex is placed on the pin site. Figure 5.24 shows the typical vortex lattice positions resulting from this model, where the vortex position moves to the pin site if it is within 6nm of the site and pp=0.05. The corresponding contour plot of magnetic field is also shown in Figure 5.24.

Each FLL configuration will be different, due to the randomness of pinning over the large muon sampling volume; vortex correlation lengths will be much smaller than the sample dimensions. Figure 5.25 shows a comparison of the data to a lineshape for this model with different penetration depths, using a similar field profile to that shown in Figure 5.24. It is clear that there is only a small dependence on the penetration depth. The symmetry chosen is hexagonal due to the earlier confirmation of the symmetry. Although the pinning model is unrealistic, as it does not take account of inter-vortex interactions, the relative strengths of pin sites and the "bendiness" of the vortices in a 3D array of pin sites, it does shows the correct generic trends and is a far better representation of the data. Although

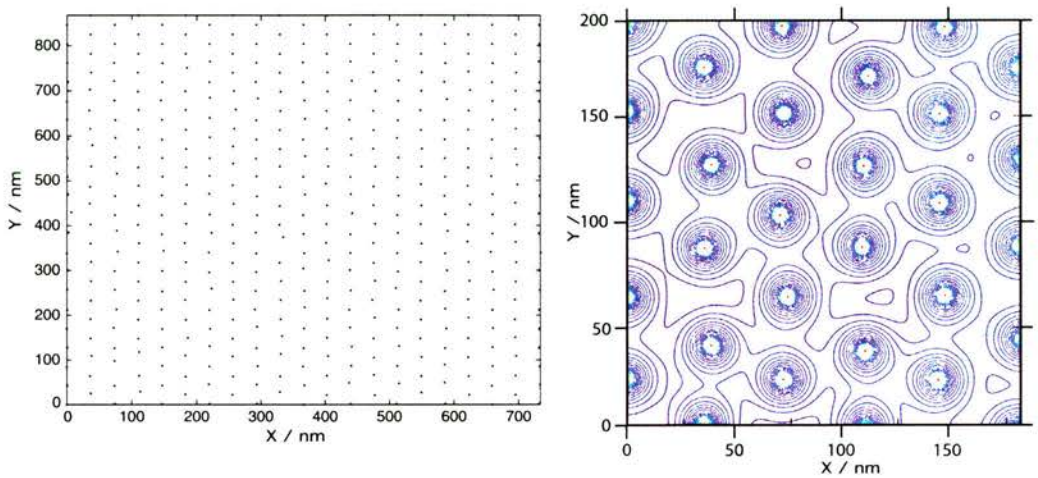

Figure 5.24: Left: Typical FLL positions calculated by a simple model (see text). pp=0.05 for a hexagonal lattice with B=100Oe. Right: Contour plot of a sample of the flux density under the same conditions with λ=2400Å.

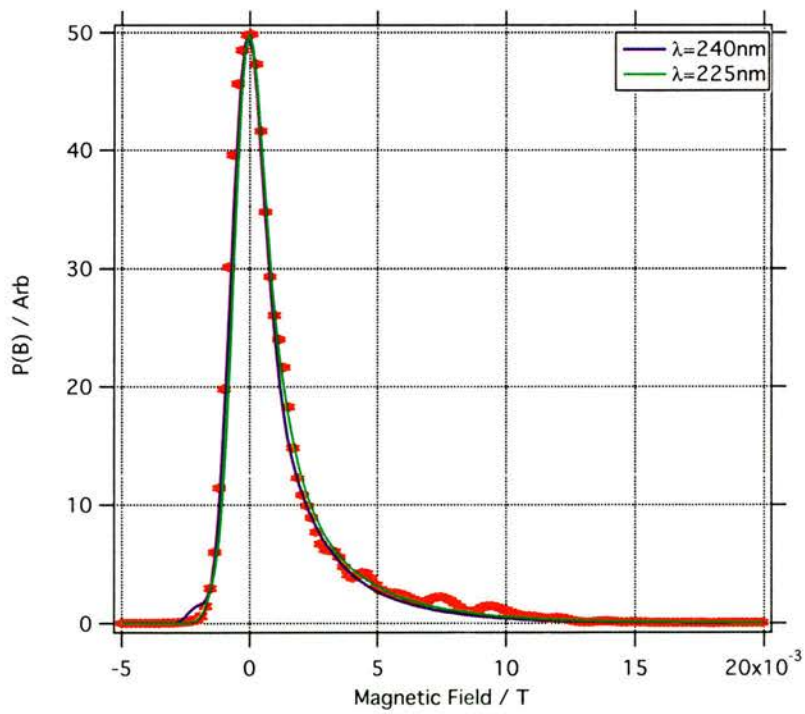

Figure 5.25: Lineshape and the pinning model (see text and Figure 5.24) for B=100 Oe with two different λ's.

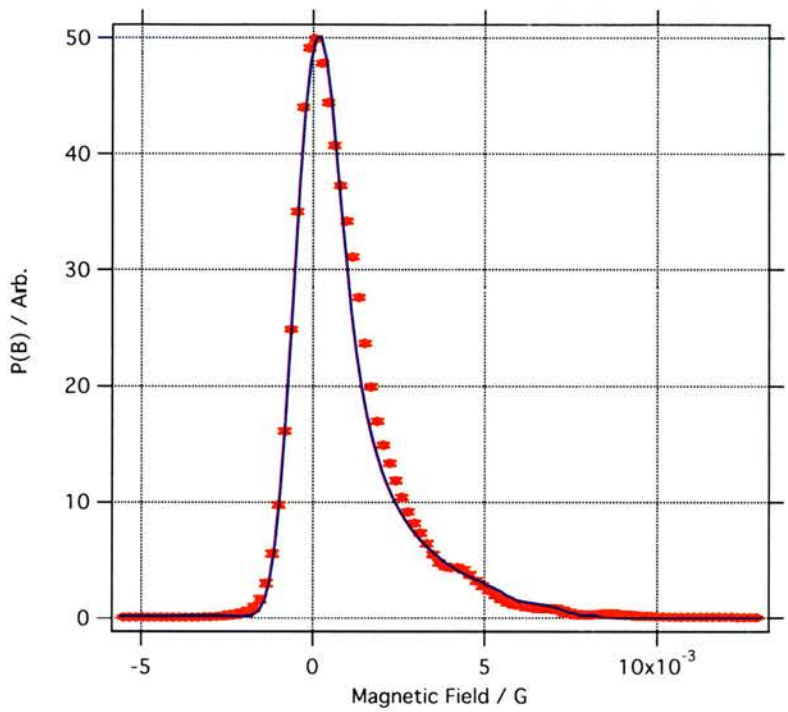

Figure 5.26: Lineshape and the pinning model for 6kOe.

similar information can be obtained simply by convoluting a larger Gaussian than is present in the normal state, this demonstrates the effect of quenched disorder on the lineshapes directly. Unfortunately it is not possible to extract a FLL symmetry or penetration depths from these lineshapes using this model with any great reliability (see Figure 5.25), but the value obtained is consistent with the other work presented elsewhere in this thesis.

It is also possible to show that pinning is reduced as the magnetic field is increased, reflecting inter-vortex interactions reducing the effect of pinning. Figure 5.26 shows the data at 6kOe with a considerably reduced pin site "area of effect", for a FLL with square symmetry. Here, $pp = 0.05$ as the number of pin sites should not have changed and the distance over which the vortex moves to the pin site has been reduced to 2.2nm, representing an increase in the elastic interactions between vortices reducing the effect of the pin site. It is clear that although this is a reasonable representation of the data compared to the non disordered lineshape (not shown, but see for example Figure 5.22).

Thermal fluctuations also play a role and have an increasing influence as the vortices become closer. Thermal fluctuations can be taken into account in a similar manner to when calculating vortex lattices with Fourier series. A Fourier transform

of the Debye-Waller factor results in

$$\int_{-\infty}^{\infty} e^{-\boldsymbol{G}^2\langle u^2\rangle/2} e^{i\boldsymbol{G}\boldsymbol{r}} d\boldsymbol{G} = \frac{e^{-\boldsymbol{r}^2/2\langle u^2\rangle}}{\sqrt{\langle u^2\rangle}} \tag{5.15}$$

which has been convoluted with the real space field distribution. Using this analysis, it is clear that the pinning at higher fields is reduced, which is also evident when calculating the second moment of the lineshapes. The observations here can also be explained by a number of other phenomena, which will be discussed later, but it becomes clear the analysis presented here is the most likely explanation of this data.

5.4.4 Lineshape Characterisation

Careful analysis of μSR lineshapes may reveal important information about the superconducting penetration depth, as well as information regarding FLL cross overs and phase transitions. Using the width of the probability distribution is often a more convenient method to extract λ, since it is easier to represent large amounts of data on one plot and the width can be modelled in a similar way to the calculation of lineshapes using a Fourier series. Unfortunately, static disorder evident in the lineshape is also found in the width; but dimensional cross overs and thermodynamic transitions are still evident and are a good way to understand the FLL. Figures 5.27 and 5.30 shows the temperature dependence of the width and alpha of the lineshapes respectively for various magnetic fields.

First, the behaviour observed in Figure 5.27 will be dealt with. It is clear that around 15K and below there is a field dependence of the width which is entirely unexpected when considering only the London model. Figure 5.28 shows a plot of the expected width for a London model with thermal fluctuations in 3D vortex lines taken into account, using Equations 3.73 and 3.74. This temperature dependence of the lineshape width can be explained by the increasing temperature truncating the high field tails, resulting from the increasing amplitude of thermally induced fluctuations of the vortex positions, on a timescale faster than the characteristic muon sampling time [Brandt, 1991a]. The muons experience a time-averaged field distribution in which the high field values arising from close to the vortex cores are smeared out. A two fluid model (dashed, Equation 2.6) and GL temperature dependence of λ (solid, Equation 2.20) has been used for the temperature dependence in λ, with γ=15 and $\lambda(0)$ = 2400Å. An increase in the ratio $\langle u^2\rangle^{1/2}/d$ in Equation 2.20 results in the field dependence of the thermal fluctuations observed, but can

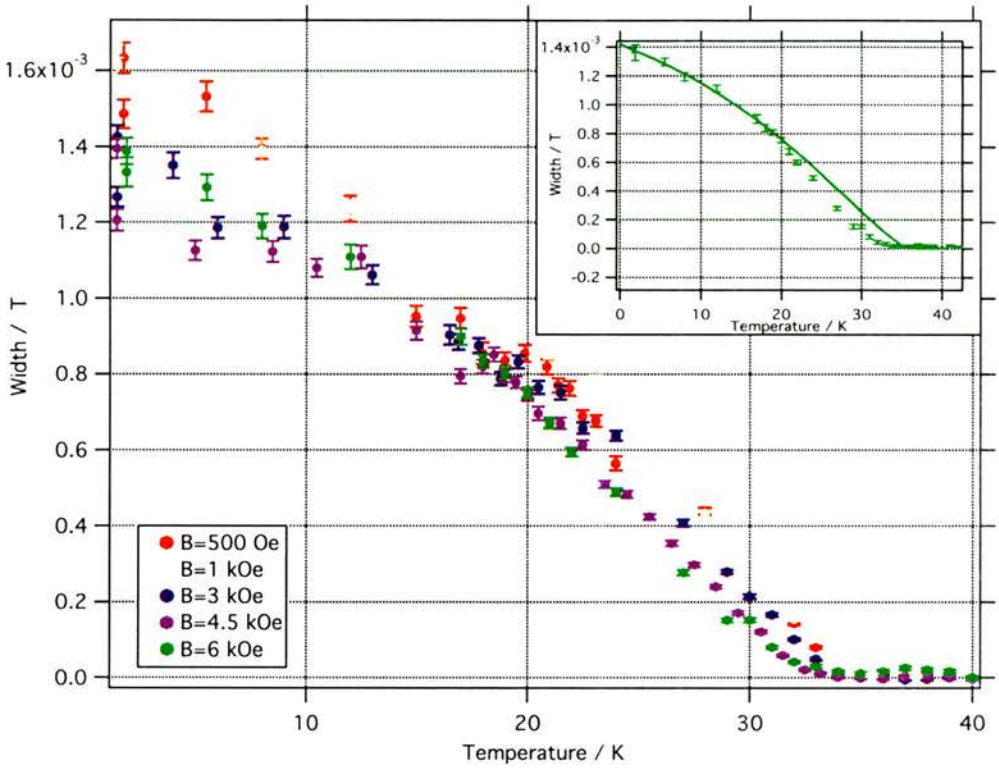

Figure 5.27: Temperature dependence of the square root of the second moment for different applied fields, normalised to the normal state width. Inset: Fit of the 6kOe data using a London model with a GL temperature dependence for λ. Note: no account has been taken of the thermal fluctuations of the vortices in the fits.

not account for the low temperature lineshape widths. It is easy to see, however, that a GL description of the temperature dependence of the penetration depth is a better qualitative description of the measured width compared to a simple two fluid model.

In the inset of Figure 5.27, a fit to the width of the largest field (where pinning is at a minimum), is shown to be in good agreement with the data at low temperatures, until the FLL finally begins to melt at around a temperature of 20K. Parameters used here are $\gamma = 15 \pm 2$ and $\lambda = 2400 \pm 50$Å.

There are several possible explanations for the field dependence of the lineshape width at low temperatures, one of which has already been discussed in the section above. Firstly, there is a hexagonal - square FLL symmetry change in this region of the magnetic phase diagram. In a square lattice, it is expected that the width will be larger than in a hexagonal lattice because the inter-vortex separation is larger for a square geometry, so is opposite to what is observed in Figure 5.27. Consequently,

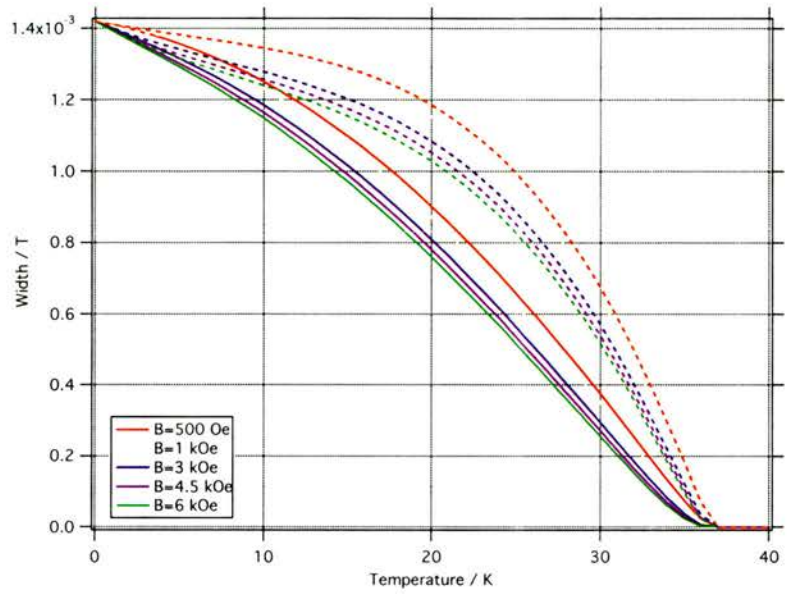

Figure 5.28: Temperature dependence of the square root of the second moment for different applied fields. Solid line: GL temperature dependence of λ. Dashed line: Two fluid temperature dependence of λ.

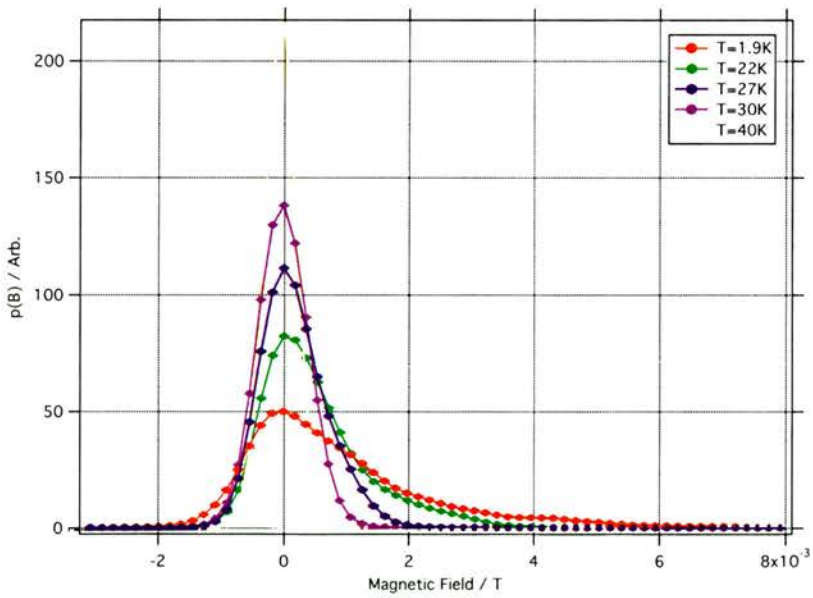

Figure 5.29: Temperature dependence of the lineshapes for 6kOe showing the high field cut off as the temperature increases.

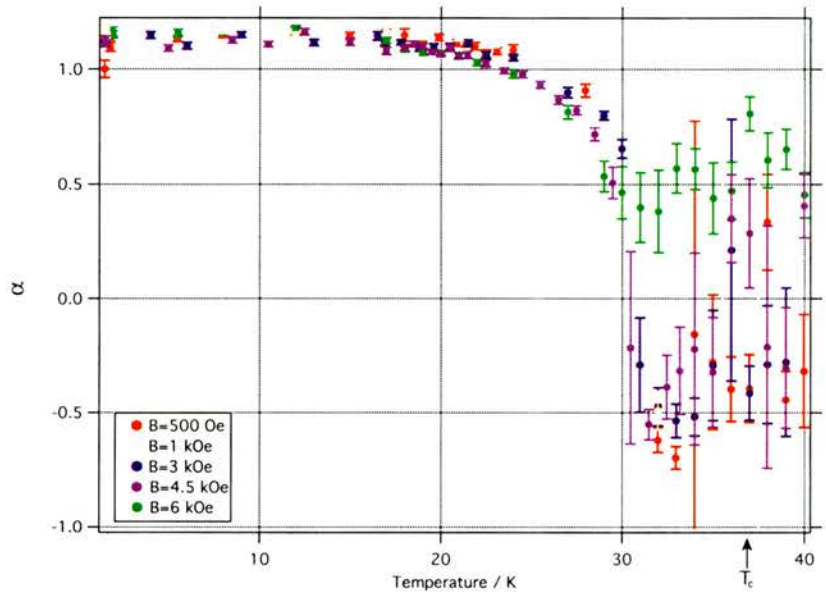

Figure 5.30: Temperature dependence of α, defined in Equation 3.72, for different applied fields.

any small change in width due to this transition is completely masked by other phenomena.

Another possible explanation of the field dependent lineshape width was first suggested by Sonier [Sonier *et al.*, 1999]. The field dependence of the width was observed in YBCO, at applied fields of up to 6T. The measurement shows similarities to what is observed in Figure 5.27, albeit at much higher fields. The YBCO experiment was analysed by applying an analytical GL model [Yaouanc *et al.*, 1997] and directly fitting the muon precession signal. From this analysis, a 25% reduction in λ is claimed on going from 0.5T to 6T, which was explained by the non local effect of the supercurrent in the vicinity of the gap nodes [Amin *et al.*, 1998]. However, they failed to take into account thermal fluctuations and static disorder from pinning. Another consideration is the FLL symmetry transition recently measured at these fields [Brown *et al.*, 2004], which will have a considerable effect on the pinning regime and intrinsic flux distribution inside the sample.

A narrowing of the lineshapes could also arise in a quasi-two dimensional pancake-vortex system, from static or dynamical transverse fluctuations [Aegerter and Lee, 1997]. However this would be extremely unlikely in this system considering the effectiveness of the Josephson currents tunneling between planes, which maintain the stiffness of the vortex. Furthermore, results presented later on the x=0.10 sample

confirm the existence of a 3D vortex glass, which is incompatible with 2D fluctuations. Considering the x=0.10 sample has γ in the region of 40, compared to around 15-20 for this doping, it is considered unlikely this is the reason for the reduction in width observed.

A change in FLL pinning could show a similar behaviour to that observed here, as an increase in the static disorder would be expected from a reduction of elastic interactions between vortices as the vortices become dilute. A reduction in static disorder will result in a decrease in lineshape width and is considered to be the most likely account for what is observed, as has already been discussed when simulating the lineshapes directly. As the field is increased, point-like defects have a decreasing effect on the positions of the vortices, as elastic inter-vortex interactions become stronger. It is only at fields above several hundred Gauss that the vortex separation becomes less than the penetration depth, whereby the shear modulus for the lattice increases significantly [Blatter *et al.*, 1994]. This is the explanation favoured, as has been demonstrated by the simulations of the lineshapes above.

Now FLL melting will be considered. In the inset of Figure 5.27, at around 20K the width deviates from what is expected for 3D fluctuations. This is the temperature at which the FLL begins the phase transition into a liquid state. At just above 30K it is clear the width reduces to the normal state width, several degrees Kelvin below the sample critical temperature, 37K. At this point the FLL is completely melted into a liquid state. Figure 5.29 shows the lineshapes for selected temperatures, at an applied field of 6kOe. The high field cut off due to thermal fluctuations is evident in the data. This thermodynamic transition is also evident in Figure 5.30, which represents the skewness of the lineshape. At low fields, the lineshape is skewed to the right (high field tail) and α should be positive. As thermal fluctuations begin to take effect, the core is smeared on the timescale of the measurement, leading to the skewness reducing until finally the lineshape is almost symmetrical. Alpha should reduce significantly to a "base level" with very large error bars, which is indeed observed. The point at which alpha reduces to this base level is defined to be the temperature at which the FLL is completely melted into a liquid state.

Combining the magnetisation, SANS and μSR measurements, a vortex phase diagram can be produced, as shown in Figure 5.31. The hexagonal to square transition and melting line are shown and interestingly the peak in χ'' is in the same vicinity as the melting transition, although it seems the peak in χ'' occurs at a slightly higher temperature. It is unclear as to whether this peak is due to the melting, or

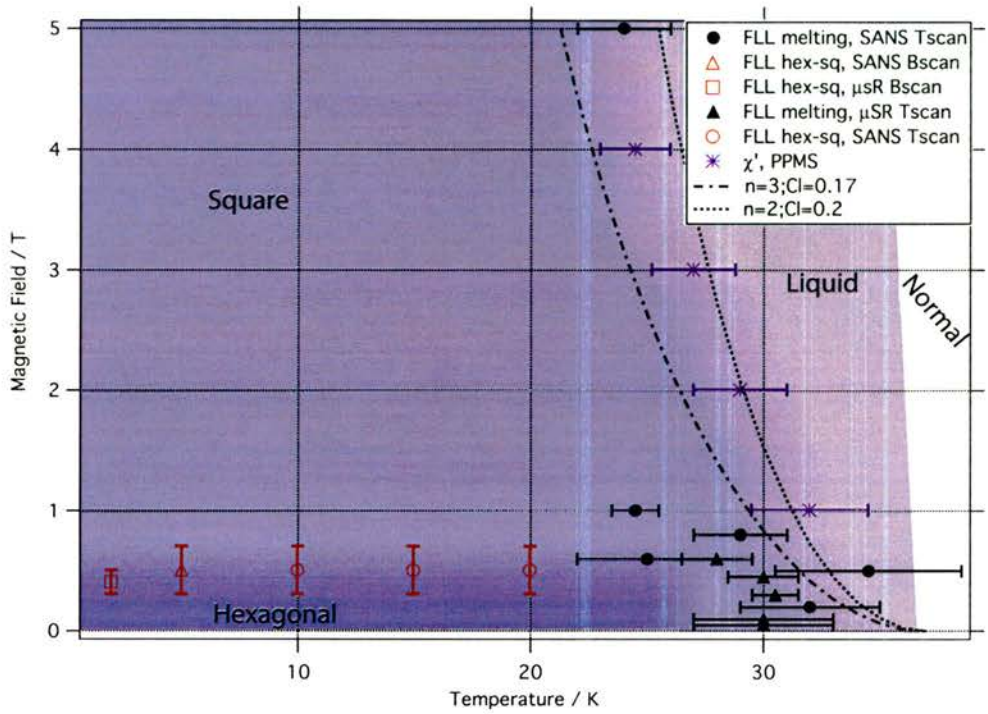

Figure 5.31: Magnetic phase diagram of LSCO x=0.17, obtained from combining results from magnetisation, μSR and SANS experiments.

a change in pinning regime [Blatter *et al.*, 1994]. The magnetisation data reflects the underlying disorder transition, but measures very different properties under different conditions to μSR. The muons measure the field probability distribution in a field-cooled state and the neutrons Bragg diffract from the ordered field cooled state. The magnetisation measurements determine the macroscopic properties of a disturbed system possessing strong macroscopic flux gradients and reflect the changing dynamic response to pinning. However, the closeness of the peak in χ'' to the melting line measure by μSR and SANS suggests strongly these two phenomena are related.

Also, the question regarding what a melting transition actually "is", is considered in the literature [for a full review, see Blatter *et al.*, 1994]. For example, there is debate regarding whether one can describe the FLL to be melted when it is still irreversible; the vortices can not be interacting as a "liquid" when their motion is still governed by pinning potential. More likely, the state observed here (between T_m and the peak in χ'') is better described as a glass, but no firm consensus is present in the literature. This, however, is somewhat irrelevant to this work, as the general trends are primarily reported here and not the intricate details of vortex

lattice dynamics.

The temperature dependence of the melting line for 3D vortex lines is predicted to be [Blatter *et al.*, 1994]

$$B_m^{3D} \approx \frac{1}{(4[\sqrt{2}-1]^2+1)^2\pi\mu_0^2}\left(\frac{\Phi_0^5 c_L^4}{(k_B T_C)^2\lambda_{ab}^4(0)\gamma^2}\right)\left(\frac{1-t^n}{t}\right)^2 \tag{5.16}$$

where $t = T/T_C$, $n = 4$ for the two fluid model and the Lindemann number $c_L \approx 0.1$ [Blatter *et al.*, 1994]. However, it does not describe the data well, although the correct general trends are shown. Figure 5.31 shows B_m^{3D} for $n = 3$ with $c_L = 0.17$ and $n = 2$ with $c_L = 0.2$, which are in reasonable agreement with the data. A possible explanation for this discrepancy, is that c_L could be doping dependent [Blatter *et al.*, 1994].

5.5 μSR Measurements on $La_{1.9}Sr_{0.10}CuO_4$

5.5.1 Experimental Detail

All measurements reported in this section were performed on $La_{1.9}Sr_{0.10}CuO_4$using the GPS spectrometer at PSI. The sample environment was the Quantum continuous flow cryostat, with a base temperature of 1.7K. The sample was mounted with the c-axis perpendicular to the applied magnetic field and was aligned by eye to within 5 degrees of the crystal orientations measured by Laue x-ray diffraction. The sample holder was a standard copper holder to ensure good thermal conductivity between the sample environment and thermometers. The holder was encased in polycrystalline haematite (Fe_2O_3) and the sample was mounted on top. This ensured any stray muons not hitting the sample would not add a background frequency, as the haematite used is an antiferromagnet with an internal magnetic field of 1.6T in a random orientation. Typical statistics are 15 million muon detection events over three detectors. The three detectors used were: Left, Right and Top. The time binning was 625ps with a maximum count time of around 10μs.

5.5.2 Data Analysis

The data was analysed using the Maximum Entropy Technique. Sigma Looseness was 1.02 to account systematic errors in the data which are not reflected in the statistics. The apodisation of errors was set to 6μs. The data was not binned other than that from the intrinsic binning of the instrument and the full time measured range was used. The number of points in the Fourier spectrum was 2^{16}.

5.5.3 Low Field Measurements

Figure 5.32 shows P(B) for low applied fields at a temperature of 5K and is the shape expected from a conventional vortex lattice or Bragg glass. As the magnetic field is increased, it is evident the distribution becomes curtailed at the high field tail. This reduction in width can also be observed in the second moment as both the temperature and magnetic field are increased, which is shown in Figure 5.33. The lineshape asymmetry also decreases as the field and temperature is increased. This is consistent with the x=0.17, where it is explained more thoroughly. A preliminary SANS experiment has also been performed on this system, but has proved thus far to be a challenging experiment due to the long $\lambda_{ab} \approx 3000$Å and short range disorder

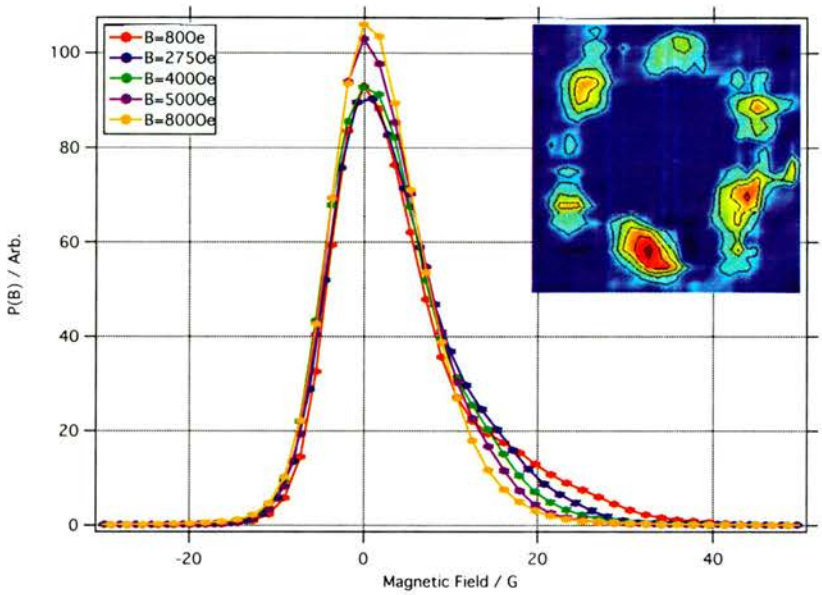

Figure 5.32: P(B)'s for different applied fields, field cooled to 5K. Inset: A preliminary SANS experiment on this system proved difficult, but shows what seems to be a FLL with a hexagonal symmetry.

at higher fields. It is clear from the inset of Figure 5.32 the vortex lattice possesses an hexagonal symmetry at B=150Oe.

The temperature dependence of the lineshapes has already been discussed for the x=0.17 case. Such narrowing can be modelled in the same manner as explained on page 75 and even though there is an increased gamma compared to the x=0.17 sample, 3D fluctuations are still more relevant than 2D fluctuations in this system.

At a given temperature the width decreases as the field is increased, mainly due to an increase in the ratio $\langle u^2 \rangle^{1/2}/d$. The 3D fluctuations have been calculated in the same way as the x=0.17 sample, by a Fourier series (detailed in section 5.4.3), but the data is simply represented in a different manner. In these simulations, $\lambda_{ab} = 2900$Å, γ=40 and $\lambda(T)$ is given by the GL equations.

While the observed changes of the lineshapes show that this reduction in width must at least partly be due to dynamical effects, the simulations in Figure 5.34 indicate that the magnitude of this narrowing cannot be entirely attributed to this. The broadening towards lower fields must also include a contribution from an increase in the static disorder due to the reduction of elastic interactions between vortices in the dilute vortex state, as already discussed with x=0.17.

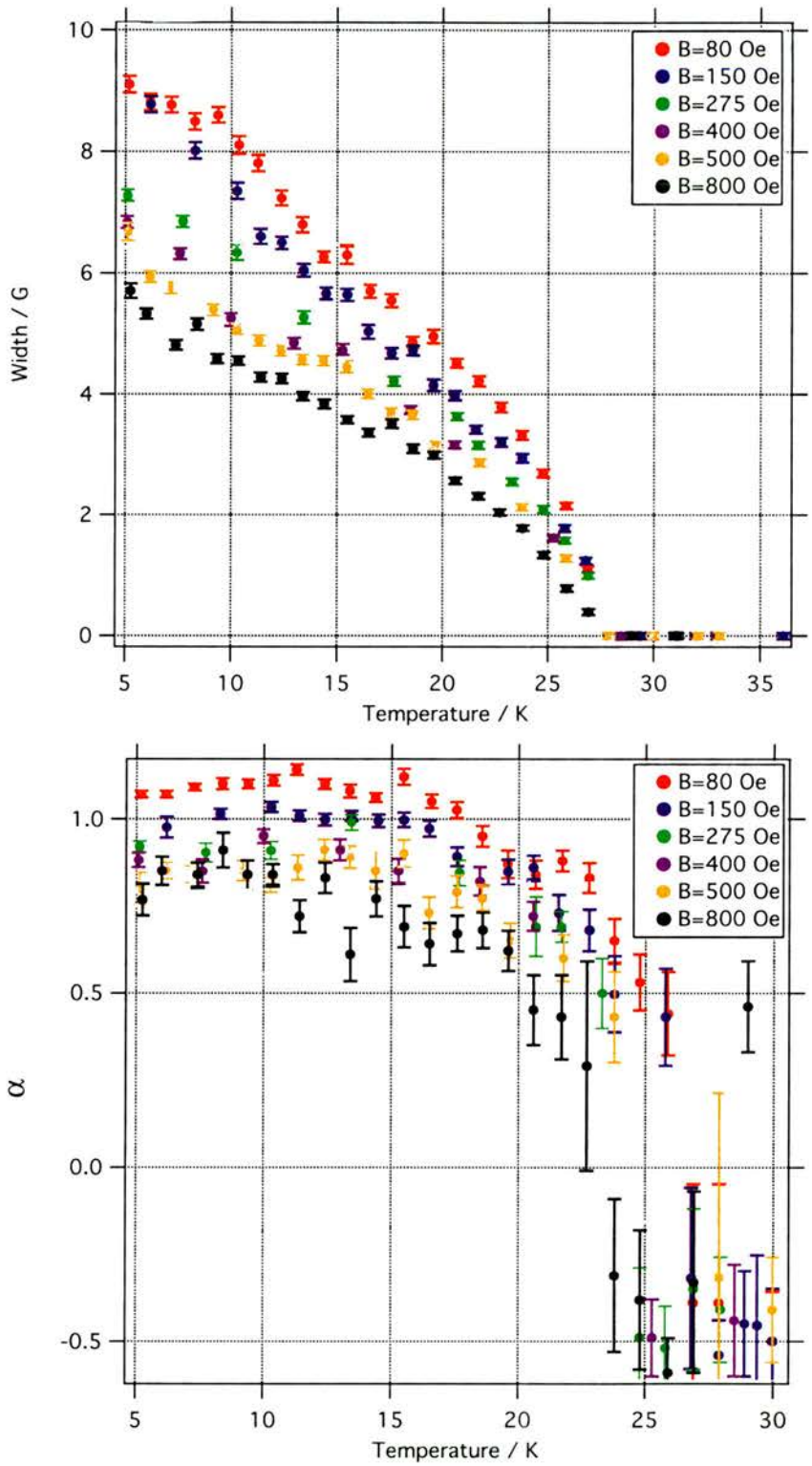

Figure 5.33: Top: Temperature dependence of the square root of the second moment of the lineshapes shown in Figure 5.32. Bottom: α for the same lineshapes.

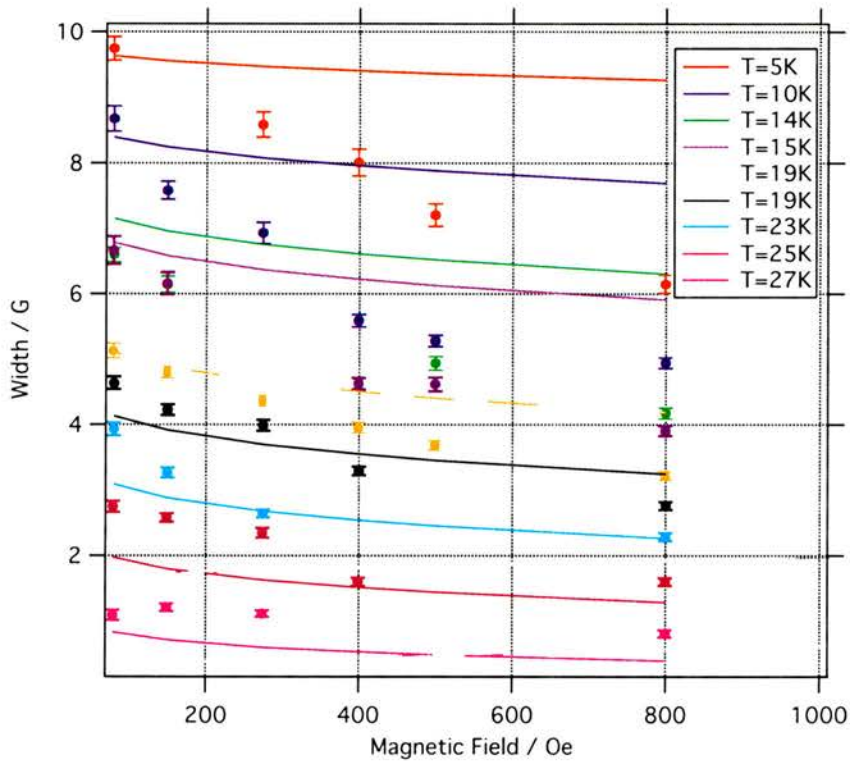

Figure 5.34: Square root of the second moment of the lineshapes shown in Figure 5.32. The lines are as expected from 3D thermal fluctuations, calculated using the Fourier method described on page 134 with parameters consistent with those expected in this system (see text).

5.5.4 High Field Measurements

Quenched random pinning of vortices destabilises the long ranged translational order, leading to a disordered phase [Blatter *et al.*, 1994]. At least two glassy phases exist as a consequence of such disorder [Fisher *et al.*, 1991; Nattermann, 1990; Giamarchi and Doussal, 1995, 1997]. The most ordered of these phases is the Bragg glass phase, where translational correlations decay as power laws [Nattermann, 1990; Giamarchi and Doussal, 1995, 1997], leading to quasi-long range order of vortices in the superconductor. Measurements presented in the previous section support the existence of a Bragg glass phase in HT_c's at low applied fields.

At increased levels of pinning, the Bragg glass is unstable and a vortex glass (VG) phase is formed, where the translational correlations decay exponentially [Giamarchi and Doussal, 1997; Gingras and Huse, 1996]. The VG phase has been reported to be a distinct thermodynamic phase [Fisher *et al.*, 1991], separated from the disordered liquid phase by a continuous phase transition [Giller *et al.*, 1997; Misat *et al.*, 1999], also known as a crossover. The main result of the high field data can be appreciated immediately by comparing the lineshapes of Figure 5.35, measured at 80Oe and 6kOe respectively at T=5K. While the 80Oe distribution has the characteristics of an ideal vortex lattice described previously, the 6kOe signal is highly symmetrical, indicating a strong departure from the ordered vortex lattice or BG state. This has been interpreted as a BG to VG crossover

Conclusive evidence for the transition from a BG to a VG phase, independent of any particular model, comes from considerations of the width of the lineshapes. This is plotted in Figure 5.36 as a function of applied field, for several temperatures. At low temperatures, the signal measured at 6kOe is considerably broader than that at 80Oe. Such a broadening of the signal from the vortex lattice can only arise from *static disorder* in the positions of vortex lines within a plane perpendicular to the field [Menon, 2002]. This is because local vortex density variations, due to positional disorder of the vortices, give rise to regions with field values both higher and lower than in the well ordered lattice. In a system composed of two-dimensional pancakes, transverse fluctuations having short wavelength along the field direction would always lead to a narrowing of P(B). This is indeed the situation found experimentally in the very anisotropic BSCCO [Aegerter and Lee, 1997]. Thus it is clear that in this case a highly disordered vortex line arrangement exists, which is identified as the vortex glass phase. The reduction in width with increasing field (up to $\approx$1kOe) has been discussed previously, but the minimum of the width can be treated as the upper limit for the BG - VG transition.

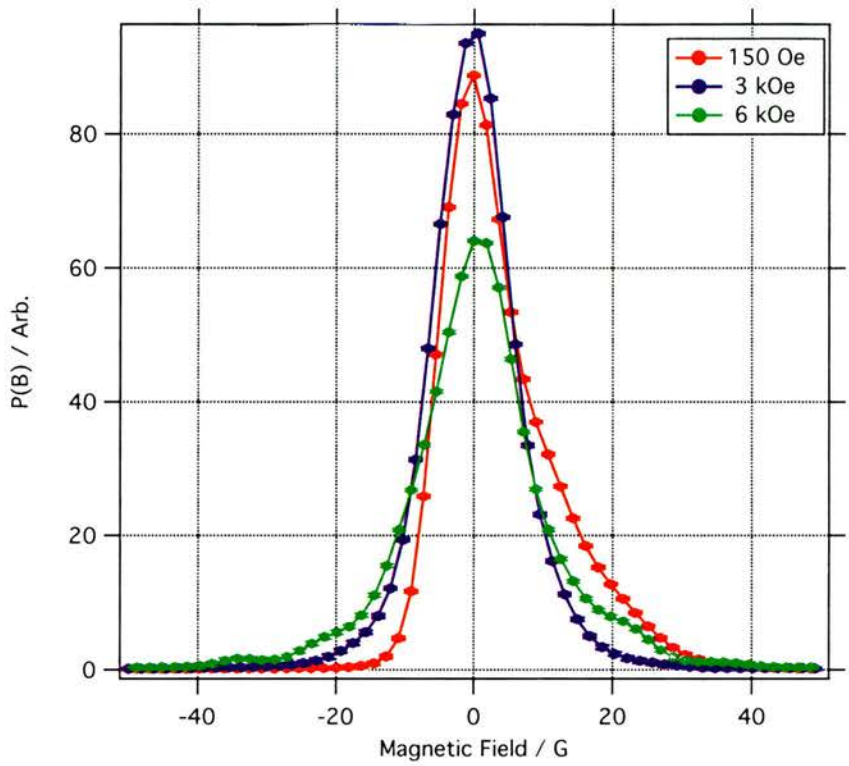

Figure 5.35: Lineshapes of B=150Oe, 3kOe and 6kOe showing the Bragg glass to vortex glass transition.

Monte Carlo simulations of a disordered vortex system, having short-ranged translational correlations of order a few inter vortex spacings [Menon, 2004], agree well with the measured lineshapes. In these simulations, the loss of long range order is due to a transition from a Bragg glass phase to a multi-domain glass, comprising of a size distribution of domains within which the vortices are locally ordered [Menon, 2002]. As the strength of pinning is increased compared to the inter-vortex interactions, the crystal of vortices breaks up into small domains, with a size of between 1-40 inter-vortex spacings. Therefore, increasing the field leads to a rapid fall in the average domain size just above the Bragg glass phase. Figure 5.37 contains the P(B) derived from Monte Carlo simulations [Menon, 2004] of a perfect triangular Abrikosov lattice and also for a vortex glass structure having short range translational correlations, of the order of ten and two inter-vortex spacings [Menon, 2002]. The disordered state was calculated by annealing 6400 rigid vortices interacting through a power law central force potential and 3700 random quenched pinning sites and the simulations were both written and performed by G. I. Menon. The effects of instrument resolution and nuclear dipolar broadening are not included.

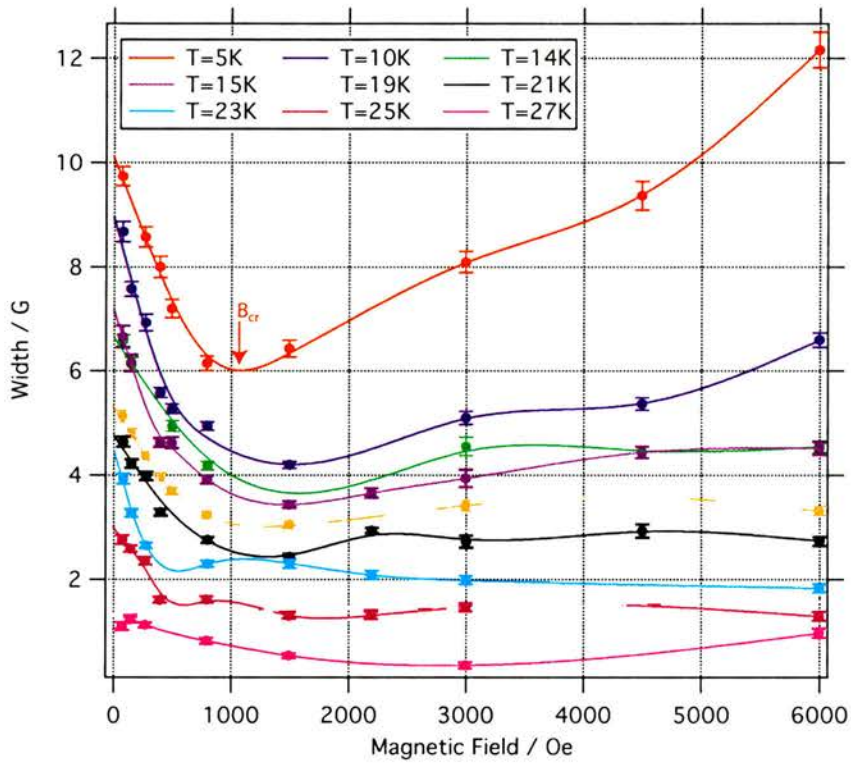

Figure 5.36: Square root of the second moment of the lineshapes, some of which are shown in Figure 5.35. As the applied field is increased, the increase in the width of the distribution is clear. The line is a cubic spline through the points and is meant as a guide to the eye only. B_{cr} is defined to be the minimum of the width and is indicative of the crossover between a VG and BG. Note that the spline is just a guide to the eye and can result in an incorrect judgement of B_{cr}.

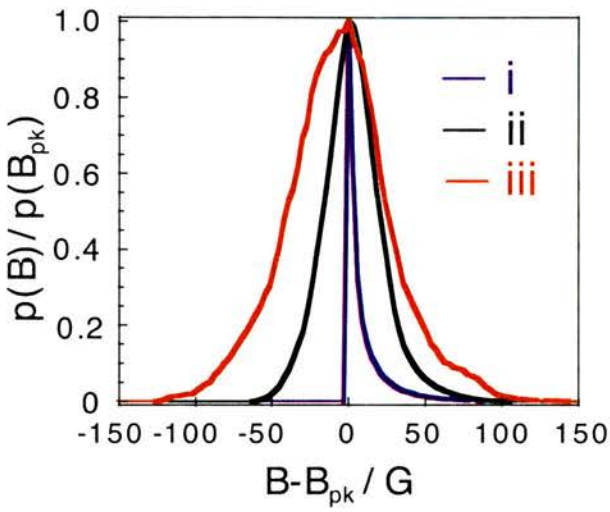

Figure 5.37: Field distribution from Monte Carlo simulations of the vortex state at 6kG, for i) an ideal vortex lattice; ii) a VG phase with a transverse correlation length of about eight lattice spacings; iii) a VG phase with correlations extending to only one or two nearest neighbours [Menon, 2002].

It is clear the shape of these distributions are reflected well in the experimental data, offering more conclusive proof a VG phase is present in this system.

The disordered VG state offers a unique opportunity to measure correlation functions in a bulk system. Explicit knowledge of three body correlation functions are required in perturbation theories for static fluids [Stell *et al.*, 1974; Madden *et al.*, 1978; Gray *et al.*, 1978], for theories of transport properties for solvent reorganisation processed around solutes [Scherwinski, 1990; Lazaridis, 2000] and in order to understand the structural properties of 2D amorphous systems [Wang *et al.*, 2002; Dhont and Nagele, 1998]. The majority of information regarding correlation functions are from numerical work on hard sphere fluids [Muller and Gubbins, 1993] and Lenard-Jones fluids [Rahman, 1964; Gupta *et al.*, 1982; Mcneil *et al.*, 1983], but experimental measurements on *bulk* three body correlation functions have remained elusive.

Indeed, two body correlations can be accessed directly and indirectly by a number of experiments (see, for example [Jiang *et al.*, 2004; Peter *et al.*, 1994; Zondervan *et al.*, 1995; Kadija, 1996]), but have proved elusive to higher dimensions for bulk measurements. Recently, 3 particle correlation functions have been measured in colloidal systems [Zahn *et al.*, 2003], where an ensemble of colloidal particles with quasi-two dimensional order on a thin film was directly imaged. However, this is still not in the bulk. The vortex glass measured here is the first bulk measurement,

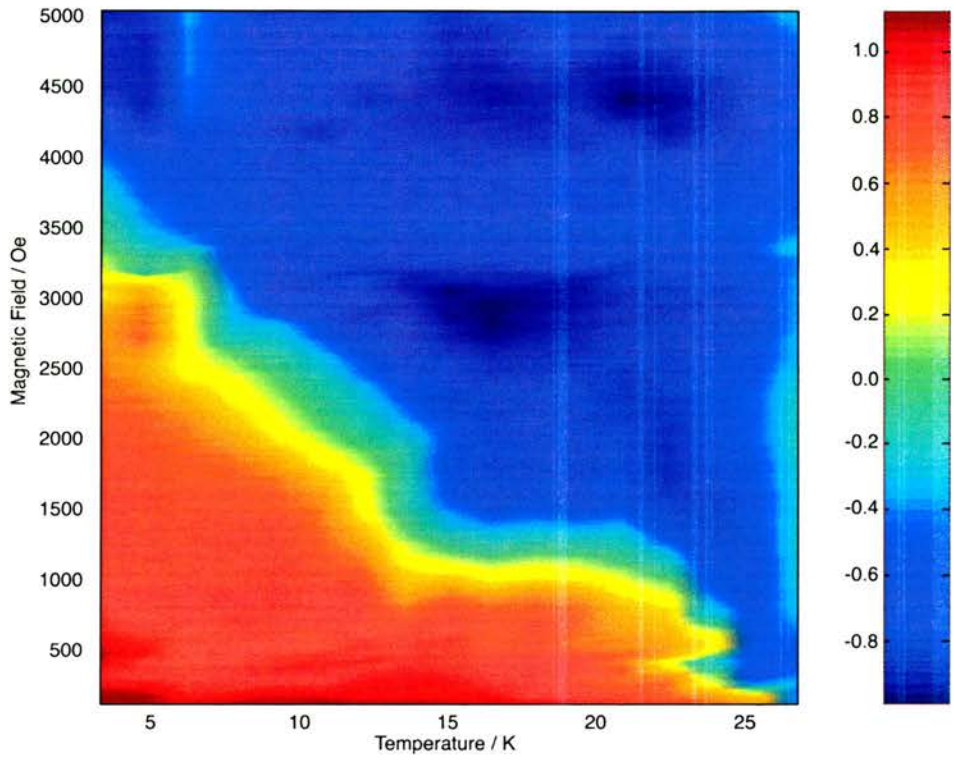

Figure 5.38: Alpha image plot as a function of applied field and temperature.

albeit indirectly, of 3 particle correlations in a bulk disordered state. The third moment of the magnetic field distribution can be directly related to an integral over a three particle structure factor [Menon, 2004], yielding information regarding pair and triplet correlations in disordered vortex structures. The third moment is defined

$$\left\langle [\Delta B]^3 \right\rangle = \frac{B}{16\phi_0\pi^4} \int\int S^{(3)}(\boldsymbol{k}_1, \boldsymbol{k}_2) b(\boldsymbol{k}_1) b(\boldsymbol{k}_1) b(-\boldsymbol{k}_1 - \boldsymbol{k}_2) d\boldsymbol{k}_1 d\boldsymbol{k}_2 \tag{5.17}$$

where $S^{(3)}(\boldsymbol{k}_1, \boldsymbol{k}_2)$ is the triplet structure factor [Hansen and Macdonald, 1986] and $b(\boldsymbol{k})$ is the field due to a single vortex and for in the London model assumes $b(\boldsymbol{k}) = B/(1 + \lambda^2\boldsymbol{k}^2)$. The second moment is related to the two particle structure factor

$$\left\langle [\Delta B]^2 \right\rangle = \frac{B}{4\phi_0\pi^2} \int S(\boldsymbol{k}) b(\boldsymbol{k}) d\boldsymbol{k}. \tag{5.18}$$

Figure 5.38 shows the lineshape anisotropy factor, α, as a function of magnetic field and temperature. The data has been interpolated with a standard 2D cubic spline in Matlab to fill in the missing data. Firstly, it is evident that at low temperatures and fields the value of α, is approximately 1, corresponding to a Bragg glass [Menon, 2004]. As the field is increased to relatively low fields, alpha begins to

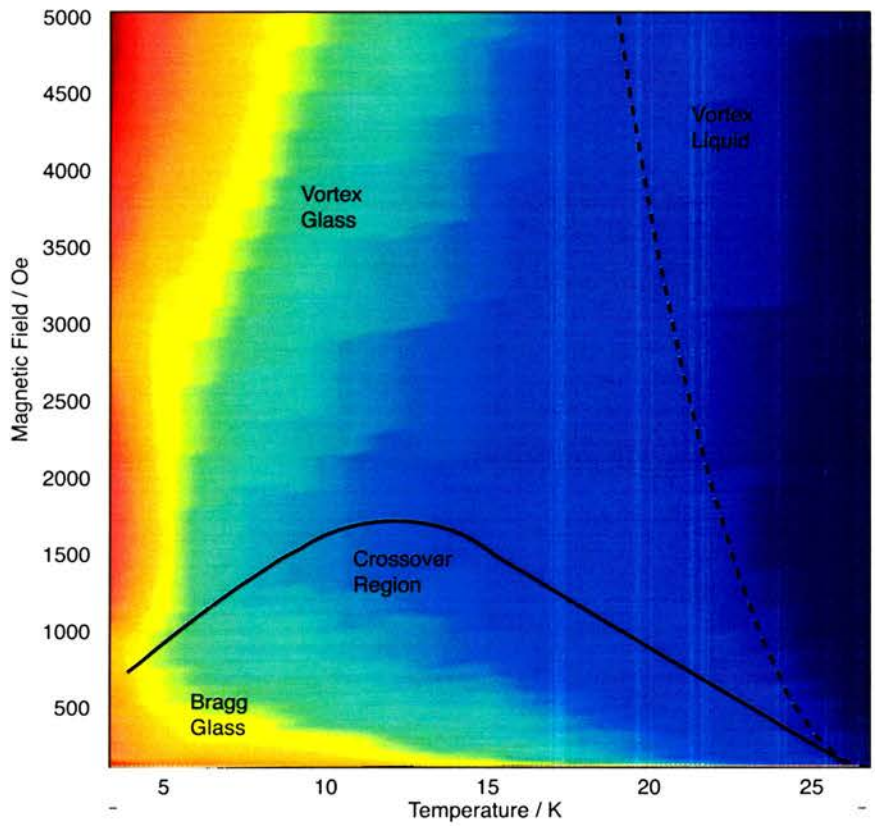

Figure 5.39: Width image plot as a function of temperature and applied field. The dashed line is the theoretical melting line using the Lindemann criterion and although only tentative, it follows the general trends of the data and acts as a guide to the eye. The crossover from a Bragg glass phase to vortex glass phase is discussed in more detail later in this chapter.

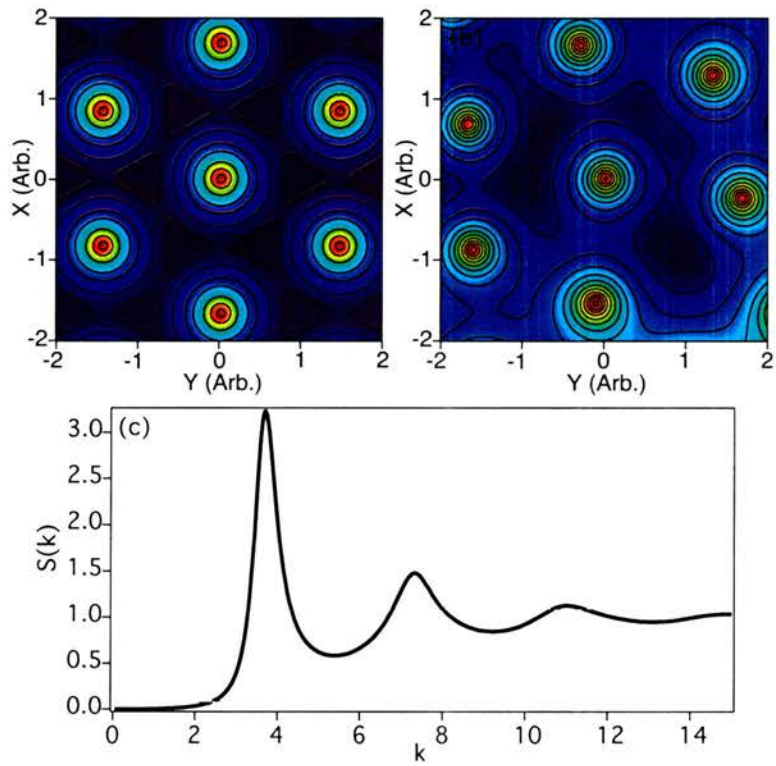

Figure 5.40: a) Contour plot of a perfect lattice for an applied field of 6kG. b) Contour plot for a disordered state with a translational correlation length of about 4 intervortex spacings. Note it lacks the precise six-fold symmetry in a), while the local coordination is still approximately six-fold, indicating the preference for the formation of triangles locally and thus the existence of local three-body correlations in the disordered state. Supplied by G. I. Menon. c) Structure factor of the plot shown in b).

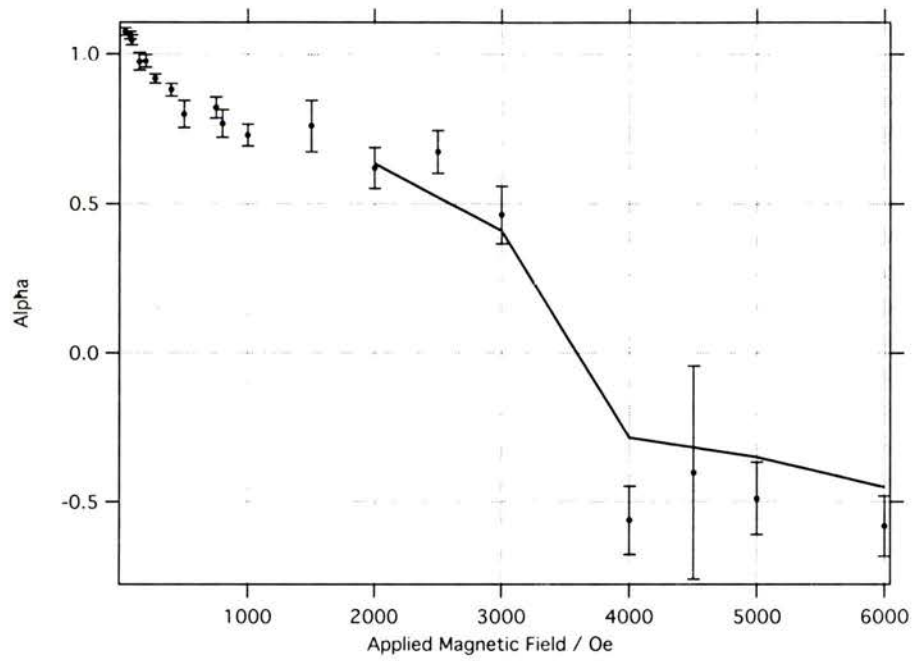

Figure 5.41: The normalised asymmetry, alpha, as obtained from experiments (points) compared with the Monte Carlo simulations (supplied by G. I. Menon) of disordered structures (line) with correlations of about 2-3 inter-particle spacings [Menon, 2004].

decrease and goes through a sign change at ~4500Oe (at 5K) to an approximately constant negative value. A negative skewness is also seen in μSR in liquid regimes [Harshman *et al.*, 1991; Blasius *et al.*, 1999] where the FLL has melted (as observed with x=0.17 above). However, as discussed above, an increase in lineshape width (Figure 5.39) is not compatible with what one would expect from a vortex liquid.

The London model, which yields the field distribution due to a single vortex, results in a vortex which diverges at the core. This unphysical divergence can be taken into account by a number of methods already discussed, but the result will always yield positive value of the third moment. Whilst core cut-off factors will reduce the value of the third moment, it will never change the sign. By allowing thermal fluctuations, the rigid lattice model used can be relaxed by adding a Dbye Waller factor $\exp^{-\langle u^2 \rangle G^2}$. The third moment once again would reduce in scale and eventually reach zero, but it would not change sign. Thus, the only factor to relax is the rigidity of the structure.

One possibility is to assume non-interacting vortex lines, resulting in a completely structureless liquid with no translational or orientational correlations, but the skewness always remains positive. Even with some level of local translational

order, the third moment can never be negative. The only model for the vortex positions that will yield both the correct scale and sign of the third moment is a vortex glass, consistent with a "frozen liquid" with short range translational and orientational correlations, extending to distances of a few inter-particle spacings [Menon, 2002].

The Monte Carlo simulations shown in Figure 5.37 reflect such a system, from which α can be calculated and compared to the experimental values, as shown in Figure 5.41. A contour plot of magnetic flux for a perfect lattice and a disordered state with translational correlations of around 4 inter-vortex spacings are shown in Figure 5.40. The corresponding structure factor is also included. Note the short range order still remains hexagonal, but over larger distances the order is lost. The calculation of α, resulting from Monte Carlo simulations of vortex arrangement with some short ranged triplet correlations (which can be seen in the approximate hexagonal arrangement of vortices in Figure 5.40), represents the data exceptionally well, providing proof of the first indirect measurement of triplet correlations in a disordered bulk system. It remains a challenge for the theoretical community to develop *analytical* constructs for triplet structure factor and compare them to this measurement, improving upon the *numerical* "proof-of-concept" comparison presented here.

5.5.5 Magnetic Phase Diagram

In order to compile the magnetic phase diagram shown in Figure 5.42, it is informative to plot the width of the field distribution and α in an image plot with magnetisation data overlaid. Firstly, T_{ir} is obtained from the different between FC and ZFC magnetisation data. This is the temperature at which the vortices overcome pinning barriers and are free to move elastically in a liquid like state. A related phenomenon, the melting line, is also plotted. FLL melting is when the vortices become freer to move due to thermal excitations, thus reducing the effect of pinning, but the vortices are still subject to dissipative interactions with pinning sites. This is estimated at low fields ($\leq$1000Oe) from the μSR data to be the point at which the lineshapes obtain a constant negative skewness. At higher fields, it can be correlated with the point at which the width falls to a constant value. From the width colour plot in Figure 5.42, it is possible to observe the melting line directly to be the point at which the colour changes from a light blue/turquoise colour to a dark blue. It is also clear that this estimate is consistent with α at low fields. B_{cr} is the minimum of the width at different applied fields, defined in Figure 5.36. The

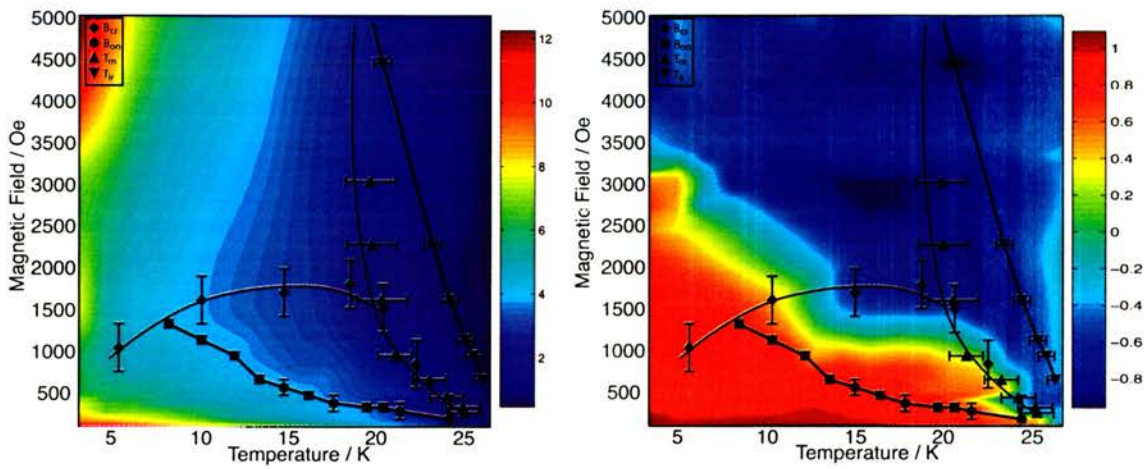

Figure 5.42: Magnetic phase diagram of LSCO x=0.1 obtained from μSR and magnetisation measurements. A plot of α on the left (Figure 5.38) and the width on the right (Figure 5.39). The lines are guides to the eye, to emphasise the general trends found in the data.

exact value of B_{cr} is only approximate, as it is difficult to define the minima well (especially at temperatures approaching 25K), but it is included as it corresponds to the glass transition beginning to dominate the linewidth and is therefore an upper limit on the BG-VG transition. It is worth noting that the muon is sensitive only to the local magnetic field, so in general this transition from BG to VG will be a crossover of behaviour which reflects the underlying transition. These results should therefore be viewed as showing the vortex glass phase exists, rather than being directly identified with the BG to VG transition.

The temperature dependence of B_{on} is also plotted, which corresponds to the onset field of the second peak in the magnetic hysteresis measurements. This reflects the change in macroscopic flux gradients inside the sample, most likely due to a change in the pinning regime. It has been associated with the BG-VG transition [Giller *et al.*, 1997], which is why it has been included. Combining different techniques can often lead to inconsistencies, such as the difference between B_{on} and B_{cr}. This is to be expected, as they do not measure the same signal. The muons measure the field probability distribution in a field-cooled state and the signature reflects two competing field-dependent processes. The magnetisation measurements determine the macroscopic properties of a disturbed ZFC system, which possesses strong macroscopic flux gradients. However, the two different techniques can be used complementary to each other in order to obtain a deeper understanding of the system.

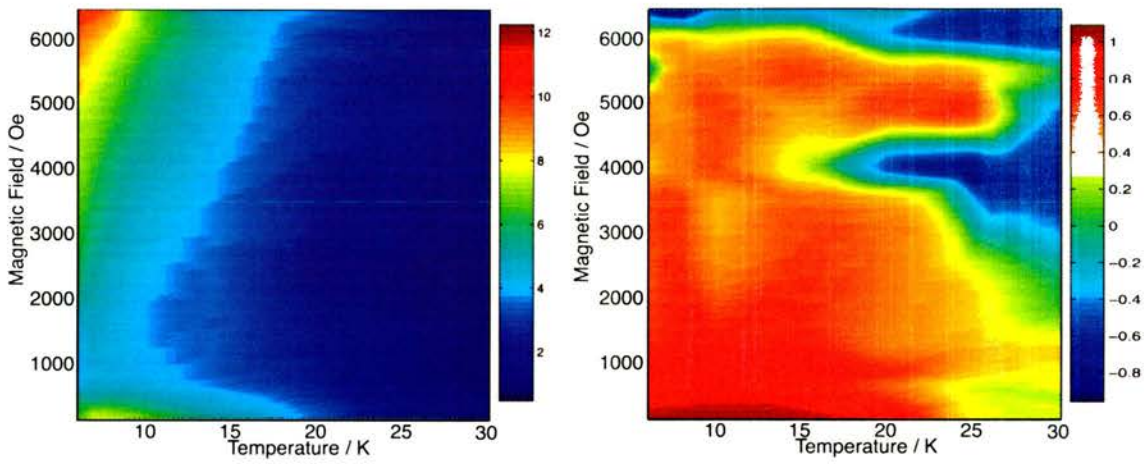

Figure 5.43: Alpha image plot and width as a function of applied field and temperature, for an applied field and muon momentum ~10° from the c-axis. The colour map has been kept the same as in Figure 5.42 to aid comparison.

Figure 5.43 shows α and the width as a function of field and temperature, with the c-axis rotated off the direction of applied field by 10 degrees, which can be directly compared to the plots in Figure 5.42. First, it is evident that the crossover from a BG to VG occurs in a similar position in the phase diagram, as the minimum in the width is almost unchanged between the two sets of data. However, the point at which α goes negative is at a significantly higher field. The point at which α turns negative depends on the initial disorder of the vortices. With the applied field close to the c-axis, it is presumed the low field state (BG state) is more disordered than when at 10° off. This additional disorder when the applied field is close to the c-axis *may* be because the correlated pinning sites are more effective. In the case of LSCO, extended defects throughout the sample corresponding to the boundaries along the twin planes are significant pinning centers. So by rotating off by approximately 10 degrees, the effectiveness of the twin planes to pin the vortices would have been reduced.

A rather strange feature is the "renetrant" behaviour of α observed at around 5000Oe at high temperatures, where a negative α at 4000Oe becomes positive as the field is increased, only to go negative at all temperatures at applied fields greater than 6000Oe. At this point an explanation for this is not possible.

5.6 Concluding Remarks

The work presented in this chapter represents the first systematic study of vortices on large, high quality LSCO single crystals using both microscopic and macroscopic techniques for two Sr dopings.

In the overdoped regime, SANS has been used to measure the first clear microscopic observation of a vortex lattice in LSCO and the first unambiguous evidence for a field induced hexagonal to square vortex lattice structural transition, which remains independent of temperature up to the FLL melting. At high applied fields, the square diffraction spots are found to lie along the CuO bond direction, which is incompatible with current theoretical constructs. The vortex lattice measurements are supported by μSR measurements, which also yield information on FLL pinning and provide further information regarding the melting transition. Combined with magnetisation data, it has been possible to draw a magnetic phase diagram for this compound.

In the underdoped regime, a preliminary SANS experiment at low applied magnetic fields suggests a BG with nominally a hexagonal structure, although this experiment proved somewhat difficult. More detailed information on the vortex lattice structure has been gathered with μSR. This is distinguished by the fact that it provides unambiguous evidence for a crossover with increasing field from a BG phase to a more disordered VG state and an upper limit on the cross over field has been estimated. The VG phase has been theoretically predicted in the literature, but not measured with local probes until now; this is the first measurement of a disordered VG state in a system of well coupled vortex lines. Furthermore, a detailed study of the evolution of short range order in the presence of weak pinning is of universal significance, as it provides useful experimental insights into space averaged many particle correlations in bulk systems. Experimental work that precedes the measurements presented here has either been limited to lower order correlation functions or to systems of reduced dimensionality.

Further work could include a detailed SANS investigation of correlation lengths in the underdoped compound, which could provide invaluable information and support the results presented here. Another possible investigation a μSR measurement with the field applied *directly* along the c-axis. This may determine the effectiveness of correlated pinning on the initial FLL disorder, thereby providing a means of measuring the different correlation lengths as a function of initial FLL disorder.

Chapter 6

Superconducting/Ferromagnetic Thin Film Heterostructures

6.1 Overview

The competition between superconducting and magnetic order has been a long-standing problem and an issue of interest in condensed matter physics. Magnetic impurities tend to polarise the conduction electrons via the exchange interaction. Superconductivity, on the other hand, generally forms spin singlet states. These two phenomena are usually mutually exclusive, coexisting in only a small number of materials. In a system where coexistence occurs among the same conduction electrons, an exotic form of superconducting order may exist such as a "spin triple" state, which may be compatible with ferromagnetic order. The magnetic excitations may also play a key role in binding the Cooper pairs, analogous to the role of phonons in conventional superconductors.

Conventional superconducting systems involve the formation of pairs of electrons in which the spins are oppositely aligned to form a spin-singlet state, for which the momenta of the electrons are also equal and opposite. A conventional Cooper pair also possesses zero net angular momentum and by analogy with atomic orbitals is described as an s-wave state. The presence of a magnetic impurity in such a system gives rise to an exchange field that will tend to align the spins of the surrounding electrons parallel to it. Since this process competes with the antiparallel alignment of spins constituting the Cooper pairs, the impurity provides a "pair breaking" mechanism which can ultimately destroy the superconducting state.

In order to explain the robustness of superconducting order to the presence of magnetic species, more exotic scenarios have to be invoked. For example, the formation of a "spin triplet" state, in which the paired spins are aligned parallel to one another, would not be susceptible to the pair breaking influence of the exchange field [Maeno *et al.*, 2001]. Due to the constraints imposed on Fermions, such a p-wave pair would possess non-zero angular momentum. This is thought to be the correct description of the superconducting state in Sr_2RuO_4 [Riseman *et al.*, 1998]. By contrast another scenario considers the spin-singlet state to persist, whereby the potential energy associated with the exchange field causes each of the two electrons to have different kinetic energy. The resultant linear momentum of the pair leads to a spatial oscillation of the superconducting wavefunction, which periodically reverses sign [Larkin and Ovchinnikov, 1964; Fulde and Ferrell, 1964]. This Larkin-Ovchinnikov-Fulde-Farrell (LOFF) state is thus an s-wave spin-singlet system but possesses non-zero linear momentum and is therefore distinct from either a p-wave or a conventional s-wave superconductor.

Conventional μSR has played a pivotal role in investigating systems in which magnetism and superconductivity coexist [Amato, 1997], but is unsuitable for thin film investigations where typical film thickness is of the order of a few hundred nm, as the typical conventional muon stopping depth is on the mm scale. The recently developed Low Energy Muon technique [Morenzoni *et al.*, 2001] addresses this problem by providing a tuneable muon implantation depth, ranging from a fraction of a nm to hundreds of nm. This technique is ideal for the study of the competing order parameters in superconducting/ferromagnetic (S/FM) multilayers, particularly in light of the recent application to measuring the depth profile of the superconducting penetration depth in high temperature superconductors [Jackson *et al.*, 2000] and the measurement of a SDW in a Fe/Ag/Fe thin film [Luetkens *et al.*, 2003].

For a normal metal/FM multilayer, the exchange field can cause a periodic oscillation of the electron-spin density inside the normal layer. The period of the oscillation is determined by extremal spanning vectors of the Fermi surface, via an enhancement of the wavevector-dependent susceptibility at these values [Martin, 1967], similar to the RKKY interaction. In the superconducting state such a periodic spin-polarisation would seem incompatible with a uniform amplitude for the superconducting wavefunction, due to the pair breaking effect of the spin polarisation.

Advances in thin film fabrication techniques ([Jin and Ketterson, 1989] and references therein) have renewed research interest in S/FM multilayers and a number of new and sometimes controversial phenomena have been observed. For S/FM multilayers, it is expected that the superconducting transition temperature decreases monotonically with increasing magnetic layer thickness. Not long after non-monotonic behaviour was observed (see for example, [Wong *et al.*, 1986]), the possibility of an oscillating T_c as the magnetic layer thickness increased was shown theoretically [Radovic *et al.*, 1991], where it was found the phase of the superconducting wavefunction exhibits oscillations in the FM layer.

For the case of a magnetic layer bound on both sides by superconducting material, the phase of the order parameter across the two superconducting layers can be different, which was convincingly reported recently [Kontos *et al.*, 2001]. The value of the phase difference depends on the layer thickness compared to the wavelength of the spatial oscillation. For example, with an odd number of half-wavelengths across the layer the phase difference would be π radians. However, the theoretical construct outlined above [Radovic *et al.*, 1991] is only valid in the case of high

transparency of the S/F boundary and for the specific structure of a FM between two superconducting films. Although a number of publications observed the non-monotonic behaviour of T_c in relevant systems [see for example, Strunk *et al.*, 1994; Jiang *et al.*, 1995; Ogrin *et al.*, 2000]), which is predicted by this theory, a number of groups observed similar behaviour in FM/S/FM tri-layers [Muhge *et al.*, 1996, 1997]. This theoretical description is therefore insufficiently general to explain these results.

An alternative theory explains both the trilayer and multilayer phenomena [Khusainov and Proshin, 1997, 2000] with no limitations on boundary transparency. The mechanism is built on a LOFF type mechanism, where the superconducting pairs tunnel into the FM region (the proximity effect) and acquire finite momentum. The superconducting ground state is therefore different from that of a BCS paired state. In this theory, the exchange field is periodically compensated by oscillations in the superconducting pair amplitude, leading to an oscillatory SDW. This oscillatory behaviour leads to a non-monotonic oscillatory dependence of the critical temperature as a function of FM thickness.

The theoretical advances described above have led to considerable experimental interest in S/FM thin films. Unfortunately, in most experimental systems studied, complications due to interface roughness/alloying mean there is not always a sharp S/FM interface, but a continuous change between the superconducting and ferromagnetic properties; the theoretical predictions are only valid for clean S/FM interfaces. Firstly, oscillatory behaviour of T_c was observed in V/Fe multilayers [Wong *et al.*, 1986], but later not observed in the same system [Koorevaar *et al.*, 1994]. The non-monotonic behaviour was reported for Nb/Gd multilayers and Nb/Gs/Nb trilayers [Jiang *et al.*, 1996, 1995], for Fe/Nb/Fe trilayers [Muhge *et al.*, 1996, 1997] and for Nb/Co and V/Co multilayers [Obi *et al.*, 1999]. However, negative results were reported for Nb/Gd/Nb trilayers [Strunk *et al.*, 1994], for Ge/Nb bilayers [Muhge *et al.*, 1998] and for Nb/Fe multilayers [Verbanck *et al.*, 1998]. Therefore it is highly desirable to have a system in which very little alloying occurs. For this reason the Pb/Fe system has been chosen, as there is very little solubility between metals (even in the liquid state!) [Kubaschewski, 1982; Lazar *et al.*, 2000]. This suggests the inter-diffusion at the S/FM boundary is negligible. Indeed, non-monotonic oscillations in T_c as a function of FM thickness are observed in sputtered Fe/Pb/Fe trilayers [Lazar *et al.*, 2000], although a non-ideal growth mechanism can lead to large interface roughness [Garif'yanov *et al.*, 1998]. Thus, care must be taken when growing films.

While the spatial modulation of the superconducting order parameter inside the ferromagnetic layer has been convincingly reported [Ryazanov *et al.*, 2001; Kontos *et al.*, 2001], relatively little (microscopic) attention has been given to any related effects occurring inside the superconducting layer, which is the motivation for this work. This chapter reports the first depth resolved microscopic measurement of magnetic flux density deep inside the superconducting layer of a Fe/Pb/Fe thin film, offering direct evidence for a modified spin density wave which coexists with bulk superconductivity. Moreover, this SDW is shown to accommodate to the presence of superconducting order, indicating an intriguing interaction of the two order parameters. This intimate coupling of the two order parameters has profound implications for theoretical descriptions of this and similar systems and could lead to novel applications in hybrid magnetic-superconducting devices.

6.2 Sample Characterisation

6.2.1 Sample Growth

The samples measured in the work presented here were grown using a DC magnetron sputterer situated in the Department of Physics, University of Leeds and is shown in Figure 6.1. The process of sputtering consists of the ablation of surface atoms on the target, due to energetic particle bombardment. The bombarding particles can be ions, neutral atoms, neutrons, electrons or energetic photons. A target atom will become sputtered if the energy transferred to it has a component normal to the surface which is greater than the surface binding energy. The sputtered atom is then incident on a substrate (or target surroundings!) and binds to form a film. The technique used at Leeds is called the dc planar magnetron sputtering, created by J. S. Chapin [Chapin, 1979]. Magnetron sputtering is a magnetically assisted discharge in which a permanent magnet array is placed underneath the target, creating a magnetic field parallel to the target and perpendicular to the electric field. This results in a closed toroidal trajectory for the electrons holding the glow discharge plasma around the target, which can be observed in Figure 6.1.

Samples were grown on {100} polished Si substrates, which were cleaned prior to growth in acetone followed by isopropanol, for approximately 30 minutes. Samples were masked with either a 22 x 20mm or 4 x 12mm mask, the former being the samples used for neutron and muon experiments and the latter for sample characterisation. The sputter chamber was pumped down overnight to 10^{-7} mbar before a cold finger was cooled with liquid N_2. This brought the vacuum down to approximately 10^{-9} mbar. Growth was carried out under 2.5 mTorr Ar, but occasionally this had to be increased temporarily to 5-10 mTorr in order to achieve a stable plasma. It was reduced back down to 2.5 mTorr before growth commenced. Ar is a Noble gas, so does not chemically react with the target and has a mass sufficiently large to be able to remove atoms from the target, so is an ideal plasma medium. Table 6.1 contains the growth conditions for all the different targets used. The targets, shown in Figure 6.1, were cleaned before growth to maximise the purity of samples. This was achieved by turning the magnetron gun on for a prolonged period of time without a substrate present over the gun.

Substrates were rotated between guns in order to grow layers of different materials, with a mask covering substrates in order to shield them from any stray material coming from the guns. Characterisation, unless otherwise stated, was performed

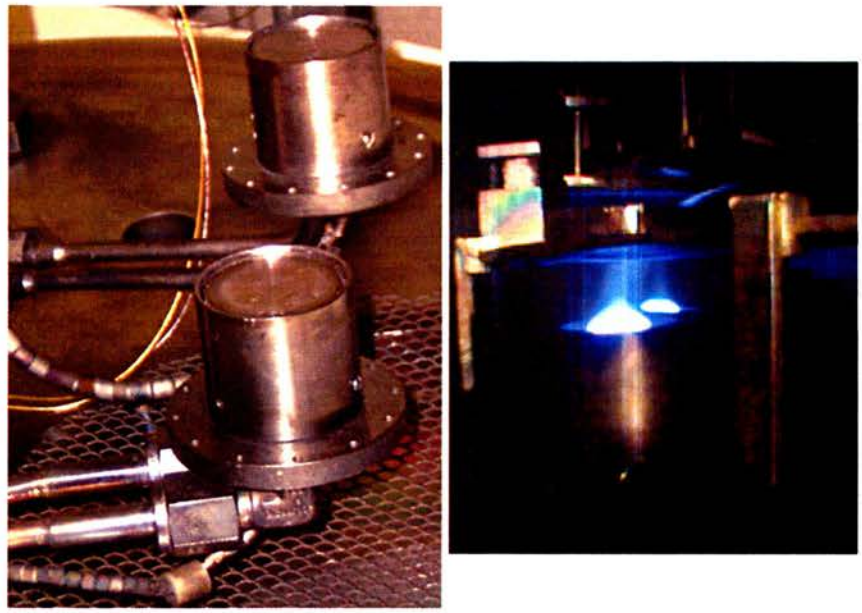

Figure 6.1: Left: Picture of targets in the sputterer. Right: Cleaning the surface of the targets prior to growth.

$Target$	$GunPower/W$	$GunCurrent/mA$	$GrowthRate/\AA s^{-1}$
Pb	7	20	5.9
Fe	37	100	2.9
Mo	20	50	3.0

Table 6.1: Sample growth parameters. Growth rates for these parameters were calibrated with ex-situ X-Ray reflectivity and SPNR.

on the same sample as used in the muon and neutron experiments. Where this is not possible, test samples, grown in the same batch under identical conditions, were used for the characterisation.

6.2.2 Transport and Magnetisation Measurements

Figure 6.2 shows the resistance of an Fe30Å/Pb2300Å/Fe30Å/Mo100Å thin film test sample. Measurements were carried out in St. Andrews with a general purpose AS Orange cryostat. Contacts were made to the thin films using Dupont 6838 silver epoxy and cured at room temperature under a vacuum for approximately 2 weeks. Although 6838 is a high temperature curing epoxy, it was considered to be inadvisable to heat the Pb films due to the possibility of oxidation. It was found that by leaving it under a vacuum for 2 weeks, contact resistances were reliably low and always considerably less than 10Ω at room temperature. Measurements were carried out using a standard 4 probe technique. In order to avoid sample heating,

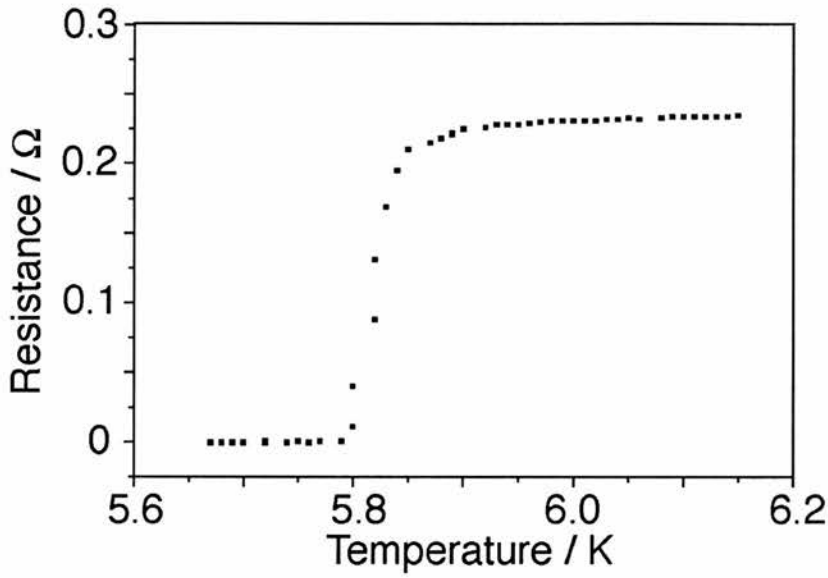

Figure 6.2: Temperature dependence of the resistance of a Fe/Pb/Fe thin film. It is clear T_C=5.8K and the films are good quality.

an AC technique was used and the current was limited to 10μA. It is clear from Figure 6.2 that the superconducting critical temperature is 5.8K with a width of no more than 0.02K, indicating the high quality nature of the film.

Figure 6.4 shows hysteresis loops of another Fe30Å/Pb2300Å/Fe30Å/Mo100Å thin film test sample for above and below T_c. Measurements were carried out in Leeds on an Oxford Instruments Vibrating Sample Magnetometer (VSM). Firstly, from the above T_c data it is clear that the film is FM and saturates at a few hundred Gauss. From the data below T_c, it is clear that the sample is a bulk irreversible superconductor, which is exactly as expected. The irreversibility can be explained in a number of ways; namely, the presence of vortices and the presence of large volumes of normal metal due to an intermediate state Tinkham [1996]. This can be clarified from magnetisation data on pure Pb thin films, where irreversibility is also observed. Considering the demagnetisation factor is unity for a thin film when the field is applied parallel to the surface, the only explanation for this behaviour is the presence of vortices. Pb is typically a Type I superconductor, but for bulk Pb κ=0.45 - close to the $\kappa = 1\sqrt{2}$ limit. The reduction in the coherence length and an increase in the penetration depth that is expected from a dirty (polycrystalline) thin film would result in Type II behaviour, as observed here. In this case, one would expect the crystal domain size to be of similar order to (no larger than) the coherence length [Niu and Hampshire, 2003]. X-ray diffraction should be able to measure the average vertical grain size of the sample, which is discussed in the next

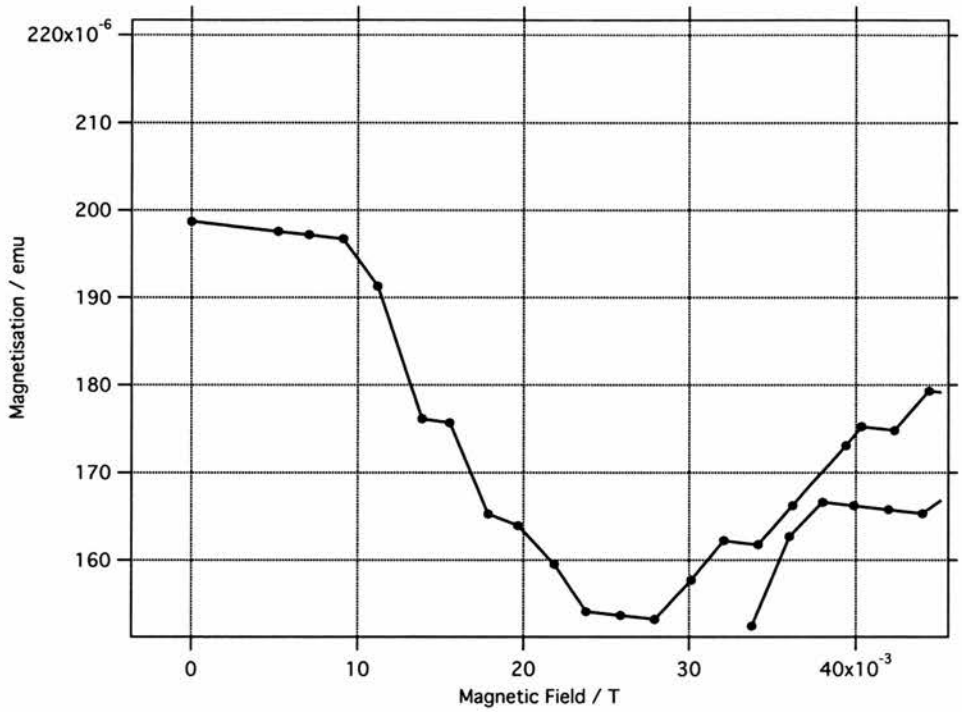

Figure 6.3: The virgin branch of the magnetisation measurements on Pb/Fe/Pb, shown in Figure 6.4 (top).

section.

To further the point, a Pb2000Å/Mo90Å film was grown and measured using the St. Andrews SQUID magnetometer. Figure 6.5 shows a hysteresis loop at 2K, where Type-II behaviour is clearly evident. H_{c1} can be estimated from the point at which the virgin branch deviates from linearity, which is approximately 300Oe. H_{c1} can also be estimated for the Fe/Pb/Fe films, which is shown in Figure 6.3. Here it is clear H_{c1} is reduced to around 100Oe, lower than the pure Pb films, which is expected due to the pair breaking mechanism associated with the ferromagnetic layer.

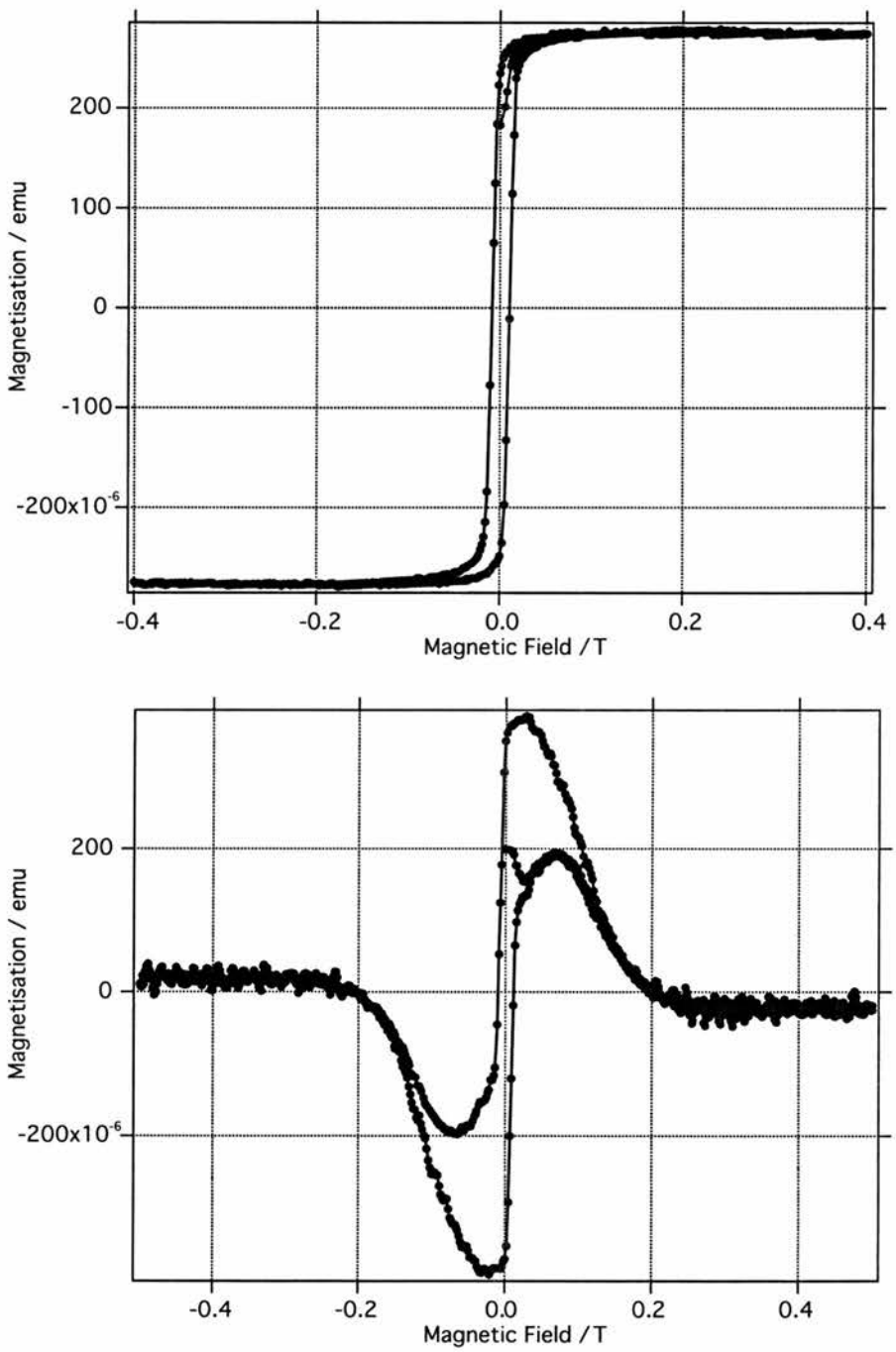

Figure 6.4: Hysteresis loop of a Fe/Pb/Fe thin film for T=6K (top) and T=2.3K (bottom). A linear background has been subtracted.

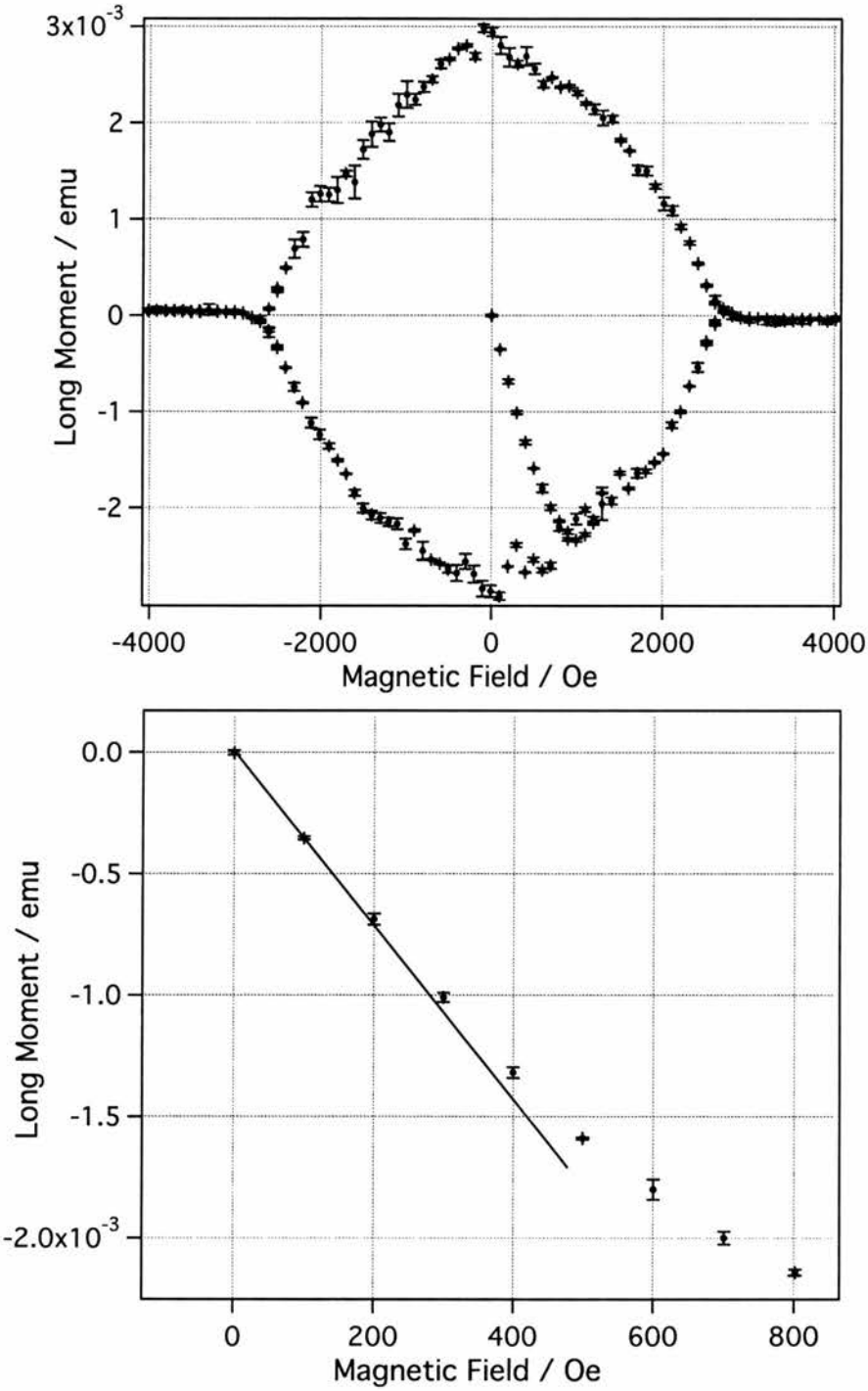

Figure 6.5: Hysteresis loop of a Pb thin film for T=2.0K (top) and the virgin branch (bottom) from which H_{c1} can be estimated to be approximately 300Oe.

6.2.3 X-ray Diffraction and Reflectometry

The structure of the sputtered Pb thin films (and therefore the electronic properties) are likely to be governed by the rate of deposition, substrate temperature, target composition and film thickness. The rate of deposition is a function of the Ar pressure, target composition, magnetron power (and temperature) and target thickness. Some of these are held constant; for example the substrate temperature, target composition and its thickness. However, magnetron power and Ar pressure can be varied and a growth rate can be established such that all films are grown at similar rates.

X-ray diffraction/reflectometry provides information such as film thickness, grain size and orientation and strain of the films. Typical X-ray instruments have a wavelength in the range of 0.5-2.5 Å. The wavelength of the X-rays used here is 1.54 Å, which corresponds to Cu-K_α lines. The X-ray scans have been used mainly to determine the growth rate of the samples, to measure roughness, the vertical coherence length and mosaic spread distribution. All X-ray experiments presented here were performed at the University of Leeds.

The instrument, located at the University of Leeds Department of Physics, is a Siemens two circle diffractometer with an x-ray tube containing a Cu target. Inside the tube there is a filament which creates a current of electrons of 30 mA, accelerated by a voltage of 40 KeV and incident on a Cu target. The lines observed are Cu K_α and K_β, due to the removal of an electron from the K shell of the Cu atoms. An electron from an outer shell (L for α and M for β) falls into the vacancy in the K shell, emitting X-rays in the process and returning the atom to its normal energy state. A Ni filter absorbs Cu-K_β, so the beam is close to monochromatic (with a wavelength of 1.54 Å). A Si monochromator is also used, placed before the scintillation detector to completely eliminate the Cu-K_β radiation and also acts to drastically reduce the background counts on the detector. Thin parallel metal sheets are placed at the exit of the x-ray tube, as the source is isotropic, thus increasing instrument resolution. A further increase in resolution can be achieved by placing another slit before the sample, but this must be balanced by the counting statistics required. Typical angular resolution for the measurements performed here is 2° and 4° for low and high angles experiments, respectively. The detector and sample are rotated at constant angular velocity by motors in such a way that the velocity of the detector is always twice the velocity of the sample.

$\theta/2\theta$ scans have been performed both at high and low angles, the typical length scales measured being different for each type of scan. At high angles, the scattering

Target	Current / mA	Power / W	Growth rate / Å s^{-1}
Pb	20	7	5.9
Fe	100	37	3.0
Mo	50	20	3.3

Table 6.2: Table of growth conditions for the different targets.

vector is of the order of the crystallographic reciprocal lattice vector and at low angles, the scattering vector is of the order of the reciprocal layer thickness. The scattering vector is always perpendicular to the surface of the sample, so only the length-scales perpendicular to the surface of the film can be measured; no information regarding the in-plane structure of the sample can be obtained.

At low angles, fringes appear for thin samples due to interference of reflected waves from the top air/metal interface and the metal/substrate interface and can be observed above the critical angle of a film as a function of the reflected beam. The reflectivity from a single layer deposited on a semi-infinite substrate is [Holy *et al.*, 1999]

$$R = \left| \frac{r_1 + r_2 e^{-2ik_{0z}t}}{1 + r_1 r_2 e^{-2ik_{0z}t}} \right|^2 \tag{6.1}$$

where $r_{1,2}$ are the Fresnel reflectivity coefficients of the free surface and substrate interface, k_{oz} the vertical component of the wavevector transmitted through the sample and t is the layer thickness. Thus a maxima exists when $e^{-2ik_{0z}t} = 1$ (at an angular position denoted by α_{im}), which corresponds to

$$2t\sqrt{\sin^2 \alpha_{im} - \sin^2 \alpha_c} = m\lambda \tag{6.2}$$

where m is an integer and the critical angle of total external reflection α_c is defined $\sin \alpha_c = \sqrt{2(1-n)}$, where n is the layer refractive index.

Figure 6.6 shows the Kiessig fringes for a growth of 100s of Fe and Mo, grown under standard conditions (described above). From these reflectivity curves it is possible to calculate the layer thickness and therefore the growth rate in order to ensure it is constant for all growth runs. It is also clear that the films are of good quality (low roughness), as many fringes are evident. Table 6.2 contains the growth rates, magnetron power and current used for all samples. For reasons unknown (possibly due to absorption), it is not possible to perform the same analysis for the Pb. SPNR was used to characterise the exact thickness of all the layers from the same sample used in the LEM experiments.

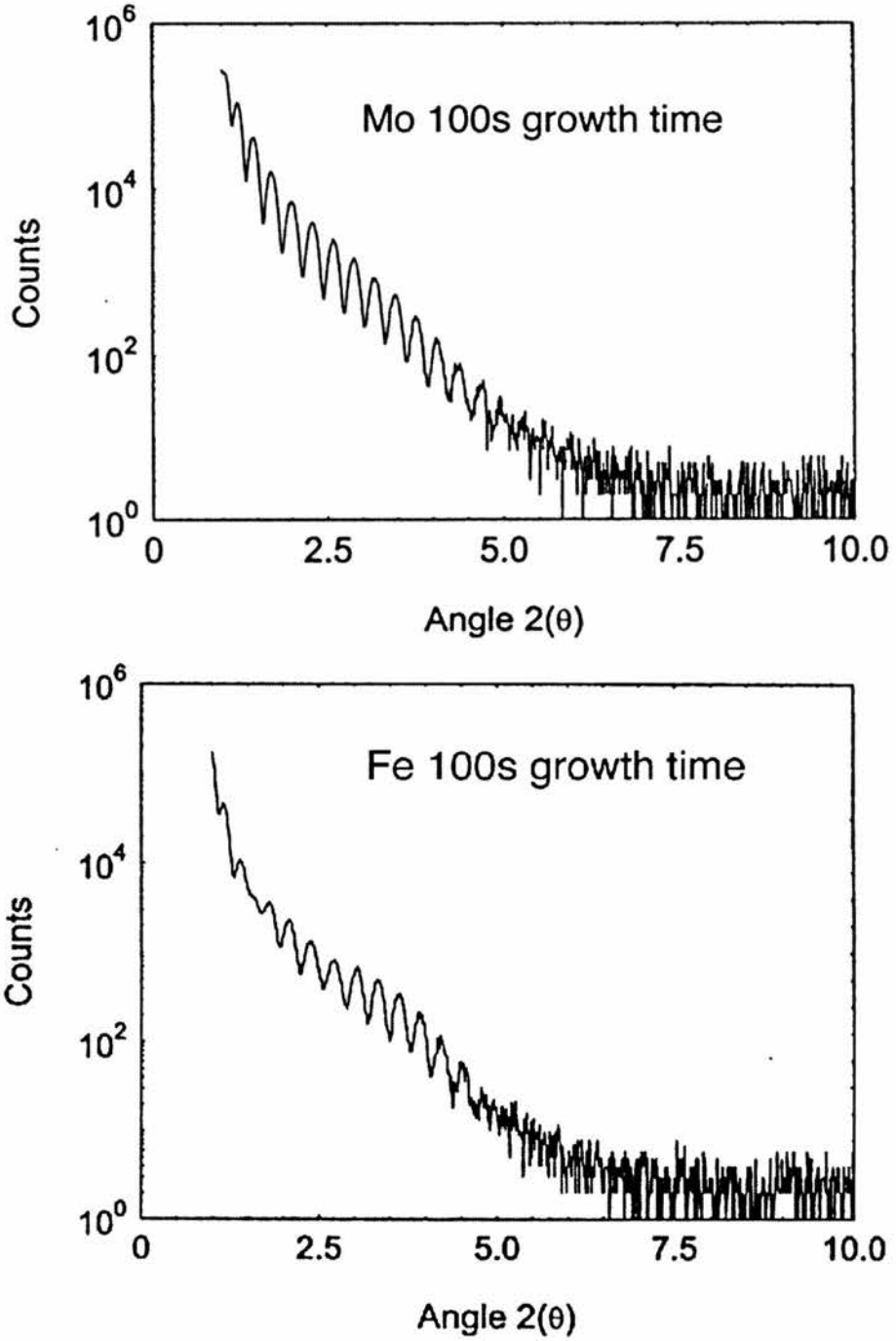

Figure 6.6: Keissig fringes for 100 seconds of growth time for Fe and Mo.

Crystal	$d_{hkl}/\mathring{A}^{-1}$	$2\theta/degrees$	A	$x_0/degrees$	B
Pb {111}	2.86	31.2	1.43 (0.06)	31.30 (0.01)	$3.1\text{x}10^{-3}$ ($2\text{x}10^{-4}$)
Pb {311}	1.57	62.1	0.09 (0.05)	62.19 (0.04)	$2\text{x}10^{-2}$ ($1\text{x}10^{-2}$)
Pb {222}	1.43	65.2	0.38 (0.09)	65.28 (0.03)	$3\text{x}10^{-2}$ ($1\text{x}10^{-2}$)
Si {400}	5.43	69.1	1.13 (0.05)	69.23 (0.01)	$7.6\text{x}10^{-4}$ ($4\text{x}10^{-5}$)
Si {400}	5.43	69.1	0.50 (0.04)	69.43 (0.01)	$7.8\text{x}10^{-4}$ ($8\text{x}10^{-5}$)

Table 6.3: Lorentzian fits to the high angle x-ray results, shown in Figure 6.2.3.

In order to determine the vertical grain size and crystallographic orientation, high angle $\theta/2\theta$ scans were performed. These scans are also performed in the specular condition, but the main difference between low angle scans and high angle scans is the different length scales that can be probed. The distance between planes is given by

$$d_{hkl} = \frac{a}{\sqrt{h^2 + k^2 + l^2}} \tag{6.3}$$

where h, k and l are the Miller indices of a particular set of planes. Applying Bragg's law it is clear that it is possible to obtain crystallographic orientations. In the first instance, one would simply use Braggs law to predict the angle where the peaks are expected. However, it soon becomes evident in Figure 6.7 the 1^{st} order peak for Si {100} is not present, as the lattice parameter is 5.43Å which corresponds to $2\theta = 16.3^o$. Si has a diamond crystal structure, which can be thought of as two penetrating fcc sublattices displaced from each other by the distance $(\frac{1}{4}, \frac{1}{4}, \frac{1}{4})$. The basis of the fcc structure is usually a cubic unit cell with 4 atoms per unit cube.These four atoms can be chosen to have the locations at $(0, 0, 0)$; $(0, 1/2, 1/2)$; $(1/2, 0, 1/2)$ and $(1/2, 1/2, 0)$, so the Si structure factor is

$$F_{di}(hkl) = f_c \left[1 + e^{\pi i(h+k)} + e^{\pi i(k+l)} + e^{\pi i(h+l)}\right] \left[1 + e^{\pi i\left(\frac{h+k+l}{2}\right)}\right], \tag{6.4}$$

where f_c is the atomic dispersion factor. As can be seen from the above equation, reflections from the planes with Miller indices {200} and {n00}, where n is an odd integer, have a zero structure factor. For this reason, the first set of planes which can be observed is {400}, with a corresponding angle of $2\theta = 69.1^o$.

Figure 6.7 shows such a measurement performed on a thin (600Å) test sample of Pb and a strong peak at around 69° is observed. It is possible to fit these peaks to a Lorentzian

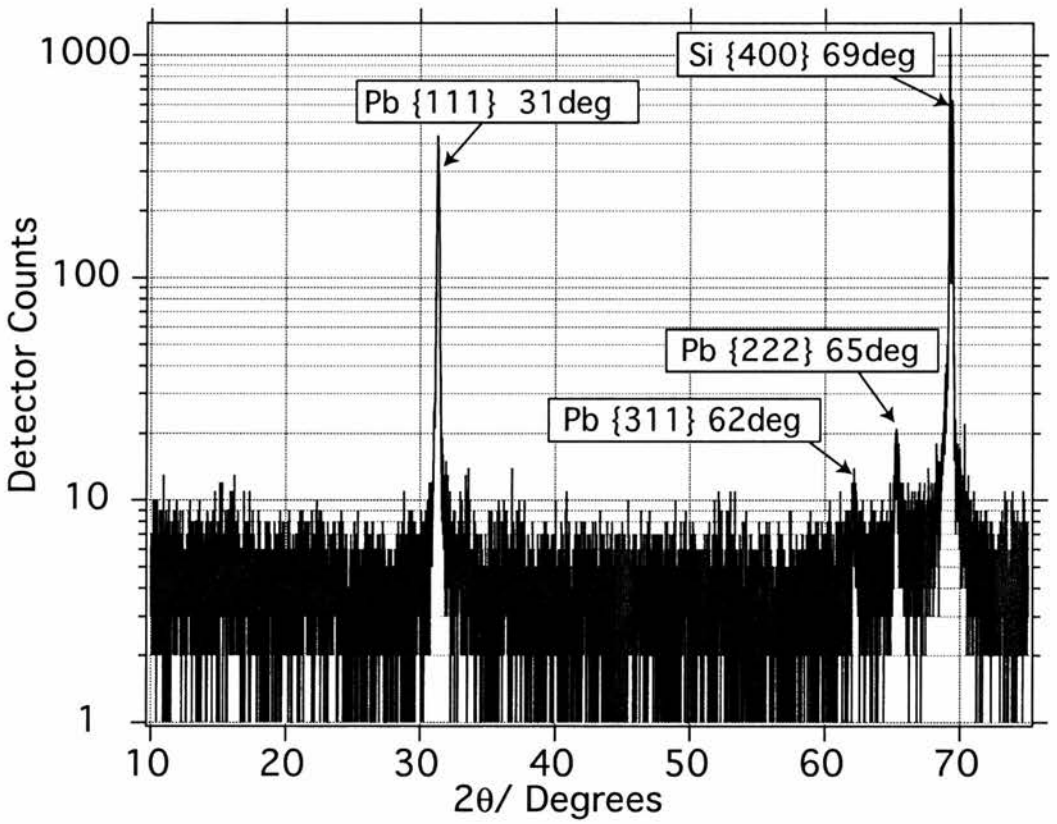

Figure 6.7: High angle X-Ray diffraction from a Pb thin film.

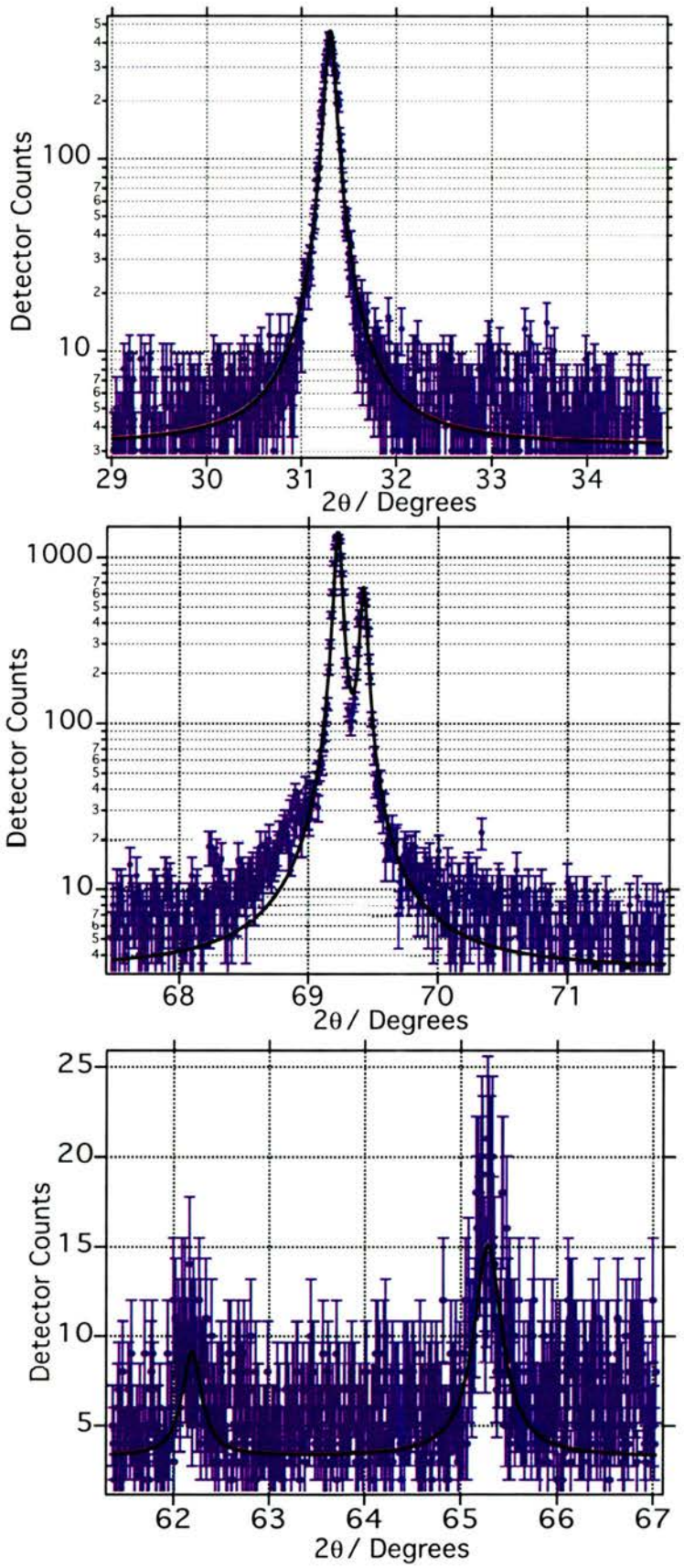

Figure 6.8: High angle X-Ray diffraction fits to a Lorentzian. Double peaks are fitted by the superposition of two Lorentzians.

$$y = y_0 + \frac{A}{(x - x_0)^2 + B} \tag{6.5}$$

which are shown in Figure 6.2.3, with the relevant fit parameters in Table 6.3. On closer inspection of the Si peak, it is clear there are two peaks at 69 degrees, which have been fitted to a linear superposition of two Lorentzians. The double peak is most likely due to the Si having two crystal domains, at slightly different angles to one another. Since this is a test sample, it is unknown if this is also the case with the slow μSR sample.

Pb has an fcc crystal structure, so the structure factor is therefore

$$F_{fcc}(hkl) = f_c \left[1 + e^{\pi i(h+k)} + e^{\pi i(k+l)} + e^{\pi i(h+l)}\right]. \tag{6.6}$$

Reflections then vanish if (hkl) contains a particular mixture of even and odd numbers. Apart from the Si peaks, three further peaks are observed. The first at 31.3° corresponding to the $\{111\}$ planes, there is another at 62.2° corresponding to the $\{311\}$ planes and a third at 65.3° corresponding to the $\{222\}$ planes. It is clear from the intensity of the peaks that the major growth direction is $\langle 111 \rangle$, but it is unfortunately not possible to confirm that this is the only growth direction due to the effects of the structure factor. However, it is considered unlikely there is any other growth direction and therefore it has been assumed the $\langle 111 \rangle$ is the only growth direction.

The vertical coherence length, $C_\perp$, represents the vertical size of the grains present in the sample. Assuming there is zero strain in the sample, the peak broadening is due to a finite number of crystal planes present in the sample, so the vertical grain size can be calculated from the FWHM of the peaks [Holy *et al.*, 1999]

$$C_\perp = \frac{180 K \lambda}{\pi \sigma \cos\theta} \tag{6.7}$$

where λ is the x-ray wavelength, θ is the Bragg angle, K is a geometrical factor related to the shape of the crystallites, approximated for these films to be 0.9 [Cullity, 1978] and σ is the FWHM. By solving Equation 6.5 at y=1/2, with the correct parameters from the fits for the $\{111\}$ planes, it is possible to calculate the vertical coherence length to be 24.4±0.6Å.

6.2.4 Spin Polarised Neutron Reflectivity

A neutron reflectometry experiment determines the variation of the intensity of a beam of neutrons reflected from a surface as a function of the scattering vector

$$q = \frac{4\pi}{\lambda} \sin \Theta \tag{6.8}$$

where λ is the neutron wavelength and 2θ is the scattering angle. The angle between the plane of the sample and the incident beam is θ. This is illustrated in Figure 6.10. The reflectivity, $\boldsymbol{R}(q)$, in a neutron experiment, is defined as $\boldsymbol{I}_r(q)/\boldsymbol{I}_i(q)$, where $\boldsymbol{I}_r(q)$ is the reflected and $\boldsymbol{I}_i(q)$ is the incident intensity.

Spin polarised neutron reflectivity (SPNR) can be used to measure the thickness and magnetisation profile of thin film multilayers. Neutron reflection provides the composition variation normal to the surface of the film, with an accuracy on a sub-nanometer length scale. This kind of information is also given by X-ray reflectivity, however the neutron performs better in two important respects. Firstly, there is the favourable difference in scattering properties between elements and isotopes of elements. With X-rays, contrast between different regions of the sample is provided by the electron density difference between molecules. The analogue for neutrons is the neutron scattering cross section. Across the periodic table, this scattering cross section appears to be not only of random magnitude, but also of sign and varies even between isotopes of a specific element. The second major advantage is that the neutron can penetrate through many engineering materials. This allows the use of neutrons in complex sample environments without the worry of absorption, which is a major problem with X-ray techniques.

The instrument used in the work presented here is CRISP, which is situated at ISIS. The CRISP reflectometer is typical of a pulsed source time-of-flight (TOF) instrument. A schematic illustration of the major optical components is shown in Figure 6.9. The moderated neutrons pass through a disc chopper to select the wavelength range. The beam is coarsely collimated by neutron absorbing jaws before entering the experimental measurement area. Fine collimation is achieved by two slits before the sample which define the illuminated area and resolution at the sample position. The resolution is given by

$$\frac{\Delta q}{q} = \frac{\tan^{-1}((s_1 + s_2)/2L_1)}{\theta} \tag{6.9}$$

where s_1 and s_2 are the heights of the two collimation slits, L_1 is the distance between the slits and θ is the incident angle. The slit widths are generally fixed at 30mm,

these widths do not effect the resolution in q.

The beam profile and intensity is monitored just before reaching the sample using a scintillator detector. Post sample, the background noise is suppressed by two further slits and a shielded detector nose cone. The nose cone is covered in boron impregnated resin (a strong absorber of neutrons) which reduces the level of background radiation on the detector. A number of other measures are taken to reduce background count rates; when the protons strike the tantalum or uranium target, a pulse of high energy neutrons and γ-rays is produced. A proportion of the neutrons are not moderated and these along with the γ-rays will contribute to the background. The chopper is timed such that it blocks the view of the target during the period of the proton pulse. The supermirror[1] will reflect neutrons into the instrument in the useful wavelength range, but high energy neutrons and γ-rays will pass straight through and are not detected. This reduces a major source of background counts.

CRISP has a wavelength range of 0.5-6.5Å with the disc chopper working at 50 Hz. This range can be extended to 12Å if the disc chopper is operated at 25 Hz, although this has the drawback of less flux, since it only collects 1 in every 2 pulses of neutrons. The instrument has been designed to be able to measure liquid surfaces and therefore has a horizontal sample geometry and an inclined beam at 1.5° to the horizontal, although this is somewhat redundant for the measurements here. Computer controlled goniometers at the sample position allow movement of solid samples (or confined liquids) to angles other than the 1.5°.

CRISP like other pulsed neutron source reflectometers has a fixed wavelength range, therefore at each incident angle on the sample a limited q range is obtained. The q range can easily be extended by running 2 or more incident angles and combining the data. The reflectivity profile at a fixed incident angle due to the polychromatic beam is therefore collected all at once and the time required to measure the total spectrum is only limited by the statistics of the collected data. This offers an advantage over other monochromatic instruments, as the resolution is not limited by a finite angle step size. Therefore CRISP can measure much thicker samples at a better resolution than other (non TOF) spectrometers, albeit with some loss of statistics.

The sample environment is an Oxford Instruments continuous flow cryostat, capable of a base temperature of 1.5K. The applied field is from a Helmholtz electromagnet and typically does not exceed a few thousand Oersteds, which is applied

[1]not shown in Figure 6.9, but is between the collimating jaws and the first slit.

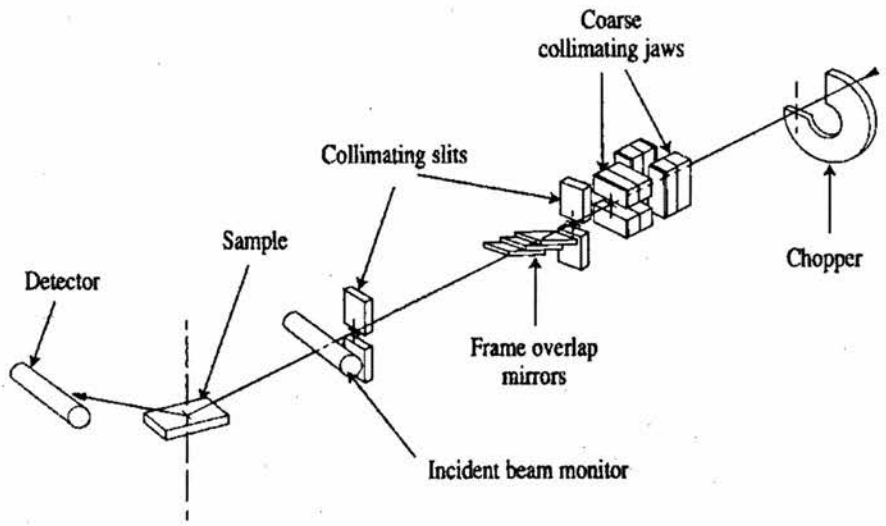

Figure 6.9: Schematic diagram of CRISP.

parallel to the neutron momentum and film surface.

The data analysis in this section concentrates on one method of data analysis - the optical matrix method [Blundell, 1992], which is suitable for the systems studied here. Appendix A deals with the model used in more detail. Two further methods of analysis use partial structure factors [Crowley *et al.*, 1991] and indirect Fourier transform [Pedersen, 1992] methods, which are not implemented.

The neutron reflectivity is modelled by considering the potential energy of the neutron passing through a solid. The neutron undergoes both nuclear and magnetic scattering, schematically shown in Figure 6.10b. Consequently, the potential energy of a neutron in the αth region is the sum of a nuclear term and a magnetic term

$$V_\alpha = \frac{\hbar^2}{2\pi m_n}\rho_\alpha b_\alpha - \boldsymbol{\mu}_n \cdot \boldsymbol{B}_\alpha \tag{6.10}$$

where $\boldsymbol{\mu}_n$ is the neutron magnetic moment, b_α is the coherent scattering length, $\boldsymbol{B}_\alpha$ is the field due to the magnetisation in region α and ρ_α is the atomic density. Thus, the reflectivity depends on the relative orientation of the neutron spin and magnetic field in each layer. By calculating a spin dependent transfer matrix (Appendix A), it is possible to write [Blundell, 1992]

$$t_u^{\uparrow} = M_{33}/(M_{11}M_{33} - M_{13}M_{31})$$
$$t_u^{\downarrow} = -M_{31}/(M_{11}M_{33} - M_{13}M_{31})$$

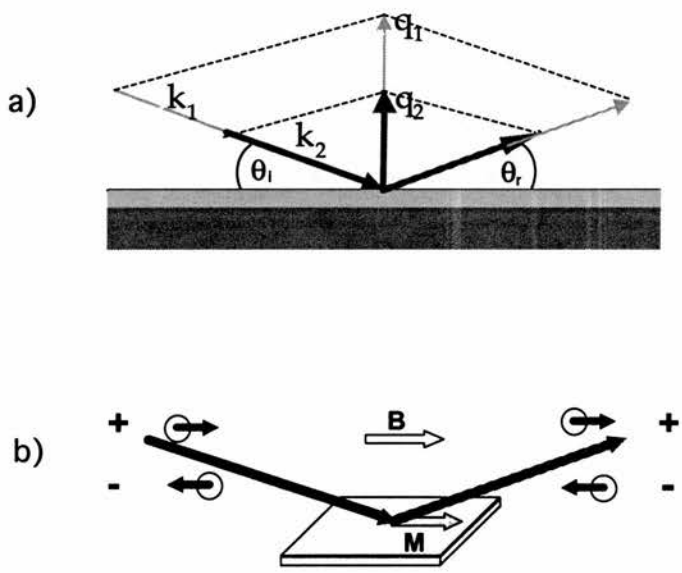

Figure 6.10: Schematic diagram of the geometry used for the CRISP experiments. a) TOF geometry, where the wavevectors 1 and 2 are incident at different times after the pulse. b) Spin dependent magnetic scattering.

$$
\begin{aligned}
r_u^{\uparrow} &= (M_{21}M_{33} - M_{23}M_{31})/(M_{11}M_{33} - M_{13}M_{31}) \\
r_u^{\downarrow} &= (M_{41}M_{33} - M_{43}M_{31})/(M_{11}M_{33} - M_{13}M_{31}) \\
\\
t_d^{\uparrow} &= -M_{13}/(M_{11}M_{33} - M_{13}M_{31}) \\
t_d^{\downarrow} &= M_{11}/(M_{11}M_{33} - M_{13}M_{31}) \\
r_d^{\uparrow} &= (M_{23}M_{11} - M_{21}M_{13})/(M_{11}M_{33} - M_{13}M_{31}) \\
r_d^{\downarrow} &= (M_{43}M_{11} - M_{41}M_{13})/(M_{11}M_{33} - M_{13}M_{31})
\end{aligned} \tag{6.11}
$$

where M is the transfer matrix, the subscripts on M are the indices to the matrix elements and the u and d correspond to the incident neutron spin. The spin asymmetry is defined

$$S = \frac{R_{\uparrow} - R_{\downarrow}}{R_{\uparrow} + R_{\downarrow}} \tag{6.12}$$

which can be rewritten in terms of the four reflection processes in Equation 6.11 as

$$S = \frac{|r_u^{\uparrow}|^2 + |r_u^{\downarrow}|^2 - |r_d^{\uparrow}|^2 - |r_d^{\downarrow}|^2}{|r_u^{\uparrow}|^2 + |r_u^{\downarrow}|^2 + |r_d^{\uparrow}|^2 + |r_d^{\downarrow}|^2}. \tag{6.13}$$

Thus, by calculating $R_{\uparrow}$ and $R_{\downarrow}$ for a neutron particular potential it is possible to directly fit both spin up and spin down reflections to obtain the layer thickness and magnetic profile of each layer. Resolution effects can be taken into account by using Equation 6.9. In an ideal world where data can be collected over an infinite q range with no resolution effects, the reflectivity, $\boldsymbol{R}(q)$, is not unique to a single composition profile because of the loss of phase information. Furthermore, a host of different composition profiles may all have very similar reflectivity profiles and in a real experimental situation these profiles will be essentially indistinguishable. However, these samples are relatively simple with few constituent layers, so it is not necessary to revert to a Maximum Entropy technique to solve this problem.

Sample roughness can seriously reduce the quality of the reflectivity curves. Figure 6.11 shows a schematic diagram of the different forms of roughness. Part (a) shows relatively realistic inter-diffusion and interlayer roughness between two layers of a multilayer (left) and a simplistic model (right), which effectively takes an average of the displacement over all of the sample. Part (b) is a description of the top layer/air interface and can be modelled in the same way as part (a). Part (c) is a description of the large scale roughness, which has not been taken into account in

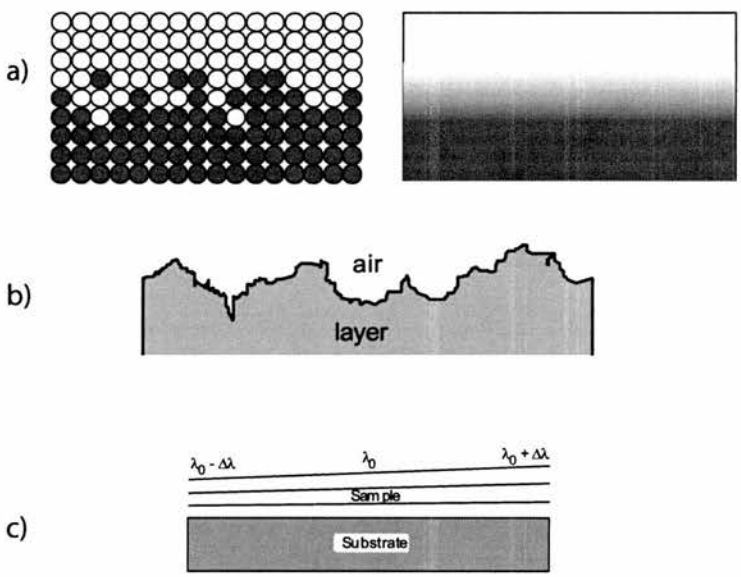

Figure 6.11: Schematic diagram of the different types of sample roughness. a) Left: Inter-diffusion between layers and interface roughness, with a typical lengthscale of less than 10nm. Right: The manner in which this type of roughness is modelled. b) Intermediate roughness at the air/sample interface, with a lengthscale between 100nm and 5μm. c) Large scale roughness, which can include strain, substrate bending and anisotropic growth. The lengthscale is typically greater than 50 μm.

this work. The model of roughness described here does not take into account conformal roughness, as it is an underdetermined problem which requires a maximum entropy algorithm to solve. This algorithm is currently in development.

Conventional simulation and fit programs for (X-ray) specular reflectivity are usually based on an independent, individual layer roughness model and this is the model used here. It is proposed that the roughness follows a Gaussian profile for random shifts from the ideal interface, leading to a Fresnel reflectivity to be altered to [Holy *et al.*, 1999]

$$r'_\alpha = r_\alpha e^{-q_z^\alpha q_z^{\alpha+1}\sigma_\alpha^2/2} \tag{6.14}$$

and a transmission of

$$t'_\alpha = t_\alpha e^{\frac{\sigma_\alpha^2}{2}\left(\frac{q_z^\alpha - q_z^{\alpha+1}}{2}\right)^2} \tag{6.15}$$

for each interface, where σ_α is the root mean-square (RMS) displacement from the ideal position for the interface between the αth and $(\alpha+1)$th region. As can be seen, the influence of roughness on transmission is relatively small, but the reflectivity is exponentially diminished. The air/first surface roughness has the effect of reducing the overall reflectivity and the interface roughness reduces the amplitude of the interference fringes.

Figure 6.12 shows the neutron reflectivity of the same Fe/Pb/Fe/Mo thin film used in the slow μSR measurements below. This measurement was performed above T_c, where the difference between spin up and spin down represents the magnetic scattering due to the Fe layers. The optical neutron reflectivity model described above can be used to obtain the layer thickness and roughness to a high degree of accuracy. Table 6.4 shows the thickness of the different layers and an estimate for the roughness. Instrument resolution has been taken into account by convoluting with a Gaussian, whose q-dependent width, Δq, is determined from Equation 6.9. It is clear that the RMS displacement is of the same order of magnitude as the vertical correlation length calculated in the section dealing with X-Ray diffraction. It should be noted that the majority of the roughness comes from the Pb layer, which is carried through the Fe and Mo layers. The Mo layer smoothes out some of the roughness inherited from the Pb, so that the Mo/Air interface is less rough than the Fe/Mo interface. The roughness in this sample is a thin layer (~1nm) on the top surface of the Pb of unknown origin, which is not easily resolvable due to the thinness of the layer. The effect of this layer is included in the slow μSR

α	*Layer* α	y_α/nm	$\sigma_{\alpha,\alpha-1}/nm$
7	Si Substrate	N/A	N/A
6	Fe	2.6 (0.2)	N/A
5	Pb	215.0 (2.0)	1.2 (0.1)
4	Unknown	1.0 (0.5)	1.2 (0.5)
3	Fe	2.8 (0.2)	1.2 (0.1)
2	Mo	9.0 (0.5)	1.1 (0.1)
1	Air	N/A	N/A

Table 6.4: Sample parameters obtained from a fit to the data shown in Figure 6.12. The roughness, $\sigma_{\alpha,\alpha-1}$ is between the current layer and the next layer closer to the surface. If σ=N/A then it is not possible to measure the roughness with any degree of accuracy and is not valid. The thickness is not valid for the air and Si substrate, so y_α=N/A in this case. Errors have been rounded up.

simulations, but is simply treated as the roughness associated with the Pb and it is assumed the superelectrons tunnel into this layer. Another source of roughness in the Pb is the vertical grain size. This model is too simplistic to take account of both the non-conformal and conformal nature of the roughness, both of which are present, other than by a simple change of the RMS roughness.

It should be noted that no incommensurate SDW can be observed with SPNR, as the length scale of such an oscillation in spin density is governed by the extremal spanning vectors of the Fermi surface, which are much smaller than the minimum length scale CRISP is able to measure. On cooling below T_c, there is little change in the reflectivity, indicating the contribution due to superconductivity is either too small to be measured (compared to the magnetic layer signal) or the length scale is also beyond the limit of the instrument (in the case of the SDW). This "masking" is because the much stronger spin-dependent scattering from the magnetic layers masks the much weaker, subtle effects from the superconductor. The local nature of the slow μSR technique avoids this difficulty and allows the effects inside the Pb film to be seen without interference from the Fe films.

In order to fully understand the Fe/Pb/Fe/Mo system, one must take into account superconductivity, as shall be discussed later. This measurement is not possible in the magnetic sample using this technique for reasons already discussed, but it is possible to take a Mo/Pb layer to draw some parallels with the magnetic system. For this reason, a Pb/Mo layer was grown under identical conditions and growth times to try and replicate grain size, roughness and layer thickness. The SPNR measurement was performed under identical conditions as the Mo/Fe/Pb/Fe film, apart from a higher magnetic field was used in order to increase the expulsion (and

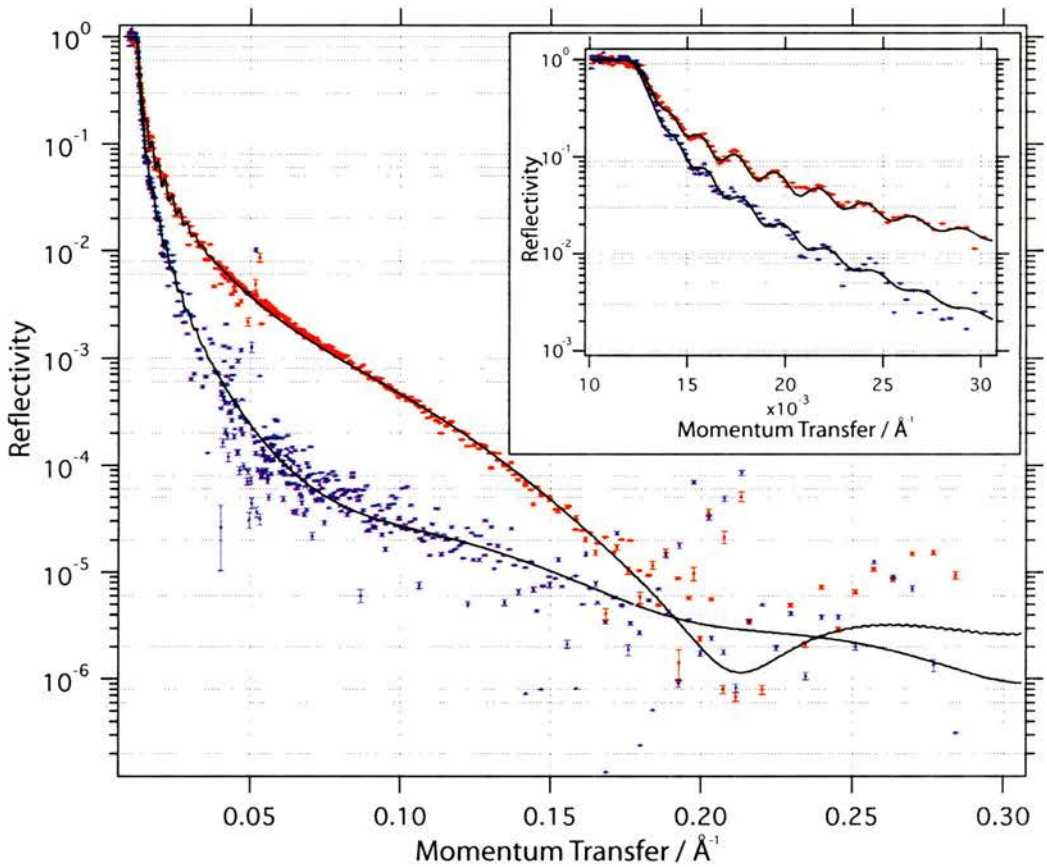

Figure 6.12: Spin up and down reflectivity of the PbFe muon sample. The lines are a fit to the optical model described in the text, from which sample dimensions to a high accuracy can be determined.

therefore magnitude of the spin asymmetry) and to ensure the film is above H_{c1}. The spin asymmetry is shown in Figure 6.13. The data is represented by the points and a model (represented by a solid line) is fitted to the data[2], which is described below.

It is clear this is unlike the spin asymmetry expected from a pure Meissner state (see, for example [Zhang *et al.*, 1995]). Magnetisation measurements of a Mo/Pb indicate these films are Type-II, so the model developed to describe this data is one with a spatial distribution of vortices in the centre of the Pb. The field penetrating from both surfaces of the film and the field from the vortices in the centre contribute to the spin asymmetry. A magnetic field $\boldsymbol{H}_{ext}$ parallel to the film yields [Han *et al.*, 1999; Zhang *et al.*, 1995]

$$\boldsymbol{B}(\boldsymbol{r}) = \mu_0 \boldsymbol{H} \frac{\cosh(y/\lambda_L)}{\cosh(t/2\lambda_L)} + \frac{\Phi_0}{2\pi\lambda_L^2} \int n_v(\boldsymbol{r}) K_0 \left(\frac{|\boldsymbol{r} - \boldsymbol{r}'|}{\lambda_L} \right) d\boldsymbol{r} + \boldsymbol{B}_f \qquad (6.16)$$

where t is the film thickness, $n_v(\boldsymbol{r}) = \sum_{p=1}^{p=N} \delta(\boldsymbol{r} - \boldsymbol{r}_p)$ is the vortex density with N vortices present, K_0 is a modified zeroth order Bessel function of the second kind and B_f is the field which satisfies the boundary condition $\boldsymbol{B} = \mu_0 \boldsymbol{H}_{ext}$.

The coherence length must also be taken into account. To a first approximation, a simple core cut off is used, such that if the radius $\boldsymbol{r} < \xi$, the field is set to the value at $\boldsymbol{r} = \xi$. A better approximation would be with a Gaussian, but this measurement is not particularly sensitive to the subtle differences between the shape of the core, especially considering this model may not be applicable to this situation. Considering the approximations and incorrect assumptions in this model, it represents the data exceptionally well. A better model would be to solve the GL equations directly, but this is a considerable task and can not be achieved given the time constraints of this Ph.D.

In this fit, the penetration depth was found to be 50nm, the coherence length 55nm and the vortices were found to be well spaced out. For a 2D linear arrangement of vortices, $d = \sqrt{\Phi_0/B}$, so one would expect a vortex spacing of approximately 200nm at 480Oe. The spacing was found to be just over twice the expected value, at 450nm, indicating the 2D spacing does not apply to a linear arrangement of flux.

[2]For details of the fitting algorithm used, please consult Appendix B.

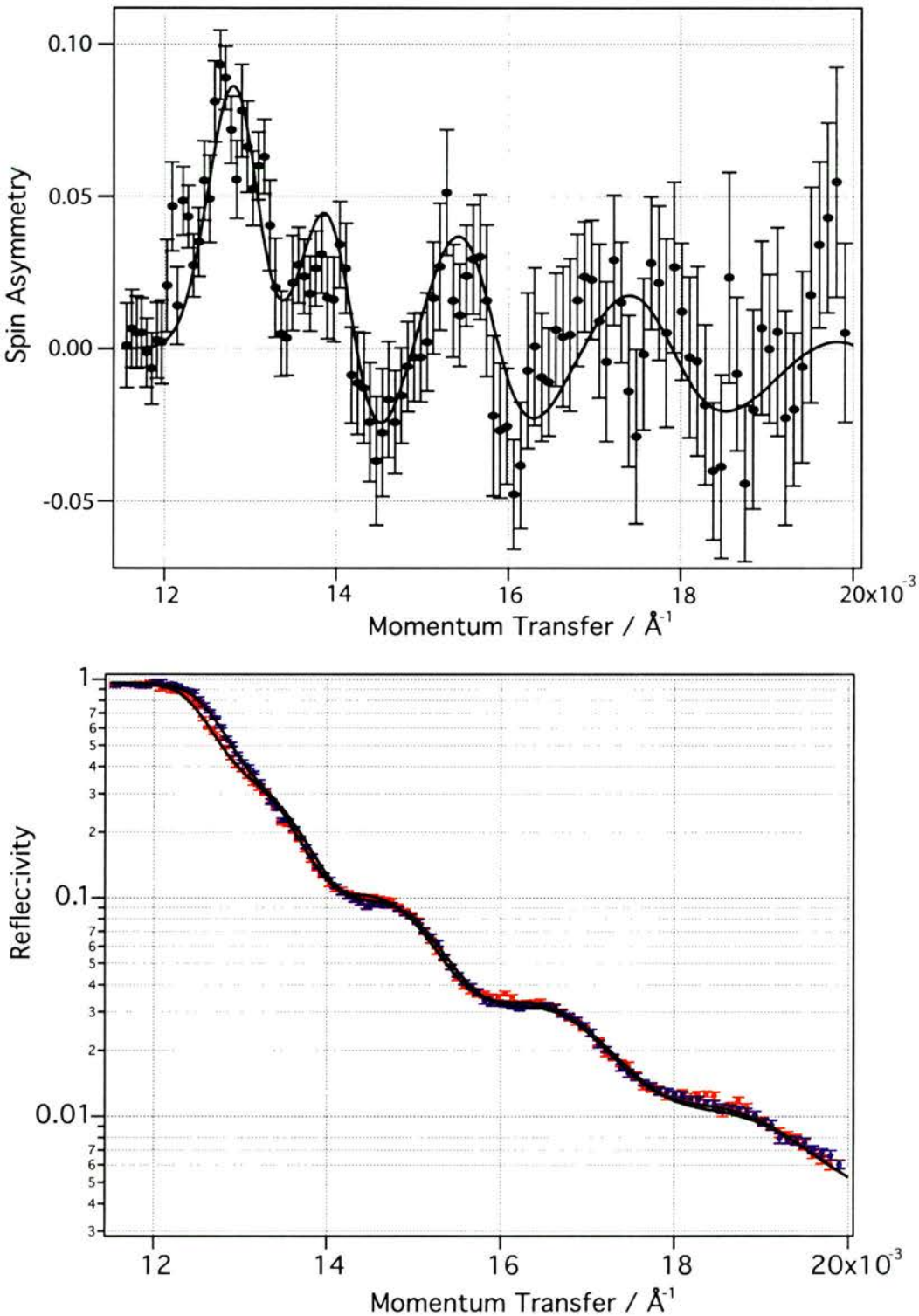

Figure 6.13: Top: Spin asymmetry of a Pb test sample of the same thickness as the PbFe muon sample, in an applied field of 480Oe. Bottom: Spin up and down reflectivity, showing good agreement between fits (line) and data (points).

6.3 Slow μSR Results

6.3.1 Experimental Setup

The main description of apparatus has already been dealt with earlier. This is just a short summary of conditions and issues involved with the measurement.

Direct microscopic measurement of spatial variation of magnetic field in thin films can be achieved by the use of the LEM spectrometer. The temporal evolution of spin polarised muons can be measured by detection of the positron emission during the muon decay. Positrons are emitted primarily along the spin direction of the muon at time of decay and are detected using an array of standard scintillation detectors. The positron time spectra collected from the muon precession ensemble contains damped oscillations from which the probability distribution of magnetic field can be obtained. Typical counting statistics are 2 million decay events. This technique offers a sufficiently high sensitivity to determine the induced polarisation at large distances from the superconducting/magnetic interface, since magnetic moments as small as 10^{-3} to $10^{-4}\mu_B$ can be detected [Luetkens *et al.*, 2003].

The muons are moderated from an incident energy of ~4MeV to epithermal energies of ~15eV via a condensed van der Waals gas layer [Morenzoni *et al.*, 1994] consisting of 1100Å of Ne and 15Åof N_2, measured by a quartz crystal microbalance. The epithermal muons are then extracted from the moderator layer by applying 20kV to the moderator substrate. After traversing an electrostatic mirror to filter un-moderated muons and positrons, the final energy of the implanted muons is determined by the potential applied to the sample. The incoming muons are detected by a trigger detector consisting of a 10nm thick carbon foil, placed at an intermediate focus upstream of the sample. Secondary electrons emitted by the foil are amplified by an MCP [Morenzoni *et al.*, 1996] and act as a trigger signal.

The sample is mounted in good thermal contact with an electrically insulated high purity silver coated aluminium plate using silver epoxy. A silver epoxy electrical contact on one corner was needed to ensure the sample was at the correct potential. The experiments are conducted under UHV conditions, where typical chamber pressure is $1x10^{-10}$mbar. The sample is cooled in a continuous flow cryostat with a minimum temperature of 2.5K, well below the superconducting transition temperature. A magnetic field of 200Oe was applied parallel to the sample surface and perpendicular to the momentum and spin of the incident muons. Prior to measuring, a magnetic field of 1T was applied parallel to the film, exceeding the saturation

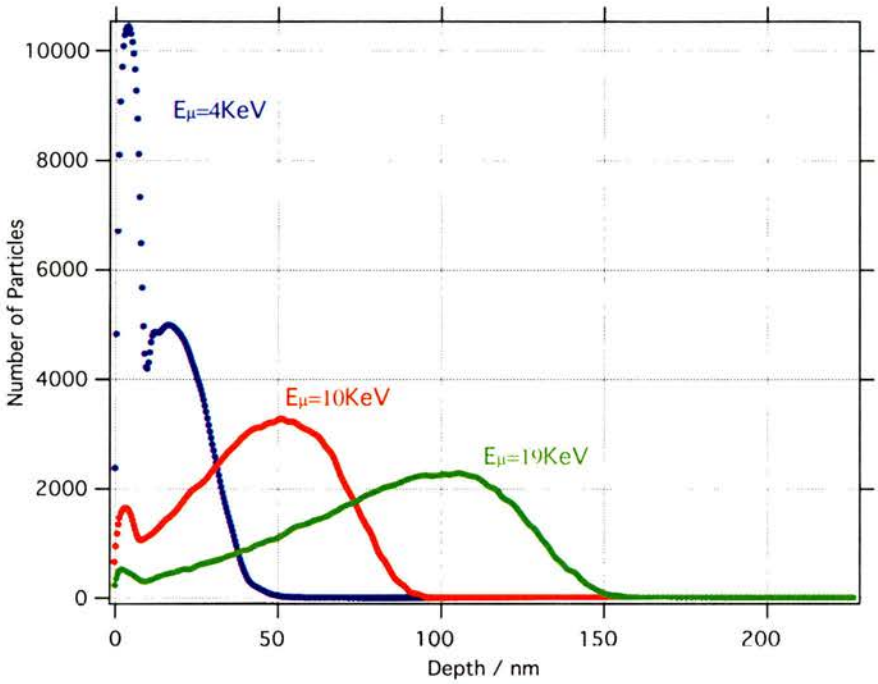

Figure 6.14: Stopping profile for muons at different energy, calculated from the TRIM.SP algorithm. Approximately 500,000 muons are used.

field by at least a factor of 4. This ensured that the Fe was a single magnetic domain prior to measurement. In a typical experimental run 2 million muon decay events were recorded and the probability distribution P(B) of the magnetic field sampled by the muon ensemble were calculated by MEM analysis.

Low energy muons stop in the sample over a range of depths depending on the incident muon energy. The muon implantation depth distribution shown in Figure 6.14 was calculated for the relevant implantation energy using the Monte Carlo algorithm TRIM.SP [Eckstein, 1992]. This algorithm has been shown to calculate muon implantation profiles accurately [Gluckler *et al.*, 2000] and a Gaussian spread of input energies of FWHM 0.5KeV has been included in the calculation to account for the straggle introduced by the MCP trigger detector [Hofer, 1998]. The sample dimensions were accurately determined from the SPNR results on this sample, shown in Figure 6.12, to be Fe26Å/Pb2150Å/Fe28Å/Mo90Å. Note that the peak in Figure 6.14 at low depths is due to the muons reflecting from layers of different densities.

6.3.2 Data Analysis

The following parameters were used in the MEM algorithm. Sigma Looseness was 1.03 and the apodisation of errors was set to 7μs. The data was not binned other than that from the intrinsic binning of the instrument and the full time measured range was used. The number of points in the Fourier spectrum was 2^{16}.

6.3.3 Above T_c

Figure 6.15 shows the probability distribution of magnetic field P(B) inside the sample in the normal metallic state at a temperature of 10K in a field of 200Oe, for muon implantation energies corresponding to those shown in Figure 6.14. The unusual p(B)s reflect a complicated flux density profile within the sample, which can be identified as arising from an RKKY-type SDW, as previously demonstrated for Fe/Ag trilayers [Luetkens *et al.*, 2003]. The peak in the centre of the field distribution is partially due to a background fraction of ~10% of the muons that miss the sample and hit the silver backplate. Local fields different from the central peak are due to hyperfine interactions with the spatially oscillating electron spin polarisation.

In Figure 6.15, the data obtained from the muon precession is represented by the points whilst the shaded area results from a fit of a simple model[3], which as can be seen, agrees very well with the data. The fits simply reflect the local depth-dependent magnetisation due to the SDW, weighted by the muon stopping profile of Figure 6.14. The magnetisation, M(z), within the Pb spacer layer is given by the superposition of the magnetic profiles induced by each of the two Fe/Pb interfaces. In the model, M(z) is assumed to take the following form [Luetkens *et al.*, 2003]

$$M(z) = \sum_i A_i \frac{sin(x_i + \phi_i)}{x_i^{n_i}} \tag{6.17}$$

where $x_i = 2k_i z$, k_i are the wavevectors of the SDW, z the distance into the spacer layer, A_i is an adjustable parameter for the coupling strength of the spins and ϕ_i the phase of the electron spin polarisation. In these fits, two components to the SDW were found to be present and the relevant parameters are given in Table 6.5.

An unfortunate complication to the model is the "aliasing" effect originating from the position in which the muon stops within the discrete crystal lattice, as the SDW's lengthscale is of the same order as the lattice parameter of Pb. The Pb grown in these films has a ⟨111⟩ primary growth direction, with only small contributions

[3]For details of the fitting algorithm used, please consult Appendix B.

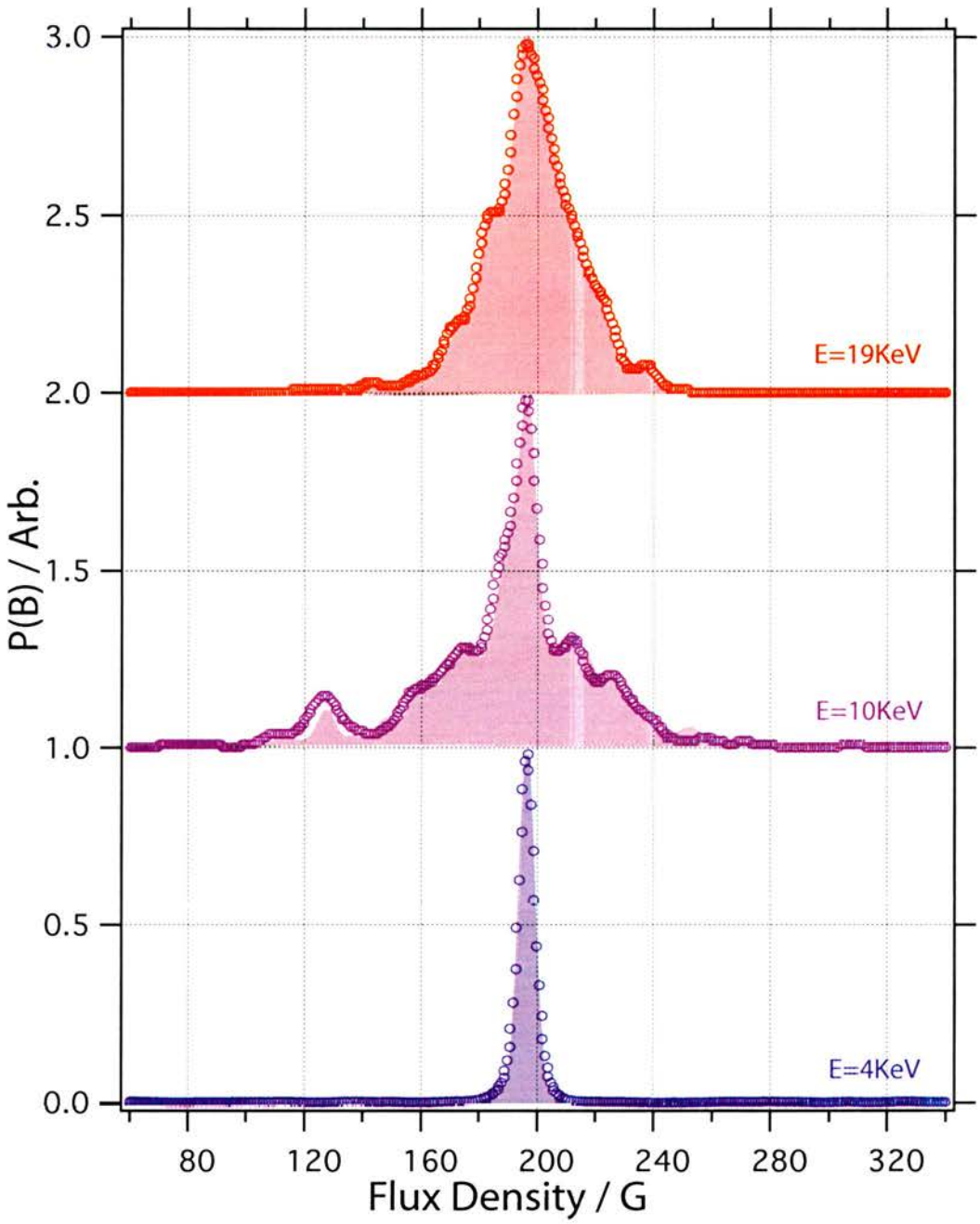

Figure 6.15: The field probability distribution P(B) for the sample measured in an applied field of 200Oe at a temperature of 10 K, revealing the presence of a spin density wave inside the Pb layer. The shaded areas are fits.

i	k_i	ϕ_i	n_i	A_i
1	0.23 (0.02)	$3\pi/2$ (0.01)	0.86 (0.02)	18
2	1.58 (0.02)	$\pi/2$ (0.01)	0.86 (0.02)	18

Table 6.5: Parameters obtained from the fits to the above T_c data. Errors represent a 95% confidence interval.

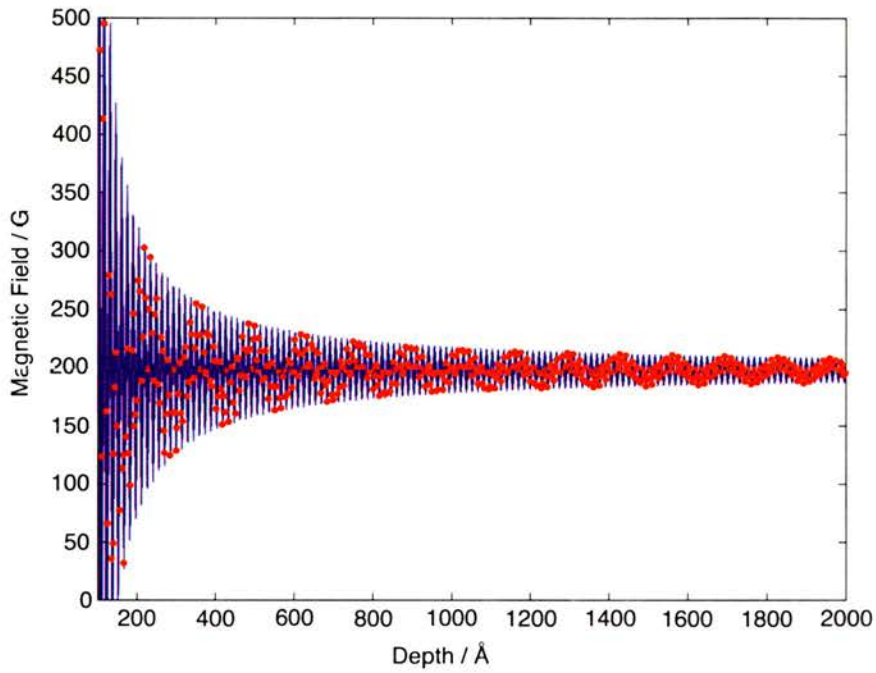

Figure 6.16: Sampling of the spin density wave from one of the surfaces.

from other crystal orientations. The muon site is generally the most electronegative point in the crystal lattice and in the case of Pb along the $\langle 111 \rangle$ direction, it will be in the centre of the pyramid shown in Figure 6.17. With a Pb lattice parameter of a=4.95Å the central position is $\sqrt{5a/16}$. Therefore the local magnetic flux density due to the incommensurate SDW is sampled every $\sqrt{5a/16}$ from the surface, from which P(B) is directly calculated. Figure 6.16 shows the sampling of the SDW from one of the surfaces. It is clear the SDW persists into the centre of the film.

The model is further complicated when sample roughness is taken into account. The muons are implanted from the surface of the thin film, which is has an rms roughness of approximately 1.1nm. The SDW "starts" from the two Pb/Fe interfaces, with a roughness of 1.2nm. For simplicity, it is assumed that there is only roughness on the top Pb/Fe boundary and at the Mo/air surface, partly because the SPNR is not sensitive to the layers at the bottom (and therefore proves difficult to measure) and also because the muons only penetrate around half way in from the surface.

The roughness is dealt with as follows. Both interfaces to be considered (Mo/air and Pb/Fe) are assumed to be of a Gaussian nature, with the centre of the Gaussian corresponding to the mean interface position and the width of the Gaussian

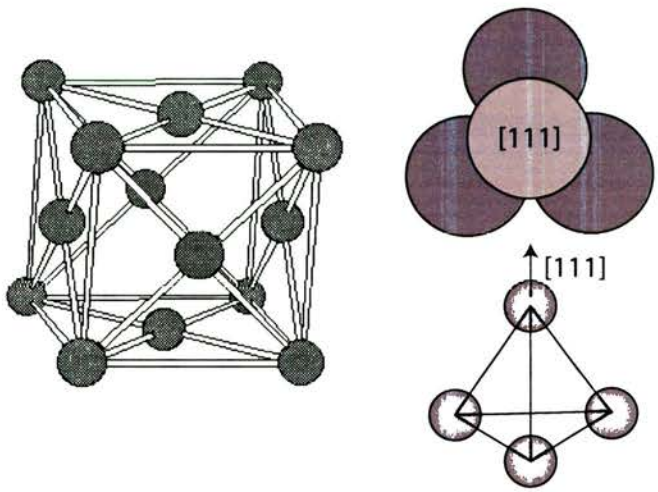

Figure 6.17: FCC crystal structure.

corresponding to the rms roughness measured with SPNR. Each SDW start point in the simulation at the Pb/Fe interface is weighted by the Gaussian distribution and summed to form the magnetisation the muons see. It should be noted that the roughness of the Pb/Fe layer is larger than the lengthscale of the oscillation, so one would expect the SDW to not be measurable. However, this can be explained by the only plausible explanation, which is that the roughness is carried up through the Mo, so the implanted muons are affected by the same roughness. Consequently, the muon implantation is weighted by the Gaussian associated with the top surface and it is the *difference* between the two roughness' that is significant, which is considerably smaller.[4]

The multi-periodic oscillations observed in this system are not as surprising as might be suggested at first inspection. There have been a number of observations of multi-periodic oscillations in the coupling of two FM layers across a non-magnetic wedge shaped spacer (using scanning electron microscopy with polarisation analysis), most notably in the Fe/Cr/Fe(001) system [Unguris *et al.*, 1991], with the superposition of short (~2 monolayers) and long (~10 monolayers) periods. Other systems to have been measured are Fe/Mn/Fe(001) [Purcell *et al.*, 1992], Co/Cu/Co(001)[Johnson *et al.*, 1992] and Fe/Au/Fe(001)[Fuss *et al.*, 1992]. However, the lengthscale of these oscillations are considerably longer than those measured here. These observations were only explained by the inclusion of discrete lattice sites, which is exactly what has been used to model the slow μSR results. If it were not for the inclusion of the "aliasing", the wavevectors measured would in

[4]although there is no *direct* evidence for this, which could be achieved by performing an off specular PNR experiment.

fact be considerably longer than the ones quoted in Table 6.5. As a consequence, the measurement presented in this work is an indirect microscopic measure of the Fermiology of Pb.

The oscillatory behaviour observed in the data resembles the RKKY interaction between magnetic impurities, so is a good starting point for the model used. However, even though the model used to fit this data was based on a modified RKKY interaction, there are some reasons why the simple RKKY model is unsuitable. For example, when the free electron approximation is used when calculating the spin susceptibility (assuming a uniform, continuous spin distribution in the FM layers), RKKY predicts a single short oscillation[Yafet, 1987], corresponding to the Fermi wavevector. Here two wavevectors are observed. Furthermore, the damping on the SDW for a simple RKKY picture is expected to go as $\sim 1/r^3$. Again, the model used here differs from the simple picture and suggests the damping is closer to $\sim 1/r$.

When a more realistic Fermi surface is used (i.e non-spherical), however, multiple-period oscillations are expected [Roth *et al.*, 1966], corresponding to spanning vectors connecting different parts of the Fermi surface. The magnitude of each oscillation corresponds to the curvature of the Fermi surface along the direction under consideration. Indeed, it is well known that anisotropic Fermi surfaces can have regions where scattering becomes more singular than in the isotropic electron liquid. When two portions of the Fermi surface are flat and parallel, nesting occurs and the k-dependant electron susceptibility diverges logarithmically, with a wavevector corresponding to the distance in k-space between the two portions of Fermi surface. To understand the effect of anisotropic Fermi surfaces further, one must calculate the real space electron-electron interaction $\Phi(\boldsymbol{R})$, taking into account indirect coupling due to conduction electrons between spins on lattice sites separated by $\boldsymbol{R}$. This is far beyond the scope of this thesis, so the main results will only be quoted here. The electron-electron interaction is [Roth *et al.*, 1966]

$$\Phi \boldsymbol{R} \propto \sum_{i,j} \frac{m_i^* m_j^*}{\boldsymbol{R}^3} \cos([\boldsymbol{k}_i - \boldsymbol{k}_j]\boldsymbol{R}) \tag{6.18}$$

where $\boldsymbol{k}_i$ and $\boldsymbol{k}_j$ are the wavevectors of two coupled electrons with an effective mass m^*, at a distance $\boldsymbol{R}$ from a magnetic impurity. As can be seen, even with the inclusion of an anisotropic Fermi surface, this is consistent with a simple free electron picture. However, the $\boldsymbol{R}$ dependence of $\Phi(\boldsymbol{R})$ becomes longer range in certain directions if m^* becomes infinite. For parallel flat or cylindrical portions of the Fermi surface, this is indeed the case. For two extended parallel flat regions of area A, the coupling becomes [Roth *et al.*, 1966] for $\boldsymbol{R}$ normal to the surface

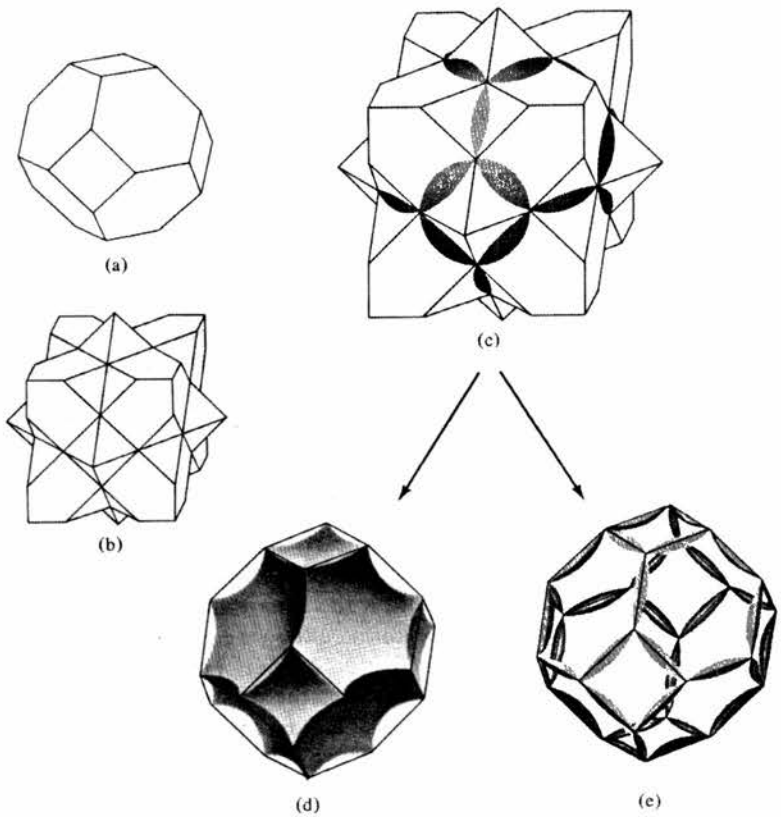

Figure 6.18: (a) The 1st Brillouin zone (BZ) for the fcc crystal structure. (b) Second BZ for an fcc crystal. (c) The free electron sphere for the trivalent fcc Bravais lattice. (d) Portion of the free electron sphere in the 2nd BZ translated back to the 1st zone. (e) Portion of the free electron sphere in the 3rd zone, translated back onto the first zone. [Ashcroft and Mermin, 1976].

$$\Phi \boldsymbol{R} \propto \sum_{i,j} A^2 \frac{\cos([k_i - k_j]\boldsymbol{R})}{(2\pi)^5 \boldsymbol{R}|\boldsymbol{v}_i - \boldsymbol{v}_j|} \tag{6.19}$$

and for a cylindrical region of length L, with $\boldsymbol{R}$ perpendicular to the axis of the cylinder

$$\boldsymbol{R} \propto \sum_{i,j} L^2 \frac{\sin([k_i - k_j]\boldsymbol{R})}{2(2\pi)^4 \boldsymbol{R}^2}. \tag{6.20}$$

Thus by simply including the effects of an anisotropic Fermi surface, one can account for a SDW with multiple oscillations which fall off as $\sim$1/r using a simple RKKY model.

Another model which can be used in this situation is a quantum confinement of conduction electrons in the Pb spacer layer [Bruno and Chappert, 1991; Bruno, 1991; Bruno and Chappert, 1992], leading to sharp features in the density of states

at specific q-vectors. In a trilayer consisting of a non-magnetic spacer between two aligned magnetic layers, where a majority of the conduction band in the spacer layer matches the conduction band in the magnetic layer, the majority of the electrons are not scattered at the interface. However, the mismatch of the conduction band at the Fermi level leads to enhanced scattering and reflection at the interface. In general, multiple reflections at the interface lead to destructive interference and these states can not exist. However, for specific wavevectors, the interference is constructive and electrons become bound in quantum well states. These wavevectors correspond to the same wavevectors as in the simple RKKY model. Both RKKY and quantum well model imply the existence of a SDW in the non-magnetic spacer layer.

The generic Fermi surface for an fcc crystal lattice (such as Pb) is to have the 1st Brillouin zone completely full, passing through the second zone into the third zone and at the corners (very slightly) into the fourth zone, shown in Figure 6.18. The schematic diagrams of the Fermi surface are for a trivalent fcc crystal. Pb is tetravalent, so the extended tubular zones in the 3^{rd} BZ are expected to be larger and flatter than those depicted here. The Pb Fermi surface is well understood by de Haas-van Alphen measurements [Gold, 1958]. It was found that along the $\langle 111 \rangle$ direction, the Fermi wavevector across the whole Fermi surface is 1.58Å^{-1} and the hole surface in the second zone and extended tubular surface in the third zone has a wavevector 0.23Å^{-1}. These values agree exceptionally well with the values obtained from the fits to Figure 6.15 and a damping of $\sim$0.86 is extremely close to the value expected from extended flat areas, as discussed above. It should be noted that when the two wavevectors are allowed to vary in the fit, they converge to these two values only when the initial guess parameters are sufficiently close to the final fit values. For example, if either wavevector initial guess is more than approximately 25% away from the values in Table 6.5, the fit fails to converge.

One further fit parameter is an energy dependent background field, corresponding to the applied magnetic field. This background peak consists of two components; the Mo capping layer is at the applied field and the beam spot size is energy dependent. The background due to the Mo layer has been intrinsically dealt with in the simulation, as the number of muons stopping inside the Mo layer is known. The beam having a different optimal focus for different energies can lead to the beam having a different spot size. The energy dependent background resulting from a different proportion of the muons missing the sample has been taken into account by adding a delta function to the P(B)'s at the applied field. The amplitude of the delta function has been constrained to be no more than 10% of the peak at

i	k_i	ϕ_i	n_i	A_i
1	0.23 (0.02)	2π (0.01)	0.86 (0.02)	21.5
2	1.58 (0.02)	$\pi/2$ (0.01)	0.86 (0.02)	21.5

Table 6.6: Parameters obtained from the fits for the below T_c data. Errors represent a 95% confidence interval.

the applied field resulting from the Mo, so is a relatively small contribution to the P(B)'s and does not change the relative amplitudes or positions of the SDW peaks.

6.3.4 Below T_c

Attention is now turned to the below T_c data. Figure 6.19 shows the probability distribution of magnetic field P(B) inside the sample in the normal metallic state at a temperature of 2.5K in a field of 200Oe, for muon implantation energies corresponding to those shown in Figure 6.14. These measurements were performed by field cooling immediately after the measurements were taken above T_c; nothing was changed in the experiment apart from the temperature, thus ensuring a direct comparison can be made between above and below T_c. Again, the fit is represented by the shaded region under the data. A summary of fit parameters is given in Table 6.6.

At first inspection, it is clear the SDW somewhat remarkably persists into the superconducting state, although there are some subtle differences. Secondly, it is immediately obvious very little magnetic flux expulsion occurs. To understand these differences, one must first turn to the field profile across a pure Pb thin film. The SPNR measurements discussed in the section above, on a 220 nm Pb/Mo film yields an answer. A non-magnetic sample is used, since using SPNR to study the effects of superconductivity is not currently feasible on FM/S/FM trilayers. This is because the much stronger spin-dependent scattering (Figure 6.12) from the magnetic layers masks the much weaker, subtle effects from the superconductor. Figure 6.13 clearly indicates the flux profile is rather different to that of a simple Meissner state, even in a pure Pb film. It is expected that the effects of the magnetic layer would only *enhance* the Type-II nature of the Pb.

Furthermore, the lack of flux expulsion in the Fe/Pb/Fe film (Figure 6.19) is even more obvious when considering slow μSR measurements performed on a pure

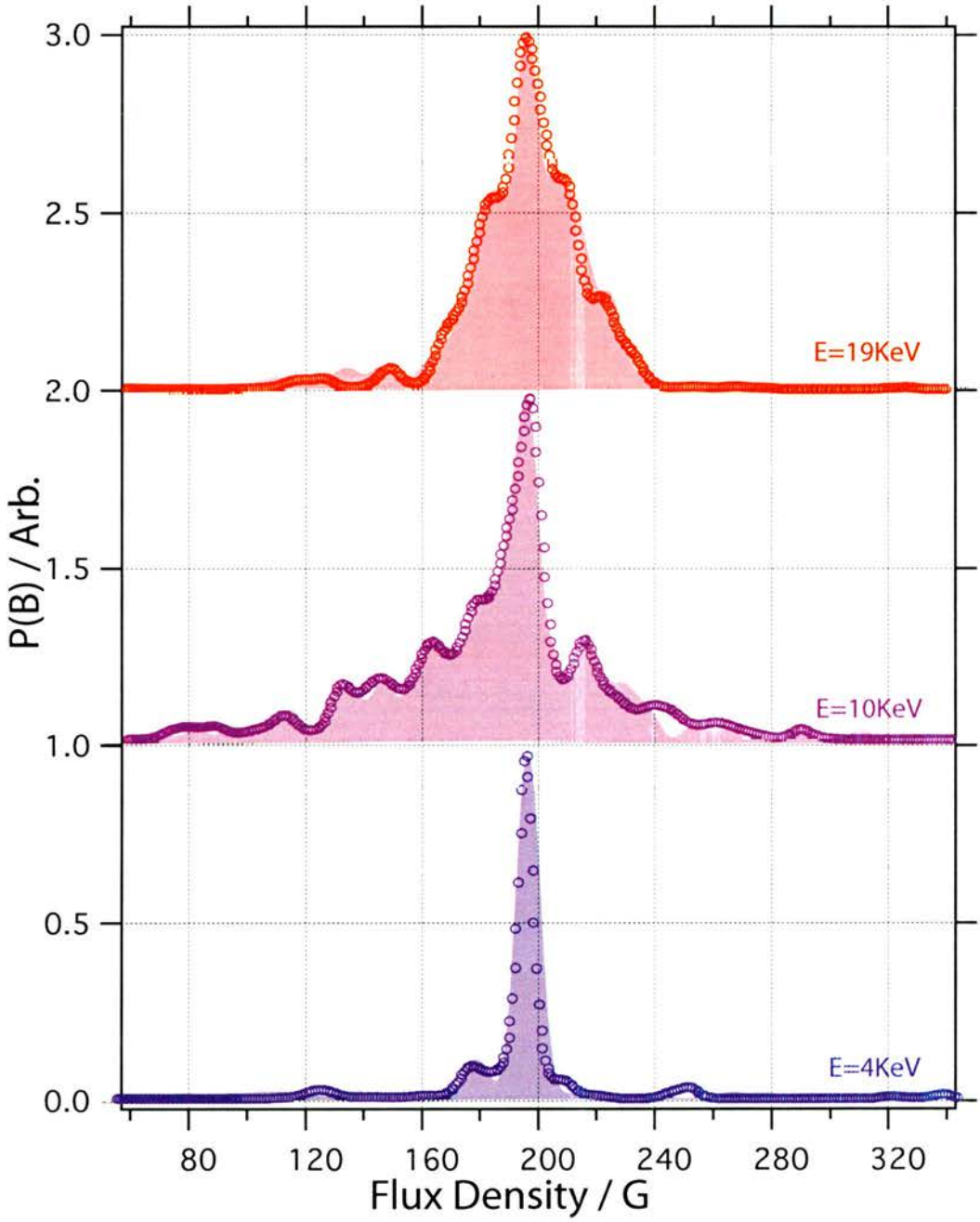

Figure 6.19: The field probability distribution P(B) for the sample, measured in an applied field of 200Oe, at temperature of 2.5 K. The shaded areas are fits involving a similar model to that used above T_c, except for a $\pi/2$ shift in the spatial phase of the short wavevector component of the SDW.

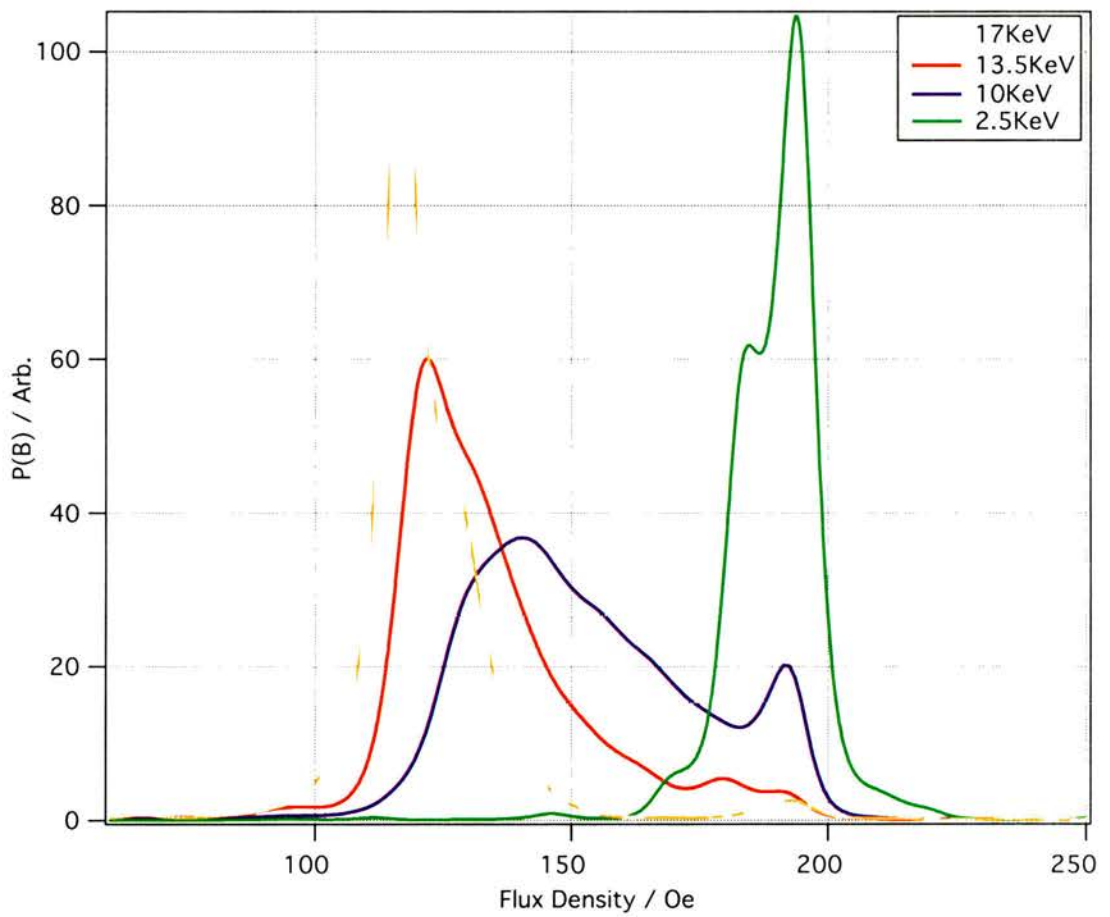

Figure 6.20: P(B)'s of a 3000Å Pb film for selection of implantation energies, demonstrating the main peak and energy dependent background peak.

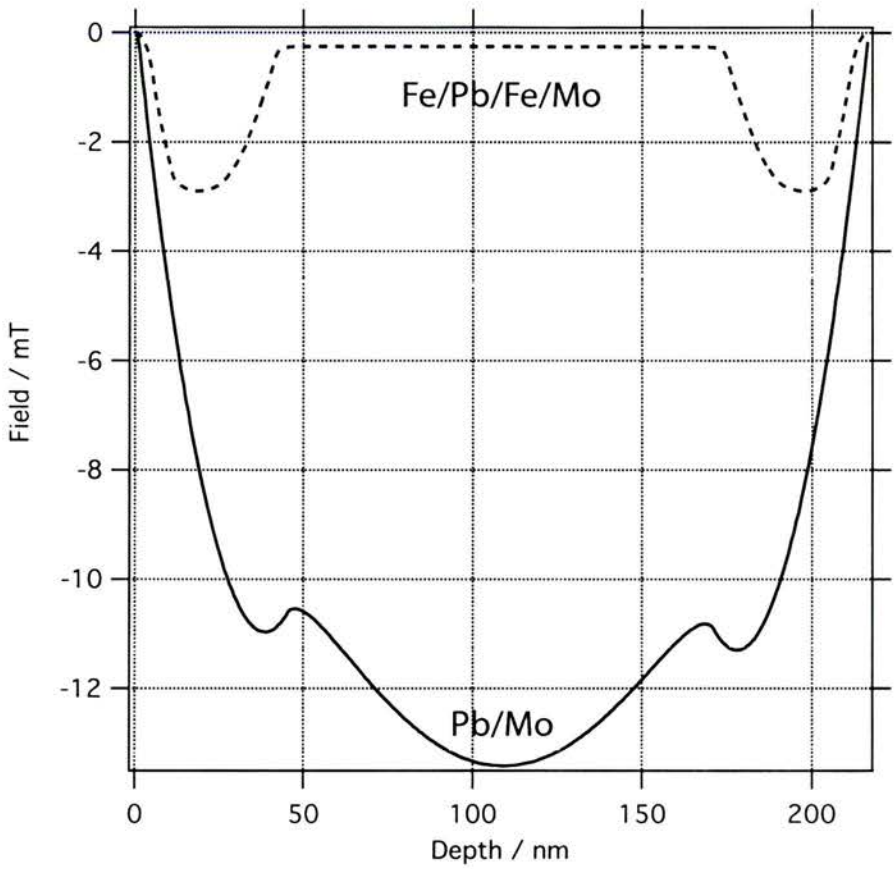

Figure 6.21: Comparison of the depth dependant flux density obtained from the fit to the spin asymmetry in Figure 6.12 and the flux density independently obtained in the below T_c slow muon results.

Pb film[5]. Figure 6.20 shows the probability of magnetic flux density for a number of muon implantation energies. Two peaks are evident; one very sharp peak, corresponding to an energy dependent background. This is due to the energy dependence in the proportion of muons missing the sample and the Mo capping layer. The other, broader peak, represents the magnetic flux density profile within the film, corresponding to the flux expulsion. This expulsion is not observed in the Fe/Pb/Fe slow μSR results, so the lack of expulsion has to be accounted for.

The model used for the Fe/Pb/Fe slow μSR data is consistent with a highly concentrated row of vortices down the centre of the sample, leading to a flux profile that exhibits a small amount of flux expulsion near the surface and a maximum in the centre. This is consistent with the picture obtained from the SPNR measurements of

[5]The dimensions of the thin film were Pb3000Å/Mo90Å and although the film is thicker, the data illustrates the point.

vortices on the Pb/Mo films. It should be noted, however, the μSR field profile was obtained by fitting the data *independently* of the SPNR measurements, as SPNR the experiment took place *after* the analysis of the μSR data. The SPNR experiment then confirmed the existence of vortices in the pure Pb films. The model consists of a simple linear superposition of the field profile shown in Figure 6.21 with the SDW.

A comparison of the field profile obtained from the μSR and the SPNR profile is shown in Figure 6.21. Although these profiles look to be somewhat different, they are in fact very similar. The only differences are as follows. A longer effective superconducting penetration depth and a slightly larger core size, as might be expected if the ferromagnetism acts to suppress the superconductivity. The SPNR measurements were also taken at the somewhat higher field of 480Oe, so the magnitude of the flux expulsion is larger. The concentration of vortices is considerably different between the two films, with the Fe/Pb/Fe film being consistent with a higher concentration of vortices than the pure Pb film. The SPNR measurements on the Pb film reveal a low concentration of vortices at 480Oe which increases in concentration at larger fields, although this data taken at higher fields remains difficult to model successfully and quantitative vortex concentrations are difficult to obtain. Again, a full solution of the current density within the film must be obtained from the GL equations.

Another point to note is that in the centre of the film, the field profile according to the muons is extremely flat. This may or may not be the case. As can be seen from Figure 6.14, the muon stopping depth is considerably broad at large implantation energies; and in order to probe the centre of the film, one must use large implantation energies. Consequently, the muons are not sensitive enough to detect the subtle changes of flux density in the centre of the film.

Further evidence for vortices exists if one plots the mode of the broad peak of the Pb/Mo slow μSR data as a function of implantation energy. This quantity is plotted in Figure 6.23. Although it is not a one-to-one relationship between energy and depth, as indicated by the Monte-Carlo simulations performed for this sample (Figure 6.22), an interesting phenomenon is observed. It is clear this *direct* measurement of flux density differs from that of a pure Meissner state. Note there is a remarkable similarity between this profile and the flux profile obtained from the SPNR fits, thus indicating the two techniques are indeed complementary. Although this is only elementary analysis, it does illustrate that this film is not in the Meissner state. A better form of analysis would be to fit the lineshapes directly, as performed on the Fe/Pb/Fe films. Unfortunately, this is a rather large undertaking and is not

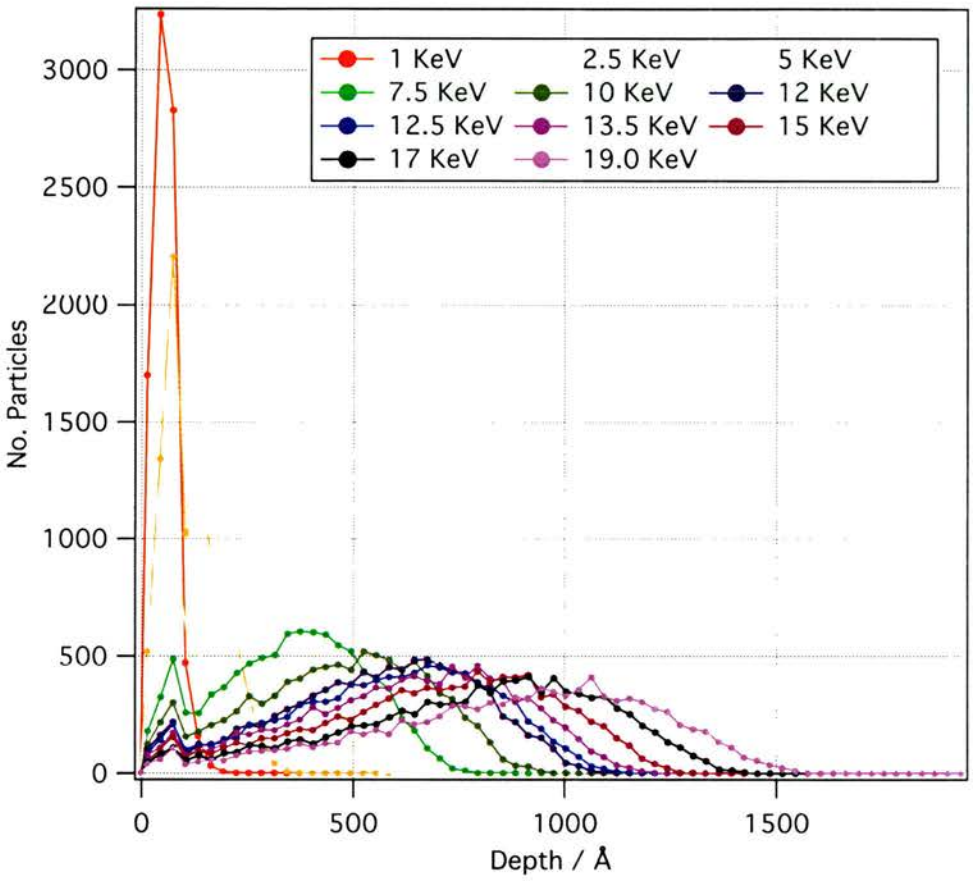

Figure 6.22: Stopping profile of a Pb3000/Mo90 film for all the different depths in Figure 6.23 for approximately 100,000 muons.

possible at this time.

The presence of vortices alone, however, does not account for the p(B) observed in the slow μSR data below T_c. In order to successfully model the field profile inside the Fe/Pb/Fe film, one must also take into account the spatial phase of the oscillations. The model shown in Figure 6.19 includes a $\pi/2$ change in phase of one of the spin density wave components compared to in the normal state, such that and are 2π and $\pi/2$ respectively. To illustrate this dramatic change further, Figure 6.24 compares a single set of data taken below T_c using a model identical to the fits of Figure 6.19, except that the phases were constrained to the values found above T_c. From this, it is clear that the phase shift is necessary to accurately model the data below T_c.

In FM/S/FM multilayers, T_c is known to oscillate as the FM layer thickness is changed (see discussion above). In samples similar to the Fe/Pb/Fe measured here, this non-monatonic behaviour has been observed using both magnetometry and transport measurements [Brown, 2002; Lazar *et al.*, 2000]. One of the competing

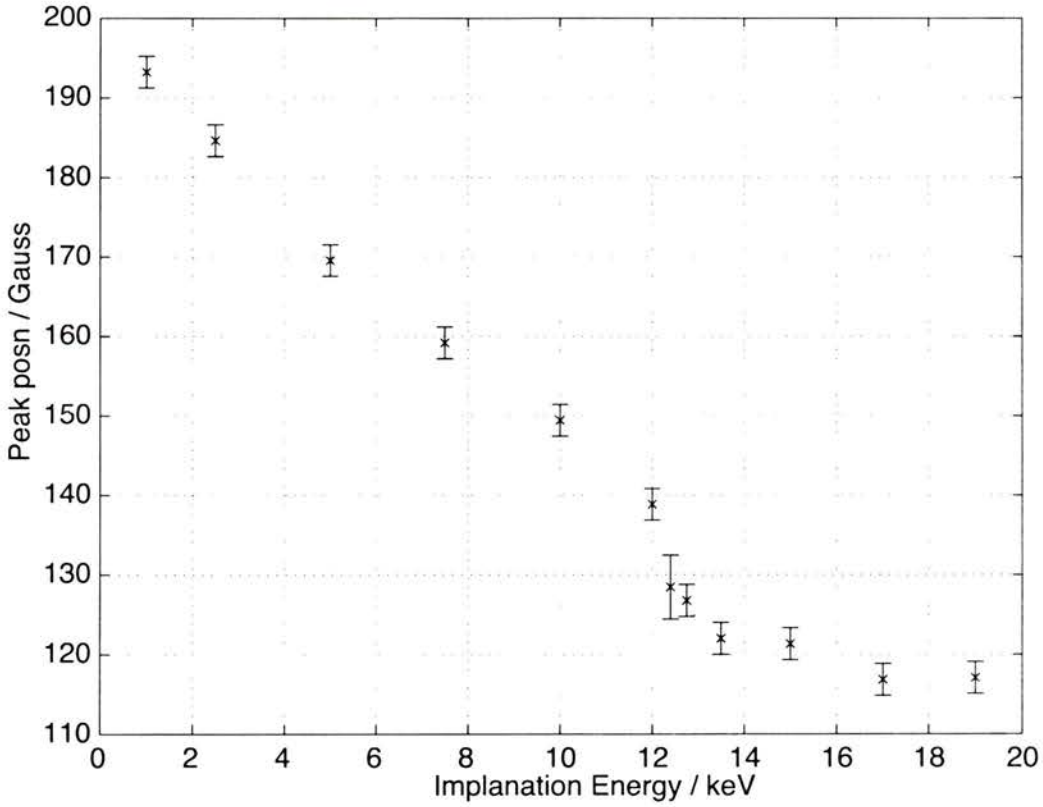

Figure 6.23: Mode flux density of the main peak in the P(B)'s shown in Figure 6.20, as a function of implantation energy. These were calculated by fitting a skewed Gaussian to the top of the peak position. The errors are only representing the uncertainty in peak position considering the quality of the lineshapes and closeness of the different peaks and are not a true statistical representation of the uncertainty in the positions.

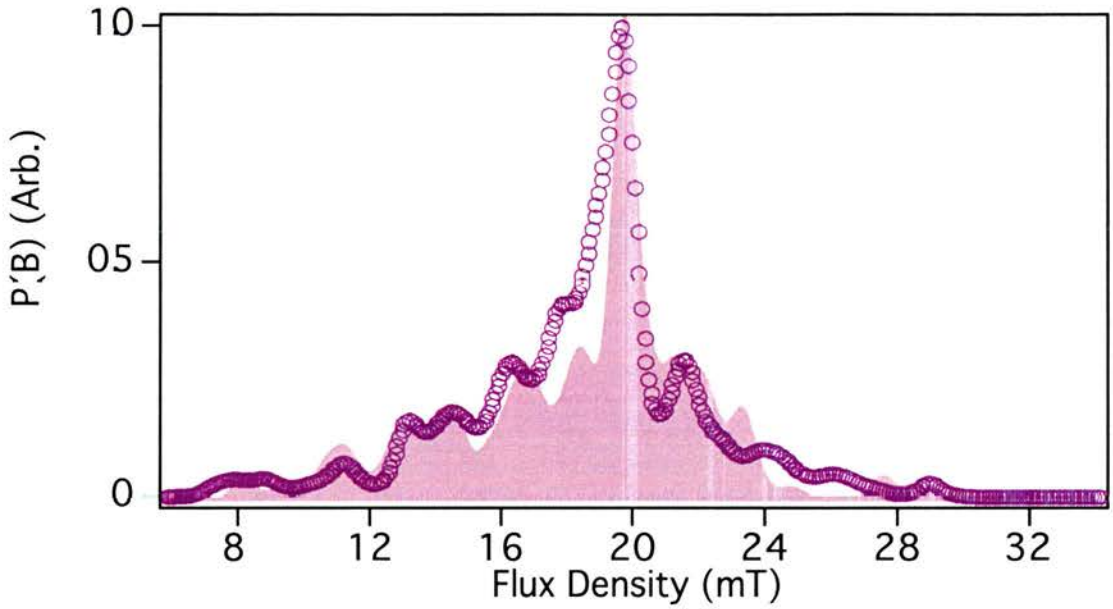

Figure 6.24: The 10KeV data set is shown in Figure 6.19 and compared with a model identical to the fits of Figure 6.19, except that the phases were constrained to the values found above T_c.

theories to explain this phenomenon of oscillating T_c's [Khusainov and Proshin, 1997, 2000] suggests the superconducting ground state is combined with a SDW in the FM layer, where the exchange field is periodically compensated by oscillations in the superconducting pair amplitude. This has been convincingly verified by a number of measurements of the tunnel current across a S/FM/S junction [Kontos *et al.*, 2001]. Considering this, it is not a large "leap of faith" that the spatially modulating wavefunction in the FM layer is related to the μSR results presented here, which confirms not only the persistence of a SDW inside the superconducting Pb, but also that the SDW *changes* in order to accommodate the superconductivity. Furthermore, the fits also require a ~25% increase in amplitude for both oscillations (Table 6.6) to describe the date, suggesting an *increase* in the coupling of spins below the superconducting transition. This suggests that what would normally be considered as competing forms of magnetic order do in fact intimately couple together to form a previously unobserved superconducting ground state.

It was proposed [Anderson and Suhl, 1959] that magnetic impurities present in a superconducting system could couple to the superconducting state. It was suggested that the suppression of the spin-susceptibility in the BCS superconducting state leads to a broad maximum at position in q-space, given by Equation 2.55. Substituting reasonable values ($k_f = 1.58\text{Å}^{-1}$ and $\xi = 550\text{Å}$) for the parameters of

the Fe/Pb samples gives q_D =0.287Å^{-1}, which is extremely close to the second component of the SDW. This proximity to the natural wavelength for spin polarisation may help explain why it is only this component of the SDW that undergoes a phase change in the superconducting state.

6.4 Concluding Remarks

In conclusion, an indirect measurement of the Fermiology of Pb has been possible, where a SDW is seen to exist in the Pb spacer layer between two Fe layers. The SDW is seen to have wavevectors that agree well with the Fermi surface of Pb. Direct evidence for the remarkable coexistence of the SDW with bulk superconductivity in the SC layer in a FM/SC/FM trilayer has been obtained. Furthermore, the apparent enhancement of the SDW amplitude in the superconducting state and moreover the $\pi/2$ phase shift of one component of the SDW below T_c, indicates a profound coupling of these two forms of spin order.

The intertwining of the phase of the superconducting wavefunction and that of SDW suggests interesting possibilities for novel electronic devices. It remains, however, a challenge to theory to explain fully this persistence and accommodation of the SDW to the onset of bulk superconductivity in these systems. There remains a possibility for further work in the investigation of the temperature dependence of the SDW, possibly in a thinner sample to remove the effects of vortices. The temperature dependence of the spatial phase change of the SDW, will hopefully lead to new insights in the theoretical mechanisms that describe superconducting/magnetic systems. Furthermore, the development of an algorithm to solve the GL equations, to obtain the current density of the non magnetic films from the SPNR and slow μSR data, should yield interesting results regarding the inter-vortex interactions in constrained dimensionality.

Chapter 7

Conclusions

7.1 Overview

The results presented in this thesis can be separated into three main sections. Firstly, a μSR study of LaNiSn has been carried out. Secondly, μSR, SANS and magnetisation measurements have been performed to understand the vortex state of LSCO for two different Sr dopings. Finally, an in-depth study of a Fe/Pb/Fe thin film yields important results, as the coupling of a conventional superconductor to magnetic order has been observed. The main conclusions and possible further work are outlined below in separate sections.

7.2 LaNiSn

The measurements on LaNiSn presented in Chapter 4 are the only microscopic study of its superconducting properties. In a FC state, a combination of Type-I and Type-II properties has been observed; both a vortex lattice and intermediate state is found to coexist. From the loss in asymmetry and the complex P(B)'s, the only plausible explanation for this compound in a field cooled state is an intermediate state with vortices in the Meissner state (between the normal regions). This has been explained by a combination of the sample geometry with respect to the applied magnetic field and the possible vicinity of LaNiSn to the Type-I/Type-II boundary. In the ZFC state, a Meissner state is only observed on the thermodynamic phase boundary where vortices begin to appear. The conclusions are only tentative, as a full study of the bulk magnetisation has not been carried out.

Future work:

- A full investigation of the ZFC and FC bulk magnetisation of the sample, which would confirm the microscopic measurements already performed.

- Heat capacity measurements would yield information on the sample's thermodynamic phase transitions.

7.3 $La_{2-x}Sr_xCuO_4$

The work presented n Chapter 5 on LSCO is the first systematic study of vortices on large, high quality LSCO single crystals using both microscopic and macroscopic techniques for two Sr dopings. Characterisation using DC magnetisation and AC susceptibility has also been carried out.

In the overdoped regime, SANS has been used to measure the first clear microscopic observation of a vortex lattice in LSCO and the first unambiguous evidence for a field induced hexagonal to square vortex lattice structural transition, which remains independent of temperature up to the FLL melting. At high applied fields, the square diffractions spots are found to lie along the CuO bond direction, which is incompatible with current theoretical constructs. The vortex lattice measurements are supported by μSR measurements, which also yield information on FLL pinning and provide further information regarding the melting transition. Combined with magnetisation data, it has been possible to draw a magnetic phase diagram for this compound.

In the underdoped regime, a preliminary SANS experiment at low applied magnetic fields suggests a BG with nominally a hexagonal structure, although this experiment proved somewhat difficult. More detailed information on the vortex lattice structure has been gathered with μSR. This is distinguished by the fact that it provides unambiguous evidence for a crossover with increasing field from a BG phase to a more disordered VG state. An upper limit on the cross over field has been estimated. The VG phase has been theoretically predicted in the literature, but not measured with local probes until now; this is the first measurement of a disordered VG state in a system of well coupled vortex lines. Furthermore, a detailed study of the evolution of short range order in the presence of weak pinning is of universal significance, as it provides useful experimental insights into space averaged many particle correlations in bulk systems. Experimental work that precedes the measurements presented here has either been limited to lower order correlation functions or to systems of reduced dimensionality.

Future work:

- A detailed SANS investigation of correlation lengths in the underdoped compound would provide invaluable information on the glass state and would support the μSR results presented in this thesis.

- A μSR measurement in the underdoped compound, with the field applied *directly* along the c-axis, is an important measurement to perform. This may determine the effectiveness of correlated pinning on the initial FLL disorder, thereby providing a means of measuring the different correlation lengths as a function of initial FLL disorder.

- Further analysis and calculations based on the data already obtained may yield a microscopic interpretation of the "second peak" observed in the magnetisation data - previously attributed to a crossover from single vortex pinning to collective vortex pinning behaviour, with no microscopic interpretation presented.

7.4 Fe/Pb/Fe Thin Films

The work presented Chapter 6 on Pb/Fe/Pb is the first depth resolved microscopic measurement on the magnetic properties of a superconducting/ferromagnetic heterostructure. Characterisation using SPNR, X-ray reflectometry, DC magnetisation and resistivity measurements have also been carried out.

Using the LEM technique, an indirect measurement of the Fermiology of Pb has been possible, where a SDW is seen to exist in the Pb spacer layer between two Fe layers. The SDW is seen to have wavevectors that agree well with the Fermi surface of Pb. Direct evidence for the remarkable coexistence of the SDW with bulk superconductivity in the SC layer in a FM/SC/FM trilayer has been obtained. Furthermore, the apparent enhancement of the SDW amplitude in the superconducting state and moreover the $\pi/2$ phase shift of one component of the SDW below T_c, indicates a profound coupling of these two forms of spin order. The intertwining of the phase of the superconducting wavefunction and that of SDW suggests interesting possibilities for novel electronic devices. It remains, however, a theoretical challenge to explain fully this persistence and accommodation of the SDW to the onset of bulk superconductivity in these systems.

Future work:

- A full investigation of the temperature dependence of the SDW may lead to new insights in the theoretical mechanisms that describe superconducting/magnetic systems.

• Measurements should be performed on similar thin films, but with the Pb thickness considerably thinner to remove the effects of vortices. This will be a challenging experiment, as the reduced superconducting critical temperature may be too low for the sample cryostat.

• Some questions remain as to whether this phenomenon (SDW persisting into the superconducting state) is a "special case" or a generic property of superconducting/magnetic multilayers. A full investigation of different superconducting (e.g Pb, Nb, PbIn...) and magnetic (e.g rare earths, Co..) multilayers would provide answers to these questions.

• The development of an algorithm to solve the GL equations, to obtain the current density of the non magnetic films from the SPNR and slow μSR data, should yield interesting results regarding the inter-vortex interactions in constrained dimensionality.

• An off specular SPNR investigation of the Pb/Mo thin films would offer conclusive information on the roughness of the thin films.

7.5 Possible Future Publications

Publications already in print can be found in Appendix C. Possible publications in the near future, as a direct result of the work presented in this thesis, are as follows:

1 Probing triplet correlations of flux lines in vortex glass phases through muon-spin rotation experiments.
Menon GI, Drew A, Divakar UK, Lee SL, Gilardi R, Mesot J, Ogrin FY, Charalambous D, Forgan EM, Momono N, Oda M, Dewhurst C, Baines C.
Submitted to Nature.

2 Coexistence and coupling of superconductivity and magnetism in thin film structures.
Drew A, Lee SL, Divakar U, Charalambous D, Potenza A, Marrows C, Luetkens H, Suter A, Prokscha T, Morenzoni E, Ucko D, Forgan EM.
Submitted to Physical Review Letters.

3 Confined vortices in Pb thin films.
Drew A, Wismayer M, Heron DOG, Lee SL, Potenza A, Marrows C.
In preparation for submission to Physical Review Letters.

4 Direct measurement of a vortex glass correlation lengths using SANS
Drew A, Divakar UK, Lee SL, Gilardi R, Mesot J, Ogrin FY, Charalambous D, Forgan EM, Momono N, Oda M, Dewhurst C.
In preparation for submission to Physical Review Letters.

Chapter 8

Appendices

8.1 Appendix A - The SPNR Optical Model

SPNR can be understood in terms of the Schrödinger equation for a neutron with a wavefunction $\Psi(\boldsymbol{r})$ [Blundell, 1992]

$$\left[\frac{-\hbar^2}{2m_n}\nabla^2 + V(\boldsymbol{r})\right]\Psi(\boldsymbol{r}) = E\Psi(\boldsymbol{r}) \tag{8.1}$$

where m_n is the neutron mass and $V(\boldsymbol{r})$ is the neutron potential energy. The neutron wavefunction can be written in terms of the neutron wavevector parallel to the surface

$$\Psi(\boldsymbol{r}) = \psi(y)e^{ik_{\|}r_{\|}} \tag{8.2}$$

such that

$$\left[\frac{d^2}{dy^2} + \left[\frac{2m_n}{\hbar^2}(E-V) - k_{\|}^2\right]\right]\psi(y) = 0. \tag{8.3}$$

The perpendicular wavevector, shown in Figure 6.10, is the only scattering vector dealt with, such that

$$\frac{\hbar^2}{2m_n}(q^2 + k_{\|}^2) = (E-V) \tag{8.4}$$

where the wavevectors for each scattering neutron are a function of time, due to the polychromatic pulsed source at ISIS. For a multilayer sample containing n regions, numbered so that 1 is a vacuum, n is the substrate and the sputtered regions are $2 \leq \alpha < n$, for the α region one has to solve

$$\left[\frac{d^2}{dy^2} + q_\alpha^2\right]\psi(y) = 0 \tag{8.5}$$

where

$$q_\alpha = \left[\frac{2m_n}{\hbar^2}(E_\perp - V_\alpha)\right]^{\frac{1}{2}} \tag{8.6}$$

and $E_\perp = E - \hbar^2 k_{\|}^2/2m_n$. The solution to this is a sum of right and left travelling waves

$$\psi_\alpha(y) = a_\alpha e^{iq_\alpha(y=y_\alpha)} + b_\alpha e^{-iq_\alpha(y=y_\alpha)}. \tag{8.7}$$

If at the interface $y = y_\alpha$, $\psi_\alpha(y)$ is represented by a vector

$$\psi_\alpha(y) = \begin{pmatrix} a_\alpha \\ b_\alpha \end{pmatrix} \tag{8.8}$$

then

$$\begin{pmatrix} 1 \\ r \end{pmatrix} = \begin{pmatrix} M_{11} & M_{12} \\ rM_{21} & M_{22} \end{pmatrix} \begin{pmatrix} t \\ 0 \end{pmatrix} \tag{8.9}$$

since at the first interface, $y = y_1 = 0$ so $\psi = \binom{1}{r}$ and at the last interface $y = y_{n-1}$ so $\psi = \binom{t}{0}$. The transmission and specular reflection coefficients are defined $t = 1/M_{11}$ and $r = M_{21}/M_{11}$. The transfer matrix $\boldsymbol{M}$ is defined

$$\boldsymbol{M} = \boldsymbol{D}^{-1}(q_1) \left[\prod_{j=2}^{N-1} [\boldsymbol{D}(1_j)\boldsymbol{P}(q_j, d_j]\boldsymbol{D}^{-1}(q_j)] \right] \boldsymbol{D}(q_N) \tag{8.10}$$

where $\boldsymbol{D}(q_\alpha)$ is the transmission matrix, $\boldsymbol{P}(q_\alpha, d_\alpha)$ is the propagation matrix and $d_\alpha = y_\alpha - y_{\alpha-1}$ is the width of the αth region. By applying the boundary conditions that ψ and $d\psi/dy$ are constant, it can be shown [Blundell, 1992]

$$\boldsymbol{D}(q_\alpha) = \begin{pmatrix} 1 & 1 \\ q_\alpha & -q_\alpha \end{pmatrix} \tag{8.11}$$

and

$$\boldsymbol{P}(q_\alpha, d_\alpha) = \begin{pmatrix} e^{-iq_\alpha d_\alpha} & 0 \\ 0 & e^{-iq_\alpha d_\alpha} \end{pmatrix} \tag{8.12}$$

The neutron undergoes both nuclear and magnetic scattering, schematically shown in Figure 6.10b. Consequently, the potential energy of a neutron in the αth region is the sum of a nuclear term and a magnetic term

$$V_\alpha = \frac{\hbar^2}{2\pi m_n} \rho_\alpha b_\alpha - \boldsymbol{\mu}_n \cdot \boldsymbol{B}_\alpha \tag{8.13}$$

where $\boldsymbol{\mu}_n$ is the neutron magnetic moment, b_α is the coherent scattering length, $\boldsymbol{B}_\alpha$ is the field due to the magnetisation in region α and ρ_α is the atomic density. Thus, the reflectivity depends on the relative orientation of the neutron spin and magnetic field in each layer. Consequently, it can be shown that the spin dependent transfer matrix is [Blundell, 1992]

$$\boldsymbol{M} = \boldsymbol{D}^{-1}(q_1, q_1)\boldsymbol{R}(\theta_{1.2}) \left[\prod_{\alpha=2}^{N-1} \{\boldsymbol{D}(q_\alpha^\uparrow, q_\alpha^\downarrow)\boldsymbol{P}(q_\alpha^\uparrow, q_\alpha^\downarrow, d_\alpha)\boldsymbol{D}^{-1}(q_\alpha^\uparrow, q_\alpha^\downarrow)\boldsymbol{R}(\theta_{\alpha,\alpha+1})\} \right] \boldsymbol{D}(\alpha_N, \alpha_N), \tag{8.14}$$

where the 4x4 generalisation of the transmission matrices is

$$\boldsymbol{D}(q_\alpha^\uparrow, q_\alpha^\downarrow) = \begin{pmatrix} \boldsymbol{D}(q_\alpha^\uparrow) & 0 \\ 0 & \boldsymbol{D}(q_\alpha^\downarrow) \end{pmatrix}, \tag{8.15}$$

the 4x4 generalisation of the propagation matrix is

$$\boldsymbol{P}(q_\alpha^\uparrow, q_\alpha^\downarrow, d_\alpha) = \begin{pmatrix} \boldsymbol{D}(q_\alpha^\uparrow, d_\alpha) & 0 \\ 0 & \boldsymbol{D}(q_\alpha^\downarrow, d_\alpha) \end{pmatrix} \tag{8.16}$$

and the matrix rotating the magnetic field at the interface $\alpha - (\alpha + 1)$ by an angle $\theta_{\alpha,\alpha+1}$ is

$$\boldsymbol{R}(\theta_{\alpha,\alpha-1}) = \begin{pmatrix} \cos(\theta_{\alpha,\alpha+1}/2)\boldsymbol{I} & \sin(\theta_{\alpha,\alpha+1}/2)\boldsymbol{I} \\ -\sin(\theta_{\alpha,\alpha+1}/2)\boldsymbol{I} & \cos(\theta_{\alpha,\alpha+1}/2)\boldsymbol{I} \end{pmatrix} \tag{8.17}$$

where $\boldsymbol{I}$ is the identity matrix. From this spin dependent transfer matrix, it is possible to write [Blundell, 1992]

$$\begin{aligned} t_u^\uparrow &= M_{33}/(M_{11}M_{33} - M_{13}M_{31}) \\ t_u^\downarrow &= -M_{31}/(M_{11}M_{33} - M_{13}M_{31}) \\ r_u^\uparrow &= (M_{21}M_{33} - M_{23}M_{31})/(M_{11}M_{33} - M_{13}M_{31}) \\ r_u^\downarrow &= (M_{41}M_{33} - M_{43}M_{31})/(M_{11}M_{33} - M_{13}M_{31}) \end{aligned}$$

$$\begin{aligned} t_d^\uparrow &= -M_{13}/(M_{11}M_{33} - M_{13}M_{31}) \\ t_d^\downarrow &= M_{11}/(M_{11}M_{33} - M_{13}M_{31}) \\ r_d^\uparrow &= (M_{23}M_{11} - M_{21}M_{13})/(M_{11}M_{33} - M_{13}M_{31}) \\ r_d^\downarrow &= (M_{43}M_{11} - M_{41}M_{13})/(M_{11}M_{33} - M_{13}M_{31}) \end{aligned} \tag{8.18}$$

where the subscripts on M are the indices to the matrix elements of M and the u and d correspond to the incident neutron spin. The spin asymmetry is defined

$$S = \frac{R_\uparrow - R_\downarrow}{R_\uparrow + R_\downarrow} \tag{8.19}$$

which can be rewritten in terms of the four reflection processes in Equation 8.18 as

$$S = \frac{|r_u^{\uparrow}|^2 + |r_u^{\downarrow}|^2 - |r_d^{\uparrow}|^2 - |r_d^{\downarrow}|^2}{|r_u^{\uparrow}|^2 + |r_u^{\downarrow}|^2 + |r_d^{\uparrow}|^2 + |r_d^{\downarrow}|^2}. \tag{8.20}$$

8.2 Appendix B - Non-Linear Regression

Every non-linear regression method follows these steps:

1. Start with an initial estimated value for each variable in the equation. The program can not determine the best-fit values unless it is first given some estimates. In most cases, these estimates do not have to be very accurate.
2. Generate the curve defined by the initial values and calculate the sum-of-squares.
3. Adjust the variables to make the curve represent the data points more accurately.
4. Repeat for many iterations.
5. Stop the calculations when the adjustments are within a stopping criteria (the sum of squares is within a certain limit).

The precise values obtained will depend in part on the initial values chosen in Step 1 and the stopping criteria of Step 5. This means that repeat analyses of the same data will not always give exactly the same results. For Step 3, the algorithm used in the work in this thesis is the method of Marquardt and Levenberg, which blends linear descent and Gauss-Newton methods of descent.

If each data point (x_i, y_i) has its own known standard deviation σ_i, then the maximum likelihood estimate of the model parameters is obtained by minimising the quantity

$$\chi^2 = \sum_{i=1}^{N} \left(\frac{y_i - y(x_i; a_1 \cdots a_M)}{\sigma_i} \right)^2 \tag{8.21}$$

where parameters $a_1, a_2, \cdots, a_M$ are varied to minimise χ^2.

The method of linear descent follows a very simple strategy. Starting from the initial values try increasing each parameter a small amount. If the sum of squares goes down, continue. If the sum of squares goes up, reverse the direction of change. Repeat as many times as necessary, reducing the sum of squares on each step wherever possible.

Sufficiently close to a minimum, the χ^2 function in parameter space is expected to be well approximated by a quadratic form [Press *et al.*, 1986], which can be written as

$$\chi^2(a) \approx \gamma - \boldsymbol{d} \cdot \boldsymbol{a} + \frac{1}{2} \boldsymbol{a} \cdot \boldsymbol{D} \cdot \boldsymbol{a} \tag{8.22}$$

where $\boldsymbol{d}$ is a vector with a length M and $\boldsymbol{D}$ is an $M \times M$ matrix[1]. If the approximation is a good one, then it is possible to jump directly from the current trial parameters $\boldsymbol{a}_{cur}$ to the correct ones $\boldsymbol{a}_{min}$

$$\boldsymbol{a}_{min} = \boldsymbol{a}_{cur} + \boldsymbol{D}^{-1} \cdot [-\nabla\chi^2(\boldsymbol{a}_{cur}).] \tag{8.23}$$

However, if the approximation is poor, there is no option but to use a linear step, thus

$$\boldsymbol{a}_{new} = \boldsymbol{a}_{cur} - C\nabla\chi^2(\boldsymbol{a}_{cur}) \tag{8.24}$$

where the constant C is small enough not to exhaust the down hill direction.

The Gauss-Newton method is somewhat more complex. As with the method of linear descent, it starts by computing how gradient of χ^2 with respect to the parameters. If the equation is linear, this is enough information to determine the shape of the entire sum of squares surface and thus calculate the best fit values in one step. With nonlinear equations, the Gauss-Newton method will not find the best-fit values in one step, but that step usually improves the fit. After repeating many iterations, the best fit is obtained. The first and second order derivative (Hessian) of χ^2 are used to estimate the direction and distance of the new values of $\boldsymbol{a}$

$$\boldsymbol{a}_{new} = \boldsymbol{a}_{cur} - \left[\frac{\left(\frac{\partial\chi^2(\boldsymbol{a}_{cur})}{\partial a_k} \right)}{C\left(\frac{\partial^2\chi^2(\boldsymbol{a}_{cur})}{\partial a_k \partial a_l} \right)} \right]. \tag{8.25}$$

The gradient is

$$\frac{\partial\chi^2(\boldsymbol{a}_{cur})}{\partial a_k} = -2\sum_{i=1}^{N} \frac{[y_i - y(x_i;\boldsymbol{a})]}{\sigma_i^2} \frac{\partial y(x_i;\boldsymbol{a})}{\partial a_k} \tag{8.26}$$

and second derivative is

$$\frac{\partial^2\chi^2(\boldsymbol{a}_{cur})}{\partial a_k \partial a_l} = 2\sum_{i=1}^{N} \frac{1}{\sigma_i} \left[\frac{\partial y(x_i;\boldsymbol{a})}{\partial a_k} \frac{\partial y(x_i;\boldsymbol{a})}{\partial a_l} - [y_i - y(x_i;\boldsymbol{a})] \frac{\partial^2 y(x_i;\boldsymbol{a})}{\partial a_k \partial a_l} \right] \tag{8.27}$$

for $k = 1, 2, \cdots, M$. Second derivatives occur because the gradient already has a dependence on $\partial y(x_i;\boldsymbol{a})/\partial a_k$. The second derivative term can be dismissed when it is zero or small enough to be negligible when compared to the term involving the first derivative. Inclusion of the second-derivative term can in fact be destabilising if the model fits badly or is contaminated by outlier points that are unlikely to be

[1] $\boldsymbol{D}$ is in fact the Hessian matrix.

offset by compensating points of opposite sign.

The method of linear descent tends to work well for early iterations, but works slowly when it gets close to the best-fit values (and the surface is nearly flat). In contrast, the Gauss-Newton method tends to work badly in early iterations, but works very well in later iterations. The two methods are blended in the method of Marquardt (also called the Levenberg-Marquardt method). It uses the method of linear descent in early iterations and then gradually switches to the Gauss-Newton approach.

The method is based on two elementary, but important, insights. Consider the constant C in Equation 8.24. There is no information about the scale (or even the order of magnitude!) of C in the gradient. Marquardts first insight [Press *et al.*, 1986] is that the components of the Hessian matrix, even if they are not directly usable, give information about the order of magnitude scale of the problem. His second insight was to realise it is possible to combine Equations 8.23 and 8.25 if a new matrix α is defined

$$\alpha_{jj} = \frac{\partial^2 \chi^2(\boldsymbol{a}_{cur})}{\partial a_j^2}(1 + C) \tag{8.28}$$

and for $j \neq k$

$$\alpha_{jk} = \frac{\partial^2 \chi^2(\boldsymbol{a}_{cur})}{\partial a_j \partial a_k} \tag{8.29}$$

such that

$$\boldsymbol{a}_{new} = \boldsymbol{a}_{cur} - \left[\frac{\left(\frac{\partial \chi^2(\boldsymbol{a}_{cur})}{\partial a_k} \right)}{\alpha_{kl}} \right]. \tag{8.30}$$

when C is very large, this is exactly Equation 8.25. When C approaches zero, it reverts to Equation 8.23.

The Marquardt recipe for a given set of parameters is then

1. Calculate $\chi^2(\boldsymbol{a})$.
2. Pick a modest value of C, for example 10^{-4}.
3. If $\chi^2(\boldsymbol{a} + \delta\boldsymbol{a}) \geq \chi^2(\boldsymbol{a})$, increase C by a factor of 10; goto 2.
4. If $\chi^2(\boldsymbol{a} + \delta\boldsymbol{a}) \leq \chi^2(\boldsymbol{a})$, decrease C by a factor of 10, substitute $\boldsymbol{a}$ with $\boldsymbol{a} + \delta\boldsymbol{a}$; goto 2.
5. 10 print "home"; 20 print "sweet"; 30 goto 10;

It is also necessary to have a stop condition, which is defined as the nth occasion χ^2 decreases by a negligible amount.

It is common practice to summarise the errors in parameter estimation in the form of confidence limits. A confidence region (or confidence interval) is just a region of that M-dimensional space that contains a certain percentage of the total probability distribution. For a given confidence region of 99%, there is a 99% chance that the true parameter values fall with in this region around the fitted value. Most errors in this thesis are quoted as confidence intervals, defined as constant χ^2 boundaries in parameter space.